Thèse

présentée pour l'obtention du titre de

Docteur de l'Université Henri Poincaré (Nancy)

en Géosciences

par

Rakhim UTEYEV

ÉTUDE THERMODYNAMIQUE ET EXPÉRIMENTALE DU CYCLE GÉOCHIMIQUE DU SOUFRE DANS LES BASSINS SÉDIMENTAIRES

A THERMODYNAMIC AND EXPERIMENTAL STUDY OF THE GEOCHEMICAL CYCLE OF SULFUR IN SEDIMENTARY BASINS

Date de soutenance : 10 mars 2011

Membres du Jury :

Rapporteurs :	M. B. FRITZ	*Directeur de Recherche (CNRS), LHYGES, Strasbourg*
	M. B. KUANDYKOV	*Président, Meridian Petroleum, Almaty (Kazakhstan)*
Examinateurs :	M. L. MARTINEZ	*Professeur, Université Henri Poincaré, Nancy*
	M. M. KARIMOV	*Ingénieur, KMG, Astana (Kazakhstan)*
Directeurs de thèse :	M. J. PIRONON	*Directeur de Recherche (CNRS), G2R, Nancy*
	M. L. RICHARD	*Géochimiste, AMPHOS 21, Barcelone (Espagne)*
	M. T. YENSEPBAYEV	*Professeur, KazNTU, Almaty (Kazakhstan)*
Invités :	M. E. BROSSE	*Ingénieur de Recherche, IFP, Rueil-Malmaison*
	M. P. LAPOINTE	*Ingénieur, Total Exploration Inc., Houston (USA)*
	M. H. PETERS	*Géochimiste, Shell International B.V., La Haye (Pays-Bas)*

Remerciement

Je remercie très chaleureusement Monsieur Jacques Pironon, Directeur de recherche CNRS et directeur de cette thèse, de m'avoir accepté, et de m'avoir donné sa confiance pour la réalisation de ce travail. Ses connaissances professionnelles et son approche pédagogique m'ont beaucoup aidé, je lui en suis vivement reconnaissant.

Je tiens à remercier très sincèrement Monsieur Laurent Richard, co-directeur de cette thèse, de m'avoir formé au travail de chercheur. Son expérience professionnelle et ses conseils m'ont beaucoup aidé et me seront précieux pour le futur. J'ai appris beaucoup de choses en observant sa façon de travailler et ses approches.

Je tiens également à remercier Monsieur Bertrand Fritz et Monsieur Baltabek Kuandykov, ainsi que les membres du jury, Monsieur Luis Martinez, Monsieur Marat Karimov, les membres invités Monsieur Etienne Brosse, Monsieur Philippe Lapointe et Monsieur Henning Peters d'avoir accepté de juger ce travail et de participer à ma soutenance.

Je pense bien sur aux forces vives du G2R. Je remercie beaucoup Monsieur Jean Dubessy pour ses conseils toujours précieux, sa disponibilité et ses qualités humaines. Je remercie Aurélien Randi pour son professionnalisme et sa bonne humeur quotidienne. Je remercie Pierre Faure pour ses analyses géochimiques et sa sympathie, Cédric Carpentier pour ses conseils en pétrographie des roches carbonatés, Cédric Demeurie pour sa rapidité à la confection des lames. Je remercie également Monsieur Nguyen-Trung Chinh pour ses conseils scientifiques et sa présence amicale. Je remercie aussi Marcel Elie pour son aide et support précieux.

Je tiens également à remercier Monsieur Michel Cathelineau et à nouveau Monsieur Jacques Pironon pour leur excellent management de G2R, ainsi que les autres personnes indispensables du labo, Roland Mairet, Patrick Lagrange, Marie-Odile Campadieu, Laurence Moine, Pierre Schuhmacher, Gilles Bessaque, Pascal Robert, Christine Léonard et notre chère Zira.

I would like to, sincerely thank Mr. Kenzhebek Ibrashev and Mr. Marat Karimov for their assistance and help in obtaining of the core samples, so needed for the thesis. I also thank to Mrs. Zeinep Yesbulatova for her support and guidance. I would also express my

Résumé

Le soufre est présent dans les systèmes pétroliers à la fois sous forme organique et minérale. Il est impliqué dans de nombreuses réactions d'oxydoréduction qui affectent la qualité des huiles (par des réactions de sulfuration ou de désulfuration) et du gaz naturel (par la génération de H_2S en contexte de réduction thermochimique des sulfates), ainsi que la porosité des roches réservoirs (par la dissolution de l'anhydrite ou la précipitation de soufre élémentaire ou de pyrobitume). Ces réactions sont gouvernées par la température (et dans une moindre mesure la pression), les conditions d'oxydoréduction et la composition chimique globale du système.

La thèse comporte trois parties : (1) une étude thermodynamique des réactions chimiques impliquant le soufre dans les bassins sédimentaires ; (2) une étude expérimentale des réactions de sulfuration et de désulfuration des composés organiques ainsi que de la réduction thermochimique des sulfates; (3) une étude pétrographique et d'inclusions fluides sur des échantillons d'un réservoir carbonaté du bassin Pré-Caspien.

Etude thermodynamique

- Des calculs thermodynamiques ont été réalisés afin de caractériser les réactions chimiques qui se produisent entre les minéraux, les eaux de formation, les hydrocarbures et les composés organiques soufrés dans les réservoirs pétroliers riches en soufre, et ce en fonction des conditions de température, de pression et d'oxydoréduction caractéristiques de ces réservoirs. Des calculs ont également été réalisés dans le cadre du développement d'un modèle thermodynamique quantitatif pour la réduction thermochimique des sulfates (TSR).

- Des calculs thermodynamiques ont également suggéré la possibilité d'une désulfuration de pétrole *in situ* et d'une précipitation de soufre élémentaire suite à des réactions entre H_2S et des composés organiques soufrés dans le contexte de la réinjection de mélanges de gaz acides CO_2-H_2S dans les réservoirs pétroliers. La vérification de cette hypothèse fait ensuite l'objet d'une étude expérimentale.

Etude expérimentale

- Des expériences de sulfuration/désulfuration de composés organiques ont été réalisées dans des capsules en or à 120-200°C et 500 bar pendant deux semaines ou plus. A la fin des expériences, les composés solides et liquides ont été analysés par chromatographie gazeuse couplée à la spectrométrie de masse (GC-MS) tandis que les composés gazeux l'ont été par microspectrométrie Raman. Certains composés organiques soufrés (thiolanes et thiophènes) réagissent avec H_2S pour former des disulfures ou des trisulfures et/ou du soufre élémentaire, tandis que les benzo[*b*]- et dibenzo[*b,d*]thiophènes ne réagissent pas. Une interprétation thermodynamique de ces observations est proposée.

- Des réactions entre des solutions aqueuses de sulfate ($MgSO_4$ et Na_2SO_4) et des hydrocarbures (*n*-octane et 1-octène), simulant la réduction thermochimique des sulfates (TSR), ont également été étudiées dans des capillaires en silice à 300-400°C pendant quelques jours. La production de H_2S dans les capillaires a été suivie par microspectrométrie Raman.

Etude pétrographique et d'inclusions fluides

- Une étude pétrographique (microscopie optique, cathodoluminescence, microscopie électronique à balayage (MEB) et microsonde électronique) et d'inclusions fluides (microthermométrie, microspectrométrie Raman, spectroscopie infrarouge et microscopie confocale) a été réalisée sur des échantillons provenant d'un réservoir carbonaté du bassin Pré-Caspien. L'analyse pétrographique a permis d'obtenir des informations sur l'histoire diagénétique du bassin. Les conditions de piégeage des fluides dans le réservoir et leur composition (CO_2-H_2S-CH_4-H_2O) ont été déterminées par l'étude des inclusions fluides.

Mots-clefs : *sulfure d'hydrogène (H_2S), bassins sédimentaires, réduction thermochimique des sulfates (TSR), soufre élémentaire, composés organiques soufrés, thermodynamique, expériences en autoclaves, inclusions fluides.*

Abstract

Sulfur occurs in petroleum systems as both organic compounds and minerals as well as under different oxidation states. It is involved in a number of redox reactions which may impact the quality of crude oils (through sulfurization or desulfurization reactions) and natural gas (through the generation of H_2S during thermochemical sulfate reduction), as well as the petrophysical properties of reservoir rocks (through the dissolution of anhydrite and the precipitation of elemental sulfur and pyrobitumen). These reactions are controlled by temperature (and to a lesser extent pressure), the redox conditions, and the overall chemical composition of the system representing the petroleum reservoir.

The thesis consists of three parts: (1) a thermodynamic study of chemical reactions involving sulfur which occur in sedimentary basins; (2) an experimental simulation of sulfurization and desulfurization reactions of organic compounds, as well as of thermochemical sulfate reduction; and (3) a petrographic and fluid inclusion study of carbonate rock samples from a sulfur-rich hydrocarbon reservoir of the northern Caspian Sea.

Thermodynamic study

- In order to characterize the chemical reactions which occur among minerals, formation waters, and the hydrocarbons and organic sulfur compounds of petroleum in sulfur-rich reservoirs, thermodynamic calculations have been performed under the temperature, pressure and redox conditions of these reservoirs. Calculations have also been carried out as part of the development of a comprehensive thermodynamic model of thermochemical sulfate reduction (TSR).

- Calculations have also been also carried out to determine the conditions under which H_2S may react with organic sulfur compounds of petroleum to produce elemental sulfur and hydrocarbons. The possibility that such reactions may occur is of major interest in the context of the injection of CO_2-H_2S acid gas mixtures in sulfur-rich reservoirs.

Experimental study

- In order to verify the predictions of the thermodynamic calculations described above, sulfurisation/desulfurisation experiments of organic sulfur compounds have been carried out at 120-200°C and 500 bar in gold capsules for durations of two weeks or more. At the end of the experiments, the gas phase has been analyzed by Raman spectroscopy, while the solid and liquid phases were analyzed by gas chromatography – mass spectrometry (GC-MS).

- Reactions simulating thermochemical sulfate reduction (TSR) have been carried out with aqueous sulfate solutions (0.5 molal Na_2SO_4 and $MgSO_4$) and hydrocarbons (*n*-octane and 1-octene) in fused silica capillaries at 300-400°C during a few days. The production of H_2S was followed by Raman microspectrometry.

Petrographic and fluid inclusion study of a sulfur-rich petroleum reservoir

- A petrographic (optical microscopy, cathodoluminescence, SEM, and electron microprobe) and fluid inclusion (microthermometry, Raman and Infrared microspectrometry, and confocal microscopy) study has been carried out on carbonate rock samples from a petroleum reservoir of the Pre-Caspian Basin. Petrographic observations allow reconstructing the succession of diagenetic events, while the fluid inclusion study was used to constrain the temperature and pressure history of the reservoir, as well as to determine the composition (CO_2-H_2S-CH_4-H_2O) of the trapped fluids.

Keywords : hydrogen sulfide (H_2S), sedimentary basins, thermochemical sulfate reduction (TSR), elemental sulfur, organic sulfur compounds, thermodynamics, autoclave experiments, fluid inclusions.

TABLE OF CONTENTS

INTRODUCTION GÉNÉRALE

La compréhension et la quantification du comportement du soufre dans les bassins sédimentaires est d'une importance primordiale pour la géologie et la géochimie du pétrole (Douglas et Mair, 1965; Orr and Sinninghe Damsté, 1990; Aizenshtat et al., 1995; Amrani et al., 2006), pour l'étude des gisements métallifères (Barton, 1967; Anderson, 1991, 2008; Ohmoto et Goldhaber, 1997; Anderson et Thom, 2008), ainsi que pour l'étude de la diagenèse des sédiments (Mango, 1983; François, 1987; Morse et Berner, 1995). Le soufre est un constituant important des systèmes pétroliers, dans lesquels il peut être présent sous différentes formes et sous différents états d'oxydation (Tableau 1.0a). Les états d'oxydation importants pour l'étude des réservoirs pétroliers et des roches mères d'hydrocarbures sont S^{+6}, $S°$, S^{-1} et S^{-2}. L'état d'oxydation S^{+6} est représenté par des minéraux de la classe des sulfates comme l'anhydrite ($CaSO_4$), le gypse ($CaSO_4 \cdot 2H_2O$), la barytine ($BaSO_4$) et la célestine ($SrSO_4$) qui sont des minéraux communs des roches sédimentaires (Hanor, 2000; Machel, 2001), ainsi que par des espèces aqueuses (SO_4^{2-}, HSO_4^-, $NaSO_4^-$). Le soufre élémentaire, correspondant à l'état d'oxydation S^0, est moins courant mais peut se former en conditions acides (pH faible) et/ou en présence de fortes concentrations de H_2S. A l'état d'oxydation S^{-1}, on trouve le soufre dans la pyrite et la marcasite (FeS_2), ainsi que dans des disulfures organiques (par exemple le 2-thiabutane $CH_3–S–S–CH_3$). L'état d'oxydation le plus réduit du soufre (S^{-2}) est représenté par le sulfure d'hydrogène (H_2S), la pyrrhotite (FeS), la galène (PbS), la sphalérite (ZnS), et la plupart des composés organiques soufrés dont les thiols, les sulfures aliphatiques et cycliques et les composés thiophéniques. Bien que des composés du soufre avec des états d'oxydation intermédiaires peuvent jouer un rôle important dans les processus diagénétiques (il s'agit par exemple des thiosulfates et des sulfites – voir Thamdrup et al., 1994), ces composés se trouvent habituellement en faible concentration par rapport aux espèces sulfates et sulfures. Par conséquent, ces états d'oxydation intermédiaires seront considérés comme anecdotiques dans le cadre de ce travail sur les systèmes pétroliers.
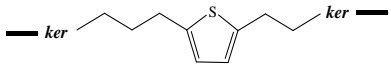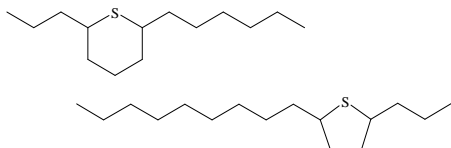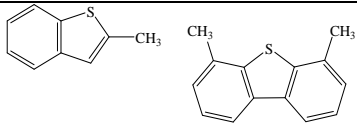
Les premiers travaux sur la géochimie du soufre dans les systèmes pétroliers ont été des études portant sur l'incorporation du soufre dans la matière organique au cours de la diagenèse (Bestougeff et Combaz, 1973), sur l'origine des pétroles riches en soufre (Gransch et Posthuma, 1974; Ho et al., 1974), et sur l'origine du gaz sulfureux dans les réservoirs carbonatés (Le Tran, 1971; Orr, 1977). Depuis les années 1980 jusqu'au début des années 1990, les recherches ont essentiellement porté sur la formation des composés organiques soufrés lors de la diagenèse des sédiments (François, 1987; Vairavamurthy et Mopper, 1987;

Sinninghe Damsté et al., 1989a) et sur l'identification de ces composés dans les kérogènes et les asphaltènes (Richnow et al., 1992; Adam et al., 1993) ainsi que dans les extraits de sédiments et les huiles (Payzant et al., 1983, 1986; Valisolalao et al., 1984; Brassell et al., 1986; Schmid et al., 1986; Sinninghe Damsté et al., 1986, 1987, 1989b; Radke et al., 1991; Radke et Willsch, 1994; van Kaam-Peters et al., 1995; Chakhmakhchev et al., 1997). Il a été conclu de ces travaux que les composés organiques soufrés étaient formés au cours de la diagenèse précoce des sédiments par des réactions entre du sulfure d'hydrogène produit par des bactéries (ou d'autres espèces inorganiques réduites du soufre) et des liaisons carbone-carbone insaturées ou des groupements fonctionnels oxygénés de biomolécules ou de matière organique sédimentaire immature (Orr et Sinninghe Damsté, 1990). Les composés formés de cette manière sont principalement des alkylthiolanes, des alkylthianes et des alkylthiophènes, qui peuvent être incorporés dans la structure moléculaires des kérogènes immatures puisqu'ils sont observés ensuite dans les huiles immatures (Orr et Sinninghe Damsté, 1990; Sinninghe Damsté et de Leeuw, 1990).

La découverte de réservoirs pétroliers associés à de fortes concentration de H_2S, par exemple dans la Péninsule Arabe (Worden et al., 1995; Worden et Smalley, 1996), dans les bassins du Tarim et du Sichuan en Chine (Cai et al., 2001, 2003, 2004) ou dans le bassin pré-caspien (Belenitskaya, 2000; Isaksen et Khalylov, 2007; Warner et al., 2007) s'est récemment traduite par un regain d'intérêt pour les études pétrographiques, expérimentales ou théoriques sur l'origines et les conséquences de la réduction thermochimique des sulfates (Machel, 1987, 1998; Sassen, 1988; Sassen et al., 1989; Goldstein et Aizenshtat, 1994; Machel et al., 1995; Heydari, 1997; Manzano et al., 1997; Nöth, 1997; Worden et Smalley, 1997; Worden et al., 2000; Bildstein et al., 2001; Yang et al., 2001; Hanin, 2002; Hanin et al., 2002; Cross et al., 2004; Mougin et al., 2007; Zhang et al., 2008).

Des travaux théoriques en géochimie organique menés au cours des vingt dernières années par Helgeson et ses étudiants (Shock et Helgeson, 1990; Shock, 1995; Amend et Helgeson, 1997a,b, 2000; Helgeson et al., 1998; Richard et Helgeson, 1998; Richard, 2001; Dick et al., 2006; LaRowe et Helgeson, 2006) ont permis de générer une base de données contenant les proprietés thermodynamiques de plusieurs centaines de composés organiques d'intérêt géochimique. Ces propriétés peuvent être utilisées pour étudier les interactions entre les composés organiques et leur environnement inorganique (et en particulier celles qui concernent le soufre – voir Richard et Helgeson, 2001; Richard et al., 2005) dans les processus géologiques.

Table 1.0a. Exemples de composés organiques et inorganiques du soufre présents dans les systèmes pétroliers.

	Espèces	Structure moléculaire ou formule chimique	Etat d'oxydation
Kérogènes immatures	Thiophènes, sulfures (disulfures), thiols		-2 (-1)
Pétroles immatures	Alkylthiolanes, alkythianes, et alkylthiophènes		-2
Pétroles matures	Benzothiophènes, dibenzothiophènes		-2
Eaux de formation	Sulfates	HSO_4^-, SO_4^{2-}, $NaSO_4^-$ …	+6
	Sulfures	H_2S, HS^-	-2
Minéraux des roches réservoirs	Anhydrite, gypse	$CaSO_4$, $CaSO_4 \cdot 2H_2O$	+6
	Soufre élémentaire	$S°$	0
	Pyrite, marcassite	FeS_2	-1
	Pyrrhotite, galène, sphalérite	FeS, PbS, ZnS	-2

Les objectifs de cette thèse sont (1) caractériser la distribution du soufre dans les réservoirs pétroliers sur la base de calculs thermodynamiques, (2) réaliser des expériences à température et pression fixées et sous des conditions contrôlées de fugacité de H_2S, (3) réaliser une étude pétrographique et d´inclusions fluides des échantillons provenant d´un réservoir carbonaté du nord de la Mer Caspienne.

Calculs thermodynamiques

Deux types de calculs thermodynamique ont été réalisés :

- des calculs visant à déterminer les conditions de formation de soufre élémentaire et d´hydrocarbures par réaction entre le sulfure d´hydrogène et des composés organiques soufrés. La possibilité de telles réactions, qui fera ensuite l´objet d´une vérification expérimentale, présente un intérêt particulier dans le contexte de la réinjection de mélanges de gaz acides CO_2-H_2S dans des réservoirs pétroliers riches en soufre.

- des diagrammes d'activité ont été construits pour étudier les relations de stabilité entre les minéraux, les eaux de formation, les hydrocarbures et les composés organiques soufrés du pétrole dans les conditions de température, de pression et d´oxydo-réduction caractéristiques des réservoirs pétroliers, en particulier les réservoirs affectés par la réduction thermochimique des sulfates (TSR).

Etudes expérimentales

- Des expériences dans des capsules en or simulant les réactions entre des composés organiques soufrés et H_2S ont été réalisées à 150-200°C et 500 bar pendant plusieurs semaines. Le sulfure d´hydrogène a été introduit dans les capsules par l´intermédiaire d´un système de remplissage de gaz mis au point au laboratoire G2R. A la fin des expériences, les phases liquide et gazeuse sont analysées par spectrométrie Raman et la composition de la phase liquide est déterminée par chromatographie gazeuse couplée à la spectrométrie de masse (GC-MS).

- Des expériences préliminaires simulant la réaction de réduction thermochimique des sulfates (TSR) dans des capillaires en silice ont également réalisées. Dans ces expériences, des hydrocarbures et des solutions aqueuses de sulfate de sodium ou de magnésium ont été amenés à réagir à 350-400°C pendant quelques jours. Les produits de réaction ont été analysés par spectrométrie Raman.

Etude pétrographique et d'inclusions fluides d´un réservoir pétrolier riche en soufre

Une étude pétrographique et d'inclusions fluides a été réalisée sur des échantillons provenant d´un réservoir carbonaté du nord de Mer Caspienne. L´étude des inclusions fluides permet de remonter aux conditions de mise en place des hydrocarbures dans la réservoir et de donner une estimation de la composition de ces fluides.

GENERAL INTRODUCTION

Understanding and quantifying the organic/inorganic behavior of sulfur in sedimentary basins is of primordial importance to petroleum geology and geochemistry (Douglas and Mair, 1965; Orr and Sinninghe Damsté, 1990; Aizenshtat et al., 1995; Amrani et al., 2006), as well as the study of ore deposits (Barton, 1967; Anderson, 1991, 2008; Ohmoto and Goldhaber, 1997; Anderson and Thom, 2008) and the diagenesis of recent sediments (Mango, 1983; François, 1987; Morse and Berner, 1995). Sulfur is an important constituent of petroleum systems, in which it can occur under different forms and oxidation states (see Table 1.0b). The oxidation states of importance for the study of hydrocarbon reservoirs and source rocks are S^{+6}, S^0, S^{-1} and S^{-2}. The S^{+6} state is encountered in sulfate minerals such as anhydrite ($CaSO_4$), gypsum ($CaSO_4 \cdot 2H_2O$), barite ($BaSO_4$), and celestite ($SrSO_4$), all of which are common constituents of sedimentary rocks (Hanor, 2000; Machel, 2001), as well as in aqueous sulfate species (SO_4^{2-}, HSO_4^-, $NaSO_4^-$). Elemental sulfur, which corresponds to the oxidation state S^0, is less common but may form under acidic (low pH) conditions and/or high concentrations of H_2S. Sulfur under the oxidation state S^{-1} occurs in pyrite and marcasite (FeS_2), as well as in organic disulfides (e.g. 2-thiabutane CH_3–S–S–CH_3). The most reduced state of sulfur (S^{-2}) is encountered in hydrogen sulfide (H_2S), pyrrhotite (FeS), galena (PbS), sphalerite (ZnS), and most organic sulfur compounds including thiols, alkyl sulfides, cyclic sulfides, and thiophenics. Although other intermediate oxidation states of sulfur have been shown to play an important role in diagenetic processes (these include for example thiosulfate and sulfite – see e.g. Thamdrup et al., 1994), they are usually found in relatively low concentration levels compared to sulfate and sulfide species. Therefore, these intermediate oxidation states will be considered as anecdotic in the context of the present work on petroleum systems.
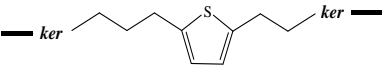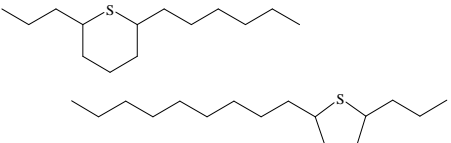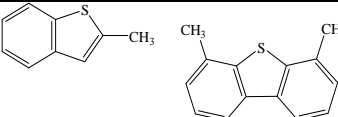
Early works on the geochemistry of sulfur in petroleum systems include studies concerned with the diagenetic incorporation of sulfur in organic matter (Bestougeff and Combaz, 1973), the origin of sulfur-rich crude oils (Gransch and Posthuma, 1974; Ho et al., 1974), and the origin of sour gas in carbonate reservoirs (Le Tran, 1971; Orr, 1977). Research efforts from the mid 1980´s to the early 1990´s were essentially focused on the formation of organic sulfur compounds during the early diagenesis of sediments (François, 1987; Vairavamurthy and Mopper, 1987; Sinninghe Damsté et al., 1989a) and the identification of organic sulfur compounds in kerogens and asphaltenes (Richnow et al., 1992; Adam et al., 1993) as well as in sediment extracts and immature and mature crude oils (Payzant et al.,

1983, 1986; Valisolalao et al., 1984; Brassell et al., 1986; Schmid et al., 1986; Sinninghe Damsté et al., 1986, 1987, 1989b; Radke et al., 1991; Radke and Willsch, 1994; van Kaam-Peters et al., 1995; Chakhmakhchev et al., 1997). These studies lead to a conclusion that organic sulfur compounds were first formed during early diagenesis by reactions among bacterially produced hydrogen sulfide (or other reduced inorganic sulfur species) with unsaturated bonds or oxygenated functional groups of biomolecules or immature sedimentary organic matter (Orr and Sinninghe Damsté, 1990). The first compounds to be formed mostly include alkylthiolanes, alkylthianes and alkylthiophenes, which may be incorporated in the molecular structure of immature kerogens since they are subsequently observed in immature crude oils (Orr and Sinninghe Damsté, 1990; Sinninghe Damsté and de Leeuw, 1990).

The discovery of petroleum reserves associated with high H_2S contents, for instance in the Arab Peninsula (Worden et al., 1995; Worden and Smalley, 1996), the Tarim and Sichuan Basins of China (Cai et al., 2001, 2003, 2004), and the North Caspian Sea Basin (Belenitskaya, 2000; Isaksen and Khalylov, 2007; Warner et al., 2007), has recently generated an increasing number of petrographical, experimental and theoretical studies on the causes and consequences of thermochemical sulfate reduction (Machel, 1987, 1998; Sassen, 1988; Sassen et al., 1989; Goldstein and Aizenshtat, 1994; Machel et al., 1995; Heydari, 1997; Manzano et al., 1997; Nöth, 1997; Worden and Smalley, 1997; Worden et al., 2000; Bildstein et al., 2001; Yang et al., 2001; Hanin, 2002; Hanin et al., 2002; Cross et al., 2004; Mougin et al., 2007; Zhang et al., 2008).

Comprehensive research in theoretical organic geochemistry carried out over the last twenty years by Helgeson and co-workers (Shock and Helgeson, 1990; Shock, 1995; Amend and Helgeson, 1997a,b, 2000; Helgeson et al., 1998; Richard and Helgeson, 1998; Richard, 2001; Dick et al., 2006; LaRowe and Helgeson, 2006) resulted in an extensive set of thermodynamic properties for solid, liquid, gas and aqueous organic compounds of geological interest. These thermodynamic properties can be used together with those for minerals, aqueous inorganic species, and inorganic gases to investigate organic/inorganic interactions (and in particular those involving sulfur – see Richard and Helgeson, 2001; Richard et al., 2005) in geological processes.

Table 1.0b. Examples of organic and inorganic sulfur species encountered in petroleum systems.

	Species	Molecular structure or chemical formula	Oxidation state of sulfur
Immature kerogens	Thiophenics, alkyl sulfides and disulfides, thiols		-2 (-1)
Immature oils	Alkylthiolanes, alkythianes, and alkylthiophenes		-2
Mature oils	Benzothiophenes, dibenzothiophenes		-2
Formation waters	Sulfates	HSO_4^-, SO_4^{2-}, $NaSO_4^-$ …	+6
	Sulfides	H_2S, HS^-	-2
Reservoir rock minerals	Anhydrite or gypsum	$CaSO_4$, $CaSO_4 \cdot 2H_2O$	+6
	Elemental sulfur	$S°$	0
	Pyrite, marcasite	FeS_2	-1
	Pyrrhotite, galena, sphalerite	FeS, PbS, ZnS	-2

The objectives of the doctoral research which is reported in the following pages were threesome: (1) characterizing from a thermodynamic point of view the reactions which govern the distribution of sulfur in hydrocarbon reservoirs, (2) carrying out experiments at fixed temperatures and pressures and under controlled fugacity of H_2S, and (3) carrying out a petrographic and fluid inclusion study on samples from a carbonate reservoir from the northern Caspian Sea.

Thermodynamic calculations

The thermodynamic calculations carried out during the course of the thesis are of two kinds.

- Calculations are carried out to determine the conditions under which H_2S may react with organic sulfur compounds of petroleum to produce elemental sulfur and hydrocarbons. The possibility for such reactions, which will also be investigated experimentally, is of interest in the context of the injection of CO_2-H_2S acid gas mixtures in sulfur-rich reservoirs.
- Equilibrium activity diagrams are constructed to investigate the stability relations among minerals, formation waters, and the hydrocarbons and organic sulfur compounds of petroleum under the temperature and redox conditions of petroleum reservoirs, with particular emphasis on reservoirs affected by thermochemical sulfate reduction (TSR).

Experimental study

- In order to verify the predictions of the thermodynamic calculations described above, experiments among elemental sulfur and hydrocarbons, as well as among organic sulfur compounds and H_2S, are carried out at 150-200°C and 500 bar in gold capsules for periods of time of a few weeks. The reactions are carried out under both hydrous and anhydrous conditions, as well in the presence of minerals or not. H_2S is introduced in the capsules using a gas-loading apparatus specially designed by the G2R laboratory. At the end of the experiments, the gas and liquid phases, as well as the condensed residual phases are analyzed using Raman spectroscopy and GC-MS to identify the main compositional changes and the formation of elemental sulfur or H_2S and organic sulfur compounds, depending on which way the reaction proceeds.

- Experimental simulations of TSR are also performed with the novel technique of the fused silica capillaries. In these experiments, hydrocarbons are reacted with aqueous sulfate solutions at 350-400°C during 4-10 days. The TSR reaction products are analyzed by Raman spectrometry.

Petrographic and fluid inclusion study of a sulfur-rich petroleum reservoir

A petrographic and fluid inclusion study of reservoir rocks from the northern Caspian Sea has been carried out in the third part of the thesis. The fluid inclusion study has been used to constrain the temperature and pressure history of the reservoir, as well as to determine the composition (CO_2-H_2S-CH_4-H_2O) of the trapped fluids.

PART I – THERMODYNAMIC ASPECTS OF THE GEOCHEMICAL CYCLE OF SULFUR IN SEDIMENTARY BASINS

The geochemical processes which accompany the evolution of petroleum systems with increasing temperature, pressure, and depth in sedimentary basins can be characterized from a thermodynamic point of view following the approach pioneered by Helgeson et al. (1993). A comprehensive thermodynamic analysis is presented below of the organic/inorganic interactions which govern the geochemical cycle of sulfur in sedimentary basins. A brief reminder of the necessary thermodynamic concepts and equations is first given. A summary of the thermodynamic properties of minerals, inorganic gases, solid, liquid and gas organic compounds, and aqueous organic and inorganic species which have been considered in the calculations is then presented. Finally, activity and fugacity diagrams generated in the present study are used in order to evaluate the extent to which the reactions responsible for the distribution of sulfur among minerals, aqueous solutions, petroleum, and natural gas proceed at or near equilibrium.

1. THERMODYNAMIC RELATIONS

1.1. The law of mass action

In order to calculate the organic / inorganic distribution of nitrogen among minerals and the oil, gas, and formation water phases in petroleum reservoirs, values of the equilibrium constant (K) obtained in the manner described below have been used in conjunction with expressions of the law of mass action

$$K = \prod_i a_i^{n_{i,r}} \tag{1.1}$$

where a_i designates the activity of the ith species in the system and $n_{i,r}$ stands for the stoichiometric coefficient of the ith species in the rth reaction, which is positive for reaction products and negative for reactants. The standard state adopted in the present study for solids and liquids is one of unit activity for the pure components at all temperatures and pressures. In the case of hydrocarbons and organic sulfur compounds in crude oil, a hypothesis of ideal mixing was assumed for which the activities a_i of the components are equal to their mole fraction X_i in the liquid petroleum mixture.

Consideration of osmotic coefficients for NaCl solutions at the temperature and pressure conditions typical of sedimentary basins indicates that the activity of H_2O is close to unity in most oil field waters (Helgeson et al., 1993). Accordingly, a value of $a_{H_2O} = 1$ has been adopted in Eqn. (1.1) for reactions involving water. The activity of a gas at a temperature T and pressure P is defined by the ratio between the fugacity f_i of the ith gas at T and P and its standard state fugacity f_i°, i.e.

$$a_i = f_i \big/ f_i^\circ \qquad (1.2)$$

Adopting for gases a standard state of unit fugacity for any temperature at 1 bar, the activity of the gas becomes equal to its fugacity. Finally, the standard state adopted for aqueous species other than H_2O is one of unit activity of the species in a hypothetical one molal solution referenced to infinite dilution at any temperature and pressure. Activities of aqueous species in formation waters have been computed from the corresponding molality (m_i) values according to

$$a_i = \gamma_i \cdot m_i \qquad (1.3)$$

where γ_i is the activity coefficient of the ith species. Values of γ_i were obtained from an extended Debye-Hückel equation written as (Helgeson, 1969)

$$\log \gamma_i = \frac{-Az_i^2\sqrt{I}}{1 + B\mathring{a}_i\sqrt{I}} + CI \qquad (1.4)$$

where A and B are the Debye-Hückel parameters (which depend on temperature and pressure), z_i is the charge of the ith aqueous species, $\mathring{a}_i$ is a distance of closest approach which is characteristic of the ith ion, C represents a deviation function from the Debye- Hückel law, and I is the ionic strength of the solution defined by

$$I = \frac{1}{2}\sum_i m_i z_i^2 \qquad (1.5)$$

where m_i is the molality of the ith aqueous species expressed in units of moles of the species per kilogram of pure H_2O.

1.2. Calculation of equilibrium constants of reactions as a function of temperature and pressure

The thermodynamic calculations reported below are based on the evaluation of equilibrium constants (K) for reactions among minerals, aqueous solutions, gas species, as

well as organic solids and liquids as a function of temperature (T) and pressure (P). The logarithm of the equilibrium constant of a reaction r is calculated from

$$\log K_r = \frac{-\Delta G_r^{\circ}}{2.303RT}$$ (1.6)

where ΔG_r° stands for the apparent standard molal Gibbs energy of reaction r, 2.303 corresponds to the natural logarithm of 10 (ln 10), R is the gas constant (8.314472 J mol^{-1}K^{-1}), and T the absolute temperature expressed in Kelvin (K). The apparent standard molal Gibbs energy of a reaction is defined by

$$\Delta G_r^{\circ} = \sum_i \hat{n}_{i,r} \Delta G_i^{\circ}$$ 1.7)

where $\hat{n}_{i,r}$ stands for the stoichiometric coefficient of the ith species in the rth reaction, ($\hat{n}_{i,r}$ is negative for reactants and positive for products), and ΔG_i° is the apparent standard molal Gibbs energy of formation of a given solid, liquid, aqueous, or gas species at the temperature T and pressure P of interest. The latter quantity is obtained from

$$\Delta G_i^{\circ} = \Delta G_f^{\circ} + (G_{T,P}^{\circ} - G_{T_r,P_r}^{\circ})\ ,$$ (1.8)

where ΔG_f° stands for the standard molal Gibbs energy of formation of the species from the elements taken under their stable form at the reference temperature (T_r) of 25°C (298.15 K) and the reference pressure (P_r) of 1 bar, and the parenthetical term $(G_{T,P}^{\circ} - G_{T_r,P_r}^{\circ})$ represents the variation of the standard molal Gibbs energy of the species between the reference temperature (T_r) and pressure (P_r) and the temperature (T) and pressure (P) of interest. This parenthetical term is evaluated by integrating the Gibbs energy function in temperature and pressure, which results in

$$G_{T,P}^{\circ} - G_{T_r,P_r}^{\circ} = -S_{P_r,T_r}^{\circ}(T - T_r) + \int_{T_r}^{T} C_{P_r}^{\circ} dT - T \int_{T_r}^{T} C_{P_r}^{\circ} d\ln T + \int_{P_r}^{P} V^{\circ} dP$$ (1.9)

where S_{T_r,P_r}°, $C_{P_r}^{\circ}$, and V° stand for the standard molal entropy of the species at the reference temperature and pressure, its standard molal heat capacity at the reference pressure, and its standard molal volume at the temperature and pressure of interest, respectively.

The calculation from Equations (1.8) and (1.9) of the apparent standard molal Gibbs energy of formation of a crystalline, liquid, gas or aqueous species requires an evaluation of the dependence of the heat capacity of the species with respect to temperature or of its standard molal volume with respect to pressure. The temperature dependence of the standard molal heat capacity of minerals, inorganic gases, and organic solids and liquids can be

22

described by the Maier-Kelley equation (Helgeson et al., 1978, 1998), which is written as (Maier and Kelley, 1932)

$$C_{P_r}^\circ = a + bT + \frac{c}{T^2} \qquad (1.10)$$

where a, b, and c represent temperature-independent coefficients. It has been shown by Helgeson et al. (1978, 2009) that along geotherms typical of sedimentary basins, the effects of thermal expansion and compressibility tend to compensate for minerals as well as for organic solids (kerogens) and liquids (petroleum hydrocarbons), so that the standard molal volume of these species can be considered as a constant in a first approximation:

$$V^\circ = V_{T_r, P_r}^\circ \ . \qquad (1.11)$$

The standard state commonly adopted for gases calls for unit activity of the pure hypothetical ideal gas at any temperature and 1 bar, which results in

$$V^\circ = 0 \qquad (1.12)$$

for ideal gases. In the case of aqueous species, the variations of the standard partial molal heat capacity ($\overline{C}_P^\circ$) and volume ($\overline{V}^\circ$) are computed from the revised Helgeson-Kirkham-Flowers (HKF) equations of state, which for $\overline{C}_P^\circ$ and $\overline{V}^\circ$ correspond to (Tanger and Helgeson, 1988)

$$\overline{C}_P^\circ = c_1 + \frac{c_2}{(T-\theta)^2} - \left(\frac{2T}{(T-\theta)^3}\right) \cdot \left(a_3(P-P_r) + a_4 \ln\left(\frac{\psi+P}{\psi+P_r}\right)\right)$$

$$+ \omega TX + 2TY\left(\frac{\partial\omega}{\partial T}\right)_P - T\left(\frac{1}{\varepsilon}-1\right) \cdot \left(\frac{\partial^2\omega}{\partial T^2}\right)_P \qquad (1.13)$$

and

$$\overline{V}^\circ = a_1 + \frac{a_2}{\psi+P} + \left(a_3 + \frac{a_4}{\psi+P}\right) \cdot \left(\frac{1}{T-\theta}\right) - \omega Q + \left(\frac{1}{\varepsilon}-1\right) \cdot \left(\frac{\partial\omega}{\partial P}\right)_T \qquad (1.14)$$

where a_1, a_2, a_3, a_4, c_1 and c_2 represent species-dependent non-solvation parameters, ω is the Born coefficient, ε is the dielectric constant of water at the temperature and pressure of interest, ψ and θ refer to solvent parameters equal to 2600 bar and 228 K, and Q, Y and X are Born functions corresponding to first and second partial derivatives of the dielectric constant of water with respect to temperature and pressure:

$$Q \equiv \frac{1}{\varepsilon}\left(\frac{\partial\ln\varepsilon}{\partial P}\right)_T \quad , \qquad (1.15)$$

$$Y \equiv \frac{1}{\varepsilon} \left(\frac{\partial \ln \varepsilon}{\partial T} \right)_P \quad , \tag{1.16}$$

and

$$X \equiv \frac{1}{\varepsilon} \left(\left(\frac{\partial^2 \ln \varepsilon}{\partial T^2} \right)_P - \left(\frac{\partial \ln \varepsilon}{\partial T} \right)_P^2 \right) \quad , \tag{1.17}$$

respectively. Combining Equation (1.9) with Equations (1.10)-(1.17) yields

$$\Delta G_{T,P}^\circ = \Delta G_f^\circ - S_{T_r,P_r}^\circ (T - T_r) + a(T - T_r) + \frac{b}{2}(T^2 - T_r^2) - c\left(\frac{1}{T} - \frac{1}{T_r} \right) - aT \ln\frac{T}{T_r} - bT(T - T_r)$$

$$+ \frac{cT}{2}\left(\frac{1}{T^2} - \frac{1}{T_r^2} \right) + V_{T_r,P_r}^\circ (P - P_r) \tag{1.18}$$

for minerals, inorganic gases, and organic solids and liquids, and

$$\Delta \overline{G}_{T,P}^\circ = \Delta \overline{G}_f^\circ - \overline{S}_{T_r,P_r}^\circ (T - T_r) - c_1 \left[T \ln\left(\frac{T}{T_r} \right) - T + T_r \right] + a_1(P - P_r) + a_2 \ln\left(\frac{\psi + P}{\psi + P_r} \right)$$

$$- c_2 \left\{ \left[\left(\frac{1}{T - \theta} \right) - \left(\frac{1}{T_r - \theta} \right) \right] \cdot \left(\frac{\theta - T}{\theta} \right) - \frac{T}{\theta^2} \ln\left[\frac{T_r(T - \theta)}{T(T_r - \theta)} \right] \right\}$$

$$+ \left(\frac{1}{T - \theta} \right) \cdot \left[a_3(P - P_r) + a_4 \ln\left(\frac{\psi + P}{\psi + P_r} \right) \right] + \omega\left(\frac{1}{\varepsilon} - 1 \right)$$

$$- \omega_{T_r,P_r}\left(\frac{1}{\varepsilon_{T_r,P_r}} - 1 \right) + \omega_{T_r,P_r} Y_{T_r,P_r}(T - T_r) \tag{1.19}$$

for aqueous species.

1.3. Mass transfer calculations

A fluid-rock system is rarely in a state of chemical equilibrium but always evolves towards it by dissolving minerals which are unstable in contact with a given aqueous solution, and/or precipitating other minerals reaching chemical equilibrium with respect to that solution as a result of changes in the concentrations of the dissolved species. If a mineral is in chemical equilibrium or not with an aqueous solution can be evaluated from the saturation index (log Ω), which is defined by (e.g. Anderson, 1995):

$$\log \Omega = \log \frac{Q_r}{K_r} \tag{1.20}$$

24

where K_r represents the equilibrium constant of the dissolution or precipitation reaction defined by Equation (1.6), and Q_r denotes the reaction quotient defined by

$$Q_r = \prod_i a_i^{\hat{n}_{i,r}} \quad , \tag{1.21}$$

where a_i again designates the activity of the ith species in the system and $\hat{n}_{i,r}$ stands for the stoichiometric coefficient of that species in the rth reaction. Three cases arise depending on the value of log Ω:

$$\log \Omega < 0 \,, \quad Q_r < K_r \quad , \tag{1.22}$$

and the solution is undersaturated with respect to the mineral which dissolves in the solution,

$$\log \Omega > 0 \,, \quad Q_r > K_r \quad , \tag{1.23}$$

and the solution is supersaturated with respect to the mineral which precipitates from the solution, and

$$\log \Omega = 0 \,, \quad Q_r = K_r \quad , \tag{1.24}$$

and the mineral and the aqueous solution are in chemical equilibirium.

The departure from equilibrium for a given reaction r can be described in terms of the chemical affinity (A_r) of this reaction. Chemical affinity has been defined by De Donder (1922) as

$$A_r = \frac{\delta Q_{irrev}}{d\xi_r} = RT \ln\frac{K_r}{Q_r} \tag{1.25}$$

where δQ_{irrev} is the quantity of heat released in an irreversible fashion over an increment of reaction $d\xi_r$, ξ_r being the reaction progress variable (De Donder, 1920). This variable, which is common to all the species involved in a given reaction, is related to the variation of the number of moles of the ith species involved in the rth reaction over an increment of reaction by

$$\xi_r = \frac{n_{i,r} - n_{i,r}^o}{\hat{n}_{i,r}} \tag{1.26}$$

where $n_{i,r}^o$ and $n_{i,r}$ are the number of moles of the ith species at $\xi_r = 0$ (i.e. before the reaction starts) and at ξ_r, and $\hat{n}_{i,r}$ is the stoichiometric coefficient of the ith species in the rth reaction, $\hat{n}_{i,r}$ being again negative for reactants and positive for products.

The differential equations permitting the application of the principles of irreversible thermodynamics to the description of fluid-rock interactions were first derived by Helgeson (1968), and subsequently integrated in various geochemical computer programs simulating water-rock interactions (Helgeson et al., 1970; Fritz, 1975, 1981; Wolery and Daveler, 1992, among others). We will only give here a brief summary of the principles and characteristics of these programs.

In a mass transfer calculation, the initial chemical composition of the system is first defined by specifying a mineralogical assemblage for the reacting rock and the total aqueous molal concentrations of the major (and if of interest, selected minor or trace) elements in the reacting fluid. All the reactant minerals are initially out of chemical equilibrium with respect to the fluid. Also defined are the temperature[1] of the interaction, the fugacity of CO_2 gas ($f_{CO_{2(g)}}$) over the system (which may vary during the interaction), and initial values for the pH and redox potential (E_h) of the reacting fluid. In some instances, it is more convenient to describe the redox conditions of the system with the fugacity of oxygen gas ($f_{O_{2(g)}}$), which may or may not vary during the interaction. Finally, a set of secondary minerals which are expected to form as a result of the interaction must be defined based on the temperature and composition of the system.

Changes in the number of moles of the mineral or aqueous species as a result of a small increment of reaction are described by reaction coefficients ($\bar{n}_i$), which are defined by (Helgeson, 1968)

$$\bar{n}_i = \frac{\Delta m_i}{\Delta \xi} \tag{1.27}$$

where m_i either represents the molality of an aqueous species or designates the number of moles of a given mineral per kilogram of H_2O, and $\Delta \xi$ represents a small variation of the reaction progress variable for the overall irreversible reaction. In practice, the numerical value corresponding to the variation of ξ is several orders of magnitude smaller than the lowest concentration defined for any chemical element in the initial aqueous solution (Helgeson, 1968). The variations of the number of moles of aqueous species or of minerals destroyed or produced during the mass transfer process are calculated from quadratic (or higher degree) Taylor expansions written as (Helgeson, 1968; Helgeson et al., 1970):

$$\Delta m_i = \bar{n}_i \Delta \xi + \bar{n}_i' \frac{(\Delta \xi)^2}{2!} + \ldots \tag{1.28}$$

where $\bar{n}_i'$ is the first derivative of $\bar{n}_i$ with respect to ξ. Expressions for evaluating $\bar{n}_i'$ may be found in Helgeson et al. (1970).

Prior to giving a detailed description of the thermodynamic calculations carried out in the present study with the aid of the equations summarized above, we well first review the thermodynamic properties of the minerals, inorganic gases, organic solids, liquids and gases, and inorganic and organic aqueous species which have been used in these calculations.

---

[1] In most geochemical programs, the pressure at which mass transfer calculations are performed is equal to 1 bar up to a temperature of 99.99ºC, and corresponds to the vapor-liquid saturation pressure (P_{sat}) of the system H_2O at higher temperatures. However, the thermodynamic databases of these programs can be easily adapted in order to carry out calculations at higher pressures.

2. THERMODYNAMIC PROPERTIES OF MINERALS, GASES, ORGANIC COMPOUNDS, AND AQUEOUS ORGANIC AND INORGANIC SPECIES[2]

2.1. Minerals

2.1.1. Anhydrite

Majzlan et al. (2002) have recently redetermined the standard molal enthalpy of formation (ΔH_f°) at 25°C and 1 bar of a synthetic sample of anhydrite. Their value (ΔH_f° = -1433.8 kJ mol^{-1}) is in close agreement with the value of -1434.1 kJ mol^{-1} previously adopted by Helgeson et al. (1978). The standard molal entropy (S°) of anhydrite at 25°C and 1 bar determined by Robie et al. (1989) is 107.4 J mol^{-1}K^{-1} and is nearly identical to that listed by Helgeson et al. (1978), i.e. 106.7 J mol^{-1}K^{-1}. The entropy value of Robie et al. (1989) has been combined with the standard molal entropies of the elements taken from Cox et al. (1989) to derive the value Gibbs free energy of formation (ΔG_f°) at 25°C and 1 bar listed in Table A1. Cell parameters determined by Majzlan et al. (2002) on their synthetic sample of anhydrite have the following values: a = 7.0024 Å, b = 6.9931 Å, and c = 6.2416 Å, which for a number Z = 4 of formula units per unit cell corresponds to a standard molal volume V° = 46.02 cm^{3}mol^{-1}. The latter value is essentially identical to that of 45.94 cm^{3}mol^{-1} adopted by Helgeson et al. (1978). High-temperature heat capacity (C_P°) measurements have been made by Robie et al. (1989) and Majzlan et al. (2002). The latter authors did not report actual heat capacity values but the following temperature-dependent heat capacity function[3]:

$$C_P^\circ(T) = a + bT + cT^{-2} + dT^{-0.5} + eT^2, \tag{1.29}$$

where C_P° is expressed in J·mol^{-1}·K^{-1}, and a = 409.7, b = -0.1764, c = 2672000, d = -5130 and e = 0.00008460. Values of C_P° computed between 0 and 300°C from the above equation are compared in Figure 1.1 to experimental values reported by Robie et al. (1989) and C_P° values computed from the Maier-Kelley equation using coefficients given by Helgeson et al. (1978). The latter coefficients were taken from an earlier publication by Kelley (1960). It can be deduced from Figure 1.1 that the experimental values of Robie et al. (1989) are higher than those determined by Majzlan et al. (2002) by ~ 4 J mol^{-1}K^{-1}, but that the two sets of values

---

[2] The properties discussed in this section are summarized in Tables A1 and A2 of the Appendix to the present chapter.

[3] It should be noted that Figure 5 in the publication of Majzlan et al. (2002) is erroneous. In contrast, the heat capacity equations given by these authors are correct (J. Majzlan, written communication to L. Richard, 2007).

show similar temperature dependences. In contrast, the linear dependence given by Kelley (1960) and adopted by Helgeson et al. (1978) appears to need revision. Consequently, the experimental data of Robie et al. (1989) corresponding to the symbols in Figure 1.1 have been regressed with the Maier-Kelley equation, which resulted in the values of a, b, and c listed in Table A1 and the dashed curve shown in Figure 1.1.
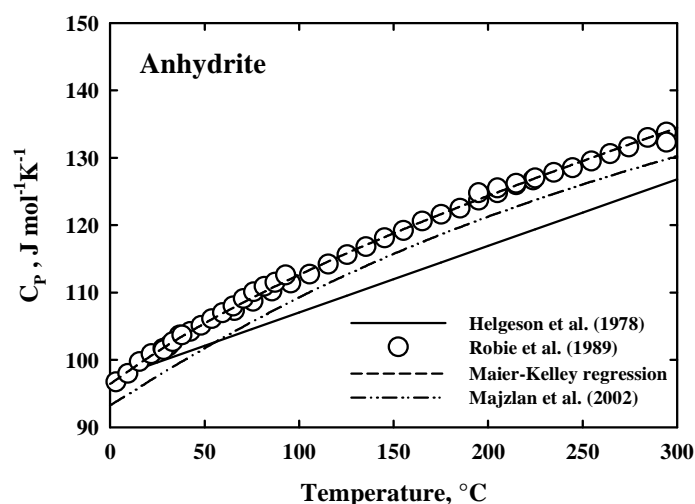
Figure 1.1. Standard molal heat capacity of anhydrite
as a function of temperature at ~ 1 bar.

The validity of the thermodynamic properties and heat capacity coefficients adopted in Table A1 for anhydrite can be independently checked by comparing solubilities reported in the literature for this mineral and solubilities calculated using a mass transfer program. The DISSOL computer program (Fritz, 1975, 1981) has been used for this puropose. The set of aqueous species considered in the solubility model described below is given in Table 1.1. The thermodynamic properties and HKF parameters for these aqueous species are summarized in Table A2. They were taken from Shock and Helgeson (1988), Shock et al. (1989, 1997), Sverjensky et al. (1997)[4], and the slop98.dat database which can be downloaded from the http://geopig.asu.edu website.

The solubility of anhydrite as a function of temperature, pressure, and ionic strength has been experimentally determined by Marshall et al. (1964), Block and Waters (1968), Blount and Dickson (1969), Freyer and Voigt (2004), and Newton and Manning (2005), among others. The temperature, pressure, and NaCl molality ranges covered by these experimental studies are summarized in Table 1.2.

---

[4] Note that the revised thermodynamic parameters given by Sverjensky et al. (1997) for the $CaCl^+$ complex result in an overestimation of the stability of this complex and are inconsistent with the solubility data for anhydrite discussed in this section. As a result, the parameters used in the calculations described in this section are those which were contained in the original SPRONS92 database of the SUPCRT92 program (Johnson et al., 1992).

28

Table 1.1. Summary of aqueous species considered for the mass transfer calculations describing the solubility of anhydrite as a function of temperature and NaCl molality.

CO_3^{2-}	$CaHCO_3^+$	Cl^-	Na^+
HCO_3^-	$CaCl^+$	$HCl_{(aq)}$	$NaCl_{(aq)}$
$H_2CO_{3(aq)}$	$CaCl_{2(aq)}$	H^+	$NaSO_4^-$
Ca^{2+}	$CaOH^+$	H_2O	SO_4^{2-}
$CaCO_{3(aq)}$	$CaSO_{4(aq)}$	OH^-	HSO_4^-

Table 1.2. Experimental studies on the solubility of anhydrite as a function of temperature and pressure in H_2O-NaCl solutions.

Study	Temperature (°C)	Pressure (bar)	m_{NaCl} (mol)
Marshall et al. (1964)	125 – 200	P_{sat}	0 – 4
Block and Waters (1968)	100	P_{sat}	0 – 4
Blount and Dickson (1969)	100 – 450	1 – 1000	0 – 6
Freyer and Voigt (2004)	100 – 200	P_{sat}	3 – 8
Newton and Manning (2005)	600 – 800	6000 – 14000	0 – 24

In order to evaluate to which ionic strength the DISSOL computer program reproduces reasonably well the solubility of anhydrite as a function of temperature at pressures corresponding to the liquid-vapor equilibrium of the system H_2O (P_{sat}), the results of dissolution calculations have been compared to experimental solubility values tabulated by Marshall et al. (1964), Block and Waters (1968) and Blount and Dickson (1969) at rounded values of temperatures and NaCl molalities for the saturation curve of H_2O (P_{sat}). These experimental values have been plotted as symbols in Figure 1.2. It can be deduced from this figure that some of the values reported by Marshall et al. (1964) plot higher than those determined by Blount and Dickson (1969). The latter values appear to be consistent with the more recent measurements of Freyer and Voigt (2004). The values of Block and Waters (1968) plot between those of Marshall et al. (1964) and Blount and Dickson (1969), with the exception of the solubility at 100°C and $m_{NaCl} = 0$, which appears to be erroneous.

The curves drawn in Figure 1.2 represent the solubilities computed with the DISSOL mass transfer program (Fritz, 1975, 1981). The values corresponding to the computed solubility curves of Figure 1.2 are compared to their experimental counterparts in Table 1.3. It can be deduced from this table that the agreement between the calculated values and their experimental counterparts is reasonably good, even at ionic strengths as high as $I = 2m$. It should perhaps be recalled that the solubility curves in Figure 1.2 have been calculated from experimental thermochemical data which are completely independent of the experimental solubilities represented by the symbols in this figure.
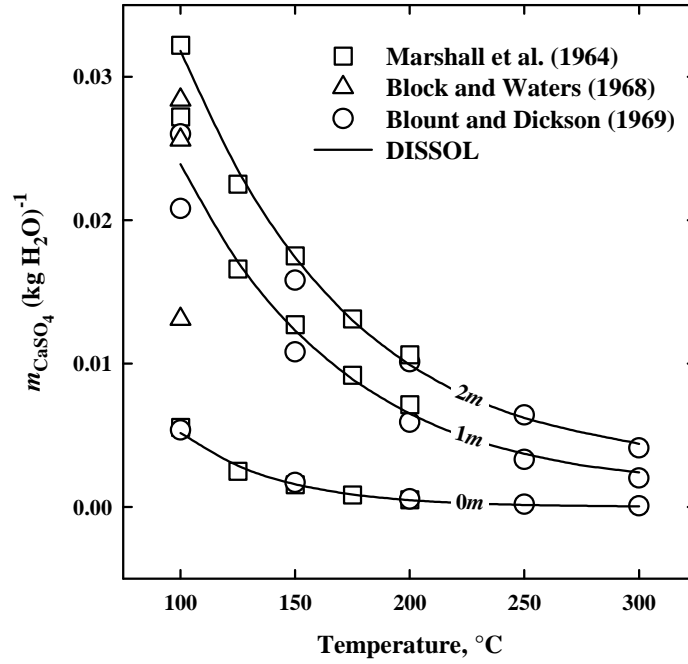
Figure 1.2. Solubility of anhydrite as a function of temperature along the vapor pressure curve for the system H$_2$O (P_{sat}). The symbols correspond to experimental data reported in the literature. The curves were computed in the present study with the DISSOL computer program (see text).

Table 1.3. Comparison between experimental solubilities of anhydrite reported in the literature and values computed in the present study using the DISSOL mass transfer program.

T (°C)	m_{NaCl}	Experimental solubilities [a]			Computed solubilities [a]
100	0	0.00535 [b]	0.01310 [c]	0.00553 [d]	0.00508
	1	0.02080 [b]	0.02560 [c]	0.02720 [d]	0.02398
	2	0.02600 [b]	0.02840 [c]	0.03220 [d]	0.03189
125	0	0.00247 [d]			0.00280
	1	0.01660 [d]			0.01719
	2	0.02250 [d]			0.02353
150	0	0.00170 [b]	0.00154 [d]		0.00151
	1	0.01080 [b]	0.01270 [d]		0.01235
	2	0.01580 [b]	0.01750 [d]		0.01745
175	0	0.00082 [d]			0.00081
	1	0.00918 [d]			0.00894
	2	0.01310 [d]			0.01361
200	0	0.00054 [b]	0.00049 [d]		0.00042
	1	0.00590 [b]	0.00712 [d]		0.00654
	2	0.01010 [b]	0.01060 [d]		0.00995
250	0	0.00017 [b]			0.00011
	1	0.00330 [b]			0.00376
	2	0.00640 [b]			0.00629
300	0	0.00006 [b]			0.00003
	1	0.00200 [b]			0.00245
	2	0.00410 [b]			0.00448

[a] mol CaSO$_4$ (kg H$_2$O)$^{-1}$ [b] Blount and Dickson (1969) [c] Block and Waters (1968) [d] Marshall et al. (1964)

2.1.2. Calcite

The standard molal thermodynamic properties and heat capacity power function coefficients adopted in the present study for calcite, which have been listed in Table A1, are those originally recommended by Helgeson et al. (1978). Although the standard molal Gibbs energy (ΔG_f°) and enthalpy (ΔH_f°) of formation at 25°C and 1 bar given by these authors differ from those adopted in the SPRONS92.DAT database of the SUPCRT92 computer program (Johnson et al., 1992), the latter values representing an adjustment of 920 J·mol^{-1} with respect to the values of Helgeson et al. (1978) based on solubility measurements reported by Plummer and Busenberg (1982)[5], simultaneous consideration of solubility data reported by Ellis (1963) for higher temperatures up to 300°C and higher ionic strengths to 1 molal NaCl, which are representative of sedimentary basin conditions, prompted us to adopt the original ΔG_f° and ΔH_f° values of Helgeson et al. (1978).

The properties and coefficients listed in Table A1 for calcite have been used along with those listed in Table A2 for the aqueous species in the system $CaCO_3$-H_2O-NaCl to calculate the solubility curves depicted in Figures 1.3 and 1.4. It can be seen in Figure 1.3 that the curves calculated with the DISSOL computer program (Fritz, 1975, 1981) for the solubility of calcite in pure water underestimate the solubilities represented by the lower temperature experimental data of Plummer and Busenberg (1982) by up to 4 mmol (kg H_2O)$^{-1}$ at 0°C but less than 1 mmol (kg H_2O)$^{-1}$ at 25°C and above, they are closely consistent with the experimental data reported by Ellis (1963) and over the 100 – 300°C temperature range at different partial pressures of CO_2 gas. It can also be deduced from Figure 1.4 that the agreement between the calculated solubilities and the experimental values of Ellis (1963) over a 150 – 300°C temperatures range, and for ionic strengths up to 1 m NaCl at a fugacity of CO_2 gas of 12.159 bar. The increasing discrepancies observed below ~ 150°C may possibly be attributed to the fact that the partial pressure of CO_2 gas used by Ellis (1963) in these experiments substantially exceeds the total pressure (P_{sat}) at which the calculations are performed by the DISSOL program.

---

[5] Note in that respect that many calcium silicates for which the standard molal Gibbs energies of formation at 25°C and 1 bar (ΔG_f°) were derived from phase equilibrium studies involving calcite have also been subject to the same adjustment. Therefore, care should be exercised when carrying out thermodynamic calculations involving these phases.
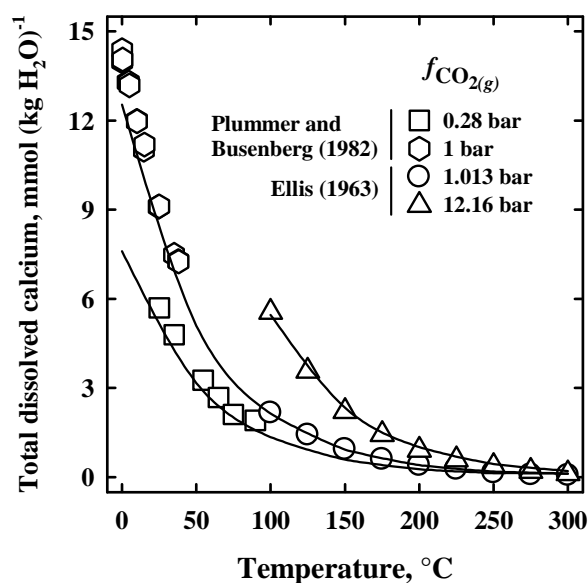
Figure 1.3. Solubility of calcite in pure water as a function of temperature and pressure. The symbols correspond to experimental data reported by Ellis (1963) and Plummer and Busenberg (1982). The curves were computed in the present study with the DISSOL computer program (see text).
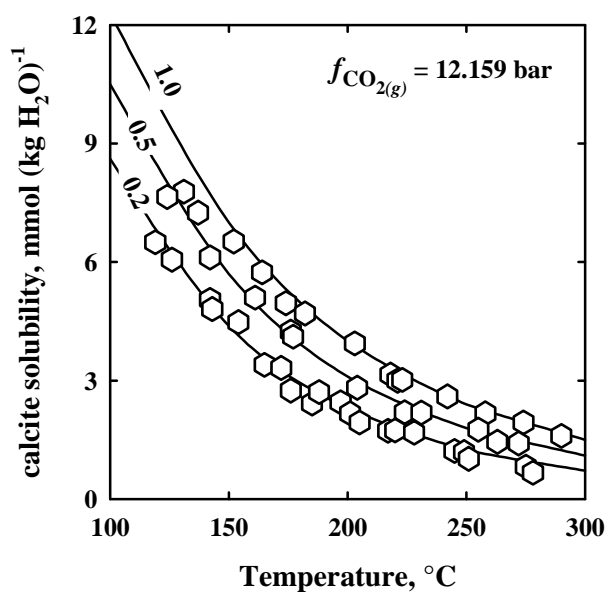
Figure 1.4. Solubility of calcite as a function of temperature and ionic strength at 12.159 bar. The symbols correspond to experimental data reported by Ellis (1963). The curves were computed in the present study with the DISSOL computer program (see text). The numbers on the curves correspond to different NaCl molalities.

2.1.3. Elemental sulfur

The standard molal thermodynamic properties and heat capacity power function coefficients adopted in the present study for elemental sulfur have been listed in Table A1. The standard molal Gibbs energy (ΔG_f°) and enthalpy (ΔH_f°) of formation of elemental sulfur at 25°C and 1 bar are equal to zero by definition. The value adopted in the present study for the standard molal entropy (S°) is the value recommended by Cox et al. (1989). The standard molal volume (V°) of rhombic sulfur at 25°C and 1 bar was taken from Robie et al. (1979). Experimental values reported in the literature for the standard molal heat capacity at 1 bar ($C_{P_r}^\circ$) of crystalline and liquid elemental sulfur above 25°C have been plotted as a function of temperature in Figures 1.5 and 1.6. It can be seen in Figure 1.5 that rhombic sulfur is affected by a lambda-type phase transition at 368.6 K (Eastman and McGavock, 1937), the enthalpy change associated with this transition being ΔH_t = 401.7 J mol^{-1} (West, 1959). Monoclinic sulfur melts at T_m = 388.36 K, with an associated enthalpy of melting ΔH_m = 1717.6 J mol^{-1} (West, 1959). The experimental heat capacity values shown in Figure 1.6 for liquid sulfur exhibit an unusual behavior, with increasing values up to a maximum at ~ 433 K and decreasing values beyond this temperature. This behavior has been interpreted as a molecular change from 8-membered rings below ~ 433 K to long sulfur chains above ~ 433 K (Powell and Eyring, 1943). The distribution of the values has been treated as if it were equivalent to a lambda transition. Accordingly, two sets of Maier-Kelley coefficients have been listed in Table A1 for liquid sulfur. These two sets of coefficients have been obtained by regressing separately with Equation (1.10) the experimental $C_{P_r}^\circ$ values reported by West (1959) below 433 K and above this temperature. The earlier values of Lewis and Randall (1911) were not considered in the regression. The enthalpy and volume changes associated to this pseudo transition are unknown. However, consideration of Figure 1.7 indicates that ignoring these changes has a negligible effect on the agreement between experimental and calculated enthalpy variations ($H_{T,P_r}^\circ - H_{T_r,P_r}^\circ$) for the complete temperature range over which sulfur exists as a liquid at the reference pressure of 1 bar.
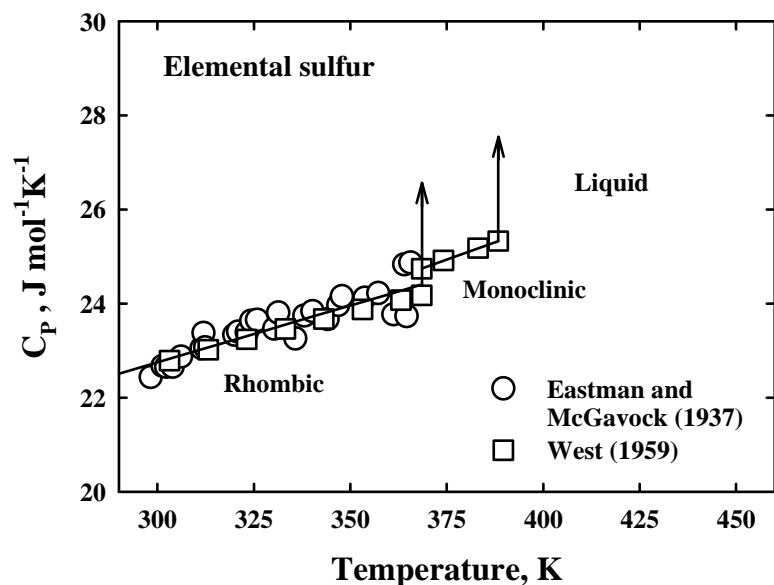
Figure 1.5. Standard molal heat capacity of crystalline sulfur as a function of temperature at ~ 1 bar. The straight lines represent regressions with Equation (1.10) of the data represented by the symbols and are consistent with the *a*, *b*, and *c* coefficients listed in Table A1 for rhombic and monoclinic sulfur.
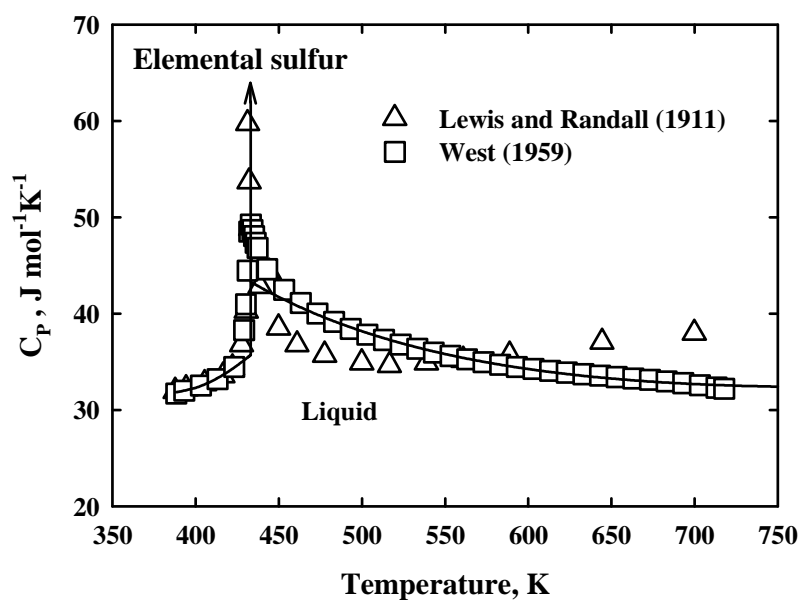
Figure 1.6. Standard molal heat capacity of liquid sulfur as a function of temperature at ~ 1 bar. The curves represent regressions with Equation (1.10) of the data represented by the symbols and are consistent with the *a*, *b*, and *c* coefficients listed in Table A1 for liquid sulfur – see text.
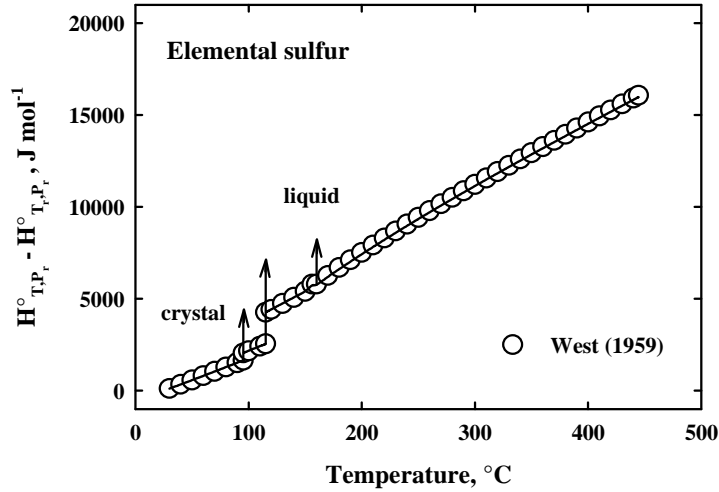
Figure 1.7. Variation of the standard molal enthalpy of crystalline and liquid sulfur as a function of temperature at ~ 1 bar computed with the SUPCRT92 computer program (Johnson et al. (1992) and the thermodynamic properties and heat capacity coefficients listed in Table A1 for elemental sulfur.

2.2. Hydrogen sulfide

2.2.1. PVT relations and phase behavior

Experimental studies which have been reported for the pressure-volume-temperature (*PVT*) relations, saturation pressures, and saturation vapor and liquid densities of hydrogen sulfide (H$_2$S) are summarized in Table 1.4. Experimental *PVT* data for H$_2$S have been reported by Reamer et al. (1950), Lewis and Fredericks (1968), Rau and Mathia (1982), and Ihmels and Ghmeling (2001). The temperature and pressure ranges covered by these studies can be compared in Figure 1.8. Sakoda and Uematsu (2004) recently proposed a 23-term equation of state for hydrogen sulfide which they developed on the basis of the above-mentioned *PVT* measurements, as well as heat capacity and vapor-liquid equilibrium data. This equation of state consists of two terms, an ideal gas term $\phi^0(\tau, \delta)$ and a residual contribution from the real fluid $\phi^r(\tau, \delta)$:

$$\phi(\tau, \delta) = \phi^0(\tau, \delta) + \phi^r(\tau, \delta) \tag{1.30}$$

where $\phi(\tau, \delta)$ is the reduced Helmoltz energy, τ is the inverse of the reduced temperature ($\tau = T/T_c$ with T_c being the critical temperature) and δ is the reduced density ($\delta = \rho/\rho_c$ with ρ_c being the density of the fluid at the critical point). The expressions for $\phi^0(\tau, \delta)$ and $\phi^r(\tau, \delta)$ are respectively written as:

$$\phi^0(\tau, \delta) = \ln(\delta) + f_1 + f_2\tau + f_3 \ln(\tau) + \sum_{i=4}^{5} f_i \ln\{1 - \exp(-g_i\tau)\} \tag{1.31}$$

and

35

$$\phi^r(\tau, \delta) = \sum_{i=1}^{11} n_i \tau^{t_i} + \sum_{i=12}^{16} n_i \, \tau^{t_i} \delta^{d_i} \exp(-\delta) + \sum_{i=17}^{19} n_i \tau^{t_i} \delta^{d_i} \exp(-\delta^2)$$

$$+ \sum_{i=1}^{21} n_i \tau^{t_i} \delta^{d_i} \exp(-\delta^3) + \sum_{i=22}^{23} n_i \tau^{t_i} \delta^{d_i} \exp(-\delta^4), \quad (1.32)$$

the f_i, g_i, t_i, n_i and d_i coefficients representing adjustment coefficients. The Sakoda-Uematsu equation of state accurately reproduces both the volumetric and phase behavior properties of H_2S, with reported uncertainties of 0.7% and 0.3% on calculated liquid and gas densities, respectively, and 0.2% on calculated saturation pressures. The equation of state of Sakoda and Uematsu (2004), which has been adopted by the National Institute of Standards and Technology (NIST, Lemmon et al., retrieved September 28, 2009), has been used in the present study to calculate molar volumes of H_2S as a function of temperature and pressure and compare these calculated values with those predicted from the classical modification by Soave (1972) of the Redlich-Kwong equation of state (Redlich and Kwong, 1949) which can be easily applied to the multicomponent systems of interest for the present study. In addition, fugacity coefficients can readily be obtained from the Soave-Redlich-Kwong (SRK) equation of state. This equation is written for a pure component under the form

$$P = \frac{RT}{v-b} - \frac{a(T)}{v(v+b)} \quad (1.33)$$

where P is the total pressure (bar), R is the ideal gas constant (8.314472 J mol^{-1}K^{-1}), T is the absolute temperature (K), v is the molar volume of the gas (cm^{3}mol^{-1}), b is the parameter (cm^{3}mol^{-1}) of the repulsion term in the Van der Waals equation of state. This parameter is defined in the SRK equation of state by

$$b = 0.08664 \frac{RT_c}{P_c} \quad (1.34)$$

where T_c and P_c represent the critical temperature and pressure of the gas. Finally, the $a(T)$ term constitues the modification introduced by Soave (1972) in the Redlich-Kwong equation of state, and correspond to the a parameter of the attraction term in the Van der Waals equation of state. This $a(T)$ term is defined by

$$a(T) = a(T_c) \cdot \alpha(T) \quad (1.35)$$

with

$$a(T_c) = 0.42748 \frac{R^2 T_c^2}{P_c} \quad (1.36)$$

and

$$\alpha(T) = [1 + (0.480 + 1.574\omega - 0.176\omega^2)(1 - \sqrt{T/T_c})]^2 \quad (1.37)$$

36
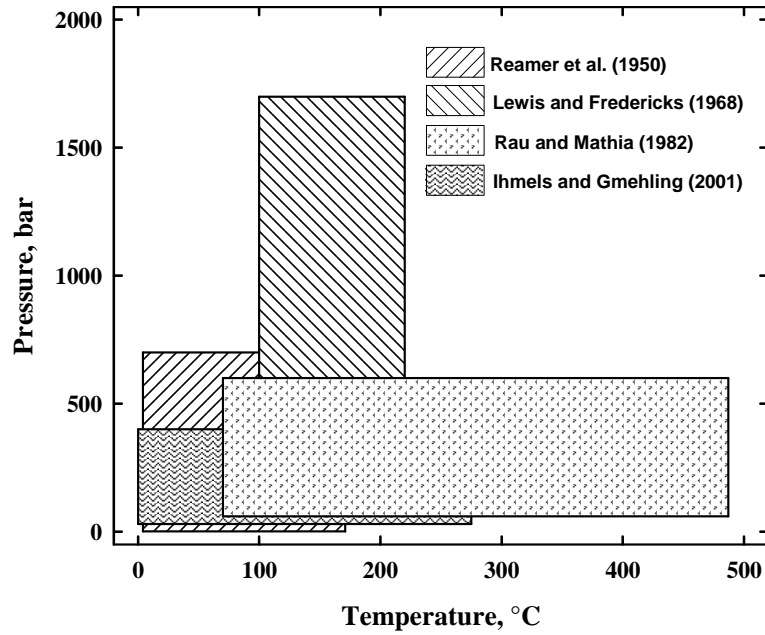
Figure 1.8. Temperature and pressure ranges of experimental measurements
on the pressure-volume-temperature relations for the system H_2S.

Table 1.4. Summary of experimental *PVT* data, vapor pressures, and saturation liquid/vapor
densities reported in the literature for hydrogen sulfide.

Authors	Property	Temperature (ºC)	Pressure (bar)
Reamer et al. (1950)	*PVT*	4.440 – 171.10	1.013 – 689.5
Lewis and Fredericks (1968)	*PVT*	99.85 – 219.85	91.00 – 1700
Rau and Mathia (1982)	*PVT*	70.00 – 486.00	60.00 – 600.0
Ihmels and Gmehling (2001)	*PVT*	0.240 – 275.10	30.00 – 400.0
Giauque and Blue (1936)	P_s, ρ^v, ρ^l	-84.75 – 59.930	0.200 – 1.000
Reamer et al. (1950)	P_s, ρ^v, ρ^l	4.440 – 100.38	11.00 – 90.00
Bierlein and Kay (1953)	P_s, ρ^v, ρ^l	13.28 – 100.38	15.19 – 90.04
Kay and Brice (1953)	P_s	10.33 – 99.880	13.78 – 89.43
Kay and Rambosek (1953)	P_s, ρ^v, ρ^l	-1.110 – 99.940	10.03 – 89.43
Clarke and Glew (1970)	P_s, ρ^v, ρ^l	-77.87 – 50.00	0.370 – 22.74
Cubitt et al. (1987)	P_s, ρ^l	-76.31 – -8.39	0.230 – 9.390

P_s: saturation vapor pressure; ρ^v, ρ^l: saturation vapor and liquid densities.

where ω is Pitzer´s acentric factor (Pitzer et al., 1955). The values of the critical parameters
and of the acentric factor of hydrogen sulfide which have been used in the present study were
taken from Reid et al. (1987), and have the following values: $T_c = 373.2$ K, $P_c = 89.40$ bar,
and $\omega = 0.097$.

The values of the standard molal volumes of H_2S computed from the Sakoda-Uematsu and SRK equations of state can be compared in Table 1.5 and Figure 1.9. It can be seen in this figure that both equations reproduce the experimental volumes fairly well, except that the SRK equation of state of Soave (1972) overestimates these volumes by ~ 3.3 cm^3mol^{-1} and ~ 2 $cm^3 \cdot mol^{-1}$ at the higher pressures of 300 and 500 bar at 200ºC. Such overestimations should however have a limited effect on the calculation of fugacities at these temperatures and pressures (see below). The discrepancy between the experimental volumes and the SRK equation of state at ~ 100ºC and 100 bar is due to an inherent difficulty to predict volumetric properties with cubic equations of state in the vicinity of the critical point.

Table 1.5. Comparison of standard molar volumes of H_2S liquid and gas computed from the Sakoda-Uematsu (roman) and Soave-Redlich-Kwong (*italics*) equations of state.

Temperature (ºC)	0	100	200	300	400
Pressure (bar)	Molar volume (cm^3mol^{-1})				
1	22484	30911	39274	47615	55946
	22500	*30910*	*39270*	*47620*	*55950*
100	40.131	67.415	322.66	439.23	540.30
	41.92	*78.81*	*323.4*	*441.0*	*543.2*
200	39.418	53.762	128.66	204.71	263.75
	40.97	*58.71*	*134.9*	*208.9*	*267.8*
300	38.817	49.954	81.722	131.44	174.14
	40.21	*53.28*	*88.87*	*137.1*	*179.2*
400	38.296	47.672	67.381	99.392	131.59
	39.58	*50.17*	*72.78*	*105.4*	*137.0*
500	37.837	46.048	60.665	83.063	107.75
	39.04	*48.03*	*64.69*	*88.42*	*113.0*
600	37.426	44.793	56.598	73.591	93.032
	38.58	*46.43*	*59.70*	*78.05*	*97.84*
700	37.054	43.772	53.778	67.456	83.252
	38.17	*45.17*	*56.23*	*71.11*	*87.49*
800	36.714	42.914	51.661	63.136	76.350
	37.81	*44.17*	*53.65*	*66.13*	*80.00*
900	36.400	42.176	49.986	59.901	71.233
	37.48	*43.27*	*51.63*	*62.36*	*74.35*
1000	36.100	41.528	48.612	57.368	67.284
	37.19	*42.52*	*50.00*	*59.41*	*69.93*
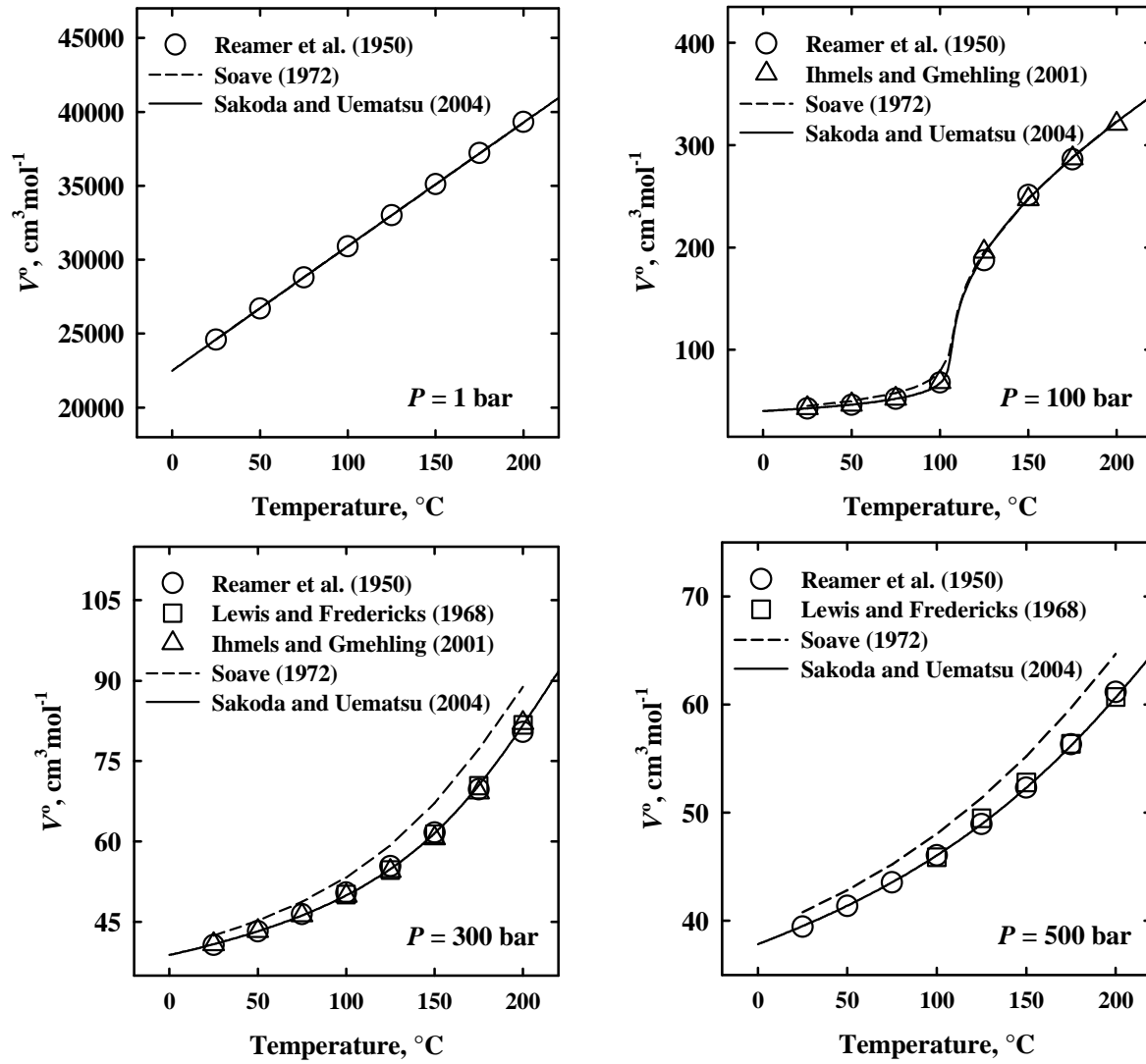
Figure 1.9. Standard molal volumes of H$_2$S liquid and gas as a function of temperature at constant pressure. The symbols correspond to experimental values reported in the literature. The solid and dashed curves represent values calculated from the Sakoda-Uematsu and SRK equations of state, respectively.

In their model for calculating the solubility of H$_2$S in brines at high temperatures and pressures (see below), Duan et al. (1996) have proposed another equation of state from which the *PVT* relations of H$_2$S can be calculated. This equation has the following form when written for the compressibility factor *z* (Duan et al., 1992, 1996):

$$z = 1 + \frac{a_1 + a_2/T_r^2 + a_3/T_r^3}{V_r} + \frac{a_4 + a_5/T_r^2 + a_6/T_r^3}{V_r^2} + \frac{a_7 + a_8/T_r^2 + a_9/T_r^3}{V_r^4}$$
$$+ \frac{a_{10} + a_{11}/T_r^2 + a_{12}/T_r^3}{V_r^5} + \frac{a_{13}}{T_r^3 V_r^2}\left(a_{14} + \frac{a_{15}}{V_r^2}\right)\exp\left(-\frac{a_{15}}{V_r^2}\right) \quad (1.38)$$

where a_1-a_{15} are parameters evaluated by fitting *PVT* and liquid-vapor phase equilibrium data, and T_r, P_r, and V_r are the reduced temperature, pressure, and volume respectively defined by $T_r = T/T_c$, $P_r = P/P_c$, and $V_r = V/V_c$, where T_c, P_c, and V_c are the critical temperature, pressure, and volume. Duan et al. (1996) first retrieved values of the a_1-a_{15} parameters by considering experimental *PVT* data reported by Reamer et al. (1950) and Rau and Mathia (1982), which were subsequently revised by Duan et al. (2007) by taking into account (supposedly) more recent experimental data. Standard molal volumes for H_2S liquid and gas calculated with the equations of state of Duan et al. (2007) and Sakoda and Uematsu (2004) can be compared in Table 1.6, where it can be seen that both equations yield very similar values of $V^°$ over the 0 – 400°C and 1 – 1000 bar temperature and pressure ranges.

Table 1.6. Comparison of standard molar volumes of H_2S liquid and gas computed from the Duan et al. (roman) and Sakoda-Uematsu (*italics*) equations of state.

Temperature (°C)	0	100	200	300	400
Pressure (bar)	Molar volume (cm³mol⁻¹)				
1	22463	30914	39282	47623	55952
	22484	*30911*	*39274*	*47615*	*55946*
100	40.347	68.219	327.97	443.86	543.15
	40.131	*67.415*	*322.66*	*439.23*	*540.30*
200	39.629	54.045	127.89	205.84	264.25
	39.418	*53.762*	*128.66*	*204.71*	*263.75*
300	39.011	50.278	81.555	130.56	173.12
	38.817	*49.954*	*81.722*	*131.44*	*174.14*
400	38.464	48.014	67.539	98.426	129.95
	38.296	*47.672*	*67.381*	*99.392*	*131.59*
500	37.974	46.388	60.864	82.462	106.17
	37.837	*46.048*	*60.665*	*83.063*	*107.75*
600	37.527	45.115	56.804	73.236	91.735
	37.426	*44.793*	*56.598*	*73.591*	*93.032*
700	37.119	44.069	53.980	67.248	82.234
	37.054	*43.772*	*53.778*	*67.456*	*83.252*
800	36.740	43.180	51.851	63.003	75.549
	36.714	*42.914*	*51.661*	*63.136*	*76.350*
900	36.387	42.406	50.158	59.809	70.588
	36.400	*42.176*	*49.986*	*59.901*	*71.233*
1000	36.055	41.721	48.760	57.295	66.749
	36.100	*41.528*	*48.612*	*57.368*	*67.284*

2.2.2. Fugacity coefficients

The fugacity *f* of a pure gas is obtained in a rigourous manner from *PVT* relations by considering the Tunell (1931) equation, which is written as

$$RT \ln f = RT \ln P - \int_0^P \left(\frac{RT}{P} - v \right) dP \qquad (1.39)$$

where R again designates the ideal gas constant, T stands for the absolute temperature (K), P represents the total pressure (bar), and v is the molar volume of the gas ($cm^3 mol^{-1}$). The fugacity f is related to the pressure P by the fugacity coefficient φ:

$$\varphi = f/P \ . \tag{1.40}$$

Carroll and Mather (1989a) have computed fugacity coefficients of H_2S gas between 20ºC and 90ºC and 1 to 10 bar from the Redlich-Kwong equation of state (Redlich and Kwong, 1949), but for the H_2S-H_2O system in which the gas phase contains a minor proportion of water. The Redlich-Kwong equation of state is written as

$$P = \frac{RT}{v-b} - \frac{a}{T^{0.5}v(v+b)} \tag{1.41}$$

with

$$a = 0.42748 \frac{R^2 T_c^{2.5}}{P_c} \tag{1.42}$$

and

$$b = 0.08664 \frac{RT_c}{P_c} \ . \tag{1.43}$$

The expression of the fugacity coefficient of a pure gas for the Redlich-Kwong equation of state is the following (Prausnitz et al., 1986):

$$\ln \varphi = \ln \frac{V}{V-b} + \frac{b}{V-b} - \frac{2a}{RT^{3/2}b} \ln \frac{V+b}{V} + \frac{a}{RT^{3/2}b}[\ln \frac{V+b}{V} - \frac{b}{V+b}] - \ln \frac{Pv}{RT} \ . \tag{1.44}$$

The corresponding expression for the Duan et al. (1992) equation of state may be written as

$$\ln \varphi = z - 1 - \ln z + \frac{a_1 + a_2/T_r^2 + a_3/T_r^3}{V_r} + \frac{a_4 + a_5/T_r^2 + a_6/T_r^3}{2V_r^2}$$

$$+ \frac{a_7 + a_8/T_r^2 + a_9/T_r^3}{4V_r^4} + \frac{a_{10} + a_{11}/T_r^2 + a_{12}/T_r^3}{5V_r^5}$$

$$+ \frac{a_{13}}{2T_r^3 a_{15}} \left[a_{14} + 1 - \left(a_{14} + 1 + \frac{a_{15}}{V_r^2} \right) \exp \left(-\frac{a_{15}}{V_r^2} \right) \right]. \tag{1.45}$$

Fugacity coefficients computed from the Duan et al. (1992) equation of state together with values for the a_1-a_{15} parameters taken from Duan et al. (2007) are compared in Table 1.7 with those predicted from the Redlich-Kwong equation of state together with parameters taken from Reid et al. (1987). It can be deduced from this table that both equations provide comparable values of φ, except at 100ºC above 100 bar. The reason for the discrepancy at that particular temperature is unclear.

Table 1.7. Comparison of fugacity coefficients of pure H$_2$S gas computed from the Duan et al. (roman) and Redlich-Kwong (*italics*) equations of state.

Temperature (°C)	0	100	200	300	400
Pressure (bar)	Fugacity coefficient (dimensionless)				
1	0.9892	0.9964	0.9985	0.9993	0.9997
	0.9907	*0.9961*	*0.9981*	*0.9990*	*0.9994*
100	0.1078	0.6169	0.8558	0.9348	0.9706
	0.1139	*0.6056*	*0.8218*	*0.9049*	*0.9477*
200	0.0643	0.3725	0.7188	0.8727	0.9430
	0.0676	*0.5193*	*0.6771*	*0.8270*	*0.9051*
300	0.0509	0.2936	0.6169	0.8181	0.9186
	0.0537	*0.4140*	*0.5823*	*0.7683*	*0.8729*
400	0.0453	0.2579	0.5577	0.7769	0.8995
	0.0479	*0.3674*	*0.5292*	*0.7286*	*0.8506*
500	0.0429	0.2402	0.5248	0.7501	0.8869
	0.0456	*0.3451*	*0.5002*	*0.7044*	*0.8373*
600	0.0422	0.2320	0.5077	0.7355	0.8811
	0.0451	*0.3357*	*0.4858*	*0.6918*	*0.8317*
700	0.0426	0.2296	0.5009	0.7302	0.8818
	0.0458	*0.3345*	*0.4807*	*0.6880*	*0.8325*
800	0.0439	0.2312	0.5013	0.7324	0.8881
	0.0474	*0.3390*	*0.4824*	*0.6910*	*0.8388*
900	0.0458	0.2359	0.5073	0.7404	0.8993
	0.0498	*0.3479*	*0.4892*	*0.6994*	*0.8496*
1000	0.0484	0.2431	0.5177	0.7534	0.9149
	0.0530	*0.3606*	*0.5003*	*0.7123*	*0.8645*

2.2.3. Solubility of H$_2$S in water

Experimental studies on the solubility of hydrogen sulfide reported in the literature are summarized in Table 1.8, along with the temperature, pressure, and NaCl molality ranges covered in these studies. The measured solubilities are reported either as Bunsen absorption coefficients (Winkler, 1906; Gillespie and Wilson, 1980), H$_2$S molalities (Kozintseva, 1964; Drummond, 1981; Barrett et al., 1988; Xia et al., 2000), H$_2$S mole fractions in the aqueous phase (Selleck et al., 1952; Clarke and Glew, 1971; Lee and Mather, 1977; Suleimenov and Krupp, 1994; Chapoy et al., 2005), or Henry's Law constants (Kozintseva, 1964; Clarke and Glew, 1971; Drummond, 1981; Suleimenov and Krupp, 1994).

The solubility of H$_2$S in water corresponds to the reaction
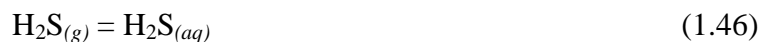
$$H_2S_{(g)} = H_2S_{(aq)} \qquad (1.46)$$

for which the law of mass action may be written as

$$K_{(1.46)} = \frac{a_{H_2S_{(aq)}}}{f_{H_2S_{(g)}}} = \frac{\gamma_{H_2S_{(aq)}} m_{H_2S_{(aq)}}}{\varphi_{H_2S_{(g)}} p_{H_2S_{(g)}}} \qquad (1.47)$$

where $f_{H_2S_{(g)}}$, $\varphi_{H_2S_{(g)}}$, and $p_{H_2S_{(g)}}$ correspond to the fugacity, fugacity coefficient and partial pressure of the gas species and $a_{H_2S_{(aq)}}$, $\gamma_{H_2S_{(aq)}}$ and $m_{H_2S_{(aq)}}$ stand for the activity, activity coefficient and molality of the aqueous species. The equations for converting experimental solubilities reported as Henry´s Law constants (k_H) to equilibrium constants have been presented by Shock et al. (1989). If the Henry´s Law constant is expressed as the ratio between the fugacity of H_2S in the gas phase ($f_{H_2S_{(g)}}$) and the mole fraction of the solute in the aqueous phase ($X_{H_2S_{(aq)}}$):

$$k_H = \frac{f_{H_2S_{(g)}}}{X_{H_2S_{(aq)}}} = \frac{\varphi_{H_2S_{(g)}} p_{H_2S_{(g)}}}{X_{H_2S_{(aq)}}} \quad , \tag{1.48}$$

the equilibrium constant for Reaction (1.46) can be expressed as

$$K_{(1.46)} = \frac{\gamma_{H_2S_{(aq)}} m_{H_2S_{(aq)}}}{k_H X_{H_2S_{(aq)}}} \quad . \tag{1.49}$$

Table 1.8. Experimental studies on the solubility of hydrogen sulfide as a function of temperature and pressure in H_2O-NaCl solutions.

Study	Temperature (°C)	Pressure (bar)	m_{NaCl} (mol)
Winkler (1906)	0 – 60	1.01325	0
Selleck et al. (1952)	37.78 – 171.11	6.895 – 344.7	0
Kozintseva (1964)	160 – 330	0.81 – 2.09	0
Clarke and Glew (1971)	0 – 50	0.547 – 0.945	0
Lee and Mather (1977)	10 – 180	1.548 – 66.7	0
Gillespie and Wilson (1980)	37.8 – 260	3.4 – 206.8	0
Drummond (1981)	30.9 – 354.7	7.10 – 195.04	0 – 6.15
Barrett at al. (1988)	25 – 95	1.01325	0 – 5
Suleimenov and Krupp (1994)	20 – 320	P_{sat}	0 – 2.5
Xia et al. (2000)	40 – 120	10.0 – 100.0	4 – 6
Chapoy et al. (2005)	25 – 65.18	5.03 – 39.62	0

If the aqueous solution is ideal, the activity coefficient of aqueous H_2S ($\gamma_{H_2S_{(aq)}}$) is equal to one. The molar fraction of aqueous H_2S in one kilogram (55.51 moles) of pure water is given by

$$X_{H_2S_{(aq)}} = \frac{m_{H_2S_{(aq)}}}{m_{H_2S_{(aq)}} + m_{H_2O_{(l)}}} = \frac{m_{H_2S_{(aq)}}}{m_{H_2S_{(aq)}} + 55.51} \quad , \tag{1.50}$$

from which the general relationship between the equilibrium constant and the Henry´s Law constant is obtained: [6]

$$K = \frac{m_{H_2S_{(aq)}} + 55.51}{k_H} \quad . \tag{1.51}$$

---

[6] Note that Equation (A) in Table 1 of Shock et al. (1989) is erroneously written as $K = 55.51/k_H$ (H.C. Helgeson, 2003, personal communication to L. Richard).

Equation (1.51) has been used to convert the solubility measurements reported by Kozintseva (1964), Clarke and Glew (1971), and Suleimenov and Krupp (1994) to equilibrium constants. In contrast, conversion of the values of the Henry´s Law constant reported by Drummond (1981) in molal units has been made using the equation (Shock et al., 1989):

$$K = \frac{0.9869}{k_D}, \tag{52}$$

where 0.9869 is equal to 1/1.01325 and represents a conversion from atmopheres to bars. Logarithmic values of the equilibrium constant (log $K_{(1.46)}$) of Reaction (1.46) derived in the manner described above from the measurements of Kozintseva (1964), Clarke and Glew (1971), Drummond (1981), and Suleimenov and Krupp (1994) are compared in Figure 1.10 to those computed using the SUPCRT92 program (Johnson et al., 1992) together with thermodynamic properties taken from Helgeson et al. (1978) and Shock et al. (1989) for gas and aqueous H_2S, respectively (see Tables A1 and A2 of the Appendix). It can be seen in this figure that the calculated curve slightly underestimates the more recent solubility measurements of Suleimenov and Krupp (1994) above ~ 250ºC. This may come from the values of the HKF parameters given by Shock et al. (1989), which probably represent a compromise between the measurements of Kozintseva (1964) and Drummond (1981).
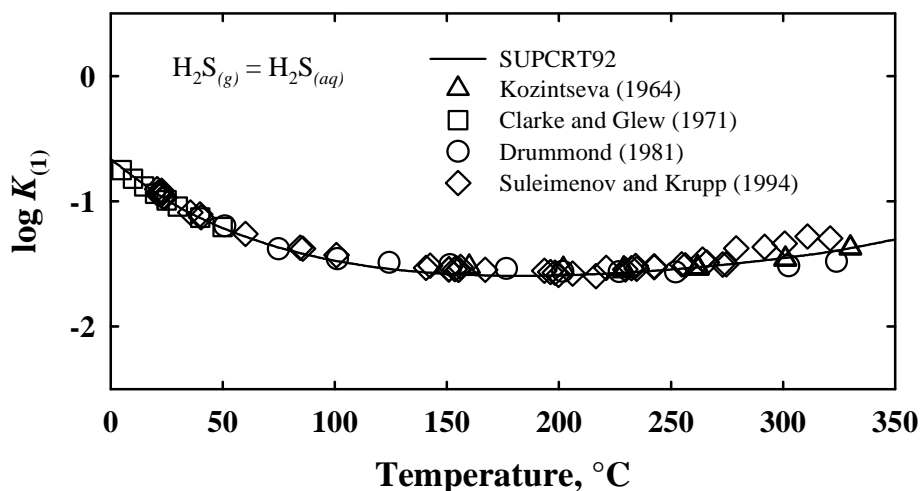
Figure 1.10. Logarithm of the equilibrium constant of Reaction (1.46) as a function of temperature at P_{sat}. The symbols correspond to values computed from experimental solubility measurements reported in the literature. The curve was calculated using the SUPCRT92 computer program (Johnson et al., 1992) together with thermodynamic properties taken from Helgeson et al. (1978) and Shock et al. (1989) – modified after Shock et al. (1989).

Experimental values taken from Lee and Mather (1977) and Barrett et al. (1988) have been plotted as symbols in Figure 1.11 to illustrate the dependence on temperature, pressure, and ionic strength of the aqueous solubility of H_2S. It can be seen in this figure that this solubility decreases with increasing temperature and NaCl molality. The decrease in the solubility of a gas with increasing ionic strength is known as the "salting-out" effect (Setchenow, 1889). In contrast, the right diagram in Figure 1.11 shows that the solubility of H_2S in water increases with increasing gas pressure in accord with Henry´s Law (see Eqn. 1.48). Duan et al. (2007) have proposed an accurate model to describe the solubility of H_2S in aqueous solutions up to 500 K (227ºC), 200 bar, and 6 m NaCl. This model is based on the equality of the chemical potentials of H_2S in the liquid (i.e. aqueous) phase ($\mu_{H_2S_{(aq)}}$) and in the vapor phase ($\mu_{H_2S_{(g)}}$):

$$\mu_{H_2S_{(aq)}} = \mu_{H_2S_{(g)}} \quad . \tag{1.53}$$

These chemical potentials are related to the activity of H_2S in the aqueous phase ($a_{H_2S_{(aq)}}$) and the fugacity of H_2S in the gas phase ($f_{H_2S_{(g)}}$), respectively, by

$$\mu_{H_2S_{(aq)}} = \mu^o_{H_2S_{(aq)}} + RT \ln a_{H_2S_{(aq)}} = \mu^o_{H_2S_{(aq)}} + RT \ln m_{H_2S_{(aq)}} + RT \ln \gamma_{H_2S_{(aq)}} \tag{1.54}$$

and

$$\mu_{H_2S_{(g)}} = \mu^o_{H_2S_{(g)}} + RT \ln f_{H_2S_{(g)}} = \mu^o_{H_2S_{(g)}} + RT \ln \varphi_{H_2S_{(g)}} + RT \ln y_{H_2S_{(g)}} \cdot P \quad , \tag{1.55}$$

where $y_{H_2S_{(g)}}$ is the mole fraction of H_2S in the gas phase, and $\mu^o_{H_2S_{(aq)}}$ and $\mu^o_{H_2S_{(g)}}$ are the chemical potentials of the subscripted components in the standard state. Equating Eqns. (1.54) and (1.55) yields

$$\ln \frac{y_{H_2S_{(g)}} \cdot P}{m_{H_2S_{(aq)}}} = \frac{\mu^o_{H_2S_{(aq)}} - \mu^o_{H_2S_{(g)}}}{RT} - \ln \varphi_{H_2S_{(g)}} + \ln \gamma_{H_2S_{(aq)}} \tag{1.56}$$

The fugacity coefficient of H_2S gas in the Duan et al. (2007) model is evaluated from Equation (1.45), while the specific interaction model of Pitzer (1973) is considered for calculating the activity coefficient of H_2S in the aqueous phase. It is out of the scope of this chapter to present the specific interaction theory in details, and we refer the reader to the excellent summary given by Pitzer (1987). The starting point is the expression for the total excess Gibbs energy of an electrolyte solution:

$$G^{ex}/n_W RT = f(I) + \sum_i \sum_j \lambda_{ij} m_i m_j + \sum_i \sum_j \sum_k \xi_{ijk} m_i m_j m_k \tag{1.57}$$

where n_W is the number of kilograms of water, $f(I)$ is a term including the Debye-Hückel limiting law (Pitzer, 1987)

$$f(I) = -AI^{3/2} \quad , \tag{1.58}$$
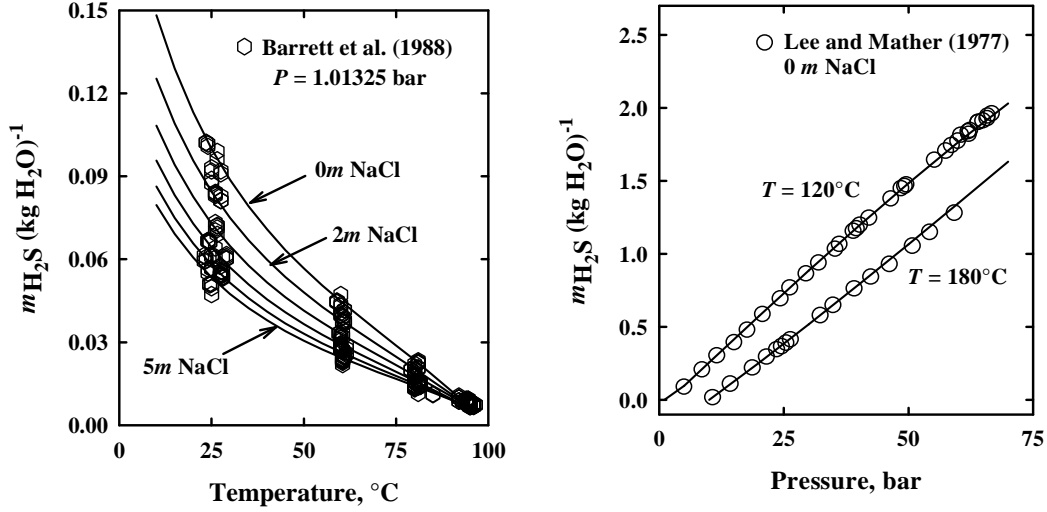
Figure 1.11. Aqueous solubility of H_2S as a function of temperature, pressure, and NaCl molality. The symbols represent experimental data reported in the literature. The curves have been calculated using the model of Duan et al. (2007).

and λ_{ij} and μ_{ijk} are second- and third-order virial coefficients accounting for interactions among two and three species, respectively. The activity coefficient is obtained from the following derivative of the total excess Gibbs energy (Anderson and Crerar, 1993, p. 448):

$$\ln \gamma_i = \left(\frac{\partial G^{ex}/n_W RT}{\partial m_i} \right)_{T,P,n_W} . \tag{1.59}$$

The expression used by Duan et al. (2007) for calculating $\ln \gamma_{H_2S_{(aq)}}$ is the following:

$$\ln \gamma_{H_2S_{(aq)}} = \sum_c 2\lambda_{H_2S-c} m_c + \sum_a 2\lambda_{H_2S-a} m_a + \sum_c \sum_a \xi_{H_2S-c-a} m_c m_a \tag{1.60}$$

where c and a designate cations and anions, respectively, m_c and m_a represent their molalities, and λ_{H_2S-c}, λ_{H_2S-a} and ξ_{H_2S-a-c} stand for the second-order and third-order interaction parameters. The second-order parameters are dependent on temperature and pressure. Because of the constraint that experimental measurements are always carried out in electrically neutral solutions, Duan et al. (2007) arbitrarily fixed the value of λ_{H_2S-Cl} to zero and determined the other parameters by adjusting solubility data in aqueous NaCl solutions. The expressions obtained for these parameters are as follows:

$$\lambda_{H_2S-Na} = 0.085004999 + (3.5330378 \times 10^{-5})T$$
$$- 1.5882605/T + (1.1894926 \times 10^{-5})P \tag{1.61}$$

and

$$\xi_{H_2S-Na-Cl} = -0.010832589 . \tag{1.62}$$

It can be deduced from Figure 1.11 that the solubility values calculated for H_2S with the model of Duan et al. (2007) as a function of temperature, pressure, and NaCl molality are in very good agreement with the experimental measurements of both Lee and Mather (1977) and Barrett et al. (1988).

46

2.2.4. Solubility of H₂S in hydrocarbons

Experimental studies on the phase behavior of H₂S-hydrocarbon mixtures have been reported for methane (Reamer et al., 1951), ethane (Kay and Brice, 1953), propane (Kay and Rambosek, 1953), *n*-butane (Robinson et al., 1964), *i*-butane (Besserer and Robinson, 1975), *n*-pentane (Reamer et al., 1953a), *n*-heptane (Ng et al., 1980), *n*-decane (Reamer et al., 1953b), methylcyclohexane (Ng and Robinson, 1979), and toluene (Ng et al., 1980). Experimental measurements of the solubility of hydrogen sulfide gas in hydrocarbon liquids have been reported by Bell (1931), Reamer et al. (1953a,b), Lenoir et al. (1971), Gerrard (1972), Eakin and De Vaney (1974), Makranczy et al. (1976), Tremper and Prausnitz (1976), King and Al-Najjar (1977), Feng and Mather (1992, 1993a,b), Yokoyama et al. (1993), Feng et al. (1995), Laugier and Richon (1995), and Fischer et al. (2002). The temperature and pressure conditions covered and hydrocarbon liquids considered in these studies are summarized in Table 1.9. Lenoir et al. (1971) and Tremper and Prausnitz (1976) reported their data as Henry´s Law constants (k_H), which have been converted in the present study to mole fractions of H₂S in the hydrocarbon liquid phase ($x_{H_2S_{(hcl)}}$) in accord with

$$x_{H_2S_{(hcl)}} = \frac{f_{H_2S_{(g)}}}{k_H} \tag{1.63}$$

and adopting a fugacity of H₂S in the gas phase ($f_{H_2S_{(g)}}$) equal to 1 bar based on the fugacity coefficients listed in Table 1.7 and the low total pressures (less than or approximately equal to 1 bar) at which Lenoir et al. (1971) and Tremper and Prausnitz (1976) carried out their measurements. Makranczky et al. (1976) reported their solubility measurements as Bunsen coefficients (α_B), which were converted to mole fractions of H₂S in the liquid hydrocarbon phase in accord with (Gamsjäger et al., 2010 – see their Eqn. 18)

$$x_{H_2S_{(hcl)}} = \frac{1}{1 + \frac{RT^\theta}{P^\theta V_{m,A}^{l,*} \alpha_B}} \tag{1.64}$$

where $V_{m,A}^{l,*}$ stands for the molar volume of the liquid solvent at reference values of temperature (T^θ) and pressure (P^θ), which in the present case are assumed to be those at which the measurements were made (i.e. 25 and 40ºC, 1.01325 bar). The values of $V_{m,A}^{l,*}$ for the twelve hydrocarbons which have been used are those recommended on the NIST website (http://webbook.nist.gov/chemistry/fluid/). The details of the conversion are given in Table 1.10. The value used for the R constant is $R = 82.05746$ cm³·atm·K⁻¹·mol⁻¹. Finally, Bell (1931), Reamer et al. (1953a,b), Gerrard (1972), Eakin and De Vaney (1974), King and Al-Najjar (1977), Feng and Mather (1992, 1993), Yokoyama et al. (1993), Feng et al. (1995),

Laugier and Richon (1995) and Fischer et al. (2002) reported their solubility data as mole fractions of H_2S in the hydrocarbon phase. Bell (1931), Gerrard (1972) and King and Al-Najjar (1977) carried out their measurements at a total pressure of ~ 1 bar. In contrast, Reamer et al. (1953a,b), Eakin and De Vaney (1974), Feng and Mather (1992, 1993), Yokoyama et al. (1993), Feng et al. (1995), Laugier and Richon (1995) and Fischer et al. (2002) reported their measurements as solubility isotherms as a function of pressure.

The temperature dependence of the solubility of H_2S gas in hydrocarbon liquids (expressed as $x_{H_2S_{(hcl)}}$) is illustrated in Figure 1.12 for n-decane ($C_{10}H_{22}$) and n-hexadecane ($C_{16}H_{34}$). It can be deduced from this figure that the solubility of H_2S decreases by a factor of ~ 2.5 when the temperature increases from 25ºC to 100ºC, and by a factor of ~ 5 when the temperature increases from 25ºC to 200ºC. It can also be seen that the solubility of H_2S in n-decane is slightly less than in n-hexadecane. In fact, the solubility of H_2S gas in liquid n-alkanes appears to be, like many other thermodynamic properties of homologous families of hydrocarbons, a regular (but not necessarily linear) function of carbon number (see below). This is apparent in Figure 1.13, where values of $x_{H_2S_{(hcl)}}$ representing the solubility of H_2S gas in liquid n-alkanes at 25ºC and ~ 1 bar have been plotted as a function of carbon number. It can be deduced from this figure that the solubility of H_2S gas in liquid n-alkanes increases from $x_{H_2S_{(hcl)}} = 0.042$ in n-pentane (C_5H_{12}) to $x_{H_2S_{(hcl)}} = 0.057$ in n-hexadecane ($C_{16}H_{34}$).
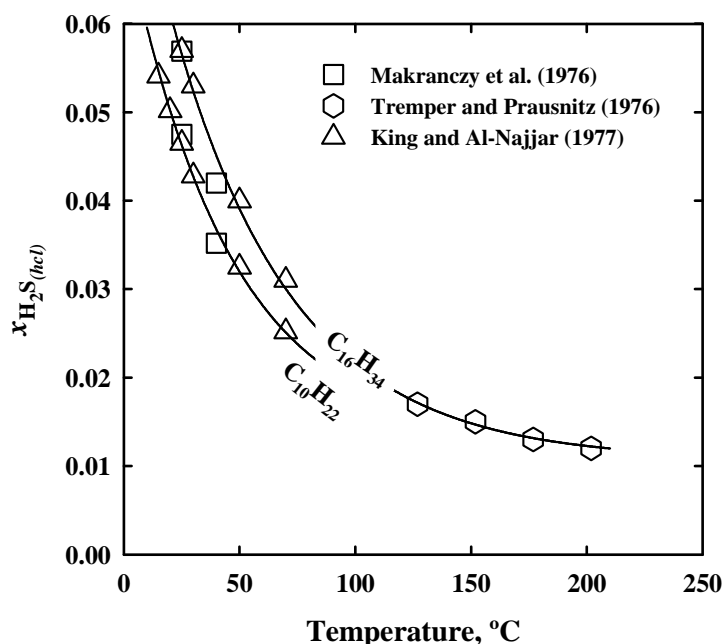
Figure 1.12. Solubility of H_2S in liquid n-decane ($C_{10}H_{22}$) and n-hexadecane ($C_{16}H_{34}$) as a function of temperature at ~ 1 bar. The symbols correspond to experimental data reported in the literature. The curves have merely been drawn to highlight the temperature dependence of the solubility of H_2S gas in the liquid hydrocarbons.

Table 1.9. Experimental studies on the solubility of hydrogen sulfide as a function of temperature and pressure in hydrocarbon liquids.

Study	Temperature (°C)	Pressure (bar)	Hydrocarbons
Bell (1931)	20	1.01325	*n*-Hexane
			n-Octane
			n-Dodecane
			n-Hexadecane
			Cyclohexane
			Benzene
			Toluene
Reamer et al. (1953a)	4.4 – 171.1	1.4 – 89.6	*n*-Pentane
Reamer et al. (1953b)	4.4 – 171.1	1.4 – 133.4	*n*-Decane
Lenoir et al. (1971)	25, 50	1.01325	Decahydronaphthalene
			n-Hexadecane
Gerrard (1972)	-8.44 – 20.00	1	*n*-Decane
			Benzene
Eakin and De Vaney (1974)	38 – 149	1.4 – 27.6	*n*-Nonane
			iso-Propylcyclohexane
			1,3,5-Trimethylbenzene
Makranczy et al. (1976)	25, 40	1.01325	*n*-Pentane
			n-Hexane
			n-Heptane
			n-Octane
			n-Nonane
			n-Decane
			n-Undecane
			n-Dodecane
			n-Tridecane
			n-Tetradecane
			n-Pentadecane
			n-Hexadecane
Tremper and Prausnitz (1976)	27 – 202	< 1.3	*n*-Hexadecane
			Diphenylmethane
			Bicyclohexyl
			1-Methylnaphthalene
King and Al-Najjar (1977)	15 – 70	1.01325	*n*-Hexane
			n-Octane
			n-Decane
			n-Dodecane
			n-Tetradecane
			n-Hexadecane
Yokoyama et al. (1993)	50 – 250	1.92 – 16.58	*iso*-Octane
			n-Decane
			n-Tridecane
			n-Hexadecane
			Squalane
Feng and Mather (1992)	50 – 150	4.0 – 76	*n*-Eicosane
Feng and Mather (1993a)	50 – 150	5.3 – 74	*n*-Hexadecane
Feng and Mather (1993b)	40 – 160	5.2 – 56	*n*-Dodecane
Feng et al. (1995)	50	10 – 30	*n*-Hexadecane
			n-Eicosane
Laugier and Richon (1995)	50 – 150	4 – 112	*n*-Hexane
			n-Pentadecane
			Cyclohexane
			Benzene
Fischer et al. (2002)	31, 50	10 – 118	Benzene

Table 1.10. Conversion with Equation (1.64) of Bunsen coefficients reported by Makranczy et al. (1976) to mole fractions of H_2S in hydrocarbon liquid phase.

Hydrocarbon	T (ºC)	α_B [a]	$V_{m,A}^{l,*}$ [b]	$x_{H_2S_{(hcl)}}$ [c]
n-Pentane	25	9.147	116.2	0.0416
	40	6.93	117.9	0.0308
n-Hexane	25	8.230	131.6	0.0424
	40	6.23	134.5	0.0316
n-Heptane	25	7.520	147.4	0.0434
	40	5.69	150.3	0.0322
n-Octane	25	6.986	163.6	0.0446
	40	5.28	166.5	0.0331
n-Nonane	25	6.560	179.6	0.0459
	40	4.96	182.6	0.0341
n-Decane	25	6.232	195.8	0.0475
	40	4.71	199.0	0.0352
n-Undecane	25	5.949	212.1	0.0490
	40	4.51	215.4	0.0364
n-Dodecane	25	5.698	228.4	0.0505
	40	4.31	231.9	0.0374
n-Tridecane	25	5.501	245.0	0.0522
	40	4.15	247.9	0.0385
n-Tetradecane	25	5.305	261.7	0.0537
	40	4.02	264.2	0.0397
n-Pentadecane	25	5.152	278.5	0.0554
	40	3.89	280.4	0.0407
n-Hexadecane	25	4.999	295.4	0.0569
	40	3.80	296.7	0.0420

[a] ml gas·(ml hydrocarbon solvent)$^{-1}$
[b] cm^3·mol^{-1}
[c] dimensionless
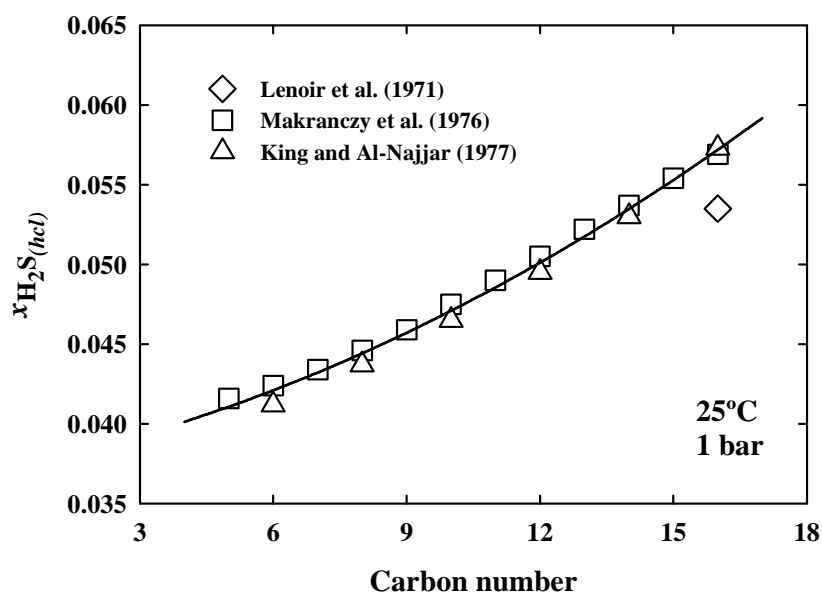
Figure 1.13. Solubility of H_2S in liquid n-alkanes as a function of carbon number at 25ºC and ~ 1 bar. The symbols correspond to experimental data reported in the literature. The curve highlights the carbon number dependence of the solubility of H_2S gas in liquid n-alkanes.
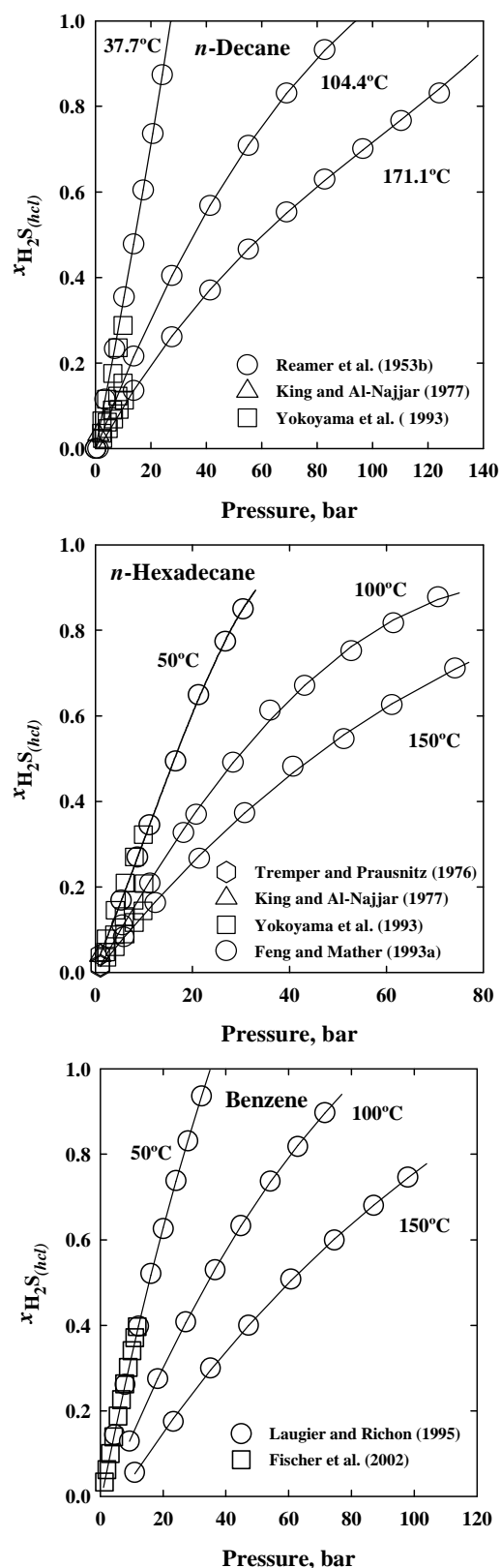
Figure 1.14. Solubility of H$_2$S in liquid hydrocarbons as a function of pressure at different temperatures. The symbols correspond to experimental data reported in the literature, while the curves have been drawn to highlight the pressure dependence of the solubilities. The data reported for *n*-decane by King and Al-Najjar (1977) and Yokoyama et al. (1993) correspond to temperatures of 50ºC, and 50, 100 and 150ºC, respectively.

The pressure dependence of the solubility of H₂S gas in liquid hydrocabons is illustrated in Figure 1.14 for *n*-decane, *n*-hexadecane, and benzene. It appears from this figure that the mole fraction of H₂S in the hydrocarbon phase increases much more with increases pressure than it decreases with increasing temperature. For example, at a temperature of ~ 150ºC, a pressure of H₂S gas of ~ 50 bar over the hydrocarbon phase would correspond to hydrocarbon-H₂S mixtures with a mole fraction of H₂S ($x_{H_2S_{(hcl)}}$) of ~ 0.5 for the three hydrocarbons considered in Figure 1.14. Such solubility values are much higher than the solubilities of water in hydrocarbon liquids at high temperatures and pressures (Helgeson et al., 2009 – see their Figure 44). It should however be recognized that the experimental data plotted in this figure have been obtained for binary H₂S-hydrocarbon systems which are by far more simple than those corresponding to petroleum systems in sedimentary basins. In particular, the presence of water (H₂O) has been shown to significantly affect the phase relations observed in binary CO₂-hydrocarbon mixtures, with an important decrease of the CO₂ content of the hydrocarbon phase (Pollack et al., 1988).

Although to a much lesser extent, the solubility of H₂S gas in liquid hydrocarbons is depends also on the molecular structure of the solvent. Tremper and Prausnitz (1976) found H₂S to be more soluble in aromatic solvents, which they explained by the fact that H₂S can get closer to and interact more strongly with the carbon atoms in such solvents because of the lack of hydrogen atoms in aromatic molecules.

Finally, although it is beyond the scope of the present work to further discuss the solubility of H₂S in hydrocarbons, mention must be made of equations of state which have been developed to correlate experimental data such as those discussed above. King et al. (1977) correlated experimental solubilities at 25ºC for H₂S in *n*-alkanes of variable chain length (C₆ to C₁₆) using an expression for the activity coefficient of H₂S in the hydrocarbon liquid ($\gamma_{H_2S_{(hcl)}}$) corresponding to

$$RT \ln \gamma_{H_2S_{(hcl)}} = RT \ln \left(x_{ideal}^{760} / x_{H_2S_{(hcl)}}^{760} \right) =$$

$$T \left[R \left(\ln \left(\phi_{H_2S} / x_{H_2S_{(hcl)}} \right) - \left(Zq_{H_2S}/2 \right) \ln \left(1 + \left(2\phi_{solvent}/Zq_{H_2S} \right) \left(\left(r_{H_2S}/r_{solvent} \right) - 1 \right) \right) \right) \right]$$

$$+ (\phi_{solvent})^2 V_{m,H_2S} \left(\left(\delta_{H_2S} - \delta_{solvent} \right)^2 + 2l_{H_2S,solvent} \delta_{H_2S} \delta_{solvent} \right), \qquad (1.65)$$

in which x_{ideal}^{760} and $x_{H_2S_{(hcl)}}^{760}$ are respectively the mole fraction of a solute calculated for the case of an ideal solution (see Equation 8 in King and Al-Najjar, 1977) and the mole fraction of H₂S in the hydrocarbon liquid solvent measured at atmospheric pressure, V_{m,H_2S} is the molar volume of H₂S, r_{H_2S} and $r_{solvent}$ are the number of segments in the subscripted species

(the solute H$_2$S being considered as a monomer, $r_{\text{H}_2\text{S}} = 1$), $\phi_{\text{H}_2\text{S}}$ and ϕ_{solvent} represent segment fractions of the subscripted species, $q_{\text{H}_2\text{S}}$ is the number of surface sites available on the subscripted species, Z is a coordination number representing the average number of nearest neighbour molecules surrounding a monomer (a value of $Z = 10$ was chosen by King et al., 1977), $\delta_{\text{H}_2\text{S}}$ and δ_{solvent} are solubility parameters, and $l_{\text{H}_2\text{S,solvent}}$ is a deviation parameter in the geometric mean mixing rule, accounting for attractive interactions between molecules of H$_2$S and molecules of the hydrocarbon solvent. Equation (1.65) represents a modification of the expression derived from regular solution theory, the starting point being the expression for the excess properties:

$$RT \ln \gamma_{\text{H}_2\text{S}_{(hcl)}} = \bar{G}^E_{\text{H}_2\text{S}_{(hcl)}} = \bar{H}^E_{\text{H}_2\text{S}_{(hcl)}} - T\bar{S}^E_{\text{H}_2\text{S}_{(hcl)}} \quad , \tag{1.66}$$

with $\bar{G}^E_{\text{H}_2\text{S}_{(hcl)}}$, $\bar{H}^E_{\text{H}_2\text{S}_{(hcl)}}$ and $\bar{S}^E_{\text{H}_2\text{S}_{(hcl)}}$ denoting the partial molar excess Gibbs energy, enthalpy, and entropy of H$_2$S in the hydrocarbon solvent.

Feng and Mather (1993b) correlated their solubility measurements as a function of temperature and pressure with the Peng-Robinson equation of state (Peng and Robinson, 1976), which is written for a pure component as

$$P = \frac{RT}{V-b} - \frac{a(T)}{V(V+b)+b(V-b)} \quad , \tag{1.67}$$

the repulsive term being obtained from

$$b = 0.07780 \frac{RT_c}{P_c} \tag{1.68}$$

while the attractive term takes the form

$$a(T) = 0.45724 \frac{R^2 T_c^2}{P_c} \left[1 + (0.37464 + 1.54226\omega - 0.26992\omega^2) \left(1 - \left(\frac{T}{T_c}\right)^{1/2} \right) \right]^2 , \tag{1.69}$$

with T_c, P_c and ω representing the critical temperature, critical pressure and acentric factor for the pure component. For a mixture, the Peng-Robinson equation of state becomes:

$$P = \frac{RT}{v_m - b_m} - \frac{a_m(T)}{v_m(v_m+b_m)+b_m(v_m-b_m)} \tag{1.70}$$

where v_m is the molar volume of the mixture which is defined by (Prausnitz et al., 1986)

$$v_m = \sum_i x_i V_i \tag{1.71}$$

and for the solubility of H$_2$S in n-dodecane (C$_{12}$H$_{26}$),

$$b_m = x_{\text{C}_{12}\text{H}_{26}} b_{\text{C}_{12}\text{H}_{26}} + x_{\text{H}_2\text{S}} b_{\text{H}_2\text{S}} \tag{1.72}$$

and

$$a_m(T) = x^2_{\text{H}_2\text{S}} a_{\text{H}_2\text{S}}(T) + x^2_{\text{C}_{12}\text{H}_{26}} a_{\text{C}_{12}\text{H}_{26}}(T)$$
$$+ 2 x_{\text{H}_2\text{S}} x_{\text{C}_{12}\text{H}_{26}} \sqrt{a_{\text{H}_2\text{S}}(T) a_{\text{C}_{12}\text{H}_{26}}(T)} \cdot (1 - k_{\text{H}_2\text{S}-\text{C}_{12}\text{H}_{26}}) \tag{1.73}$$

where $k_{H_2S-C_{12}H_{26}}$ represents an interaction parameter, for which Feng and Mather (1993b) found that a zero value was best describing their experimental data. The comparison between these experimental data and values of $x_{H_2S_{(hcl)}}$ computed from the Peng-Robinson equation of state is presented in Figure 1.15. The values of the critical parameters and of the acentic factor used in the calculation for H$_2$S and *n*-dodecane were taken from Reid et al. (1987) and are the following:

	T_c (K)	P_c (bar)	ω
H$_2$S	373.2	89.4	0.097
C$_{12}$H$_{26}$	658.0	18.2	0.576
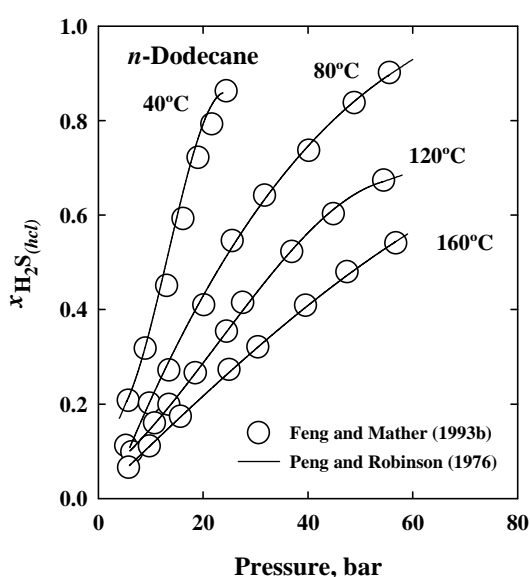
Figure 1.15. Solubility of H$_2$S in liquid *n*-dodecane as a function of pressure at different temperatures. The symbols correspond to experimental data reported by Feng and Mather (1993b). The curves have been calculated with the Peng-Robinson equation of state (the calculation was performed on http://www.cheng.cam.ac.uk/~pjb10/thermo/mixture.html) – after Feng and Mather (1993b).

As already mentioned above, no thermodynamic model has been developed which describes the solubility of H$_2$S in hydrocarbon liquids in the presence of aqueous solutions (with or without NaCl), since the experimental data required for developing such a model are scarce, if not inexistant (de Hemptinne and Béhar, 2000).

2.3. Organic solids, liquids, and gases

A comprehensive thermodynamic database for hundreds of organic compounds of interest to petroleum geochemistry has been constituted over a period of ten years by Helgeson and coworkers. This thermodynamic database is described in details in a series of

publications by Helgeson et al. (1998), Richard and Helgeson (1998), and Richard (2001). The approach followed in the retrieval of the thermodynamic properties at 25ºC and 1 bar as well as of the coefficients of heat capacity equations for these organic compounds consisted in the regression of experimental data together with carbon number systematics and group additivity algorithms. Carbon number systematics refers to the observation that within homologous families of aliphatic organic compounds (e.g. *n*-alkanes, *n*-alkanethiols, etc.), the thermodynamic properties and heat capacity coefficients of these compounds are a regular (and often a linear) function of the number of atoms of carbon (*n*) in their structures, which may be expressed as (Helgeson et al., 1998)

$$\Xi = k_1 + k_2 n \, , \tag{1.74}$$

where k_1 and k_2 are parameters characteristic of a given thermodynamic property or heat capacity coefficient, which depend on both temperature and pressure. In addition, the carbon number dependence is the same for different families of organic compounds containing an aliphatic chain. This is illustrated in Figure 1.16, where experimental values reported in the literature for the standard molal enthalpy of formation (ΔH_f°) at 25ºC and 1 bar of liquid *n*-alkanes, *n*-alkylcyclohexanes, *n*-alkylbenzenes, and *n*-1-alkanethiols have been plotted as a function of carbon number. It can be deduced from this figure that the carbon number slope is nearly identical for the four homologous families, and consistent with a k_2 value of -25.73 kJ·mol^{-1} for the standard molal enthalpy of formation (ΔH_f°) at 25ºC and 1 bar for the methylene (–CH$_2$–) repeating unit in all families of aliphatic compounds.

Group additivity algorithms have been developed by Richard and Helgeson (1998) and Richard (2001) to estimate the thermodynamic properties and heat capacity coefficients of geochemically important organic molecules (e.g. steranes and hopanes) for which no experimental data were available in the literature. In the group contribution approach, group properties and coefficients are first retrieved from those of relatively simple "reference compounds" for which the thermodynamic properties are known. For example, by dividing the thermodynamic properties of cyclohexane (C_6H_{12}) by six, one can obtain the properties of a CH$_2$ group in a C$_6$ saturated ring. This group is noted
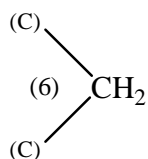
By considering as additional reference compounds cyclopentane, methylcyclopentane, methylcyclohexane, 1,1-dimethylcyclopentane 1,1-dimethylcyclohexane, *cis*- and *trans*-1,2-

dimethylcyclopentane, *cis-* and *trans*-1,2-dimethylcyclohexane, *cis-* and *trans*-1,2-dimethyl-cyclopentane, *cis-* and *trans*-hexahydroindan, *cis-* and *trans*-decalin, as well as longer chain *n*-alkylcyclopentanes and *n*-alkylcyclohexanes, Richard and Helgeson (1998) were able to generate such group additivity algorithms as

$$8 \text{ x } \underset{(C)}{\overset{(C)}{\diagdown}}\text{CH}_2 \quad + \quad 2 \text{ x } \underset{(C)}{\overset{(C)}{\diagdown}}\text{CH}_2 \quad + \quad 3 \text{ x } \textit{trans} \underset{\text{H}}{\overset{(6) \mid (6)}{\text{C}}} \quad + \quad \textit{trans} \underset{\text{CH}_3}{\overset{(6) \mid (6)}{\text{C}}}$$
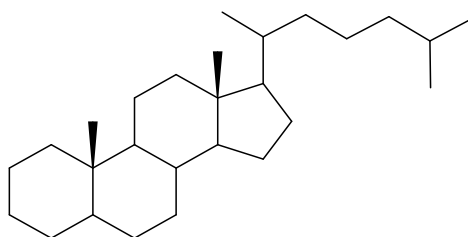
$$+ \textit{ trans} \underset{\text{H}}{\overset{(6) \mid (5)}{\text{C}}} \quad + \textit{ trans} \underset{\text{CH}_3}{\overset{(6) \mid (5)}{\text{C}}} \quad + \quad \underset{(C)}{\overset{(C)}{\diagdown}}\text{CH(CH}_2)_3\text{CH}_3 \quad + \quad 2 \text{ x } \underset{}{\overset{\text{CH}_3}{\underset{\mid}{\text{CH}}}}$$
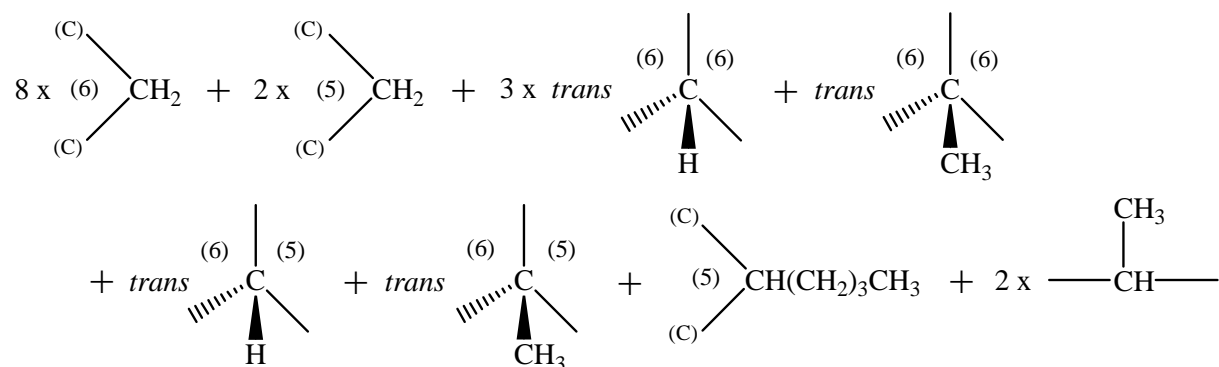
to estimate the thermodynamic properties and coefficients of the two isomers of 5α(H)-cholestane (C$_{27}$H$_{48}$),

as well as those of other steranes, tricyclic diterpanes and hopanes. The group additivity algorithms developed by Richard and Helgeson (1998) and Richard (2001) have also been used to estimate the thermodynamic properties and heat capacity coefficients of kerogen and pyrobitumen models in the C-H-O or C-H-O-S systems using contributions for crystalline hydrocarbon, oxygen-bearing, and sulfur-bearing groups (Helgeson et al., 2009; Richard et al., 2010 – see Section 4 below).

A brief summary will now be given of the families of organic compounds for which thermodynamic properties and heat capacity coefficients have been calculated.

2.3.1. Hydrocarbons

The hydrocarbons for which Helgeson et al. (1998) and Richard and Helgeson (1998) have calculated values of the standard molal Gibbs energy (ΔG_f°) and standard molal enthalpy of formation (ΔH_f°) at 25ºC and 1 bar, standard molal entropy (S°) and volume (V°) at 25ºC and 1 bar, and heat capacity coefficients (*a*, *b*, and *c*) are listed in Table 1.11, together with the physical state considered and carbon number range covered for each family of compounds. The corresponding molecular structures are shown in Figure 1.17. The numerical

values of the properties and coefficients for the hydrocarbons used in the calculations carried out in the present study are listed in Table A1 of the Appendix to the manuscript.

2.3.2. Organic sulfur compounds

The organic sulfur compounds for which thermodynamic properties and heat capacity coefficients have been calculated by Helgeson et al. (1998) and Richard (2001) are listed in Table 1.12 and their molecular structures shown in Figure 1.18. The numerical values of the properties and coefficients for the liquid and ideal gas organic sulfur compounds considered in the calculations reported below can also be found in Table A1 of the Appendix to the manuscript.
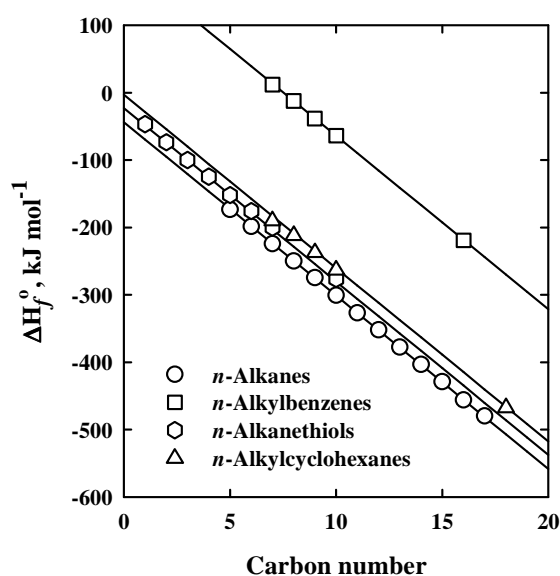
Figure 1.16. Standard molal enthalpy of formation (ΔH_f°) at 25°C and 1 bar as a function of carbon number for different homologous families of aliphatic organic liquids. The symbols correspond to experimental values reported in the literature – see Domalski and Hearing (1993) for original references. The straight lines, which correspond to values calculated by Helgeson et al. (1998) and Richard and Helgeson (1998) from group contributions given by Domalski and Hearing (1993), have a slope of -25.73 kJ·mol^{-1}. The intercepts are characteristic of a given family and reflect the different nature of the molecular groups (i.e. methyl, cyclohexyl, phenyl or thiol) attached to the aliphatic chains.

Table 1.11. Families of hydrocarbon compounds for which thermodynamic properties and heat capacity coefficients have been calculated by Helgeson et al. (1998) and Richard and Helgeson (1998).

| Hydrocarbons	State	Carbon number range
n-Alkanes	Crystalline	C_5-C_{100}
	Liquid	C_1-C_{100}
	Ideal gas	C_1-C_{40}
2-Methylalkanes	Liquid	C_4-C_{20}
	Ideal gas	C_4-C_{20}
3-Methylalkanes	Liquid	C_6-C_{20}
	Ideal gas	C_6-C_{20}
Miscellaneous branched alkanes	Liquid	C_7, C_8
	Ideal gas	C_7, C_8
Regular isoprenoids	Crystalline	C_{15}-C_{25}
	Liquid	C_{15}-C_{25}
Irregular isoprenoids	Crystalline	C_{30}, C_{40}
	Liquid	C_{30}, C_{40}
Highly branched isoprenoids	Crystalline	C_{20}, C_{25}, C_{30}
	Liquid	C_{20}, C_{25}, C_{30}
Unsubstituted cycloalkanes	Liquid	C_3-C_8
	Ideal gas	C_3-C_8
Alkylcyclopentanes	Crystalline	C_5-C_{17}
	Liquid	C_7-C_{17}
Alkylcyclohexanes	Crystalline	C_6-C_{18}
	Liquid	C_6-C_{18}
Bicycloalkanes	Crystalline	C_9, C_{10}
	Liquid	C_9, C_{10}
Tricyclic diterpanes	Crystalline	C_{20}-C_{30}
	Liquid	C_{20}-C_{30}
Steranes	Crystalline	C_{19}-C_{30}
	Liquid	C_{19}-C_{30}
Hopanes	Crystalline	C_{26}-C_{40}
	Liquid	C_{26}-C_{40}
Alkylbenzenes	Liquid	C_6-C_{20}
	Ideal gas	C_6-C_{20}
Methylated biphenyls	Crystalline	C_{12}-C_{14}
	Liquid	C_{12}-C_{14}
Methylated naphthalenes	Crystalline	C_{12}-C_{14}
	Liquid	C_{12}-C_{14}
Methylated phenanthrenes	Crystalline	C_{12}-C_{14}
	Liquid	C_{12}-C_{14}
Methylated anthracenes	Crystalline	C_{12}-C_{14}
	Liquid	C_{12}-C_{14}
Methylated pyrenes	Crystalline	C_{12}-C_{14}
	Liquid	C_{12}-C_{14}
Methylated chrysenes	Crystalline	C_{12}-C_{14}
	Liquid	C_{12}-C_{14}
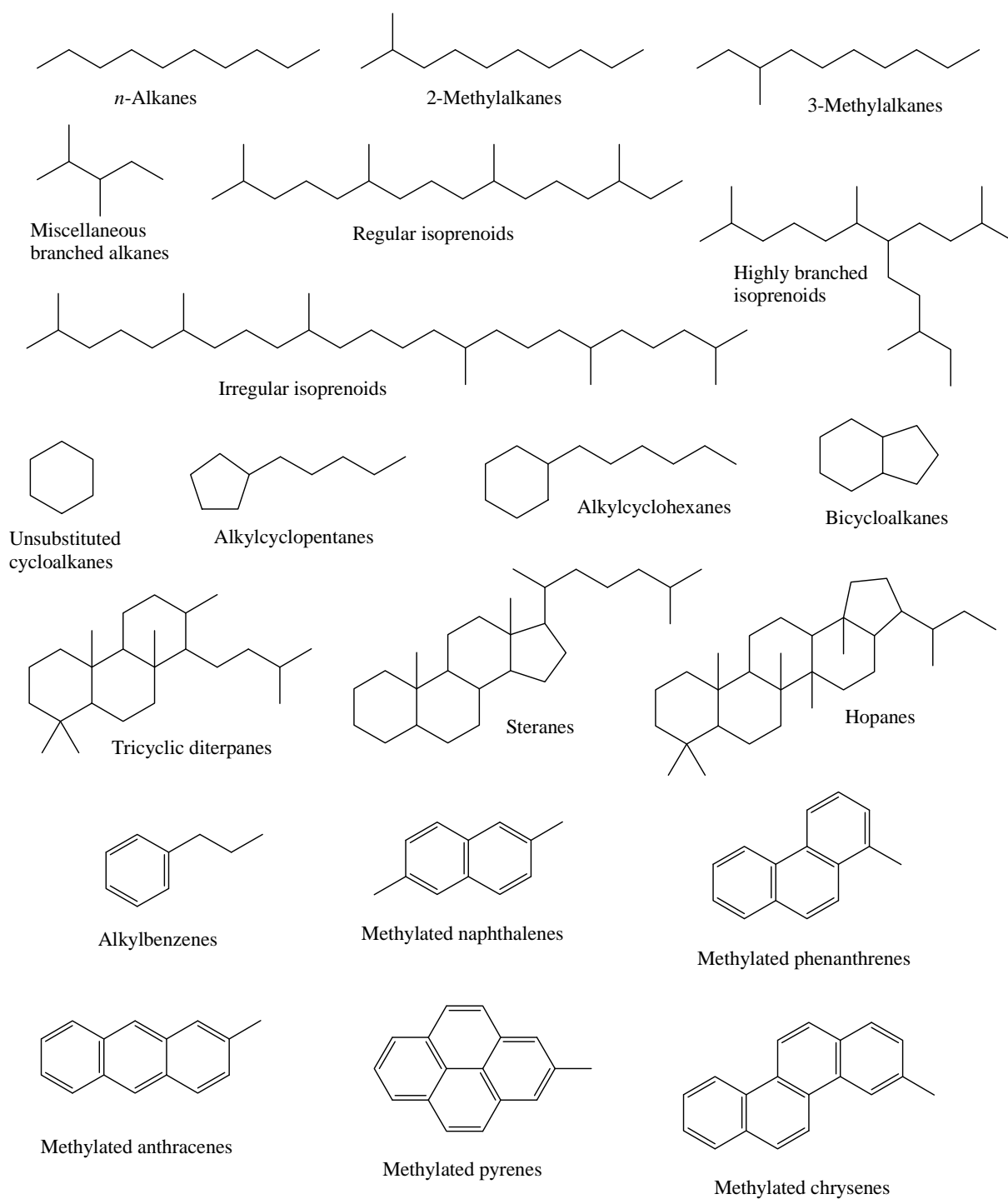
Figure 1.17. Molecular structures of the hydrocarbon compounds discussed in Section 2.3.1.

Table 1.12. Families of organic sulfur compounds for which thermodynamic properties and heat capacity coefficients have been calculated by Helgeson et al. (1998) and Richard (2001).

| Hydrocarbons	State	Carbon number range
Carbon disulfide	Liquid	C_1
	Ideal gas	C_1
n-1-Alkanethiols	Liquid	C_1-C_{20}
	Ideal gas	C_1-C_{20}
Branched thiols	Liquid	C_3-C_6
	Ideal gas	C_3-C_6
Cyclic thiols	Liquid	C_5, C_6
	Ideal gas	C_5, C_6
	Crystalline	C_6
Aromatic thiols	Liquid	C_6-C_7
	Ideal gas	C_6-C_7
n-Alkyl sulfides	Liquid	C_2-C_{10}
	Ideal gas	C_2-C_{10}
Branched sulfides	Liquid	C_4-C_{10}
	Ideal gas	C_4-C_{10}
Cyclic sulfides	Liquid	C_2-C_6
	Ideal gas	C_2-C_6
Aromatic sulfides	Crystalline	C_6, C_7, C_{12}
	Liquid	C_6, C_7, C_{12}
n-Alkyl disulfides	Liquid	C_2-C_{10}
	Ideal gas	C_2-C_{10}
Thiophenics	Crystalline	C_4, C_8, C_{12}
	Liquid	C_4-C_8, C_{12}
	Ideal gas	C_4-C_7
Thianthrene	Crystalline	C_{12}
	Liquid	C_{12}
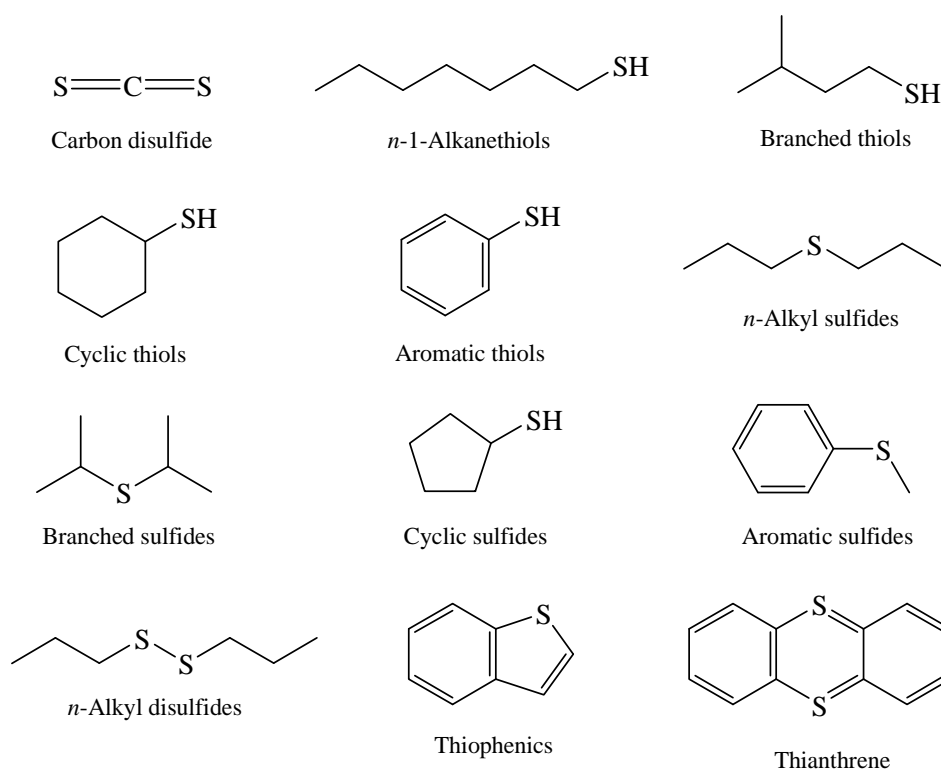
Figure 1.18. Molecular structures of the organic sulfur compounds discussed in Section 2.3.2.

2.4. Aqueous species

The standard partial molal thermodynamic properties at 25ºC and 1 bar and the parameters for the revised Helgeson-Kirkham-Flowers (HKF) equation of state of the inorganic and organic aqueous species which have been considered in the fluid-rock interaction calculations reported in Section 4 have been listed in Table A2 of the Appendix.

The properties and HKF parameters for the single ion inorganic species as well as for the bicarbonate (HCO_3^-) and hydrogenosulfate (HSO_4^-) species are those recommended by Shock and Helgeson (1988), whereas with the exception of the $CaCl^+$ complex, those for the inorganic complexes correspond to those recommended by Shock et al. (1997) and Sverjensky et al. (1997). As mentioned in Footnote 4, the properties and coefficients given by Sverjensky et al. (1997) for the $CaCl^+$ complex are inconsistent with measurements of the solubility of anhydrite in NaCl solutions. Adopting instead for this complex the properties and coefficients included in the original SUPCRT92 database (SPRONS92.DAT) results in fairly good predictions of the solubility of anhydrite up to 300ºC and 2 molal NaCl – see above. A comparison of experimental data reported in the literature for the dissociation constant of the $CaCl^+$ complex with their counterparts computed using the thermodynamic data of the original SUPCRT92 database and those given by Sverjensky et al. (1997) is shown in Figure 1.19. It appears from this figure that D. Sverjensky initially adjusted the thermodynamic properties and HKF parameters based on the dissociation constant reported by Simonson et al. (1985)[7] and Williams-Jones and Seward (1989), and then revised his first estimates based on subsequent measurements of Gillespie et al. (1992) which appear to be consistent with the lower temperature data of Majer and Štulík (1985). This revision resulted in a higher stability of the $CaCl^+$ complex. As a direct consequence, the predicted solubility of anhydrite in NaCl solutions was found increasingly overestimated with increasing NaCl concentration.

Finally, also listed in Table A2 of the Appendix are thermodynamic properties and HKF parameters for a few selected aqueous organic species and organic-metal complexes, which include acetic acid, acetate, Na- and Ca-acetate complexes, and methanethiol. These properties and coefficients were taken from Shock and Helgeson (1990), Shock and Koretsky (1993), and Schulte and Rogers (2004).

---

[7] Note that the log K value reported by Gillespie et al. (1992) at 250ºC is for a total pressure of 200 bar, whereas the saturation pressure of water (P_{sat}) at this temperature somewhat lower (~ 40 bar).
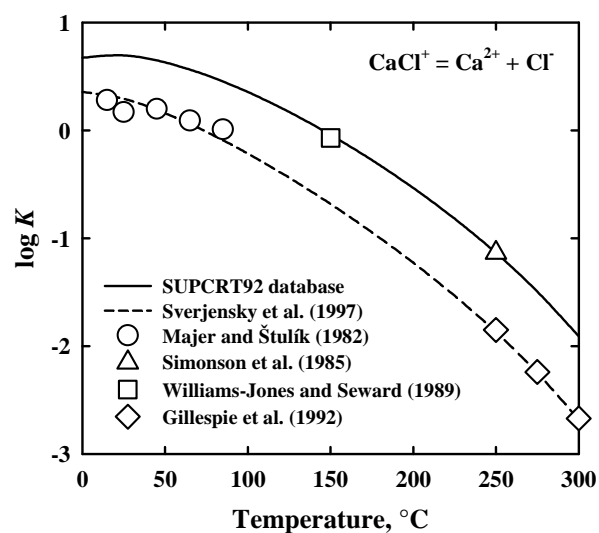
Figure 1.19. Comparison of experimental values reported in the literature for the logarithm of the equilibrium constant (log K) of the dissociation constant of the $CaCl^+$ complex as a function of temperature at P_{sat}. The solid and dashed curves correspond to values computed using two different sets of thermodynamic properties and HKF parameters for the $CaCl^+$ complex – see text.

3. THERMODYNAMIC DESCRIPTION OF REACTIONS AMONG HYDROCARBONS, ELEMENTAL SULFUR, H₂S, AND ORGANIC SULFUR COMPOUNDS AT TEMPERATURES AND PRESSURES CHARACTERISTIC OF HYDROCARBON RESERVOIRS

It has long been known from experimental studies that hydrocarbons react with elemental sulfur to produce organic sulfur compounds and hydrogen sulfide gas (e.g. Friedmann, 1916; Baker and Reid, 1929, Horton, 1949; Bestougeff and Combaz, 1973; Valitov and Valitov, 1975; Schmid, 1986; Schmid et al., 1987; Kowalewski et al., 2008). This reaction, which is an oxidation-reduction reaction, may be written for any C_pH_r hydrocarbon and any C_nH_mS organic sulfur compound under the general form

$$n\ C_pH_{r(l)} + [p + (nr - mp)/2]\ S_{(c\ or\ l)} = p\ C_nH_mS_{(l)} + (nr - mp)/2\ H_2S_{(g)}\ . \qquad (1.75)$$
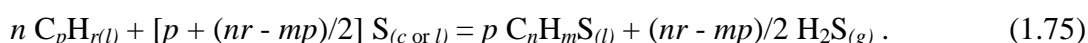
It has been suggested by Richard et al. (2005) that reactions of this type may control the partial pressures of H₂S in carbonate reservoirs. If $(nr - mp) > 0$ in Reaction (1.75), H₂S and the organic sulfur compound appear on the same side of the reaction and it can be deduced from the stoichiometry of the reaction that increasing the partial pressure of H₂S will displace the equilibrium towards the left, that is H₂S will react with the organic sulfur compound to produce a hydrocarbon and elemental sulfur. This is of course of tremendous importance in the context of the injection of acid gas CO₂-H₂S mixtures in depleted hydrocarbon reservoirs, as it would provide an efficient mean of sequestering H₂S under the form of elemental sulfur. Accumulation of elemental sulfur is known to occur during thermochemical sulfate reduction (TSR) as a result of a partial reoxidation of H₂S, provided that no reactive hydrocarbons remain in the system (Machel, 2001). As it will be shown in Section 4, the stability field of elemental sulfur corresponds to redox conditions which are much more oxidizing than those characteristic of typical petroleum reservoirs. It is possible that the redox conditions in TSR reservoirs are changing towards the end of the reaction process, which may favor the formation of elemental sulfur and may also coincide with the precipitation of pyrobitumen in these reservoirs.

Equilibrium states such as those represented by Reaction (1.75) may be graphically depicted in $T - \log f_{H_2S_{(g)}}$ diagrams which are somewhat analogous to the well-known $T - \log X_{CO_2}$ and $T - \log X_{H_2O}$ diagrams first introduced in metamorphic petrology by Greenwood (1967) to describe devolatilization equilibria. Examples of such $T - \log f_{H_2S_{(g)}}$ diagrams at a total pressure of 500 bar (which is the pressure used for the experiments described in the second part of the manuscript) are shown in Figure 1.20 for a number of representative organic sulfur compounds and hydrocarbons which are identified in Table 1.13. The

molecular structures of these compounds are shown in Figure 1.21. The univariant curves in the diagrams of Figure 1.20 have been computed from the logarithmic values of the equilibrium constants listed in Table 1.14 and appropriate expressions of the law of mass action which under its complete form corresponds to

$$\log K_{(1.75)} = p \log a_{C_n H_m S_{(l)}} + \frac{(nr-mp)}{2} \log f_{H_2 S_{(g)}}$$
$$- n \log a_{C_p H_{r(l)}} - \left[p + \frac{(nr-np)}{2} \right] \log a_{S_{(c \text{ or } l)}} \quad . \tag{1.76}$$

For practical reasons, most of the reactions in Table 1.14 have been written for equal carbon numbers in the hydrocarbon and organic sulfur compound (i.e. $n = p$). Under these circumstances, if we assume a unit activity for crystalline (or liquid)[8] elemental sulfur and adopt a convention of equal activities of the liquid hydrocarbon and organic sulfur compound involved in a given reaction, the equations of the univariant curves are given by

$$\log f_{H_2 S_{(g)}} = \frac{2 \log K_{(1.75)}}{nr-mp} \quad . \tag{1.77}$$

There are however some organic sulfur compounds for which reactions cannot be written with $n = p$. This comes from the oxidation-reduction constraint that as sulfide from both H_2S and the organic sulfur compound are oxidized to elemental sulfur, the average oxidation state of carbon in the hydrocarbon must be such that electrons are conserved in the reaction. In the case of Reaction (1) in Table 1.14, which involves n-decanethiol, simple inspection of the chemical formulas indicates that analog of Reaction (1.75) cannot be written with n-decane because H_2S would not appear in the reaction. The average oxidation state of carbon in n-decanethiol is $\bar{z}_C = -2.0$ whereas it is $\bar{z}_C = -2.2$ in n-decane (Helgeson, 1991). Therefore, only 0.2 mole of electrons are transfered per carbon atom, which happen to balance the electron transfer corresponding to the oxidation of the sulfide atom of n-decanethiol to elemental sulfur. If we consider n-pentane instead of n-decane, the average oxidation state of carbon is $\bar{z}_C = -2.4$ and Reaction (1) in Table 1.14 results. In those cases where the stoichiometric coefficients are different for the reactant and product (i.e. Reactions (1) and (4) in Table 1.14), activities of 0.5 have been assumed. It should perhaps be reminded here that univariant curves drawn for equal activities of the hydrocarbon and organic sulfur compound in any given reaction actually represent a projection from a surface corresponding to a continuum of parallel univariant curves, each of which representing different activity ratios of the hydrocarbon and the organic sulfur compound in the liquid phase. This is illustrated in Figure

---

[8] The fact that elemental sulfur may be crystalline or liquid for the temperature and pressure conditions of sedimentary basins is implicitly taken into account in the calculation of the equilibrium constants (see paragraph 2.1.3 above).

1.20 (a), where the solid curve corresponds to $a_{C_{10}H_{22}S_{(l)}} = a_{C_5H_{12(l)}} = 0.5$ and the dashed curves correspond to $a_{C_5H_{12(l)}} = 0.1$ and $a_{C_{10}H_{22}S_{(l)}} = 0.9$, and $a_{C_5H_{12(l)}} = 0.9$ and $a_{C_{10}H_{22}S_{(l)}} = 0.1$.

It can be deduced from the nine diagrams shown in Figure 1.20 that the equilibrium curves plot at different fugacities of H_2S gas at any given temperature, depending on the organic sulfur compound and, to a lesser extent, on the hydrocarbon. For example, a comparison between Figures 1.20*e* and 1.20*f* indicates that at 200ºC, 2-methylthiacyclopentane and 2-methylthiophene should desulfurize to produce *n*-pentane and elemental sulfur above H_2S fugacities of ~ 18 bar and ~ 112 bar, respectively. Recalling from Table 1.7 that the fugacity coefficient of pure H_2S gas at 200ºC and 500 bar is $\varphi_{H_2S_{(g)}}$ ~ 0.52, these fugacities would correspond to partial pressures of H_2S of ~ 35 bar and ~ 215 bar. The latter values are not physically unrealistic within the context of petroleum reservoirs affected by thermochemical sulfate reduction. In contrast, desulfurization of the benzothiophenes and dibenzothiophenes (Figures 1.20*g–i*) would require much higher values of $\varphi_{H_2S_{(g)}}$, above 400-

Table 1.13. Hydrocarbons and organic sulfur compounds considered for constructing the stability diagrams depicted in Figure 1.20.

|	Class of compounds	Compound	Formula
Hydrocarbons	*n*-Alkanes	*n*-Butane	C_4H_{10}
		n-Pentane	C_5H_{12}
		n-Hexane	C_6H_{14}
		n-Octane	C_8H_{18}
		n-Nonane	C_9H_{20}
		n-Dodecane	$C_{12}H_{26}$
		n-Tridecane	$C_{13}H_{28}$
		n-Tetradecane	$C_{14}H_{30}$
	Cycloalkanes	Cyclohexane	C_6H_{12}
	n-Alkylbenzenes	Ethylbenzene	C_8H_{10}
		n-Propylbenzene	C_9H_{12}
	Polynuclear aromatic hydrocarbons	2,7-Dimethylnaphthalene	$C_{12}H_{12}$
Organic sulfur compounds	*n*-Alkanethiols	*n*-Decanethiol	$C_{10}H_{22}S$
	Cyclic thiols	Cyclohexanethiol	$C_6H_{12}S$
	Aromatic thiols	Benzenethiol	C_6H_6S
	n-Alkyl sulfides	*n*-Butyl methyl sulfide	$C_5H_{12}S$
	Cyclic sulfides	Thiacyclopentane	C_4H_8S
		2-Methylthiacyclopentane	$C_5H_{10}S$
	Thiophenes	Thiophene	C_4H_4S
		2-Methylthiophene	C_5H_6S
	Benzothiophenes	Benzo[*b*]thiophene	C_8H_6S
		2-Methylbenzo[*b*]thiophene	C_9H_8S
	Dibenzothiophenes	Dibenzo[*b,d*]thiophene	$C_{12}H_8S$
		4-Methyldibenzo[*b,d*]thiophene	$C_{13}H_{10}S$
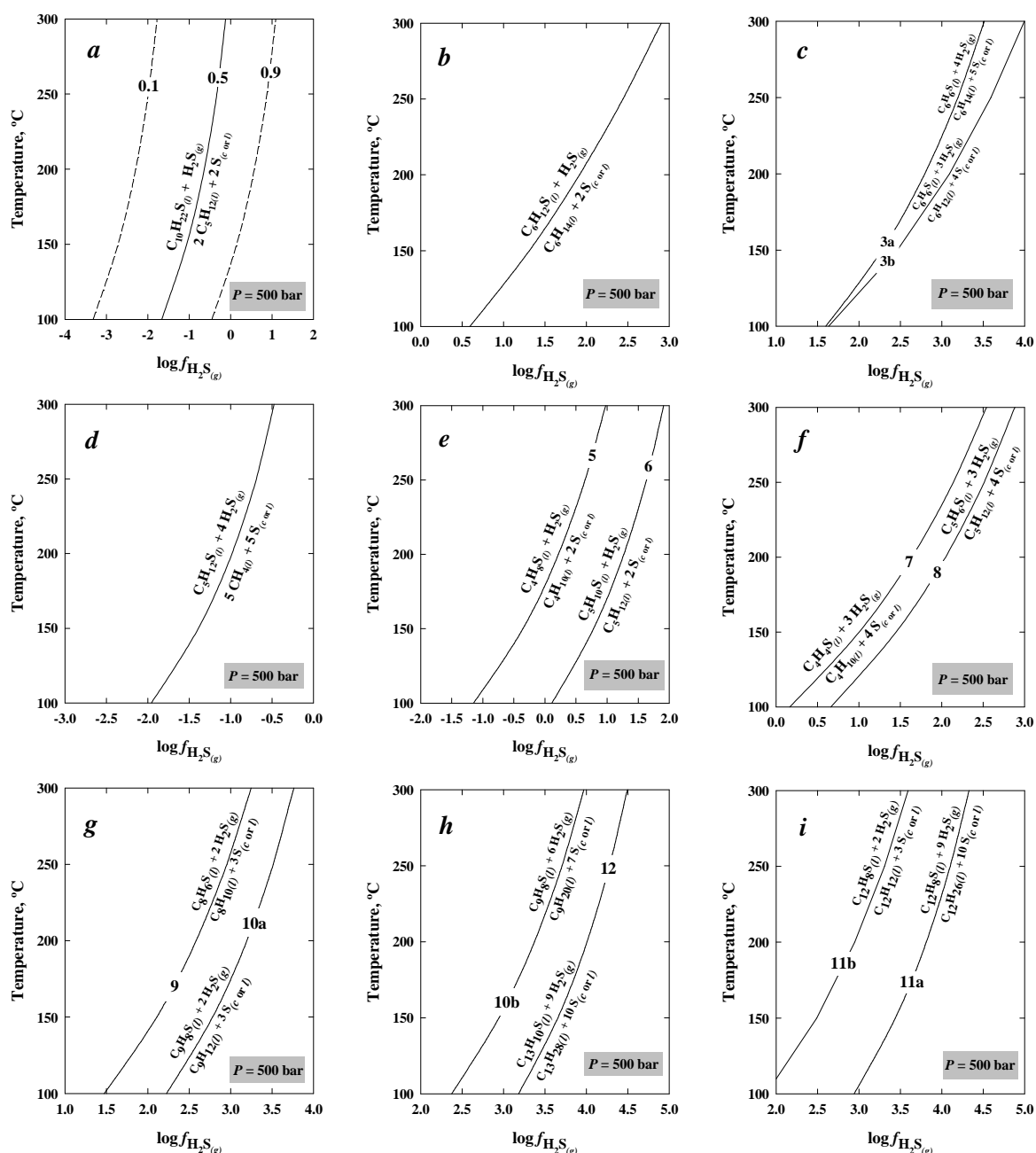
Figure 1.20. T – log $f_{H_2S_{(g)}}$ diagrams at 500 bar depicting the equilibrium relations among hydrocarbons, organic sulfur compounds, elemental sulfur and H_2S gas. *a. n*-Decanethiol – *n*-pentane: the numbers on the curves correspond to different activities of *n*-pentane in the liquid mixture. *b.* Cyclohexanethiol – *n*-hexane. *c.* Benzenethiol – cyclohexane (Reaction 3a) and benzenethiol – *n*-hexane (Reaction 3b). *d. n*-Butyl methyl sulfide – methane. *e.* Thiacyclopentane – *n*-butane (Reaction 5) and 2-methylthiacyclopentane – *n*-pentane (Reaction 6). *f.* Thiophene – *n*-butane (Reaction 7) and 2-methylthiophene – *n*-pentane (Reaction 8). *g.* Benzo[*b*]thiophene – ethylbenzene (Reaction 9) and 2-methylbenzo[*b*]thiophene – *n*-propylbenzene (Reaction 10a). *h.* 2-Methylbenzo-[*b*]thiophene – *n*-nonane (Reaction 10b) and 4-methyldibenzo[*b,d*]thiophene – *n*-tridecane (Reaction 12). *i.* Dibenzo[*b,d*]thiophene – *n*-dodecane (Reaction 11a) and dibenzo[*b,d*]thiophene – *n*-hexylbenzene (Reaction 11b). The equilibrium curves have been calculated from expressions of the law of mass action (Equation 1.76) together with the logarithmic values of the equilibrium constants listed in Table 1.14 – see text.
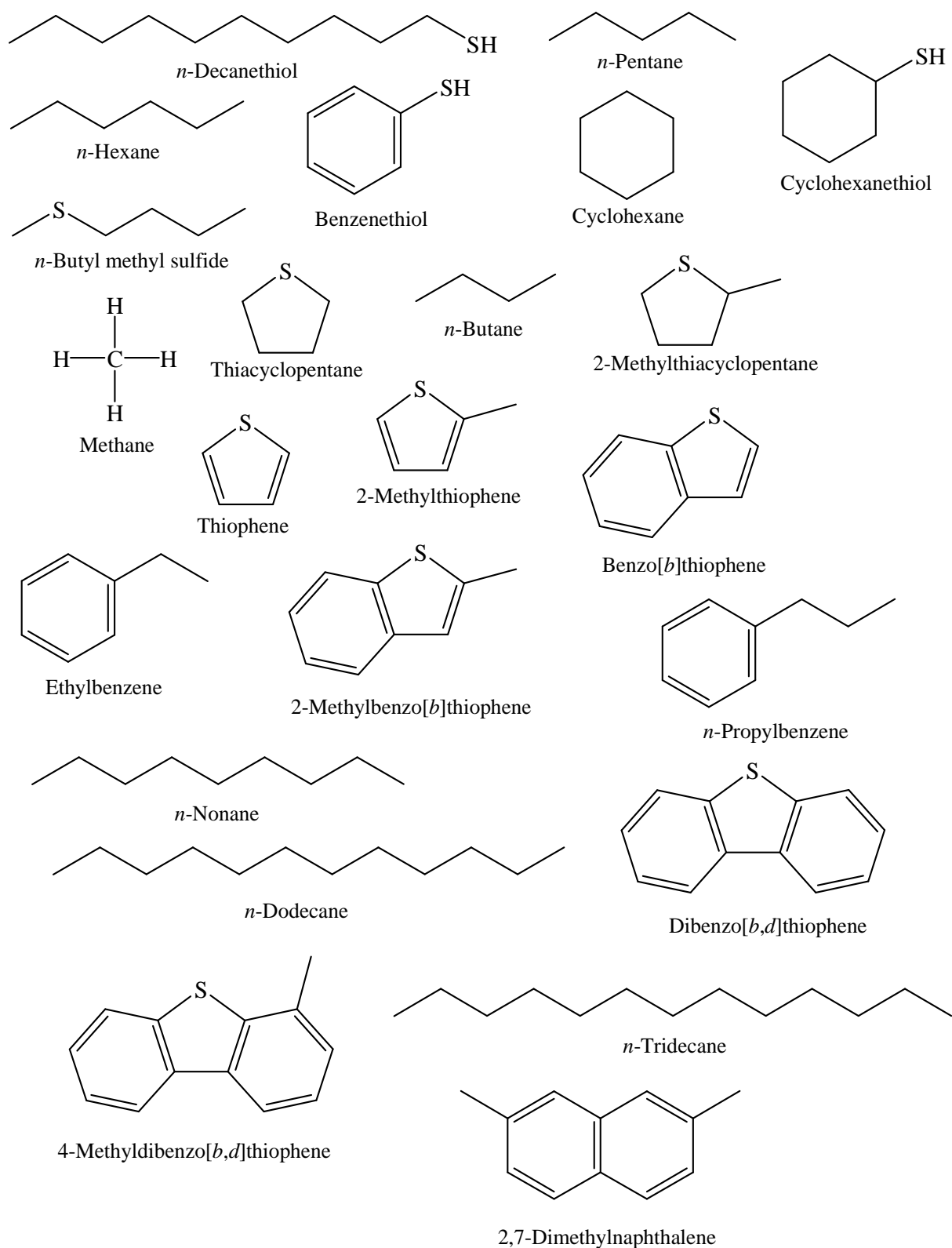
66

Figure 1.21. Molecular structures of the hydrocarbons and organic sulfur compounds listed in Table 1.13.

Table 1.14. Logarithmic values of the equilibrium constants as a function of temperature at 500 bar for reactions representing equilibrium among hydrocarbons, hydrogen sulfide, organic sulfur compounds and elemental sulfur in hydrocarbon reservoirs.

Reaction	Number	100°C	150°C	200°C	250°C	300°C
Thiols						
$C_{10}H_{22}S_{(l)} + H_2S_{(g)} = 2\ C_5H_{12(l)} + 2\ S_{(c\ or\ l)}$	(1)	1.36	0.76	0.33	0.03	-0.18
$C_6H_{12}S_{(l)} + H_2S_{(g)} = C_6H_{14(l)} + 2\ S_{(c\ or\ l)}$	(2)	-0.59	-1.31	-1.92	-2.44	-2.90
$C_6H_6S_{(l)} + 3\ H_2S_{(g)} = C_6H_{12(l)} + 4\ S_{(c\ or\ l)}$	(3a)	-4.91	-7.38	-9.28	-10.77	-11.98
$C_6H_6S_{(l)} + 4\ H_2S_{(g)} = C_6H_{14(l)} + 5\ S_{(c\ or\ l)}$	(3b)	-6.40	-9.12	-11.17	-12.77	-14.04
Sulfides						
$C_5H_{12}S_{(l)} + 4\ H_2S_{(g)} = 5\ CH_{4(l)} + 5\ S_{(c\ or\ l)}$	(4)	5.03	2.76	1.14	-0.04	-0.89
$C_4H_8S_{(l)} + H_2S_{(g)} = C_4H_{10(l)} + 2\ S_{(c\ or\ l)}$	(5)	1.16	0.38	-0.19	-0.63	-0.96
$C_5H_{10}S_{(l)} + H_2S_{(g)} = C_5H_{12(l)} + 2\ S_{(c\ or\ l)}$	(6)	-0.11	-0.78	-1.27	-1.63	-1.91
Thiophenics						
$C_4H_4S_{(l)} + 3\ H_2S_{(g)} = C_4H_{10(l)} + 4\ S_{(c\ or\ l)}$	(7)	-0.49	-3.01	-4.93	-6.42	-7.62
$C_5H_6S_{(l)} + 3\ H_2S_{(g)} = C_5H_{12(l)} + 4\ S_{(c\ or\ l)}$	(8)	-1.98	-4.35	-6.14	-7.54	-8.65
$C_8H_6S_{(l)} + 2\ H_2S_{(g)} = C_8H_{10(l)} + 3\ S_{(c\ or\ l)}$	(9)	-2.97	-4.26	-5.20	-5.94	-6.42
$C_9H_8S_{(l)} + 2\ H_2S_{(g)} = C_9H_{12(l)} + 3\ S_{(c\ or\ l)}$	(10a)	-4.45	-5.57	-6.39	-7.03	-7.52
$C_9H_8S_{(l)} + 6\ H_2S_{(g)} = C_9H_{20(l)} + 7\ S_{(c\ or\ l)}$	(10b)	-14.24	-17.67	-20.25	-22.24	-23.82
$C_{12}H_8S_{(l)} + 9\ H_2S_{(g)} = C_{12}H_{26(l)} + 10\ S_{(c\ or\ l)}$	(11a)	-26.47	-30.96	-34.32	-36.91	-38.96
$C_{12}H_8S_{(l)} + 2\ H_2S_{(g)} = C_{12}H_{12(l)} + 3\ S_{(c\ or\ l)}$	(11b)	-3.76	-4.98	-5.90	-6.62	-7.19
$C_{13}H_{10}S_{(l)} + 9\ H_2S_{(g)} = C_{13}H_{28(l)} + 10\ S_{(c\ or\ l)}$	(12)	-28.64	-32.90	-36.08	-38.52	-40.45

10,000 bar depending on the reaction. On the basis of the calculations reported above, it can be concluded that thiols, sulfides, and low-molecular-weight thiophenes would undergo desulfurization under high partial pressures of H_2S gas, while benzothiophenes and dibenzothiophenes would not. The experimental verification of this theoretical result is presented in the second part of the manuscript.

4. A THERMODYNAMIC ANALYSIS OF ORGANIC/INORGANIC INTERACTIONS DURING THERMOCHEMICAL SULFATE REDUCTION (TSR)

This section stems from a communication presented at the *Goldschmidt Conference* held in Davos (Switzerland) on June 21st-26th, 2009. It is presented hereafter under the form of a manuscript which will be submitted for publication to the *Marine and Petroleum Geology*.

A thermodynamic and mass transfer analysis of organic/inorganic interactions during thermochemical sulfate reduction in carbonate reservoirs

RAKHIM UTEYEV[1], LAURENT RICHARD[1],
JEROME STERPENICH[1], ALAIN CLEMENT[2],
AND DANIEL DESSORT[3]

[1] Nancy-Université, Géologie et Gestion des Ressouces Minérales et Energétiques, 54506 Vandoeuvre-lès-Nancy, France
[2] EOST, Laboratoire d'Hydrologie et de Géochimie de Strasbourg, 1 rue Blessig, 67084 Strasbourg, France
[3] Total Exploration & Production, Geoscience Technologies, Avenue Larribau, F-64018 Pau, France

Thermochemical sulfate reduction (TSR) occurs in deep carbonate reservoirs at temperatures ranging between 100 and 180°C [1]. TSR involves the reaction of aqueous sulfate with hydrocarbons, which produces hydrogen sulfide (H_2S), organic sulfur compounds, elemental sulfur, carbon dioxide (CO_2), pyrobitumen, and other oxidized species of carbon [1, 2]. Water (H_2O) may be a reactant or product of TSR, depending on the H/C ratio of the reacting hydrocarbon phase.

Although the overall TSR process is irreversible under sedimentary basin conditions, many of the reactions involved in this process appear to proceed at or near equilibrium. For example, gas-phase concentrations of methanethiol (CH_3SH) in carbonate reservoirs from the Sichuan Basin [3] are consistent with metastable equilibrium involving CO_2 and H_2S at redox conditions close to the pyrite-pyrrhotite-magnetite buffer. These redox conditions are also consistent with the organic sulfur content of crude oils, which increases with increasing H_2S content of the gas phase. In contrast, the anhydrite-calcite-sulfur assemblage cannot be stable under these conditions in the presence of an aqueous phase. Accordingly, anhydrite should dissolve irreversibly unless protected by secondary calcite [4].

Based on these observations, mass transfer calculations have been carried out at 150°C and 500 bar to quantify the relative importances of anhydrite dissolution, hydrocarbon destruction, CO_2 and H_2S generation, petroleum sulfurization, and calcite, sulfur and pyrobitumen precipitation during thermochemical sulfate reduction.

[1] Machel (2001) *Sediment. Geol.* **140**, 143-175.
[2] Goldstein & Aizenshtat (1994) *J. Therm. Anal.* **42**, 241-290. [3] Cai et al. (2003) *Chem. Geol.* **202**, 39-57.
[4] Bildstein et al. (2001) *Chem. Geol.* **176**, 173-189.

A thermodynamic analysis of organic/inorganic interactions during thermochemical sulfate reduction (TSR)

Rakhim Uteyev [a], Laurent Richard [a,*], Jérôme Sterpenich [a],

Alain Clément [b], and Daniel Dessort [c]

[a] Nancy-Université, G2R, BP 70239, 54506 Vandoeuvre-lès-Nancy cedex, France

[b] Ecole et Observatoire des Sciences de la Terre, Laboratoire d´Hydrologie et de Géochimie de Strasbourg, 1 rue Blessig, 67084 Strasbourg cedex, France

[c] Total, Centre Scientifique et Technique Jean Féger, F-64018 Pau cedex, France

Abstract

Thermodynamic calculations have been carried out at 150ºC and 500 bar to analyze and quantify the organic/inorganic reactions occuring during thermochemical sulfate reduction (TSR). The dissolution of anhydrite, generation of CO_2 and H_2S, formation of organic sulfur compounds, destruction of hydrocarbons, and precipitation of elemental sulfur and pyrobitumen are discussed as a function of the composition of the system using activity diagrams. If the overall TSR reaction is irreversible, it appears that many of the reactions involved in TSR proceed at or near equilibrium. The calculations allow for example to predict the total concentration and speciation of organic sulfur in crude oils as a function of the fugacities of CO_2 and H_2S, or to predict the concentrations of mercaptans in the gas phase of sulfur-rich petroleum reservoirs. These calculations also suggest a change with increasing TSR from redox conditions under which petroleum is stable to more oxidizing conditions under which pyrobitumen and elemental sulfur are stable.

1. Introduction

A number of oil and gas fields contain high amounts of H_2S (up to several tens in volume percent H_2S in the gas phase – e.g. see Orr, 1977) which have been generated by thermochemical sulfate reduction (TSR). The oxidation counterpart of the TSR reaction
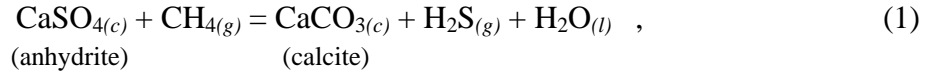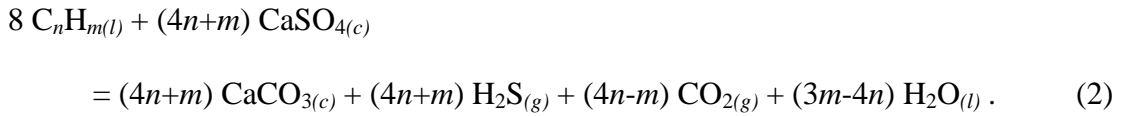
---

results in a destruction of petroleum hydrocarbons to produce CO_2 gas, aqueous bicarbonate and acetate ions, and other oxidized species of carbon. High concentrations of H_2S demonstrably attributed to TSR have been reported in the Devonian Nisku Formation of South-Central Alberta, Canada (Machel, 1987; Machel et al., 1995; Manzano et al., 1997), the Smackover Jurassic Formation of the southeastern United States (Orr, 1977; Sassen, 1988; Heydari and Moore, 1989, Heydari, 1997), and the Permian Khuff Formation of Abu Dhabi (Worden and Smalley, 1996; Worden et al., 1995, 1996, 2000), among other formations. Thermochemical sulfate reduction occurs in deep (2,000 to 6,000 m) carbonate (or more rarely clastic) reservoirs, implying temperatures typically ranging between 100 and 150°C. At these temperatures, aqueous sulfate (either in formation waters or derived from the dissolution of anhydrite or gypsum) react with hydrocarbons to produce H_2S and oxidized species of carbon. This redox reaction can ultimately result in the complete destruction of petroleum (Heydari, 1997). Numerous experimental studies have been carried out on TSR (Toland, 1960; Kiyosu, 1980; Nikolayeva et al., 1982; Trudinger et al., 1985; Cross et al., 2004; Zhang et al., 2008). In contrast, relatively few studies have attempted to quantify the mass transfer processes involved in the overall TSR reaction. Bildstein et al. (2001) have carried out calculations considering the reaction between anhydrite and methane. However, these authors did not consider higher molecular weight organic compounds despite the fact that methane is generally considered to be the least reactive hydrocarbon species during TSR (Machel, 1998). In this paper, we present a comprehensive thermodynamic analysis of TSR which takes into account liquid hydrocarbons and other organic species which are known to be formed or consumed during TSR.

2. The overall TSR reaction

The TSR reaction is written under its simplest form by considering methane as the hydrocarbon reactant (e.g. Worden et al., 1995; Bildstein et al., 2001; Cross et al., 2004):

72

$$CaSO_{4(c)} + CH_{4(g)} = CaCO_{3(c)} + H_2S_{(g)} + H_2O_{(l)} \quad , \tag{1}$$
$$\text{(anhydrite)} \qquad \qquad \text{(calcite)}$$

where the subscripts *(c)*, *(l)*, and *(g)* refer to the crystalline, liquid, and gas states, respectively. The stoichiometry and irreversible nature of Reaction (1) together with fluid inclusion and oxygen isotopic considerations has led Worden et al. (1996) to propose that significant amounts of water could be produced as a result of the TSR reaction. This conclusion has been challenged by Machel (1998) based on the fact that methane is the least reactive hydrocarbon species during the TSR reaction, and because one can also write balanced TSR reactions in which water appears as a reactant. In fact, it can be shown that whether water is a reactant or a product of the TSR reaction directly depends on the H/C ratio of the reacting hydrocarbon species being considered. Reaction (1) can be rewritten under a general form for any liquid hydrocarbon $C_nH_{m(l)}$ as

$$8\,C_nH_{m(l)} + (4n{+}m)\,CaSO_{4(c)}$$

$$= (4n{+}m)\,CaCO_{3(c)} + (4n{+}m)\,H_2S_{(g)} + (4n{-}m)\,CO_{2(g)} + (3m{-}4n)\,H_2O_{(l)} \,. \tag{2}$$

It can be deduced from Reaction (2) that water will be produced during TSR for hydrocarbon reactants C_nH_m with $3m > 4n$, which include *n*-alkanes and methylalkanes (C_nH_{2n+2}), alkylcyclopentanes and alkylcyclohexanes (C_nH_{2n}), tricyclic diterpanes (C_nH_{2n-4}), steranes (C_nH_{2n-6}), hopanes (C_nH_{2n-8}), and alkylbenzenes (C_nH_{2n-6}) with $n > 7$. In contrast, reacting benzene, toluene, alkylnaphthalenes (C_nH_{2n-12}), alkylbiphenyls (C_nH_{2n-14}), alkylphenanthrenes (C_nH_{2n-18}), and other polynuclear aromatic hydrocarbons will consume water. It also appears from Reaction (2) that substantial amounts of CO_2 gas can be produced in the TSR process. For example, the destruction of 1 mole of *n*-tetradecane ($C_{14}H_{30}$) would lead to a production of 3.25 mole of CO_2, while the destruction of 1 mole of phenanthrene ($C_{14}H_{10}$) would result in 5.75 mole of CO_2 being produced. The number of moles of H_2O and CO_2 produced or consumed during the overall TSR reaction has been plotted as a function of the H/C ratio of the reacting hydrocarbon in Figure 1, where it can be seen that the amount of H_2O produced

increases with increasing H/C of the reacting hydrocarbon, whereas the amount of CO_2 produced decreases with increasing H/C of the reacting hydrocarbon. It can also be deduced from Figure 1 that the TSR reaction written for any hydrocarbon with H/C < 1.3 will consume water.

3. Metastable equilibrium states and irreversible reactions in the overall TSR process

Although there is substantial debate over the lower temperature limit at which TSR starts to proceed in natural settings (Machel, 2001), the reaction is known to be thermodynamically favored from the surface conditions of 25°C and 1 bar (Dhannoun and Fyfe, 1972) to deep into sedimentary basins. This can best be illustrated by considering liquid n-dodecane as an example and rewriting Equation (2) as

$$C_{12}H_{26(l)} + 9.25\ CaSO_{4(c)} = 9.25\ CaCO_{3(c)} + 9.25\ H_2S_{(g)} + 2.75\ CO_{2(g)} + 3.75\ H_2O_{(l)} \qquad (3)$$
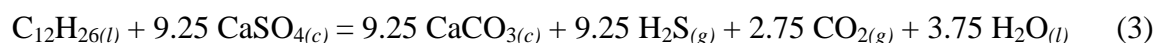
The standard molal Gibbs free energy for Reaction (3) ($\Delta G^{\circ}_{(3)}$) has been computed as a function of temperature and pressure using the SUPCRT92 computer program (Johnson et al., 1992) together with thermodynamic properties for minerals, gases, and liquid n-dodecane taken from Helgeson et al. (1978, 1998). The computed values of $\Delta G^{\circ}_{(3)}$ have been plotted as a function of temperature for different pressures in Figure 2. It can be seen in this figure that the standard molal Gibbs free energy of Reaction (3) becomes more negative with increasing both temperature and pressure, which renders this reaction more and more favorable with increasing depth in sedimentary basins.

Specifying unit activities for the minerals[1] as well as for liquid water[2], a statement of the law of mass action for Reaction (3) may be written under logarithmic form as

---

[1] The standard state adopted in the present study for minerals and solid pyrobitumens as well as liquid hydrocarbons and organic sulfur compounds is one of unit activity of the thermodynamic components of stoichiometric minerals and pure liquids at any temperature and pressure. The standard state for aqueous species other than H_2O calls for unit activity of the species in a hypothetical one molal solution referenced to infinite

$$\log K_{(3)} = 9.25 \log f_{H_2S_{(g)}} + 2.75 \log f_{CO_{2(g)}} - \log a_{C_{12}H_{26(l)}} \tag{4}$$

where $f_{H_2S_{(g)}}$ and $f_{CO_{2(g)}}$ are the fugacities of H_2S and CO_2 in the gas phase, and $a_{C_{12}H_{26(l)}}$ represents the activity of *n*-dodecane in liquid petroleum. Equilibrium fugacities of CO_2 and H_2S have been computed for representative activities of liquid *n*-dodecane in petroleum at 150°C and 500 bar from Equation (4) and the logarithm of the equilibrium constant for Reaction (3) listed in Table 1. These equilibrium fugacities have been plotted against each other in Figure 3. It can be deduced from this figure that the computed values of $f_{H_2S_{(g)}}$ for common fugacities of CO_2 gas in sedimentary basins (Shock, 1988) are in the range $10^9 - 10^{12}$ bar, which by far exceeds the total pressure of the system and represents physically unattainable values. Therefore, Reaction (3) is an irreversible reaction, the chemical affinity $\mathbf{A}_r$ of which may be evaluated from (Helgeson et al., 1993)

$$\mathbf{A}_r = 2.303 \, RT \log (K_r/Q_r) \tag{5}$$

where K_r stands for the equilibrium constant of the subscripted reaction and Q_r is the activity quotient defined as

$$Q_r = \prod_i a_i^{\nu_i} \tag{6}$$

where a_i is the activity of the subscripted species, and ν_i is the stoichiometric coefficient of the species in the *r*th reaction, ν_i being positive for products and negative for reactants. Taking account of the standard states specified above and assuming unit activity for liquid water, the logarithmic analog of Equation (7) can be written for Reaction (3) as:

$$\log Q_{(3)} = 9.25 \log f_{H_2S_{(g)}} + 2.75 \log f_{CO_{2(g)}} - \log a_{C_{12}H_{26(l)}} \ . \tag{7}$$

---

dilution at any temperature and pressure. For the thermodynamic components of gases, the standard state is specified as unit fugacity of the pure hypothetical ideal gas at 1 bar and any temperature.

[2] Consideration of osmotic coefficients for NaCl solutions at the temperature and pressure conditions typical of sedimentary basins indicates that the activity of H_2O is close to unity in most oil field waters (Helgeson et al., 1993).

The latter expression has been combined together with Equation (5) and the value of log $K_{(3)}$

listed in Table 1 to calculate the chemical affinity of Reaction (3) for fugacities of H_2S gas

and CO_2 gas ranging from 10^{-2} bar to 100 bar and two representative activities of liquid n-

dodecane in petroleum of 10^{-4} and 10^{-2} (Helgeson et al., 1993). It can be deduced from Figure

4 that this chemical affinity increases from ~ 130 kcal (mol $C_{12}H_{26(l)}$)$^{-1}$ to ~ 190 kcal (mol

$C_{12}H_{26(l)}$)$^{-1}$ with a fugacity of H_2S gas decreasing from 10 bar to 10^{-2} bar at a constant fugacity

of CO_2 gas of 1 bar.

Concentrations of H_2S in carbonate reservoirs of the Alberta Basin (Canada) have

been reported as a function of temperature and depth by Manzano et al. (1997) and Hutcheon

(1999). A general increase in the H_2S content with depth (and therefore present-day reservoir

temperatures) has been noted by Manzano et al. (1997), while Hutcheon (1999) observed that

the concentration of CO_2 was increasing along with H_2S, but that the concentrations of CO_2

were significantly lower than those of H_2S. The latter observation is consistent with Reaction

(3), in which the ratio between the stoichiometric coefficients ($\hat{n}_i$) of $H_2S_{(g)}$ and $CO_{2(g)}$ is

equal to

$$\frac{\hat{n}_{H_2S_{(g)}}}{\hat{n}_{CO_{2(g)}}} = 3.36 \ . \tag{8}$$

If 2,6-dimethylnaphthalene ($C_{12}H_{12}$) is considered as a reactant instead, this ratio deceases to

1.67, while it increases to 7.0 when ethane (C_2H_6) is the reacting hydrocarbon. Partial

pressures of CO_2 and H_2S reported by Hutcheon (1999) for carbonate reservoirs of the Alberta

Basin have been plotted against each other in Figure 5. The straight lines shown in this figure

correspond to the ratio of the stoichiometric coefficients of $H_2S_{(g)}$ and $CO_{2(g)}$ in Reaction (3)

and other analogs of Reaction (2) written for different reacting hydrocarbons. It can deduced

from Figure 5 that most of the gas compositions can be accounted for by different analogs of

Reaction (2) written for different reacting hydrocarbons, which can be thought of as

representative of varying petroleum compositions. It should however be realized that the partial pressures of $H_2S_{(g)}$ and $CO_{2(g)}$ may also be affected by secondary processes such as the precipitation of elemental sulfur or pyrobitumen. The effect of the latter and other reactions on the overall TSR process are evaluated in the detailed thermodynamic analysis presented below.

3.1. Anhydrite solubility as a function of oxygen fugacity

A number of experimental investigations have been reported on the stoichiometric (or congruent) solubility of anhydrite at temperatures between 25°C and 300°C and ionic strengths up to 6 m NaCl at pressures corresponding to the liquid-vapor saturation curve of the system H_2O (Marshall et al., 1964; Block and Waters, 1968; Blount and Dickson, 1969; Freyer and Voigt, 2004). Experimental data reported at rounded temperatures and for ionic strengths up to 2 m NaCl have been plotted in Figure 6. It can be seen in this figure that the stoichiometric solubility of anhydrite is decreasing with increasing temperature but increasing with increasing ionic strength. The curves shown in Figure 6 have been computed with the DISSOL mass transfer computer program (Fritz, 1981) and an updated SUPCRT92 (Johnson et al., 1992) thermodynamic database consistent with the calorimetric data of Majzlan et al. (2002) and Robie et al. (1989) for anhydrite. It can be deduced from Figure 6 that the agreement between the experimental and computed solubilities is acceptable, even for the higher ionic strengths (2 m NaCl) although an extended Debye-Hückel model is used in the DISSOL program for the calculation of ionic activity coefficients.

Newton and Manning (2005) have recently reported a study on the solubility of anhydrite under redox controlled conditions, but their study was carried out at magmatic temperatures (600-800°C) and pressures (6-14 kbar). Although aqueous sulfide and sulfate species are not necessarily in chemical equilibrium with each other at diagenetic or hydrothermal temperatures (Ohmoto and Lasaga, 1982 – see below), the speciation

calculations represented in Figure 7 which describe the solubility of anhydrite as a function of oxygen fugacity ($f_{O_{2(g)}}$) at 150°C, P_{sat} and for a constant fugacity of CO_2 gas ($f_{CO_{2(g)}}$) equal to 1 bar are predicated on the hypothesis that such an equilibrium is indeed established. The thick solid curve in this figure represents the logarithm of the number of moles of anhydrite dissolved at each fixed value of $\log f_{O_{2(g)}}$. The various solid and dashed curves under this thick solid curve represent the detailed speciation of calcium and sulfur in the aqueous solution at each $\log f_{O_{2(g)}}$ value. It can be deduced from Figure 7 that the solubility of anhydrite increases drastically from a value of $\log f_{O_{2(g)}} = -47$, which is ~ 4 log units more oxidizing than that corresponding to the pyrite-pyrrhotite-magnetite assemblage which has been shown to be representative of the redox conditions prevailing in hydrocarbon reservoirs and source rocks (Helgeson et al., 1993, 2009). Under these circumstances, the persistence of anhydrite in carbonate reservoirs has to be explained either by a slow dissolution rate and a slow reduction rate of the aqueous sulfate, or by the precipitation of a protective layer of calcite around the unstable anhydrite (Bildstein et al., 2001). Also indicated in Figure 7 are the equilibrium pH values computed from the equilibrium distribution of all the aqueous species present in the system and for $f_{CO_{2(g)}} = 1$ bar. Note that for the reducing conditions at which the solubility of anhydrite starts to increase (i.e. at which the concentration of the sulfide species exceed that of the sulfate species), the computed pH values (~ 8) are obviously higher than those typical of formation waters in which the pH values are either buffered by equilibrium among K-feldspar, quartz and clays in the case of sandstone reservoirs (Smith and Ehrenberg, 1989), or by equilibrium among acetic acid and acetate or by the inorganic equilibria of the carbonate system in the case of carbonate reservoirs (Lundegard and Land, 1989). In their comprehensive thermodynamic analysis of the composition of formation waters from the Texas Gulf Coast, Helgeson et al. (1993) computed pH values of the order of

78

~ 5.5 at 150°C assuming a metastable equilibrium state among authigenic minerals and the organic and inorganic aqueous species in the formation waters. In fact, the high pH values of aqueous solutions in equilibrium with anhydrite at 150°C and $\log f_{O_{2(g)}} < \sim$ -47 merely result from the chemical composition of the system being considered.

3.2. Aqueous sulfate reduction

Several experimental studies on the reduction of solid or aqueous sulfate by organic compounds have been reported in the literature (e.g. Toland, 1960; Kiyosu, 1980; Nikolayeva et al., 1982; Trudinger et al., 1985; Cross et al., 2004; Zhang et al., 2008), although only those concerned with aqueous sulfate are of geological interest (Machel, 2001). Ohmoto and Lasaga (1982) developed a detailed kinetic model for the reactions between sulfate and sulfide species in hydrothermal systems. This model, which was based on experimental studies on the isotopic exchange of sulfur, allowed Ohmoto and Lasaga (1982) to calculate the time required for attaining isotopic (and by extension chemical) equilibrium as a function of temperature and solution pH. The calculations indicated that sulfate and sulfide aqueous species do not necessarily reach chemical equilibrium over geologically reasonable time scales, particularly at low temperatures and high pH values. For example, the time required for attaining 90 percent equilibrium between aqueous sulfate and sulfide species for a total concentration of sulfur equal to 10^{-2} molal is 400,000 years at 100°C and 4000 years at 150°C for pH values between 4 and 7. In contrast, this time increases to 10^{12} and 10^9 years for a pH value of ~ 9. Ohmoto and Lasaga (1982) further calculated reaction rate constants and activation energies for TSR based on the experimental data of Kiyosu (1980). They suggested that the rate of TSR should vary with the nature of the reacting organic species, and that for a given reactant, this rate was probably a function of the total concentration of sulfate species, the concentration of the organic reactant, temperature, as well as pH.

Cross et al. (2004) recently studied the kinetics of sulfate reduction by acetate between 280-350°C at pressures of 250 and 500 bars, and in-situ pH values (5.2-6.8) in the range of those typical of formation waters. As expected, the rate of sulfate reduction was found to be highly dependent on temperature, but showed little dependence on both pressure and solution pH (although the pH range covered in the experiments was relatively narrow). Adopting a first order kinetic rate law with respect to sulfate, Cross et al. (2004) derived an activation energy of 142 kJ mol^{-1} and a half-life of 1650 years for sulfate at 150°C, thereby showing that the reaction of sulfate reduction is rapid on a geological time scale. This led Cross et al. (2004) to conclude that the fact that sulfate minerals and petroleum coexist in many hydrocarbon reservoirs cannot be explained by a kinetic control.

3.3. Formation of organic sulfur compounds

Thiols and thiophenes have been reported to occur in the gas phase of several carbonate reservoirs of the Sichuan Basin (Cai et al., 2003). The concentrations of these organic sulfur compounds were found to increase with the H_2S content of the reservoirs. In order to evaluate if gaseous organic sulfur compounds can be in metastable equilibrium with gaseous CO_2 and H_2S in these reservoirs, one can write for the simplest of these compounds (methanethiol) the following redox reaction

$$CO_{2(g)} + H_2S_{(g)} + H_2O_{(l)} = CH_3SH_{(g)} + 1.5\ O_{2(g)}\ ,\qquad(9)$$
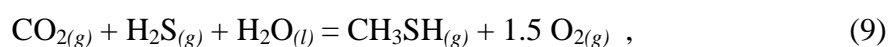
the equilibrium constant of which has been calculated at 150°C and 500 bar using the SUPCRT92 (Johnson et al. 1992) with thermodynamic properties for methanethiol gas taken from Helgeson et al. (1998). This equilibrium constant, which is listed in Table 1, has been used with an appropriate expression of the law of mass action to generate the fugacity diagram depicted in Figure 8, where it can be seen that the computed fugacities of CH_3SH gas for representative fugacities of CO_2 and H_2S in sedimentary basins would correspond to detectable traces of methanethiol in the gas phase, in accord with the observations of Cai et al.

(2003). The possibility of such metastable equilibrium states involving the organic sulfur compounds in crude oil has been previously suggested by Richard and Helgeson (2001) and Richard et al. (2005). Accordingly, Reaction (9) can be generalized for any liquid organic sulfur compound $C_nH_mS_{p(l)}$ in petroleum by writing

$$C_nH_mS_{p(l)} + (4n+m-2p)/4 \; O_{2(g)} = n \; CO_{2(g)} + p \; H_2S_{(g)} + (m-2p)/2 \; H_2O_{(l)} \tag{10}$$
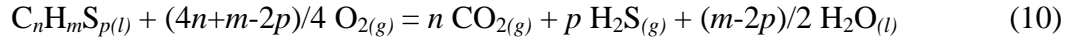
where n, m and p correspond to the number of moles of carbon, hydrogen, and sulfur atoms in one mole of the organic sulfur compound, and $O_{2(g)}$ and $H_2O_{(l)}$ respectively designate oxygen gas and liquid water. Values of the equilibrium constant of Reaction (10) computed at 150°C and 500 bar for the twenty organic sulfur compounds depicted in Figure 9 using thermodynamic properties taken from Richard (2001) have been listed in Table 2 and used in conjunction with an expression of the law of mass action written under the form

$$\log a_{C_nH_mS_{p(l)}} = -\log K_{(10)} + n \log f_{CO_{2(g)}} + p \log f_{H_2S_{(g)}}$$

$$+ (m-2p)/2 \log a_{H_2O_{(l)}} - (4n+m-2p)/4 \log f_{O_{2(g)}} \tag{11}$$

to generate the activity diagrams depicted in Figure 10. The lines in these diagrams have been drawn for a unit activity of liquid water (see footnote 2) and the values of $\log f_{CO_{2(g)}}$ and $\log f_{H_2S_{(g)}}$ specified in each diagram. The latter values have been chosen by consideration of the partial pressures represented in Figure 5. The horizontal grey lines in the four diagrams of Figure 10 correspond to $\log a_{C_nH_mS_{p(l)}} = 0$, i.e. to a given pure organic sulfur liquid compound. The regions above these horizontal grey lines represent activity values which are physically unattainable. The dashed vertical lines correspond to the values of $\log f_{O_{2(g)}}$ for the pyrite-pyrrhotite-magnetite (PPM) and hematite-magnetite (HM) assemblages (see below). It can be deduced from the diagrams of Figure 10 that appreciable and realistic concentrations of organic sulfur compounds are obtained at values of $\log f_{O_{2(g)}}$ which are close to those

corresponding to the PPM assemblage. Note that increasing both $f_{H_2S_{(g)}}$ and $f_{CO_{2(g)}}$ to 100 bar displaces the equilibrium activity lines towards more oxidizing conditions, which as will be shown in the next section has a direct implication on the formation of elemental sulfur during TSR. In addition, the speciation of organic sulfur appears to be highly dependent on $\log f_{O_{2(g)}}$. For example, the slopes of the activity lines for methanethiol (CH_4S) and 4,6-dimethyldibenzothiophene ($C_{14}H_{12}S$) which are drastically different, cross approximately at $\log f_{O_{2(g)}} \sim -51$ for $f_{CO_{2(g)}} = f_{H_2S_{(g)}} = 10$ bar. Therefore, the speciation of organic sulfur would be dominated by short-chain alkanethiols under more oxidizing conditions and by dibenzothiophenes under more reducing conditions. Note however, that a speciation of organic sulfur dominated by methanethiol corresponds to much lower total concentrations of organic sulfur in crude oil.
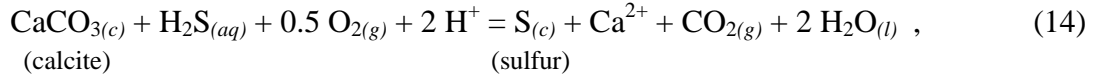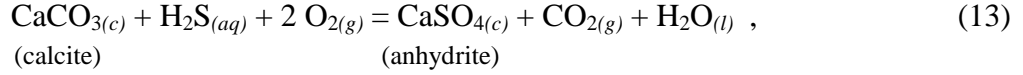
3.4. Precipitation of elemental sulfur

Elemental sulfur is commonly observed in hydrocarbon reservoirs where thermochemical sulfate reduction has reportedly occurred (e.g. Heydari, 1997). According to Machel (2001), elemental sulfur first forms in TSR settings as an intermediate product due to a partial reoxidation of H_2S by excess sulfate[3], but most of this sulfur is subsequently reduced back to H_2S. Elemental sulfur only starts to accumulate in a reservoir when all of the reacting hydrocarbons have been consumed (Machel, 2001). If hydrocarbons are present, they will reduce elemental sulfur to H_2S according to

$$(4n+m)/2\ S_{(c)} + C_nH_{m(l)} + 2n\ H_2O_{(l)} = (4n+m)/2\ H_2S_{(g)} + n\ CO_{2(g)}\ , \tag{12}$$
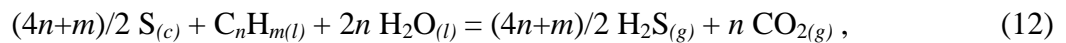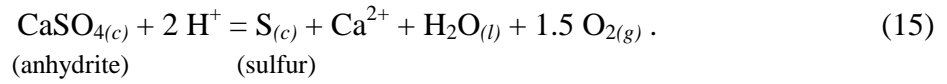
which is essentially equivalent to Reaction (8) in Machel (2001). Although not directly apparent from Reaction (12), the latter observation is interesting because it suggests an evolution of the redox conditions during TSR. In order to better constrain the conditions under

---

[3] Note that the occurrence of this reaction has been questioned by several authors (see Zhang et al., 2008 for a discussion).

which and the reaction paths through which elemental sulfur may form during TSR, the stability relations among elemental sulfur, anhydrite, calcite, CO_2 gas, and aqueous H_2S at 150°C and 500 bar are depicted in Figures 11 and 12. The stability limits in Figure 11 correspond to the reactions
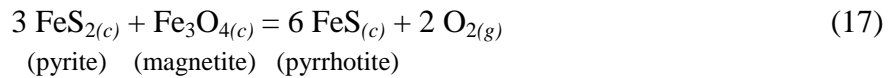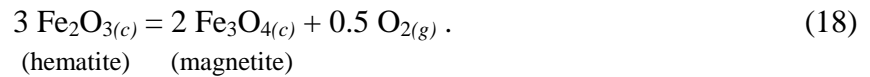
$$CaCO_{3(c)} + H_2S_{(aq)} + 2\ O_{2(g)} = CaSO_{4(c)} + CO_{2(g)} + H_2O_{(l)}\ , \qquad (13)$$
$$\text{(calcite)} \qquad\qquad\qquad \text{(anhydrite)}$$

$$CaCO_{3(c)} + H_2S_{(aq)} + 0.5\ O_{2(g)} + 2\ H^+ = S_{(c)} + Ca^{2+} + CO_{2(g)} + 2\ H_2O_{(l)}\ , \qquad (14)$$
$$\text{(calcite)} \qquad\qquad\qquad\qquad \text{(sulfur)}$$

and

$$CaSO_{4(c)} + 2\ H^+ = S_{(c)} + Ca^{2+} + H_2O_{(l)} + 1.5\ O_{2(g)}\ . \qquad (15)$$
$$\text{(anhydrite)} \qquad\qquad \text{(sulfur)}$$

The solid line in Figure 12 corresponds to the reaction

$$S_{(c)} + H_2O_{(l)} = H_2S_{(aq)} + 0.5\ O_{2(g)}\ , \qquad (16)$$
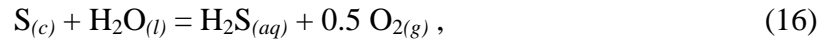
while the dashed equilibrium lines separating the stability domains of calcite and anhydrite for CO_2 gas fugacities equal to 1 bar and 100 bar correspond to Reaction (13). The logarithmic values of the equilibrium constants (log K) which have been used to calculate these stability limits are listed in Table 1. The stability limits in Figure 11 have been constructed for two different log $f_{O_{2(g)}}$ values corresponding to those set by the pyrite-pyrrhotite-magnetite (PPM) and hematite-magnetite (HM) buffers in accord with reactions written as
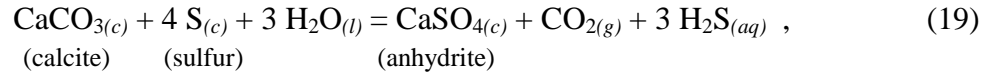
$$3\ FeS_{2(c)} + Fe_3O_{4(c)} = 6\ FeS_{(c)} + 2\ O_{2(g)} \qquad (17)$$
$$\text{(pyrite)}\quad \text{(magnetite)}\quad \text{(pyrrhotite)}$$

and

$$3\ Fe_2O_{3(c)} = 2\ Fe_3O_{4(c)} + 0.5\ O_{2(g)}\ . \qquad (18)$$
$$\text{(hematite)} \qquad \text{(magnetite)}$$

From the equilibrium constants listed in Table 1 for Reactions (17) and (18) and the standard state adopted for minerals (see footnote 1), values of log $f_{O_{2(g)}}$ respectively equal to -51.3 and -46.9 are obtained.

It can be deduced from Figures 11 and 12 that the calcite-anhydrite-sulfur assemblage corresponding to

$$CaCO_{3(c)} + 4\ S_{(c)} + 3\ H_2O_{(l)} = CaSO_{4(c)} + CO_{2(g)} + 3\ H_2S_{(aq)}\ , \qquad (19)$$
$$\text{(calcite)} \quad \text{(sulfur)} \qquad\qquad \text{(anhydrite)}$$

can only be in equilibrium with an aqueous solution under the specified conditions of temperature and pressure for redox conditions which either are approximately equal to or are more oxidizing than the $\log f_{O_{2(g)}}$ value corresponding to the HM buffer. More reducing conditions would correspond to unrealistically high values of $\log a_{H_2S_{(aq)}} > 0$, i.e. several orders of magnitude above the 10^{-4} to 10^{-2} mol·L^{-1} concentrations of H_2S measured for instance by Connolly et al. (1990) in formation waters from Devonian and Cretaceous reservoirs of the Western Canada Sedimentary Basin. However, the latter concentrations were most probably generated as a result of bacterial rather than thermochemical sulfate reduction. If we adopt a maximum $\log a_{H_2S_{(aq)}}$ value of ~ 0 in the aqueous phase, this would correspond to a fugacity of H_2S gas of ~ 100 bar and would therefore be reasonable for TSR reservoirs. It can also be seen in Figure 12 that the coexistence of calcite, elemental sulfur and an aqueous solution is limited to a very narrow $a_{H_2S_{(aq)}} - f_{O_{2(g)}}$ window. The conditions required for the formation of elemental sulfur during thermochemical sulfur reduction will further be discussed in the context of mass transfer calculations described below.

3.5. Hydrocarbon oxidation

Although all hydrocarbon species may be subject to oxidation during thermochemical sulfate reduction, several lines of evidence suggest that the aliphatic compounds (branched and *n*-alkanes) in the gasoline (C_5-C_{10}) range show the highest reactivity, followed by cycloalkanes and monoaromatic species (Machel, 2001). Methane appears to be the least reactive hydrocarbon during thermochemical sulfate reduction (Machel, 1998, 2001). Note in

that respect that methane is known to be slow to react in general under sedimentary basin conditions of temperature and pressure (e.g. Shock, 1988). The most important products of hydrocarbon oxidation are aqueous carboxylic acids and their dissociated (carboxylate) counterparts, as well as aqueous carbonate species, and solid pyrobitumen. It has been shown that the concentrations of carboxylic acids and carboxylate anions in formation waters were representing chemical equilibrium with CO_2 gas (and by extension the aqueous carbonate species in formation waters) in hydrocarbon reservoirs (Shock, 1988), but also with most of the petroleum hydrocarbons under redox conditions approximately corresponding to the oxygen fugacity ($f_{O_{2(g)}}$) defined by the pyrite-pyrrhotite-magnetite (PPM) assemblage (Helgeson et al., 1993). In contrast, pyrobitumen is thought to form during TSR as a result of petroleum destruction (Machel et al., 1995). This destruction must therefore happen for redox conditions under which petroleum is not stable, i.e. redox conditions which are more oxidizing than PPM. This can be demonstrated by calculating the stability field of pyrobitumen in $\log f_{O_{2(g)}} - \log f_{CO_{2(g)}} - \log a_{H_2S_{(aq)}}$ space. The molecular structure of the pyrobitumen model considered for the calculation is shown in Figure 13. This pyrobitumen model has a chemical formula corresponding to $C_{100}H_{50}O_3S_5$, which is representative of the elemental compositions reported by Kelemen et al. (2008) for pyrobitumens from the Nisku Formation of the Brazeau River area (Alberta, Canada). The average atomic H/C, O/C, and S/C ratios of these pyrobitumens are 0.51, 0.034, and 0.047, respectively. Thermodynamic properties and Maier-Kelley heat capacity coefficients have been generated for the pyrobitumen model from group additivy contributions given by Richard and Helgeson (1998) and Richard (2001). These properties and coefficients are the following: $\Delta G_f^\circ = 1555.388$ kJ·mol⁻¹, $\Delta H_f^\circ = 657.951$ kJ·mol⁻¹, $S^\circ = 1298.98$ J·mol⁻¹·K⁻¹, $V^\circ = 1134.5$ cm³·mol⁻¹, $a = 646.00$ J·mol⁻¹·K⁻¹, $b = 2.9369$ J·mol⁻¹·K⁻², and $c = -15.77 \cdot 10^5$ J·K·mol⁻¹. The stability field of

pyrobitumen is represented in the $\log f_{O_{2(g)}} - \log f_{CO_{2(g)}}$ and $\log a_{H_2S_{(aq)}} - \log f_{O_{2(g)}}$ diagrams shown in Figures 14 and 15. It can be deduced from Figure 14 that redox conditions corresponding approximately to the PPM buffer ($\log f_{O_{2(g)}} = -51.3$), n-dodecane (therefore petroleum) is stable but pyrobitumen is not. In contrast, moving to higher $\log f_{O_{2(g)}}$ values decreases the activity of n-dodecane in petroleum, and as a result displaces the system towards the stability field of pyrobitumen. This latter stability field is compared in Figure 15 to the stability limit corresponding to the saturation of the aqueous solution with respect to elemental sulfur. Also plotted in Figure 15 is the projected equilibrium line separating the stability fields of calcite and anhydrite. If we consider as a reference for an advanced stage of TSR a value of $\log a_{H_2S_{(aq)}} = 0$ (which is identified in the diagram by the vertical dotted lines), the stability limit for which sulfur will precipitate is intersected at $\log f_{O_{2(g)}} \sim -47.4$, which coincides with the stability field of calcite. For the same $\log f_{O_{2(g)}}$ value, the activity of n-dodecane in equilibrium with the pyrobitumen becomes vanishingly low at $a_{C_{12}H_{26(l)}} \sim 10^{-17.1}$.

This very low value is consistent with the suggestion of Machel (2001) that elemental sulfur only accumulates towards the end of the TSR process when all of the reactive hydrocarbons have been consumed. It can be concluded from Figure 15 that with increasing TSR, the progressive destruction of petroleum and subsequent precipitation of pyrobitumen and elemental sulfur must coincide not only with an increase of dissolved H_2S in the aqueous phase, but also with a change in the redox conditions, from redox conditions close to the PPM buffer for which petroleum is stable to redox conditions approaching the HM buffer for which pyrobitumen and elemental sulfur are stable.

4. Conclusions

A thermodynamic analysis has been made of the organic/inorganic reactions which affect the distribution of sulfur among minerals, petroleum, formation waters and the gas phase of hydrocarbon reservoirs during thermochemical sulfate reduction (TSR). From the observations summarized above, it appears that although the overall TSR process is irreversible, the liquid hydrocarbons and organic sulfur compounds in crude oil, water, CO_2 gas, H_2S gas and the sulfur- and carbon-bearing species in oil field waters may evolve in mutual equilibrium by readjusting their relative concentrations throughout the TSR process. The formation of elemental sulfur and pyrobitumen at advanced stages of TSR is consistent with a redox evolution of the system towards more oxidizing conditions.

Acknowledgements

References

Bildstein, O., Worden, R.H., Brosse, E., 2001. Assessment of anhydrite dissolution as the rate-limiting step during thermochemical sulfate reduction. Chemical Geology 176, 173-189.

Block, J., Waters, O.B., Jr., 1968. The $CaSO_4$-Na_2SO_4-$NaCl$-H_2O system at 25° to 100°C. Journal of Chemical and Engineering Data 13, 336-344.

Blount, C.W., Dickson, F.W., 1969. The solubility of anhydrite ($CaSO_4$) in $NaCl$-H_2O from 100 to 450°C and 1 to 1000 bars. Geochimica et Cosmochimica Acta 33, 227-245.

Cai, C., Worden, R.H., Bottrell, S.H., Wang, L., Yang, C., 2003. Thermochemical sulphate reduction and the generation of hydrogen sulphide and thiols (mercaptans) in Triassic carbonate reservoirs from the Sichuan Basin, China. Chemical Geology 202, 39-57.

Connolly C.A., Walter L.M., Baadsgaard H., and Longstaffe F.J. (1990) Origin and evolution of formation waters, Alberta Basin, Wetsern Canada Sedimentary Basin. I. Chemistry. Applied Geochemistry 5, 375-395.

Cross, M.M., Manning, D.A.C., Bottrell, S.H., Worden, R.H., 2004. Thermochemical sulphate reuction (TSR): experimental determination of reaction kinetics and implications of the observed reaction rates for petroleum reservoirs. Organic Geochemistry 35, 393-404.

Dhannoun, H.Y., Fyfe, W.S., 1972. Reaction rates of hydrocarbons with anhydrite. Progress in Experimental Petrology 2, 69-71.

Freyer, D., Voigt, W., 2004. The measurement of sulfate mineral solubilities in the Na-K-Ca-Cl-SO$_4$-H$_2$O system at temperatures of 100, 150 and 200°C. Geochimica et Cosmochimica Acta 68, 307-318.

Fritz, B., 1981. Etude thermodynamique et modélisation des réactions hydrothermales et diagénétiques. Mémoire des Sciences Géologiques 65, 197 p.

Helgeson, H.C., Delany, J.M., Nesbitt, H.W., Bird, D.K., 1978. Summary and critique of the thermodynamic properties of rock-forming minerals. American Journal of Science 278-A, 1-229.

Helgeson, H.C., Knox, A.M.,Owens, C.E., Shock, E.L., 1993. Petroleum, oil field waters, and authigenic mineral assemblages: Are they in metastable equilibirum in hydrocarbon reservoirs? Geochimica et Cosmochimica Acta 57, 3295-3339.

Helgeson, H.C., Owens, C.E., Knox, A.M., Richard, L., 1998. Calculation of the standard molal thermodynamic properties of crystalline, liquid, and gas organic molecules at high temperatures and pressures. Geochimica et Cosmochimica Acta 62, 985-1081.

Helgeson H.C., Richard L., McKenzie W.F., Norton D.L., Schmitt A., 2009. A chemical and thermodynamic model of oil generation in hydrocarbon source rocks. Geochimica et Cosmochimica Acta 73, 594-695.

Heydari, E., 1997. The role of burial diagenesis in hydrocarbon destruction and H_2S accumulation, Upper Jurassic Smackover Formation, Black Creek Field, Mississippi. American Association of Petroleum Geologists Bulletin 81, 26-45.

Heydari, E., Moore, C.H., 1989. Burial diagenesis and thermochemical sulfate reduction, Smackover Formation, southeastern Mississipi salt basin. Geology 17, 1080-1084.

Hutcheon, I., 1999. Controls on the distribution of non-hydrocarbon gases in the Alberta Basin. Bulletin of the Canadian Petroleum Geologists 47, 573-593.

Johnson, J.W., Oelkers, E.H., Helgeson H.C., 1992. SUPCRT92: A software package for calculating the standard molal thermodynamic properties of minerals, gases, aqueous species, and reactions from 1 to 5000 bar and 0 to 1000ºC. Computer and Geosciences 18, 899-947.

Kelemen S.R., Walters C.C., Kwiatek P.J., Afeworki M., Sansone M., Freund H., Pottorf R.J., Machel H.G., Zhang T., Ellis G.S., Tang Y., and Peters K.E. (2008) Distinguishing solid bitumens formed by thermochemical sulfate reduction and thermal chemical alteration. Organic Geochemistry 39, 1137-1143.

Kiyosu, Y., 1980. Chemical reduction and sulfur-isotope effects of sulfate by organic matter under hydrothermal conditions. Chemical Geology 30, 47-56.

Lundegard, P.D., Land, L.S., 1989. Carbonate equilibria and pH buffering by organic acids – response to changes in p_{CO_2}. Chemical Geology 74, 277-287.

Machel, H.G., 1987. Some aspects of diagenetic sulphate-hydrocarbon redox reactions. In: Marshall, J.D. (Ed.), Diagenesis of Sedimentary Sequences, Geological Society Special Publication No. 36, pp. 15-28.

Machel, H.G., 1998. Comment on "The effects of thermochemical sulfate reduction upon formation water salinity and oxygen isotopes in carbonate gas reservoirs" by R.H. Worden, P.C. Smalley, and N.H. Oxtoby. Geochimica et Cosmochimica Acta 62, 337-341.

Machel, H.G., 2001. Bacterial and thermochemical sulfate reduction in diagenetic settings — old and new insights. Sedimentary Geology 140, 143-175.

Machel, H.G., Krouse, H.R., Sassen, R., 1995. Products and distinguishing criteria of bacterial and thermochemical sulfate reduction. Applied Geochemistry 10, 373-389.

Majzlan, J., Navrotsky, A., Neil, J.M., 2002. Energetics of anhydrite, barite, celestine, and anglesite: A high-temperature and differential scanning calorimetry study. Geochimica et Cosmochimica Acta 66, 1839-1850.

Manzano, B.K., Fowler, M.G., Machel, H.G., 1997. The influence of thermochemical sulphate reduction on hydrocarbon compoisition in Nisku reservoirs, Brazeau river area, Alberta, Canada. Organic Geochemistry 27, 507-521.

Marshall, W.L., Slusher, R., Jones, E.V., 1964. Aqueous systems at high temperature. XIV. Solubility and thermodynamic relationships for $CaSO_4$ in $NaCl$-H_2O solutions from 40° to 200°C., 0 to 4 molal $NaCl$. Journal of Chemical and Engineering Data 9, 187-191.

Newton, R.C., Manning, C.E., 2005. Solubility of anhydrite, $CaSO_4$, in $NaCl$-H_2O solutions at high pressures and temperatures: Applications to fluid-rock interaction. Journal of Petrology 46, 701-716.

Nikolayeva, O.V., Ryzhenko, B.N., Germanov, A.I., 1982. Reduction of sulfate sulfur by hydrocarbons and alcohols in aqueous solution at 200-300°C. Geochemistry International 19, 88-104.

Ohmoto, H., Lasaga, A.C., 1982. Kinetics of reactions between aqueous sulfates and sulfides in hydrothermal systems. Geochimica et Cosmochimica Acta 46, 1727-1745.

Orr, W.L., 1977. Geologic and geochemical controls on the distribution of hydrogen sulfide in natural gas. In: Campos, R, Goñi, J. (Eds.), Advances in Organic Geochemistry 1975. Empresa Nacional Adaro De Investigaciones Mineras, Madrid, pp. 571-597.

Richard, L., 2001. Calculation of the standard molal thermodynamic properties as a function of temperature and pressure of some geochemically important organic sulfur compounds. Geochimica et Cosmochimica Acta 65, 3827-3877.

Richard, L., Helgeson, H.C., 1998. Calculation of the thermodynamic properties at elevated temperatures and pressures of saturated and aromatic high molecular weight solid and liquid hydrocarbons in kerogen, bitumen, petroleum, and other organic matter of biogeochemical interest. Geochimica et Cosmochimica Acta 62, 3591-3636.

Richard, L., Helgeson, H.C., 2001. Thermodynamic calculation of the distribution of organic sulfur compounds in crude oil as a function of temperature, pressure, and H_2S fugacity. Proceedings of the 10th International Symposium on Water-Rock Interaction (R. Cidu, ed.), pp. 333-335. Balkema.

Richard, L., Neuville, N., Sterpenich, J., Perfetti, E., Lacharpagne, J.-Cl., 2005. Thermodynamic analysis of organic/inorganic reactions involving sulfur: Implications for the sequestration of H_2S in carbonate reservoirs. Oil & Gas Science and Technology 60, 275-285.

Robie, R.A., Russell-Robinson, S., Hemingway, B.S., 1989. Heat capacities and entropies from 8 to 1000 K of langbeinite ($K_2Mg_2(SO_4)_3$), anhydrite ($CaSO_4$) and of gypsum ($CaSO_4.2H_2O$) to 325 K. Thermochimica Acta 139, 67-81.

Sassen, R., 1988. Geochemical and carbon isotopic studies of crude oil destruction, bitumen precipitation, and sulfate reduction in the deep Smackover Formation. Organic Geochemistry 12, 351-361.

Shock, E.L., 1988. Organic acid metastability in sedimentary basins. Geology 16, 886-890.

Smith, J.T., Ehrenberg S.N., 1989. Correlation of carbon dioxide abundance with temperature in clastic hydrocarbon reservoirs: relationship to inorganic chemical equilibrium. Marine and Petroleum Geology 6, 129-135.

Toland, W.G., 1960. Oxidation of organic compounds with aqueous sulfate. Journal of the American Chemical Society 82, 1911-1916.

Trudinger, P.A., Chambers, L.A., Smith, J.W., 1985. Low-temperature sulphate reduction: biological versus abiological. Canadian Journal of Earth Sciences 22, 1910-1918.

Worden, R.H., Smalley, P.C., 1996. H_2S-producing reactions in deep carbonate gas reservoirs: Khuff Formation, Abu Dhabi. Chemical Geology 133, 157-171.

Worden, R.H., Smalley, P.C., Oxtoby, N.H., 1995. Gas souring by thermochemical sulfate reduction at 140°C. American Association of Petroleum Geologists Bulletin 79, 854-863.

Worden, R.H., Smalley, P.C., Oxtoby, N.H., 1996. The effects of thermochemical sulfate reduction upon formation water salinity and oxygen isotopes in carbonate gas reservoirs. Geochimica et Cosmochimica Acta 60, 3925-3931.

Worden, R.H., Smalley, P.C., Cross, M.M., 2000. The influence of rock fabric and mineralogy on thermochemical sulfate reduction: Khuff Formation, Abu Dhabi. Journal of Sedimentary Research 70, 1210-1221.

Zhang, T., Amrani, A., Ellis, G.S., Ma, Q., Tang, Y., 2008. Experimental investigation on thermochemical sulfate reduction by H_2S initiation. Geochimica et Cosmochimica Acta 72, 3518-3530.

Fig. 1. Number of moles of liquid H_2O and CO_2 gas produced or consumed as a function of the atomic H/C ratio of the hydrocarbon reactant in the generalized TSR Reaction (2).

Fig. 2. Standard molal Gibbs free energy of Reaction (3) as a function of temperature for different pressures. The lines were generated using the computer program SUPCRT92 (Johnson et al., 1992).

Fig. 3. Logarithm of the fugacity of H_2S gas as a function of the logarithm of CO_2 gas at 150°C and 500 bar. The equilibrium lines were computed from Eqn. (4) for different activities of liquid *n*-dodecane in petroleum which correspond to the values on each line.

Fig. 4. Chemical affinity of Reaction (3) as a function of $\log f_{H_2S_{(g)}}$ for different values of $\log f_{CO_{2(g)}}$ corresponding to the numbers on the solid and dashed contours.

Fig. 5. Partial pressure of $H_2S_{(g)}$ versus partial pressure of $CO_{2(g)}$ in carbonate reservoirs affected by TSR. The symbols represent compositional data reported by Hutcheon (1999). The straight lines correspond to the ratio of the stoichiometric coefficients of $H_2S_{(g)}$ and $CO_{2(g)}$ in analogs of Reaction (2) written for different reacting hydrocarbons.

Fig. 6. Stoichiometric solubility of anhydrite as a function of temperature and ionic strength. The symbols correspond to experimental data reported in the literature. The curves have been computed with the DISSOL mass transfer computer program – see text.

Fig. 7. Solubility of anhydrite as a function of the logarithm of oxygen fugacity ($\log f_{O_{2(g)}}$) at 150°C and P_{sat} – see text.

Fig. 8. Fugacity diagram illustrating the metastable equilibrium relations among CO_2, H_2S, and CH_3SH gases at 150°C, 500 bar and $\log f_{O_{2(g)}} = -51.25$, which corresponds to the value fixed by the pyrite-pyrrhotite-magnetite assemblage. The labels on the equilibrium lines correspond to logarithmic values of the fugacity of methanethiol gas.

Fig. 9. Molecular structures of the twenty organic sulfur compounds considered for the calculation of sulfur speciation in crude oil – see text.

Fig. 10. Logarithm of the activity of liquid organic sulfur compounds ($a_{C_nH_mS_{P(l)}}$) in crude oil as a function of the logarithm of the fugacity of oxygen gas ($f_{O_{2(g)}}$) at 150°C and 500 bar. The equilibrium lines have been computed for different values of the fugacities of CO_2 ($f_{CO_{2(g)}}$) and H_2S ($f_{H_2S_{(g)}}$) gases, which are specified in each diagram. The vertical dashed lines correspond to reference values of $f_{O_{2(g)}}$ corresponding to the pyrite-pyrrhotite-magnetite (PPM) and hematite-magnetite (HM) assemblages. The horizontal thick gray lines correspond to unit activity of the organic sulfur compounds. The regions above these lines are not physically attainable.

Fig. 11. Activity diagram depicting the stability fields of calcite, anhydrite, and elemental sulfur at 150°C, 500 bar, and $f_{CO_{2(g)}}$ = 100 bar. The solid and dashed stability limits have been computed for two different values of oxygen fugacity corresponding to the pyrite-pyrrhotite-magnetite (PPM) and hematite-magnetite (HM) buffers, respectively.

Fig. 12. Activity-fugacity diagram representing the stability field of elemental sulfur at 150°C and 500 bar. The dashed line which represents equilibrium between calcite and anhydrite has been computed for a value of $f_{CO_{2(g)}}$ = 100 bar.

Fig. 13. Molecular structure of the pyrobitumen model considered in the calculations, and corresponding to a chemical formula $C_{102}H_{52}O_3S_5$ consistent with H/C = 0.51, O/C = 0.029 and S/C = 0.049.

Fig. 14. Fugacity diagrams illustrating the metastable equilibrium relations among pyrobitumen, n-dodecane in petroleum, and CO_2 and H_2S at 150ºC and 500 bar. The numbers on the stability limits separating the domains of n-dodecane and pyrobitumen correspond to different activities of n-dodecane in crude oil.

Fig. 15. Activity-fugacity diagram comparing the stability fields of elemental sulfur and pyrobitumen at 150°C and 500 bar. The dashed line which represents equilibrium between calcite and anhydrite has been computed for a value of $f_{CO_{2(g)}} = 100$ bar, while that representing equilibrium between pyrobitumen and n-dodecane has been drawn for an activity of n-dodecane equal to $10^{-17.1}$, which is consistent with the $\log f_{O_{2(g)}}$ value for which the precipitation of elemental sulfur from the aqueous solution occurs at equilibrium for $\log a_{H_2S_{(aq)}} = 0$ – see text.
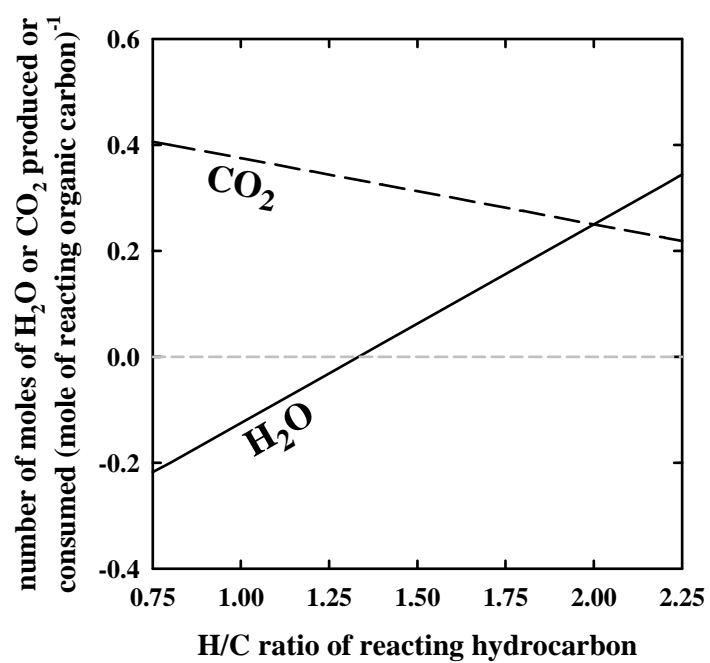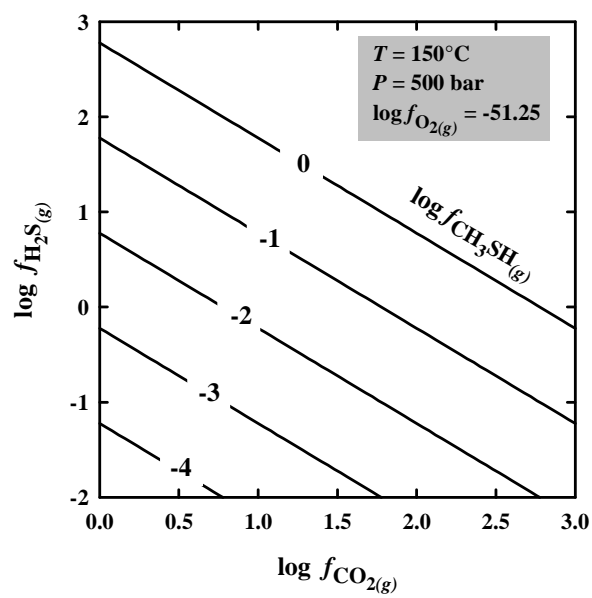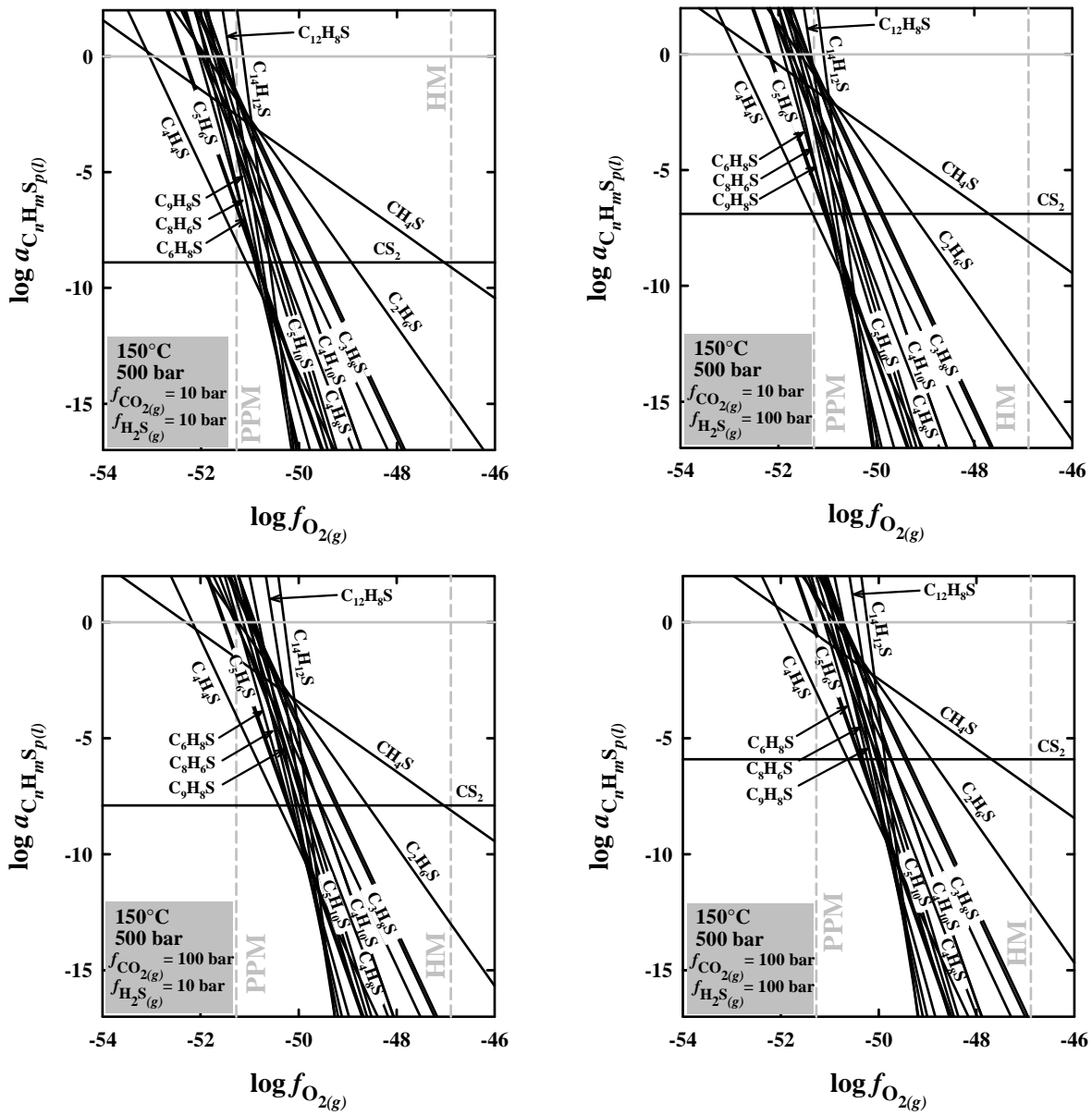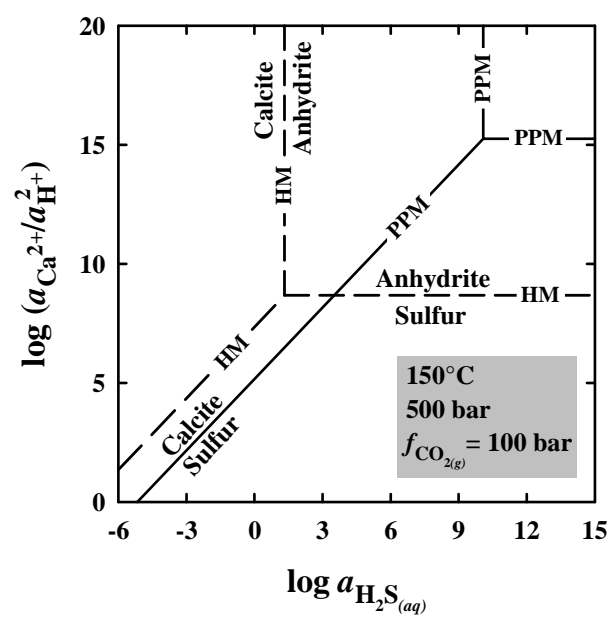
Figure 1
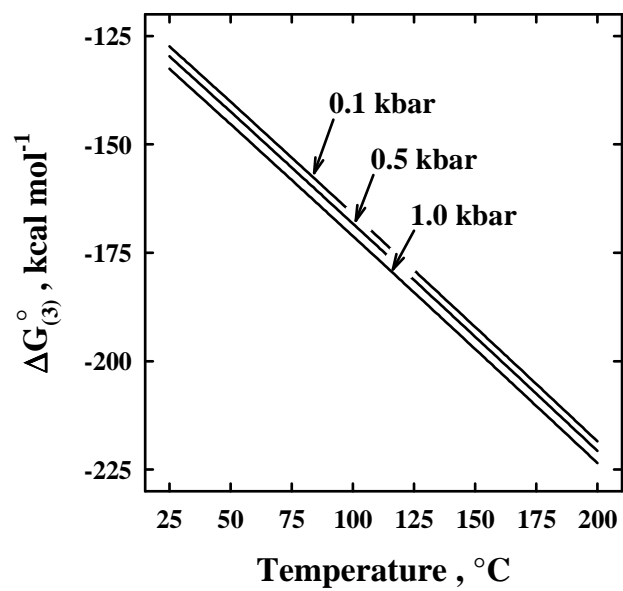
Figure 2
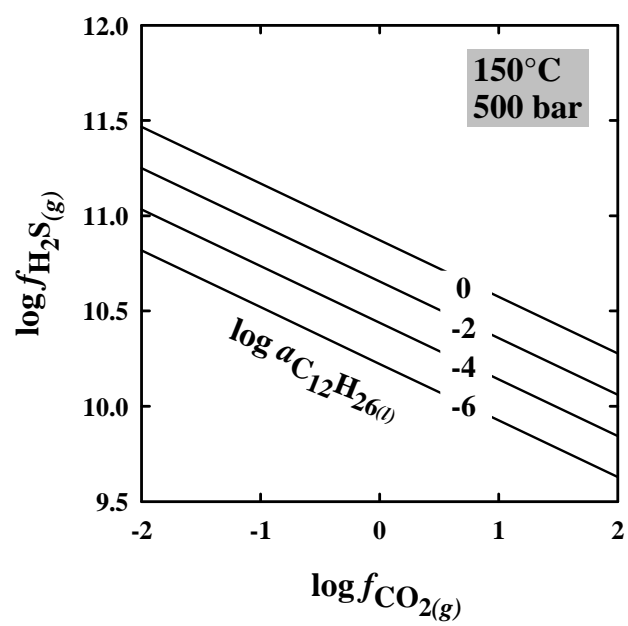
Figure 3
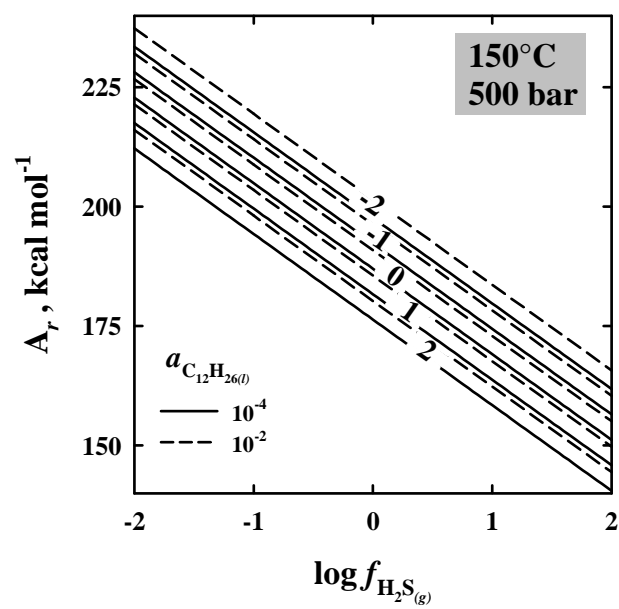
Figure 4

Figure 5

Figure 6

equilibrium pH

Figure 7

Figure 8

Carbon disulfide   Methanethiol   Ethanethiol   1-Propanethiol

2-Propanethiol

2-Thiabutane

1-Butanethiol

2-Butanethiol

Thiacyclopentane

2-Methylthiacyclopentane   3-Methylthiacyclopentane   Thiacyclohexane   Thiophene

2-Methylthiophene   3-Methylthiophene   2,5-Dimethylthiophene   Benzothiophene

2-Methylbenzothiophene   Dibenzothiophene   4,6-Dimethyldibenzothiophene
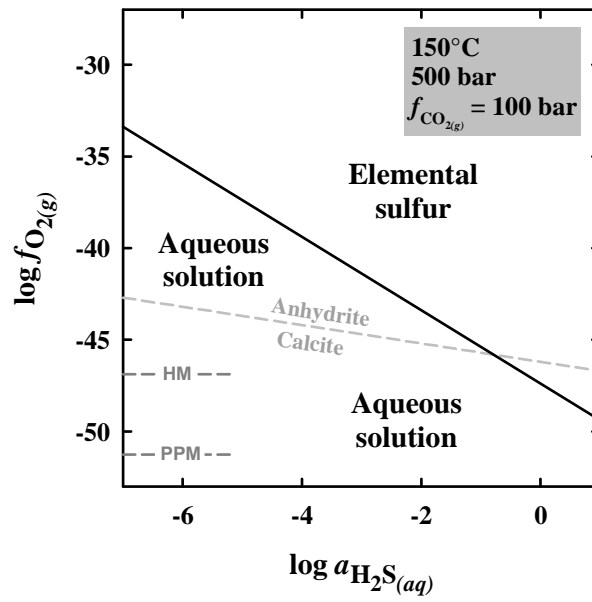
Figure 9

105

Figure 10
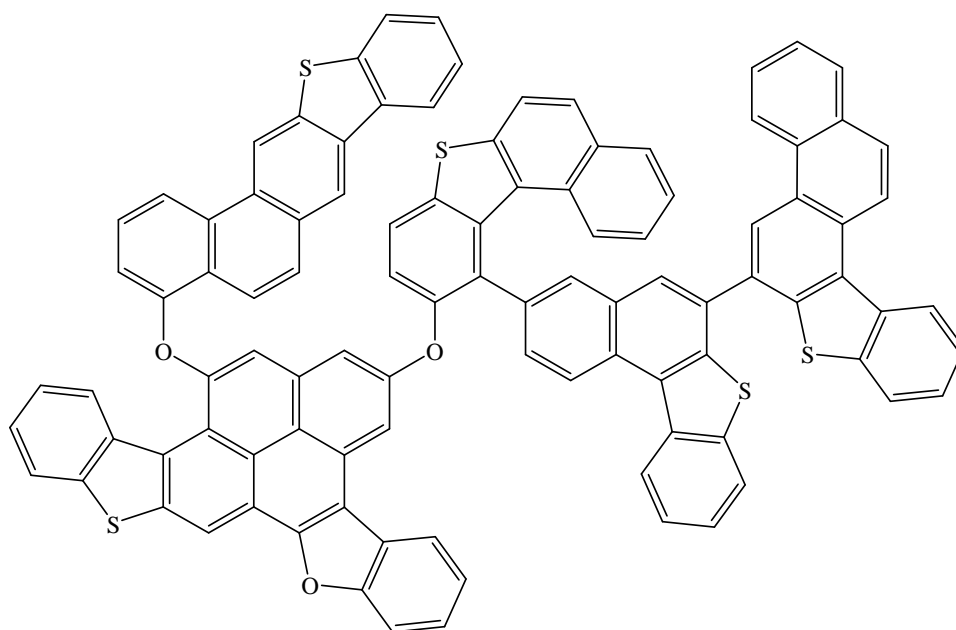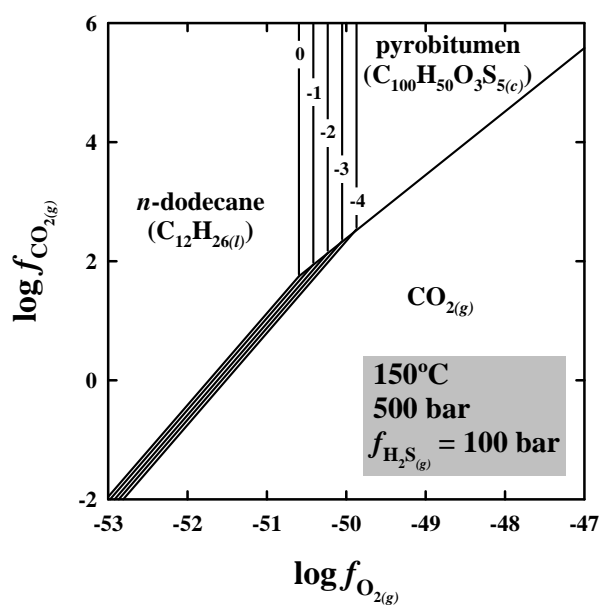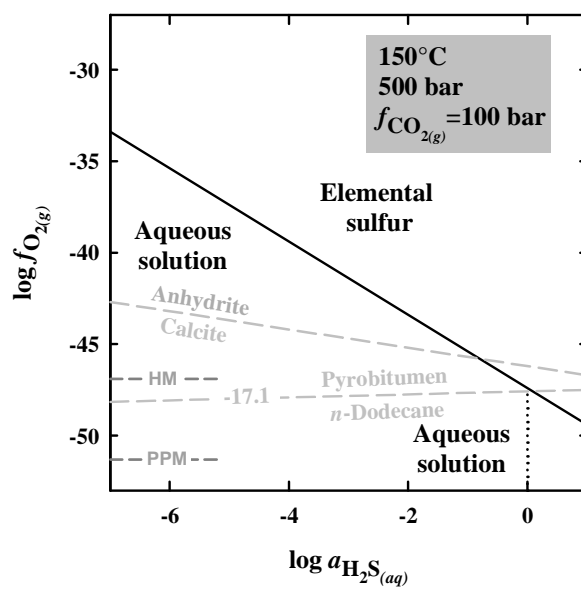
106

Figure 11

Figure 12

Figure 13

Figure 14

Figure 15

Table 1. Logarithms of the equilibrium constants at 150ºC and 500 bar of reactions used to construct the activity and fugacity diagrams discussed in the text, which involve minerals, hydrocarbons, organic sulfur compounds, water, and aqueous and gaseous organic and inorganic species.

Reactions	log K	Figures
$C_{12}H_{26(l)}$ + 9.25 $CaSO_{4(c)}$ = 9.25 $CaCO_{3(c)}$ + 9.25 $H_2S_{(g)}$ + 2.75 $CO_{2(g)}$ + 3.75 $H_2O_{(l)}$ (*n*-dodecane) (anhydrite) (calcite)	100.564	3,4
$CO_{2(g)}$ + $H_2S_{(g)}$ + $H_2O_{(l)}$ = $CH_3SH_{(g)}$ + 1.5 $O_{2(g)}$ (methanethiol)	-79.656	8
$CaCO_{3(c)}$ + $H_2S_{(aq)}$ + 2 $O_{2(g)}$ = $CaSO_{4(c)}$ + $CO_{2(g)}$ + $H_2O_{(l)}$ (calcite) (anhydrite)	94.395	11,12
$CaSO_{4(c)}$ + 2 H^+ = $S_{(c\ or\ l)}$ + Ca^{2+} + $H_2O_{(l)}$ + 1.5 $O_{2(g)}$ (anhydrite) (sulfur)	-61.595	11
$CaCO_{3(c)}$ + $H_2S_{(aq)}$ + 2 H^+ + 0.5 $O_{2(g)}$ = $S_{(c\ or\ l)}$ + Ca^{2+} + $CO_{2(g)}$ + 2 $H_2O_{(l)}$ (calcite) (sulfur)	32.800	11
$CaCO_{3(c)}$ + 4 $S_{(c\ or\ l)}$ + 3 $H_2O_{(l)}$ = $CaSO_{4(c)}$ + $CO_{2(g)}$ + 3 $H_2S_{(aq)}$ (calcite) (sulfur) (anhydrite)	-0.391	11
3 $FeS_{2(c)}$ + $Fe_3O_{4(c)}$ = 6 $FeS_{(c)}$ + 2 $O_{2(g)}$ (pyrite) (magnetite) (pyrrhotite)	-102.505	11,12
3 $Fe_2O_{3(c)}$ = 2 $Fe_3O_{4(c)}$ + 0.5 $O_{2(g)}$ (hematite) (magnetite)	-23.435	11,12
$S_{(c\ or\ l)}$ + $H_2O_{(l)}$ = $H_2S_{(aq)}$ + 0.5 $O_{2(g)}$ (sulfur)	-23.696	12
$C_{12}H_{26(l)}$ + 18.5 $O_{2(g)}$ = 12 $CO_{2(g)}$ + 13 $H_2O_{(l)}$ (*n*-dodecane)	957.015	14
$C_{100}H_{50}O_3S_{5(c)}$ + 108.5 $O_{2(g)}$ = 100 $CO_{2(g)}$ + 5 $H_2S_{(g)}$ + 20 $H_2O_{(l)}$ (pyrobitumen)	5677.181	14
0.3 $C_{100}H_{50}O_3S_{5(c)}$ + 26.5 $H_2O_{(l)}$ = 2.5 $C_{12}H_{26(l)}$ + 1.5 $H_2S_{(g)}$ + 13.7 $O_{2(g)}$ (pyrobitumen) (*n*-dodecane)	-689.384	14
3.7 $C_{100}H_{50}O_3S_{5(c)}$ + 208.1 $H_2O_{(l)}$ = 21.7 $C_{12}H_{26(l)}$ + 18.5 $H_2S_{(g)}$ + 109.6 $CO_{2(g)}$ (pyrobitumen) (*n*-dodecane)	238.336	14
0.3 $C_{100}H_{50}O_3S_{5(c)}$ + 26.5 $H_2O_{(l)}$ = 2.5 $C_{12}H_{26(l)}$ + 1.5 $H_2S_{(aq)}$ + 13.7 $O_{2(g)}$ (pyrobitumen) (*n*-dodecane)	-692.092	15

Table 2. Logarithms of the equilibrium constants at 150ºC and 500 bar of reactions representing metastable equilibrium among organic sulfur compounds, CO_2 and H_2S gases, and liquid H_2O.

Compound	Reaction	$\log K_{150°C,\ 500\ bar}$
Carbon disulfide	$CS_{2(l)} + 2\ H_2O_{(l)} = CO_{2(g)} + 2\ H_2S_{(g)}$	11.896
Methanethiol	$CH_3SH_{(l)} + 1.5\ O_{2(g)} = CO_{2(g)} + H_2S_{(g)} + H_2O_{(l)}$	81.441
Ethanethiol	$C_2H_5SH_{(l)} + 3\ O_{2(g)} = 2\ CO_{2(g)} + H_2S_{(g)} + 2\ H_2O_{(l)}$	158.677
1-Propanethiol	$C_3H_7SH_{(l)} + 4.5\ O_{2(g)} = 3\ CO_{2(g)} + H_2S_{(g)} + 3\ H_2O_{(l)}$	236.507
2-Propanethiol	$C_3H_7SH_{(l)} + 4.5\ O_{2(g)} = 3\ CO_{2(g)} + H_2S_{(g)} + 3\ H_2O_{(l)}$	236.259
2-Thiabutane	$C_3H_7SH_{(l)} + 4.5\ O_{2(g)} = 3\ CO_{2(g)} + H_2S_{(g)} + 3\ H_2O_{(l)}$	314.336
1-Butanethiol	$C_4H_9SH_{(l)} + 6\ O_{2(g)} = 4\ CO_{2(g)} + H_2S_{(g)} + 4\ H_2O_{(l)}$	314.365
2-Butanethiol	$C_4H_9SH_{(l)} + 6\ O_{2(g)} = 4\ CO_{2(g)} + H_2S_{(g)} + 4\ H_2O_{(l)}$	237.819
Thiacyclopentane	$C_4H_8S_{(l)} + 5.5\ O_{2(g)} = 4\ CO_{2(g)} + H_2S_{(g)} + 3\ H_2O_{(l)}$	290.931
2-Methylthiacyclopentane	$C_5H_{10}S_{(l)} + 7\ O_{2(g)} = 5\ CO_{2(g)} + H_2S_{(g)} + 4\ H_2O_{(l)}$	367.597
3-Methylthiacyclopentane	$C_5H_{10}S_{(l)} + 7\ O_{2(g)} = 5\ CO_{2(g)} + H_2S_{(g)} + 4\ H_2O_{(l)}$	368.206
Thiacyclohexane	$C_5H_{10}S_{(l)} + 7\ O_{2(g)} = 5\ CO_{2(g)} + H_2S_{(g)} + 4\ H_2O_{(l)}$	368.904
Thiophene	$C_4H_4S_{(l)} + 4.5\ O_{2(g)} = 4\ CO_{2(g)} + H_2S_{(g)} + H_2O_{(l)}$	243.730
2-Methylthiophene	$C_5H_6S_{(l)} + 6\ O_{2(g)} = 5\ CO_{2(g)} + H_2S_{(g)} + 2\ H_2O_{(l)}$	320.221
3-Methylthiophene	$C_5H_6S_{(l)} + 6\ O_{2(g)} = 5\ CO_{2(g)} + H_2S_{(g)} + 2\ H_2O_{(l)}$	320.034
2,5-Dimethylthiophene	$C_6H_8S_{(l)} + 7.5\ O_{2(g)} = 6\ CO_{2(g)} + H_2S_{(g)} + 3\ H_2O_{(l)}$	397.287
Benzothiophene	$C_8H_6S_{(l)} + 9\ O_{2(g)} = 8\ CO_{2(g)} + H_2S_{(g)} + 2\ H_2O_{(l)}$	476.021
2-Methylbenzothiophene	$C_9H_8S_{(l)} + 10.5\ O_{2(g)} = 9\ CO_{2(g)} + H_2S_{(g)} + 3\ H_2O_{(l)}$	552.513
Dibenzothiophene	$C_{12}H_8S_{(l)} + 13.5\ O_{2(g)} = 12\ CO_{2(g)} + H_2S_{(g)} + 3\ H_2O_{(l)}$	707.013
4,6-Dimethyldibenzothiophene	$C_{14}H_{12}S_{(l)} + 16.5\ O_{2(g)} = 14\ CO_{2(g)} + H_2S_{(g)} + 5\ H_2O_{(l)}$	858.794

PART II – EXPERIMENTAL STUDIES OF ORGANIC/INORGANIC INTERACTIONS INVOLVING SULFUR UNDER SEDIMENTARY BASIN CONDITIONS

We report in this second part of the manuscript the results of experimental studies which have been undertaken with the aim of unraveling the nature of the organic/inorganic reactions which govern the distribution of sulfur among petroleum, aqueous sulfur species and sour gas under the conditions of hydrocarbon reservoirs. We will emphasize the utility of carrying out exploratory thermodynamic calculations to (1) predict if a particular reaction may or may not occur under fixed conditions of temperature and pressure, and (2) to guide experiments examining the extent to which metastable equilibrium states among hydrocarbons, organic sulfur compounds (OSC), hydrogen sulfide and elemental sulfur may be established under the conditions of sedimentary basins. Two kinds of experiments have been carried out in the present study. A first set of experiments evaluates the possibility of desulfurization reactions under H_2S pressure in the context of enhanced oil recovery (EOR) through acid gas injection in hydrocarbon reservoirs. Experiments on thermochemical sulfate reduction (TSR) have been carried out in a second series of experiments, which take advantage of the new technique of fused silica capillaries. Before presenting these experiments in detail, a summary is first given of the experimental work accomplished prior to our own study.

1. REVIEW OF PREVIOUS WORK

1.1. Reactions among hydrocarbons and either elemental sulfur or hydrogen sulfide

The first experimental investigations on reactions among hydrocarbons and sulfur date back to the beginning of the twentieth century. We selected for the summary given below both investigations which are merely of historical interest, and those investigations which are directly relevant to the problematics of sulfur petroleum geochemistry. For some of these investigations, a brief thermodynamic analysis is also presented. The molecular structures of the compounds discussed in this section are shown in Figure 2.1.

- Capelle (1908) reacted acetylene (i.e. ethyne, C_2H_2) with boiling sulfur and reported the formation of thienothiophene ($C_6H_4S_2$).
- Friedmann (1916) reacted n-octane (C_8H_{18}) with elemental sulfur at 270-280°C under an unspecified pressure for 24 hours and reported the formation of an alkylthiophene

($C_8H_{12}S$, 2.3% yield) together with a minor amount of a thienothiophene ($C_8H_8S_2$). Friedmann also reports the generation of *an extraordinarily high* [gas] *pressure* in his experiments, which he attributes partly to hydrogen sulfide (H_2S) and partly to other gases.

The experimental observations of Friedmann (1916) may be represented by a reaction written as

$$C_8H_{18(l)} + 4\ S_{(c\ or\ l)} = C_8H_{12}S_{(l)} + 3\ H_2S_{(g)} \tag{2.1}$$
$$\text{(\textit{n}-octane)} \qquad \text{(\textit{n}-butylthio-}$$
$$\text{phene)}$$
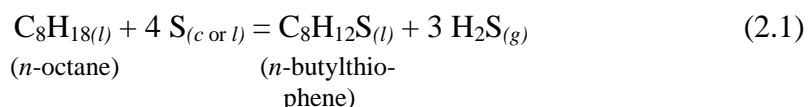
The logarithms of the equilibrium constants (log K) of Reaction (2.1) computed between 100 and 300ºC at pressures ranging from 100 to 500 bars are listed in Table 2.1. The thermodynamic properties and heat capacity coefficients used for the calculations are listed in Table 2.2. The calculated log K values have been used together with an expression of the law of mass action written as

$$\log K_{(2.1)} = \log \frac{a_{C_8H_{12}S_{(l)}}}{a_{C_8H_{18(l)}}} + 3 \log f_{H_2S_{(g)}} \tag{2.2}$$

to generate the temperature – log $f_{H_2S_{(g)}}$ diagram shown in Figure 2.2*a*. The equilibrium curves shown in this figure have been drawn for equal activities of the organic sulfur compound and the hydrocarbon. Consideration of the fugacity coefficients of pure H_2S at the temperatures of the experiments of Friedmann (1916) indicates that the equilibrium fugacities of $H_2S_{(g)}$ predicted from the calculations would correspond to pressures which would be close to physically attainable values in sedimentary basins.

- Baker and Reid (1929) heated *n*-butane (C_4H_{10}) and *n*-heptane (C_7H_{16}) at 300-350°C in the presence of elemental sulfur and observed the formation of thiophene (C_4H_4S) and of a substituted alkylthiophene ($C_7H_{10}S$), respectively. Mercaptans and sulfides were not detected. The yields of the reactions were found to be small. However, they report the formation of a considerable amount of hydrogen sulfide in the reaction involving *n*-butane at 335°C.

- Although at temperatures too high (300-600°C) to be of geological interest, Rasmussen et al. (1946) also report the industrial formation of thiophene (C_4H_4S) when reacting butane with liquid or gas elemental sulfur.

HC≡CH
Ethyne
(C$_2$H$_2$)

Thienothiophene
(C$_6$H$_4$S$_2$)

n-Butylthiophene
(C$_8$H$_{12}$S)

2-Ethylthienothiophene
(C$_8$H$_8$S$_2$)

Benzylthiol
(C$_7$H$_8$S)

2-Methyl-5-n-tridecylthiophene
(C$_{18}$H$_{32}$S)

2-Phenylbenzo[b]thiophene
(C$_{14}$H$_{10}$S)

2-(Diphenylmethyl)-benzo[b]thiophene
(C$_{21}$H$_{16}$S)

Dibenzyl disulfide
(C$_{14}$H$_{14}$S$_2$)

S-benzyl monothiobenzoic acid ester
(C$_{14}$H$_{12}$SO)

Tetraphenylthiophene
(C$_{28}$H$_{20}$S)

E-Stilbene (C$_{14}$H$_{12}$)

Z-Stilbene (C$_{14}$H$_{12}$)

Dibenzyl (C$_{14}$H$_{14}$)

n-Octane (C$_8$H$_{18}$)

1-Octene (C$_8$H$_{16}$)

2-Octanone (C$_8$H$_{16}$O)

1-Octanol (C$_8$H$_{18}$O)

n-Octylbenzene (C$_{14}$H$_{22}$)

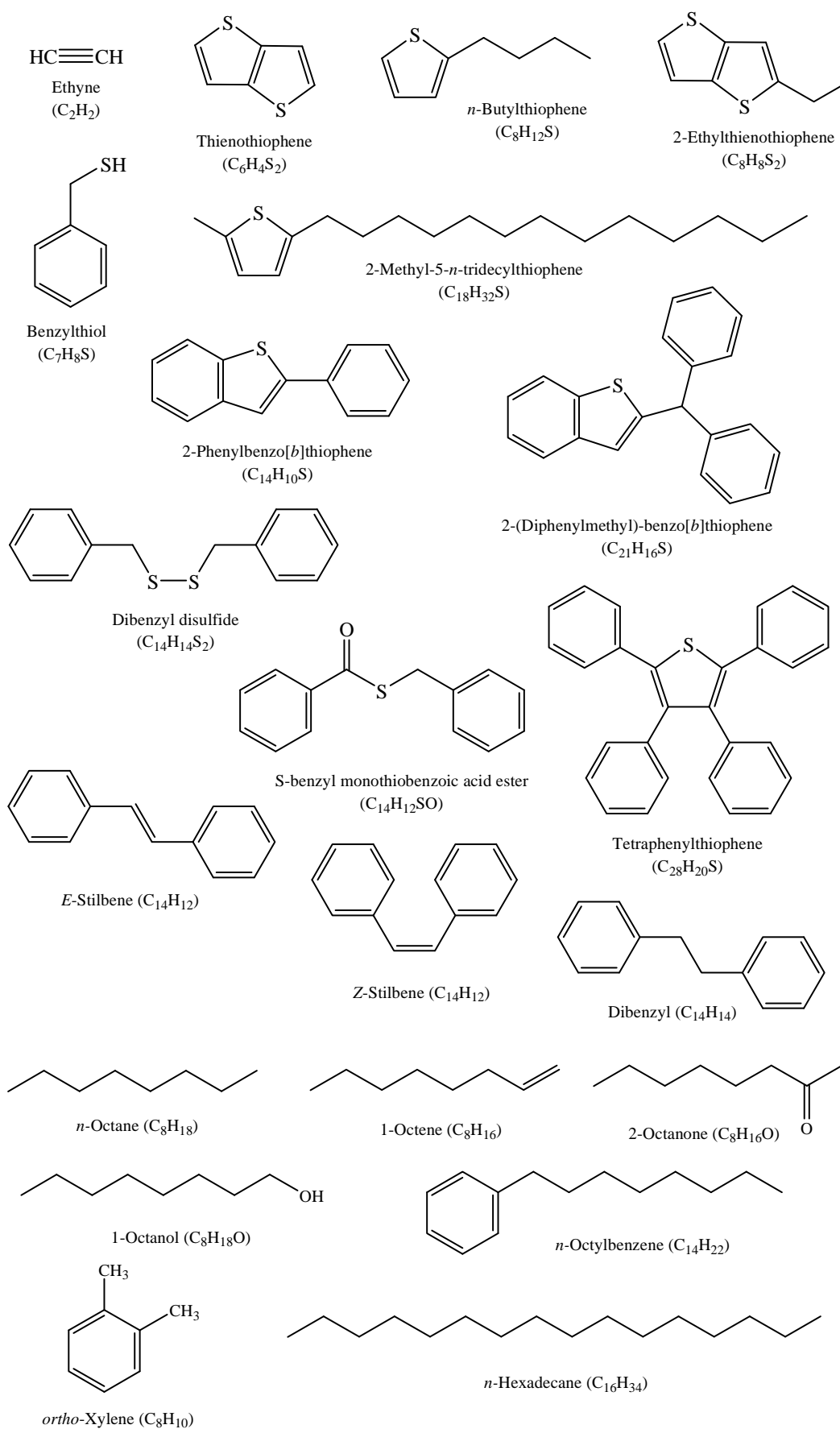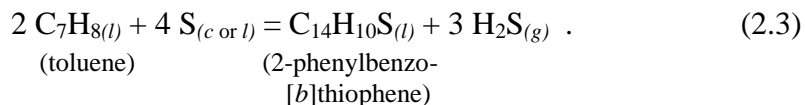ortho-Xylene (C$_8$H$_{10}$)

n-Hexadecane (C$_{16}$H$_{34}$)

Figure 2.1. Molecular structures of the compounds discussed in Section 1.

- Horton (1949) showed that the reaction between toluene (C_7H_8) and elemental sulfur was producing 2-phenylbenzo[b]thiophene ($C_{14}H_{10}S$) in accord with a reaction written as

$$2\ C_7H_{8(l)} + 4\ S_{(c\ or\ l)} = C_{14}H_{10}S_{(l)} + 3\ H_2S_{(g)}\ . \qquad (2.3)$$
$$\text{(toluene)} \qquad \text{(2-phenylbenzo-}[b]\text{thiophene)}$$

The logarithms of the equilibrium constant of Reaction (2.3) computed as a function of temperature and pressure using the thermodynamic properties and heat capacity coefficients listed in Table 2.2 are given in Table 2.1. Estimates for the thermodynamic properties and heat capacity coefficients for liquid 2-phenylbenzo[b]thiophene were generated in the present study from the properties and coefficients given by Richard and Helgeson (1998) and Richard (2001) for benzo[b]thiophene (C_8H_6S), thiophene (C_4H_4S), 2-methylthiophene (C_5H_6S), a –CH_3 methyl group and biphenyl ($C_{12}H_{10}$) in accord with

$$\Xi_{C_{14}H_{10}S_{(l)}} = \Xi_{C_8H_6S_{(l)}} - \Xi_{C_4H_4S_{(l)}} + \Xi_{C_5H_6S_{(l)}} - \Xi_{-CH_{3(l)}} + 0.5\ \Xi_{C_{12}H_{10(l)}}\ . \qquad (2.4)$$

The log K values listed in Table 2.1 have been used together with an expression of the law of mass action written as

$$\log K_{(2.3)} = \log \frac{a_{C_{14}H_{10}S_{(l)}}}{a^2_{C_7H_{8(l)}}} + 3 \log f_{H_2S_{(g)}} \qquad (2.5)$$

to generate the temperature – log $f_{H_2S_{(g)}}$ diagram shown in Figure 2.2b. Although it can be seen in this figure that the equilibrium curves[1] plot at higher fugacities of H_2S gas than those for the equilibrium involving n-octane and n-butylthiophene, these H_2S fugacities are still physically attainable for temperatures up to 150-175ºC. For example, the equilibrium fugacity of H_2S at 150ºC for a total pressure of 500 bar would be approximately 300 bar. Note that at the temperatures above 200ºC at which Horton (1949) conducted his experiments, the formation of 2-phenylbenzo[b]thiophene from toluene also appears to be favored from our calculations.

- Bestougeff and Combaz (1973) have studied reactions between various natural organic substances ("fresh" organic matter such as algae, ooze or coorongite, as well as kerogens and petroleums) and both elemental sulfur and, more importantly, hydrogen sulfide. The reactions were carried out in steel autoclaves. The partial pressure of H_2S was varied between 18 and 75 atmospheres. The temperatures of the experiments were

---

[1] These equilibrium curves have again been drawn for equal activities of toluene and 2-phenylbenzo[b]thiophene, but this time by specifying arbitrary values of 0.5 for these activities due to the stoichiometric constraint imposed by Reaction (2.3). Alternative values for the activities of both compounds result in higher or lower fugacities of H_2S depending on which of the two compounds predominates in the reaction mixture.

25°C and 80-90°C for the biomolecules, and 80-90°C for the kerogens and petroleums. Bestougeff and Combaz have noted an increase in the content of organic sulfur in all experiments and, in several instances, the formation of elemental sulfur.

- Valitov and Valitov (1975) have studied the reactions of mixtures of light alkanes with elemental sulfur in the 50-200°C temperature range. They observed a sulfurization of the alkane mixtures (i.e. formation of organic sulfur compounds) at 50-100°C and the generation of H_2S at higher temperatures (175-200°C).

- Przewocki et al. (1984) have studied the reaction between toluene (C_7H_8) and elemental sulfur at 200°C. After 120 hours, they reported the formation of various phenyl and benzyl derivatives, several of which containing sulfur. Among the organic sulfur compounds being formed, benzylthiol (C_7H_8S), 2-phenylbenzo[*b*]thiophene ($C_{14}H_{10}S$), S-benzyl monothiobenzoic acid ester ($C_{14}H_{12}SO$), dibenzyl disulfide ($C_{14}H_{14}S_2$), 2-(diphenylmethyl)-benzo[*b*]thiophene ($C_{21}H_{16}S$), and tetraphenylthiophene ($C_{28}H_{20}S$) were identified. At much shorter reaction times, the formation of dibenzyl ($C_{14}H_{14}$) and *E*-stilbene ($C_{14}H_{12}$) was observed by Przewocky et al. (1984), *E*-stilbene being formed first. These authors subsequently studied the reaction between dibenzyl and elemental sulfur, which produced toluene, *E*- and *Z*-stilbenes, and other compounds. The reaction between *Z*-stilbene and sulfur produced dibenzyl. Przewocky et al. (1984) were thereby able to demonstrate that these reactions were reversible. Another important observation made by Przewocky et al. is that when H_2S was evacuated from the reactor, the reaction between *Z*-stilbene and elemental sulfur did not yield dibenzyl, which indicated that H_2S had to be involved in these reversible reactions.

- Schmid (1986) and Schmid et al. (1986) have reported the formation of a mixture of C_{18} 2,5-dialkylthiophenes ($C_{18}H_{32}S$) by reacting *n*-octadecane ($C_{18}H_{38}$) with elemental sulfur at 200-250°C during ~ 3 days. Schmid (1986) further reports the detection of H_2S being formed as a reaction product. Considering 2-methyl-5-*n*-tridecylthiophene as an example of the alkylthiophenes being formed, log K values have been calculated as a function of temperature and pressure for the reaction

$$C_{18}H_{38(l)} + 4\ S_{(c\ or\ l)} = C_{18}H_{32}S_{(l)} + 3\ H_2S_{(g)} \qquad (2.6)$$

$$\underset{(\textit{n}\text{-octadecane})}{} \qquad \underset{\substack{(\text{2-methyl-5-}\textit{n}\text{-} \\ \text{tridecylthiophene})}}{}$$
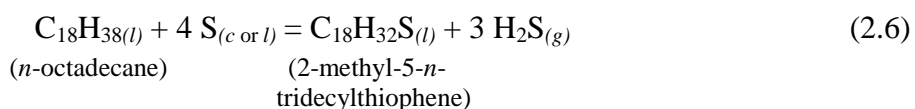
using the thermodynamic properties and heat capacity coefficients listed in Table 2.2.

Table 2.1. Logarithms of the equilibrium constants of reactions discussed in the text.

| Reaction	P (bar)	100°C	150°C	200°C	250°C	300°C
$C_8H_{18(l)} + 4\ S_{(c\ or\ l)} = C_8H_{12}S_{(l)} + 3\ H_2S_{(g)}$	100	1.478	3.921	5.773	7.221	8.377
	300	1.659	4.081	5.915	7.349	8.495
	500	1.840	4.240	6.058	7.478	8.612
$2\ C_7H_{8(l)} + 4\ S_{(c\ or\ l)} = C_{14}H_{10}S_{(l)} + 3\ H_2S_{(g)}$	100	5.329	7.495	9.217	10.617	11.777
	300	5.475	7.624	9.332	10.721	11.872
	500	5.620	7.752	9.446	10.825	11.967
$C_{18}H_{38(l)} + 4\ S_{(c\ or\ l)} = C_{18}H_{32}S_{(l)} + 3\ H_2S_{(g)}$	100	2.385	4.663	6.377	7.708	8.764
	300	2.554	4.812	6.510	7.829	8.874
	500	2.722	4.960	6.643	7.949	8.984
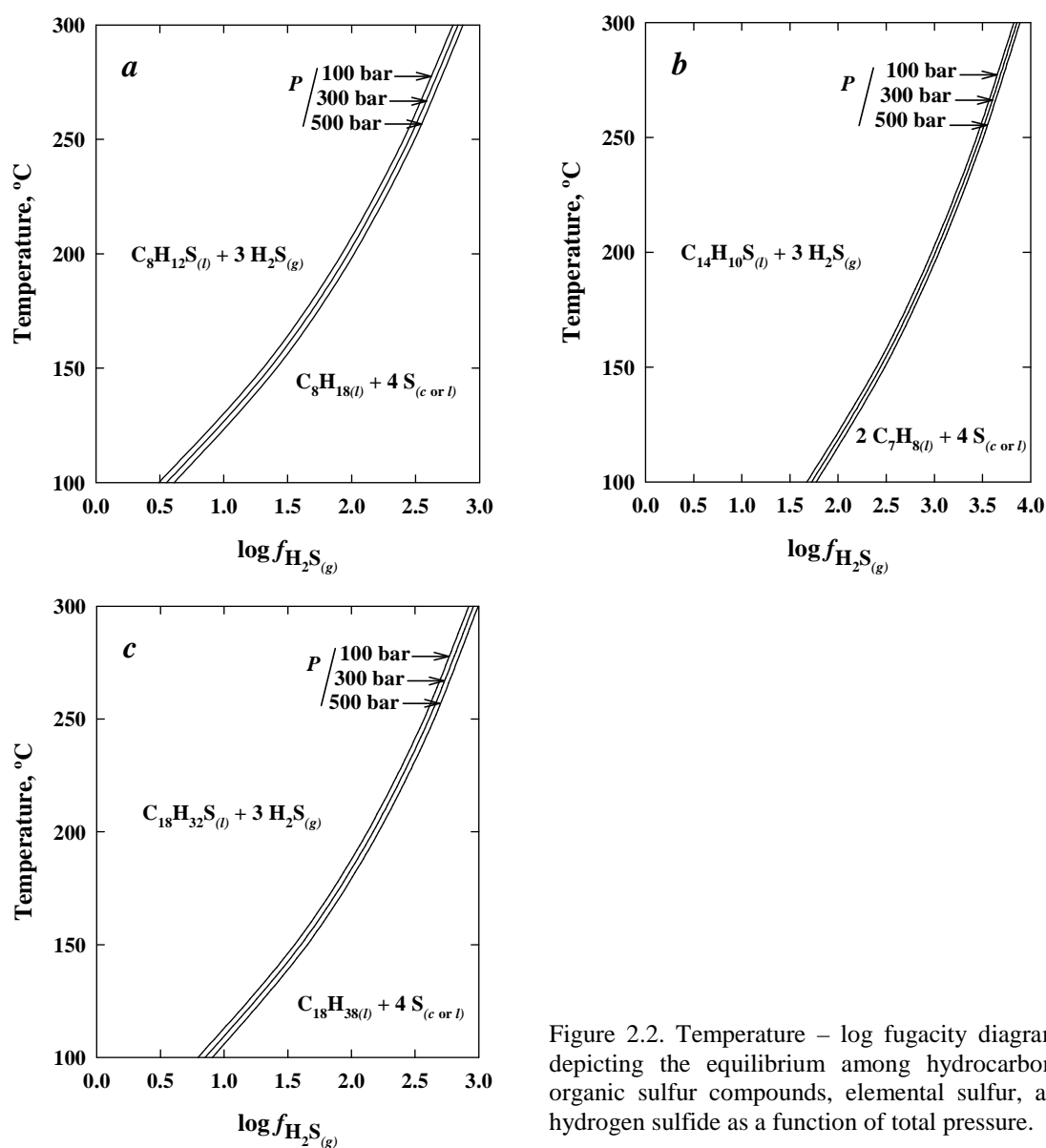
Figure 2.2. Temperature – log fugacity diagrams depicting the equilibrium among hydrocarbons, organic sulfur compounds, elemental sulfur, and hydrogen sulfide as a function of total pressure.

Table 2.2. Standard molal thermodynamic properties and heat capacity power function coefficients of liquid hydrocarbons and organic sulfur compounds, H_2S gas, and elemental sulfur used to calculate the log K values listed in Table 2.1.

Species	Formula	ΔG_f° [a]	ΔH_f° [a]	S° [b]	V° [c]	C_P° [b]	a [b]	b [d] x10³	c [e] x10⁻⁵
n-Octane [f]	C_8H_{18}	7.16	-249.6	380.87	158.7	254.59	22.05	664.4	30.623
n-Octadecane [f]	$C_{18}H_{38}$	60.05	-506.9	684.67	325.4	565.05	157.99	1125.5	63.551
Toluene [g]	C_7H_8	113.95	12.0	220.96	106.4	157.29	36.19	364.8	10.962
2-n-Butylthiophene [h]	$C_8H_{12}S$	131.25	-31.0	317.86	156.2	235.00	84.81	448.1	14.749
2-Methyl-5-n-tridecyl-thiophene [h]	$C_{18}H_{32}S$	177.07	-297.2	635.55	327.2	534.22	200.83	925.9	50.969
2-Phenylbenzo[b]-thiophene [i]	$C_{14}H_{10}S$	324.65	185.2	298.11	176.3	295.58	186.56	396.2	-8.096
Hydrogen sulfide [j]	H_2S	-33.44	-20.6	205.79	0	34.21	32.68	12.4	-1.925
Sulfur [k]	S	0	0	32.05	15.5	22.70	15.48	24.2	0
							13.90	29.4	0
							-238.1	469.6	132.10
							8.57	20.3	48.67

[a] kJ mol⁻¹ [b] J mol⁻¹K⁻¹ [c] cm³mol⁻¹ [d] J mol⁻¹K⁻² [e] J K mol⁻¹ [f] Helgeson et al. (1998) [g] Richard and Helgeson (1998) [h] Richard (2001) [i] Estimated from Eqn. (4) [j] Helgeson et al. (1978) [k] Properties and coefficients compiled or retrieved in the present study (see part 1)

using the thermodynamic properties and heat capacity coefficients listed in Table 2.2. The obtained log K values have been listed in Table 2.1 and used together with an expression of the law of mass action written as

$$\log K_{(2.6)} = \log \frac{a_{C_{18}H_{32}S_{(l)}}}{a_{C_{18}H_{38(l)}}} + 3 \log f_{H_2S_{(g)}} \qquad (2.7)$$

to generate the temperature – log $f_{H_2S_{(g)}}$ diagram shown in Figure 2.2c. It can be deduced from this diagram that the equilibrium curves again correspond to physically attainable H_2S fugacities, suggesting that equilibrium states may establish among hydrocarbons, organic sulfur compounds, elemental sulfur and hydrogen sulfide under the conditions of sedimentary basins. The consequences of this observation are discussed in detail below and verified experimentally in Section 2.
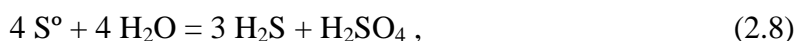
1.2. Thermochemical sulfate reduction

A number of experimental studies have been conducted on thermochemical sulfate reduction (TSR), the process by which organic compounds react with solid or dissolved sulfate species at high temperature to generate hydrogen sulfide. A summary of these studies is given below.

- Although not specifically related to TSR, one of the first studies on the reactions of organic compounds with sulfates is the classical work of Toland (1960) who demonstrated that hydrocarbons were easily oxidized to carboxylic acids by

ammonium or other sulfate solutions at 315 - 350ºC in the presence of small amounts of sulfur compounds with lower valence states (e.g. H_2S or elemental sulfur) to trigger the reactions.

- Kiyosu (1980) reacted 0.2 M solutions of H_2SO_4, $NaHSO_4$ and Na_2SO_4 with dextrose ($C_6H_{12}O_6$) between 250ºC and 340°C. He observed the reduction of sulfuric acid to H_2S above 250°C, and the reduction of sodium bisulfate and sodium sulfate above 300°C. Kiyosu concluded that the rate of sulfate reduction was dependent upon temperature, pH, and the species of sulfate.

- Nikolayeva et al. (1982) have studied the reduction of 0.1 M and 0.01 M Na_2SO_4 solutions by toluene, phenol, *n*-hexane, cyclohexane, cyclohexanol, and graphite at temperatures between 200ºC and 300ºC. The duration of the experiments varied between 10 days and 4 months. The results of the experiments indicated a limited production of H_2S when using graphite as a reductant, while higher degrees of reduction were attained with the hydrocarbons and particularly with cyclohexanol, although the reason for that is far from being obvious since the average oxidation state of carbon in cyclohexanol is higher than in both *n*-hexane and cyclohexane.

- Trudinger et al. (1985) reacted ^{35}S-labelled sulfate with a variety of organic substances (naphthenic-aromatic, paraffinic and light crude oils, coal, cyanobacterial organic matter, and glucose) at 80-190ºC for periods of 10 days to 5 months. They suggested that the [35]H_2S being formed under their experimental conditions was the result of an isotope exchange reaction among elemental sulfur, the ^{35}S-labelled sulfate, and hydrogen sulfide:

$$4 \, S^o + 4 \, H_2O = 3 \, H_2S + H_2SO_4 \,, \tag{2.8}$$

the elemental sulfur being used as an initiator, rather then the result of thermochemical sulfate reduction. Trudinger et al. also observed that glucose (and to a lesser extent crude oil) were preventing Reaction (2.8) to occur, which they attributed to the pH of the reaction mixture which was unfavorable for elemental sulfur to be present. However, the conclusion drawn by Trudinger et al. (1985) from their experiments that low pH and high sulfur concentrations were required for abiological sulfate reduction at moderate (i.e. < 200ºC) temperatures appears to be erroneous in light of our thermodynamic analysis of both the stability and importance of elemental sulfur in the overall TSR process.
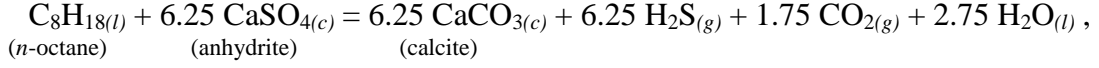
- Cross et al. (2004) carried out experimental simulations of TSR by reacting sulfate solutions (0.04 M Na_2SO_4) with acetic acid at 280-350°C under pressures of 250 to

500 bars and at *in situ* pH values between 5.2 and 6.8. The reactions were initiated by adding some elemental sulfur to the solutions, and the experiments were carried out in the presence of sodium acetate to buffer the pH of the solutions. Cross et al. (2004) presented a detailed kinetic analysis of their experiments and concluded that TSR was a fast process on geologic timescales, with half-lives of dissolved sulfate of ~ 1650 years at 150°C.
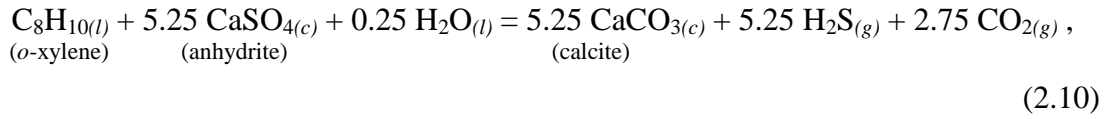
- Ding et al. (2007) reacted anhydrite ($CaSO_4$) with a natural gas mixture containing C_1-C_6 hydrocarbons and CO_2 in a stainless steel autoclave, the walls of which were protected by a quartz tube from the corrosive action of the H_2S being formed in the experiments. These experiments were carried out at temperatures as high as 490-600°C (i.e. much higher than those representative of sedimentary basin conditions) under relatively low pressures of 50-70 bar. The duration of the experiments was increasing with decreasing temperature from 66 hours at 600°C to 90 hours at 490°C. Among the reaction products observed were calcite ($CaCO_3$), CO_2, H_2S, H_2O and a solid carbon phase (pyrobitumen or graphite). The amount of CO_2 produced (3 – 5%) was exceeding that of H_2S (less than 0.2%) at all temperatures, which is contrary to the natural observations. Elemental sulfur was not observed among the reaction products. Although Ding et al. (2007) suggested that it may have formed as a reaction intermediate which subsequently reacted with the hydrocarbon gases, thermodynamic calculations such as those presented in the first part of the thesis would suggest that it may not have formed because there was insufficient H_2S in the system, or because the conditions were too reducing during the experiments. Evidence for reducing conditions is the presence of H_2 gas (0.4 – 2.5%) among the reaction products, which is not discussed by Ding et al. (2007).

- Zhang et al. (2007) carried out hydrous pyrolysis experiments to investigate the effect of the chemical composition of the organic reactants on TSR rates. In a first series of experiments, they reacted model compounds with different functional groups (*n*-octane, 1-octene, 2-octanone, 1-octanol, *o*-xylene, and *n*-octylbenzene) with $MgSO_4$ [2] at 350°C and 241 bar for 24 hours. Zhang et al. observed that the amount of H_2S generated by TSR was the highest for 1-octene and 1-octanol (which are not ubiquitously present in petroleum), 3 to 4 times less for *n*-octane (an ubiquitous species in natural crude oils), and very low for octanoic acid and the aromatics (*o*-

---

[2] Tang and coworkers found that using $MgSO_4$ as oxidant in experiments on TSR did not require to use hydrogen sulfide as an initiator (Goldschmidt Conference abstract, cited by Zhang et al., 2007).

xylene, and octylbenzene). These observations, which are in general agreement with a decrease in the saturated/aromatic ratio with increasing TSR in petroleum reservoirs, may also be explained in terms of different chemical affinities for reactions involving different individual organic reactants. In accord with the general TSR reaction established in Part 1 of the present manuscript, we can write for n-octane and o-xylene

$$C_8H_{18(l)} + 6.25\ CaSO_{4(c)} = 6.25\ CaCO_{3(c)} + 6.25\ H_2S_{(g)} + 1.75\ CO_{2(g)} + 2.75\ H_2O_{(l)}\ ,$$
(n-octane)   (anhydrite)   (calcite)

and   (2.9)

$$C_8H_{10(l)} + 5.25\ CaSO_{4(c)} + 0.25\ H_2O_{(l)} = 5.25\ CaCO_{3(c)} + 5.25\ H_2S_{(g)} + 2.75\ CO_{2(g)}\ ,$$
(o-xylene)   (anhydrite)   (calcite)

(2.10)

for which the logarithmic values of the equilibrium constants are

$$\log K_{(2.9)} = 69.327 \tag{2.11}$$

and

$$\log K_{(2.10)} = 61.844\ . \tag{2.12}$$

These equilibrium constants have been used together with appropriate expressions of the law of mass action and the relation

$$A_r = 2.303 \log\left(K_{(r)}/Q_{(r)}\right) \tag{2.13}$$

to generate the chemical affinity diagrams shown in Figure 2.3. It can be deduced from these diagrams that the chemical affinity of the TSR reaction for n-octane is indeed greater than that for o-xylene for all values of H_2S and CO_2 fugacities ($f_{H_2S_{(g)}}$), which agrees both with the experiments of Zhang et al. (2007) and the decrease of the ratio between saturated and aromatic hydrocarbons with increasing thermochemical sulfate reduction.

In a second set of experiments, a paraffin mixture and three crude oils with different organic sulfur (S_{org}) contents were reacted non-isothermally (~350ºC to ~550ºC at 241 bar with a heating rate of 2ºC per hour) with $MgSO_4$ in the presence of water. Zhang et al. (2007) observed a clear effect of the bulk compositions of the oils on the temperature for the onset of TSR (for their experimental conditions). They tentatively attributed this effect to the presence of labile organic sulfur (thiols and sulfides) in the asphaltene and resin fractions of the crude oils, but could not demonstrate it unambiguously.
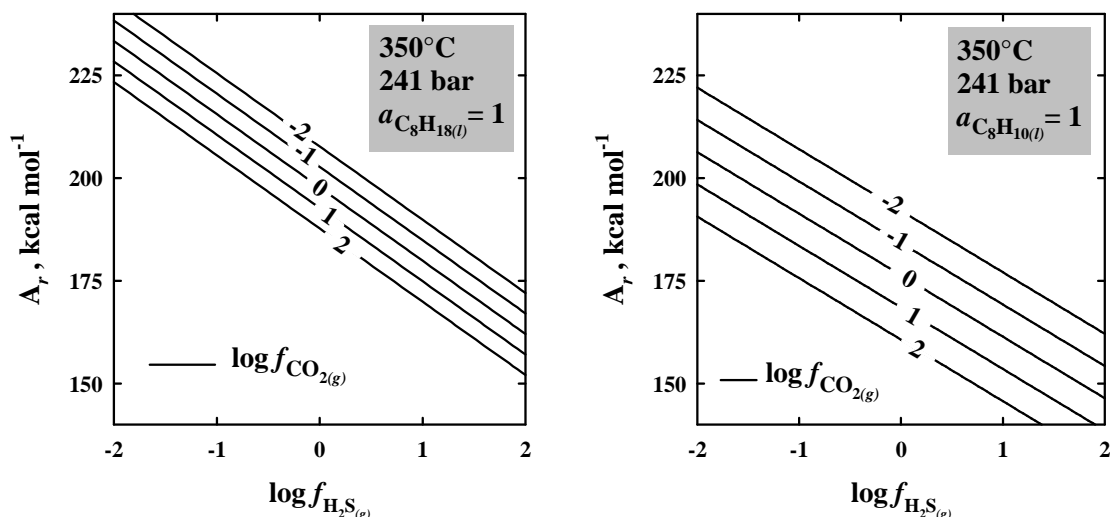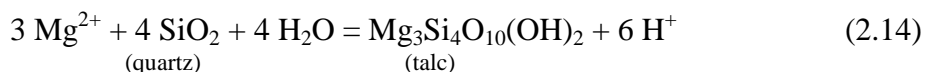
Figure 2.3. Chemical affinity of Reactions (2.9) and (2.10) as a function of log $f_{H_2S_{(g)}}$ for different values of log $f_{CO_{2(g)}}$ corresponding to the numbers on the solid and dashed contours. These contours have been drawn for unit activities of the pure hydrocarbon model reactants.
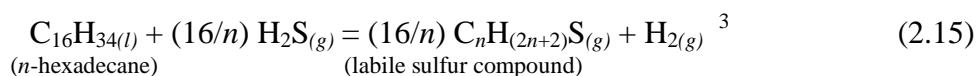
- Zhang et al. (2008) have carried out further hydrous pyrolysis experiments to determine the mechanism by which H_2S was initiating TSR. They first reacted a mixture of C_{21}-C_{35} n-alkanes (paraffin wax) with bassanite ($CaSO_4 \cdot H_2O$) in the presence of aqueous solutions and under variable H_2S partial pressures at 330ºC and 241 bar for 24 hours. The pH of the aqueous solutions was varied between 3 and 5 and controlled both by a talc-quartz buffer (Seewald et al., 2000) in accord with

$$\underset{\text{(quartz)}}{3\,Mg^{2+} + 4\,SiO_2} + 4\,H_2O = \underset{\text{(talc)}}{Mg_3Si_4O_{10}(OH)_2} + 6\,H^+ \qquad (2.14)$$

Varying the concentration of magnesium in solution yielded *in situ* pH values of 3.0-3.5 (note that these values were not measured but recalculated using a geochemical software). Zhang et al. (2008) also buffered pH at a higher value (5.0) using dolomite, but it is not clear how they controlled the fugacity of CO_2 gas (and by inference the concentration of aqueous carbonate species) in their experiments. Zhang et al. (2008) have observed a correlation between the rate of TSR and the amount of H_2S initially present in the system at acidic pH values (3.0-3.5). In contrast, no TSR was observed at pH 5.0, which led Zhang et al. to propose that low pH conditions may play an important role in the reduction of sulfate by hydrocarbons.

Zhang et al. (2008) subsequently attempted to evaluate the role of thiols and sulfides (designated by the authors as labile sulfur compounds) in lowering the onset temperature of TSR. They reacted pure n-hexadecane ($C_{16}H_{14}$) and the paraffin

mixture used in the previous experiments with H_2S at 300-370ºC and 241 bar and observed the formation of C_1-C_3 alkanethiols and dimethylsulfide. A reaction may be written for the reaction of *n*-hexadecane with H_2S as

$$C_{16}H_{34(l)} + (16/n) \; H_2S_{(g)} = (16/n) \; C_nH_{(2n+2)}S_{(g)} + H_{2(g)} \quad {}^3 \qquad (2.15)$$
$$\text{(\textit{n}-hexadecane)} \qquad\qquad \text{(labile sulfur compound)}$$

The amounts of organic sulfur compounds formed were proportional to the amount of H_2S initially loaded in the system. This formation of labile sulfur compounds led Zhang et al. (2008) to propose that these compounds, which appear to be more reactive than inorganic sulfur species (i.e. elemental sulfur or H_2S), may constitute an explanation for the catalysis of TSR by H_2S.

▪ Kowalewski et al. (2008) carried out pyrolysis experiments with various reactants at 320ºC and 105 bar (i.e. P_{sat}) in order to evaluate the possibility that H_2S and organic sulfur compounds might form as a result of artificially induced TSR in sulfate-rich shallow reservoirs during thermally induced enhanced oil recovery operations. The duration of the experiments was between 3 to 30 days. In one series of experiments (similar to those carried out earlier by Schmid et al., 1987), *n*-alkanes with carbon numbers ranging between 8 and 14 were reacted with elemental sulfur in the presence of water. This led to the formation of alkylthiophenes, alkylbenzenes, C_{10}-C_{13} benzothiophenes, and C_{12}-C_{14} dibenzothiophenes, as well as of gas H_2S, C_1-C_4 *n*-alkanes, and minor CO_2 and H_2. In as second series of experiments simulating artificially induced TSR, solid $MgSO_4$ was reacted with the C_8-C_{14} *n*-alkanes in the presence of water and elemental sulfur used as an initiator of the TSR reaction. This resulted in the production of C_{10}-C_{12} benzothiophenes and C_{12}-C_{14} dibenzothiophenes, as well as of abundant H_2S, CO_2, CH_4, but lesser amounts of C_2-C_4 *n*-alkane and H_2 gases. The higher amount of CO_2 generated compared to the first series of experiments may be due to more oxidizing conditions resulting from the presence of sulfate. No alkylthiophenes or alkylbenzenes were observed in this second series of experiments.

2. EXPERIMENTS ON DESULFURIZATION UNDER H_2S PRESSURE

All the experiments reviewed in Section 1.1, which involve hydrocarbons and elemental sulfur as reactants to produce organic sulfur compounds and H_2S gas, correspond to a general reaction written as

---

[3] The production of H_2 gas was observed in the experiments of Zhang et al. (2008), but in higher molar proportions than that corresponding to the stoichiometry of Reaction (2.15). It is probable that H_2 was also generated in the experiments as a result of the thermal cracking of *n*-hexadecane.

$$n\ C_pH_{r(l)} +\ p + \left(\frac{r \times n - p \times m}{2} \right)\ S_{(c)} = p\ C_nH_mS_{(l)} + \left(\frac{r \times n - p \times m}{2} \right)\ H_2S_{(g)}\ . \qquad (2.16)$$

Reactions of this type have been shown by Richard et al. (2005) to control the partial pressure of H_2S in carbonate reservoirs. It is therefore possible that increasing the partial pressure of H_2S by reinjection of acid gas mixtures in reservoirs containing sulfur-rich crude oils may drive the reaction backwards, that is convert H_2S and the organic sulfur compounds to elemental sulfur and hydrocarbons.

In order to evaluate the possibility of desulfurization of sulfur-rich crude oils under the temperature, pressure, and redox conditions prevailing in the context of the injection of CO_2-H_2S acid gas mixtures in petroleum reservoirs, an experimental study has been undertaken in which organic sulfur compounds are reacted with hydrogen sulfide (H_2S) at 200°C and 500 bar, the reaction resulting in the production of elemental sulfur. We present below the materials, experimental techniques as well as the analytical methods which have been used both for the experiments and the determination of the reaction products.

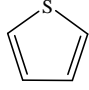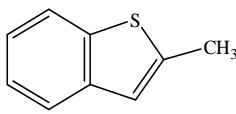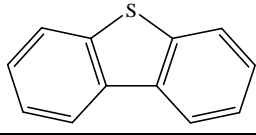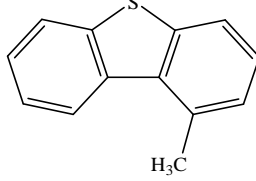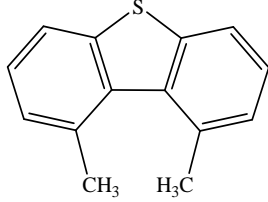## 2.1. Materials and methods

2.1.1. Reactants
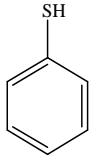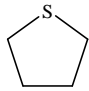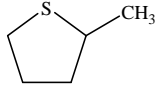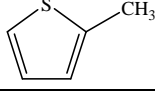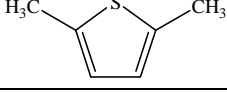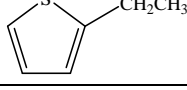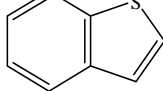
All the organic reactants used in the experiments were of reagent grade. They are listed in Table 2.3, along with their chemical formulas, molecular structures, melting points at 1 bar (T_{m,P_r}), purities and names of their providers. Ultra pure water (ELGA LabWater PURELAB OPTION-Q) was used in all experiments. Sulfur (AnalaR NORMAPUR 99.5%) was purchased from VWR BDH Prolabo. Pure hydrogen sulfide gas (ALPHAGAZ[TM] – COS and $CS_2 < 2000$ ppm, CH_4 and $N_2 < 500$ ppm, $CO_2 < 100$ ppm, $H_2O < 10$ ppm) was purchased from Air Liquide (B5 cylinder, 2 m[3] content).

2.1.2. Sample preparation

<u>2.1.2.1. Gold capsules</u>

The experiments were carried out in sealed gold capsules. It has been recognized that gold is chemically inert under hydrothermal conditions of temperature and pressure in the presence of high H_2S concentrations (Zhang et al., 2008), even though the HS^- ion is known to be an excellent complexing agent for the transport of gold in natural hydrothermal solutions (Benning and Seward, 1996). Other advantages of using gold include its flexibility (which allows to accomodate the external total pressure imposed on the system and transfer it within the capsule), and its good thermal conductivity.

Table 2.3. Characteristics of the hydrocarbon and organic sulfur compounds used in the experiments.

Compound	Formula	T_m, °C	Purity	Provider	Molecular Structure
n-Octane	C_8H_{18}	-57	> 99 %	Sigma-Aldrich	$CH_3-(CH_2)_6-CH_3$
n-Octadecane	$C_{18}H_{38}$	26-29	~ 99 %	Sigma-Aldrich	$CH_3-(CH_2)_{16}-CH_3$
n-Butyl methyl sulfide	$C_5H_{12}S$	-97.9	97 %	Sigma-Aldrich	$CH_3-(CH_2)_3-S-CH_3$
Benzenethiol	C_6H_6S	-15	99 %	Acros	
Thiacyclopentane	C_4H_8S	-96	99 %	Sigma-Aldrich	
2-Methylthiacyclopentane	$C_5H_{10}S$	-100.8	> 98 %	Alfa Aesar	
Thiophene	C_4H_4S	-38.2	99.5 %	Fluka	
2-Methylthiophene	C_5H_6S	-63	98 %	Sigma-Aldrich	
2,5-Dimethylthiophene	C_6H_8S	-62.6	98.5 %	Acros	
2-Ethylthiophene	C_6H_8S	—	97 %	Sigma-Aldrich	
Benzo[*b*]thiophene	C_8H_6S	32	97 %	Acros	
2-Methylbenzo[*b*]thiophene	C_9H_8S	51-52	99 %	Acros	
Dibenzo[*b*,*d*]thiophene	$C_{12}H_8S$	97	99 %	Sigma-Aldrich	
4-Methyldibenzo[*b*,*d*]thiophene	$C_{13}H_{10}S$	64-68	96 %	Sigma-Aldrich	
4,6-Dimethyldibenzo[*b*,*d*]thiophene	$C_{14}H_{12}S$	153-157	97 %	Sigma-Aldrich	

A 50-cm gold tube (Figure 2.4a) with an inside diameter of 5 mm and a wall thickness of 0.4 mm was cut into five gold capsules of 10-cm length, yielding an approximate internal volume of 1.6 cm^3. Prior to loading, the capsules were heated at a temperature of 700°C during 45 minutes to remove any trace of organic contamination and subsequently placed in a 0.1 molal solution of HCl, washed with industrial soap, and rinsed with water and ethanol. The gold capsules were then ultrasonically cleaned for 15 minutes, again rinsed with ethanol, and finally let drying for 2 hours. Following this procedure, each capsule was crimped and argon-arc welded at one end with a graphite welding rod (Figure 2.4b).

2.1.2.2. Sample loading

All solid and liquid reactants were weighed on a Mettler AT 201 Electronic Analytical SemiMicro Balance (Figure 2.4c). The weighed quantities were typically of the order of 0.05-0.7 g (see below), with a precision of 0.01 mg. Each gold capsule was weighed prior to being filled with the reactants. Liquid reactants were introduced into the capsules with a pipette. Liquid hydrocarbons and organic sulfur compounds were always introduced before water. The mass of each reactant being introduced in a capsule was determined by difference at each step. Organic solids with melting points in the 30-60°C range were first melted in a beaker placed on a heating plate and transferred in the capsules with a pipette. Organic solids with melting points above 60°C as well as elemental sulfur were introduced as solids in the capsules using a piece of aluminum foil.

For the experiments involving hydrocarbons, elemental sulfur and water, the open end of each gold capsule was crimped and argon-arc welded (Figure 2.4b). The gold capsule was gripped into a vise in vertical position, and the reactants were held in a frozen state by immersing the capsule in liquid nitrogen during the welding.

For those experiments in which H_2S was used as a reactant (desulfurization experiments), sample loading was a two step process. Solid and liquid organic sulfur compounds as well as liquid water were first introduced in the capsules. After sample loading, each of the gold capsules was weighed in order to estimate the amount of gas introduced in the capsules by the difference of mass determined after welding (see below). Hydrogen sulfide gas was subsequently added into the capsules using a procedure originally described in Jacquemet et al. (2005) and subsequently modified by Renard (2010). The gas-loading system, which is depicted in Figure 2.5, consists in the following successive operations. The tubing line of the gas-loading system is first pumped to remove any air present before introducing the H_2S into the gold capsule. Each gold capsule is subsequently connected to the

gas-loading connecter (valve D) and submerged in a liquid nitrogen trap (-196ºC) in order to hold the solid and liquid reactants at the bottom of the capsules. Valves C, D and G are subsequently opened, and pumping of the system is again made by opening valve B (during which pumping valves A, E and F are closed). After this pumping, valves B and D are closed. The cold trap is submerged into liquid nitrogen and valves A and C are opened, which introduces H_2S in the gas-loading system. The cold trap allows to collect the gas, and the amount of gas in the line is indicated by the pressure sensor. Valves A and C are finally closed. The pressure of H_2S in the line is limited to 15-20 bar for security reasons, the total volume of the line being 5.42 cm^3.
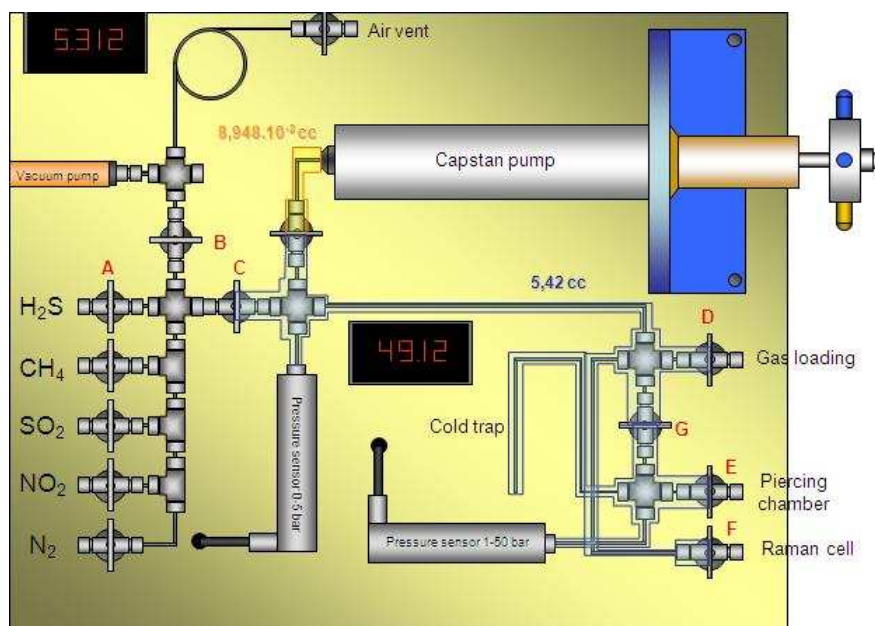

(a)   (b)

(c)

Figure 2.4. (a) Gold capsules used for the experiments. (b) Microbalance.
(c) Argon-arc welding of the capsules.

Figure 2.5. Gas-loading system (Renard, 2010 – modified after Jacquemet et al., 2005).

The amount of H_2S gas introduced in the line and corresponding to pressure P_1 is then transferred and trapped into the gold capsule by opening valve D, the gold capsule being submerged into liquid nitrogen. Following the transfer of H_2S from the line to the capsule, the measured drop in pressure from P_1 to P_2 indicates that approximately 95 percent of the gas has been transferred. A first estimation of the amount of gas introduced in the capsule can then be obtained from the perfect gas law and the pressure difference $P_1 - P_2$.

After the gas has been loaded, valve D is closed and the top end of the gold capsule which is connected to the gas line is first gripped with grip pliers and then cut with cut pliers. The open end of the cut capsule is then crimped and argon-arc welded, the gold capsule still being dipped in liquid nitrogen to hold H_2S and any other volatile compound produced during the welding process inside the capsule. After welding, the gold capsule is submerged in water to check for the existence of leaks. The capsule containing the reactants and the part cut to separate the capsule from the gas line are then weighed together in order to determine the amount of H_2S introduced in the capsule from the difference between the mass measured prior to welding and that measured after welding. Hence, the weighed amount of H_2S loaded in the capsule can be compared to the amount computed from the pressure difference and the ideal gas law (see above).

2.1.3. Experiments at high temperatures and pressures

The general experimental setup used in the present study is represented schematically in Figure 2.6a. The gold capsules containing the various reactants have been inserted in 100 cm^3 cold-seal, stainless steel autoclaves manufactured by Autoclave Engineers (Figure 2.6b), which were themselves introduced in cylindrical ovens (Figure 2.6c). All experiments were carried out at a constant temperature between 150ºC and 300ºC. The temperature was

130

controlled with JUMO sensors connected to chromel-alumel type K thermocouples (precision ± 1.5ºC). The pressure at which the experiments were carried out was set at 500 bar. This pressure was generated by a compressed air driven hydraulic pump (Figure 2.6d), and transmitted to the autoclave using a water-oil mixture as a pressure transmission fluid. A typical path through which the desired temperature and pressure were reached for an experiment at 150ºC and 500 bar consisted in the following steps: (1) preheating the oven to 300ºC, (2) inserting the autoclave into the oven, (3) setting the pressure in the autoclave to 300 bar, and (4) decreasing the temperature of the oven to 160ºC. As a result of the temperature increase in the autoclave, pressure also increases towards the final value of 500 bar. The time required to reach the desired temperature and pressure was of the order of 15-20 minutes. The duration of the experiments was typically one to two weeks. At the end of the experiments, the autoclaves were removed from the oven and rapidly cooled using a water circulation system.
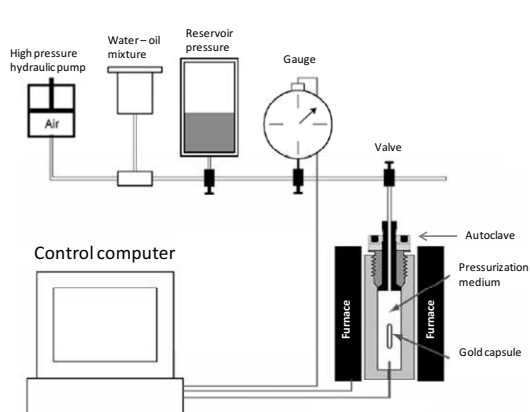
Figure 2.6. (a) Schematic representation of the experimental setup. (b) Cold-seal, stainless steel autoclave. (c) Cylindrical oven. (d) Pressure control system.

2.1.4. Gas phase analysis

At the end of the experiments, the capsules have been weighed to check for any mass difference with respect to the mass measured prior to the experiment. The capsules have subsequently been pierced in a glass chamber by means of a rotating stainless steel device, and the gases transferred into fused silica capillaries for Raman analysis. The procedure for collecting the gas is detailed in Figure 2.7. After the piercing of the capsule, the gas occupies a volume V_1 of the gas line while valve A is closed. Upon opening valve A, the gas occupies volume $V_1 + V_3$ (32.1186 cm^3). The pressure in the line is indicated by the pressor sensor P_2, which allows to evaluate the amount of gas in the line from the ideal gas law. The gas is subsequently collected in a cold trap (cooled with liquid nitrogen) by opening valve B. After the transfer of the gas in the cold trap, valve A is closed and the cold trap heated to room temperature to liberate the gas in the volume represented by $V_2 + V_3$ (2.7776 cm^3), from which the number of moles of gas can again be determined (see below). A fused silica capillary tube connected to valve E is purged up to three times using a vacuum pump to eliminate the air present. Valves D and E are then closed and a fraction of the gas present in volume $V_2 + V_3$ is transferred into volume V_4 by opening valve C. This fraction of gas, which corresponds to a pressure of ~ 4 bar indicated by the pressure sensor P_1, is finally transferred into the capillary tube, the lower end of which is submerged into liquid nitrogen to freeze and hold the gas. Valve E is then closed and the capillary tube sealed under a propane/oxygen flame.
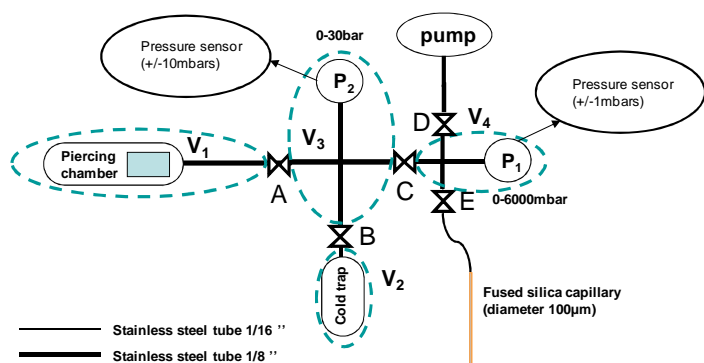

Figure 2.7. Piercing chamber and recovery of the gas phase from the gold capsules after the experiments – see text. The volumes V_1-V_4 have the following values: $V_1 = 30.291 \pm 0.06$ cm^3; $V_2 = 0.95 \pm 0.004$ cm^3; $V_3 = 1.8276 \pm 0.0035$ cm^3; $V_4 = 1.5864 \pm 0.0015$ cm^3 (designed by Aurélien Randi, G2R, Nancy).

The gas recovered at the end of each experiment has been analyzed by Raman spectroscopy to detect the presence of gases other than H_2S which might have been generated during the experiments. Raman quantitative analysis was performed using a HORIBA Jobin-Yvon LabRAM® Raman spectrometer equipped with an argon laser operating at a wavelength of 514.4 nm.

2.1.5. Gas chromatography coupled to mass spectrometry (GC-MS)

Solid and liquid reaction products were recovered from the gold cells and piercing chamber walls. Solids were recovered by scratching, while a syringe was used to collect the liquids. A small amount of the solid or liquid reaction products recovered at the end of each experiment was subsequently dissolved in dichloromethane (DCM, 4-8 mg of reaction product per ml of DCM) prior to the GC-MS analysis. The dichloromethane (HPLC grade, purity 99.8%) was supplied by Carlo Erba Reagenti. The GC-MS anayses were carried out using a HP 5890 Series II gas chromatograph coupled to a HP 5971 mass spectrometer, both designed and manufactured by Hewlett-Packard. The different components which constitute a GC-MS equipment are depicted in Figure 2.8, and briefly discussed below.

2.1.5.1. Gas chromatography

Gas chromatography (GC) allows the separation of individual organic compounds from a mixture. The GC equipment which has been used in the present study consists of an Agilent J&W Scientific DB-5 chromatographic capillary column (length 60 m; diameter 0.25 mm). The stationary phase, which is coated on the inner surface of the column, consists of a 5%-phenyl-95%-dimethylarylene siloxane copolymer. The coating has a thickness of 0.1 µm. Helium was used as the carrier gas at a flow rate of 1 ml/min. The chromatographic column is located inside an oven. An aliquot of ~ 1 µl of a DCM solution containing reaction products is injected in automatic splitless mode within a heated chamber, where the sample is vaporized before being brought to the head of the chromatographic column by the carrier gas. The separation of the organic compounds on the column is obtained by increasing the temperature of the oven from 60 to 130ºC at a rate of 15ºC/min, then from 130 to 315ºC at a rate of 3ºC/min. The compounds are retained differently onto the column depending on their molecular weight, their molecular structures, or the nature and number of their functional groups. The retention time of organic compounds on a capillary column increases with increasing molecular weight. In the case of identical molecular weights, isomers usually have different retention times. For instance, branched alkanes have shorter retention times

compared to the corresponding *n*-alkanes. Finally, the retention time of organic compounds on a capillary column increases with an increasing number of functional groups.
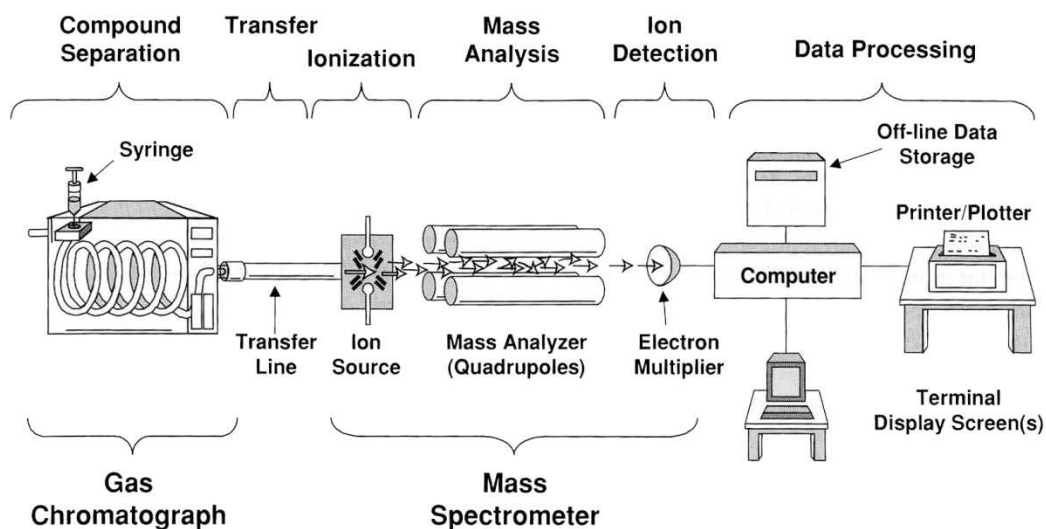

Figure 2.8. Schematic representation of a GC-MS equipment (Peters et al., 2005).

2.1.5.2. Mass spectrometry

Mass spectrometry (MS) allows the identification of the compounds which have been separated by gas chromatography. A mass spectrometer typically consists of three separate units, including an ionization chamber, a mass separator, and a detector. In the ionization chamber, the molecules arriving from the gas chromatograph are bombarded with electrons under high vacuum ($< 10^{-5}$ torr). The electrons, generated by the excitation of a rhenium (Re) filament, carry an energy of 70 eV. The bombardment results in the formation of positively charged molecular fragments (i.e. molecular ions). These fragments are subsequently separated according to their mass over charge (m/z) ratios by an electromagnetic field generated from a quadrupole. Finally, the m/z ratios of the molecular ions are determined over a 50 to 550 m/z range by the detector which consists of electron multipliers. There exists two detection modes, a full scan mode and a selected-ion monitoring mode. The full scan mode allows to detect all molecular ions in the 50 to 550 m/z range. The selected-ion monitoring mode covers a very narrow m/z range, and detects only a limited number of molecular ions. Both modes have been used in the present study.

2.1.5.3. Interpretation of GC-MS results

The GC-MS results obtained under the form of chromatograms have been interpreted using the GC/MSD G1034C Chemstation software of Agilent Technologies, together with an automated library search of the Wiley 275.L database of Agilent, which contains some

134

275,871 spectra. In some cases, the NIST mass spectral database was consulted for the purpose of comparison or when some compounds could not be identified with the Wiley database (http://webbook.nist.gov/chemistry/form-ser.html).

2.2. Descriptive summary of the experiments

The temperature and pressure conditions and durations of the experiments as well as the amounts of reactants used in these experiments are summarized in Table 2.4. The experiments were carried out for 2 weeks to 1 month at 120 or 150ºC and under a total pressure of 500 bar. The mass (m OSC) of each reacting organic sulfur compound to be used in a given reaction was estimated from the stoichiometry of a reasonable desulfurization reaction and the maximum amount of H_2S which can be introduced into a gold capsule. The latter amount is dictated by the pressure (P_1 H_2S) which can be reached in the gas-loading system, i.e. slightly less than 15 bar, which translates to approximately 0.09 g or 0.003 mol H_2S. Let us consider as an example the reaction between thiacyclopentane and H_2S, which is designated by Experiment 2a in Table 2.4. If we assume that *n*-butane is a possible reaction product, than the desulfurization reaction may be written as

$$C_4H_8S + H_2S = C_4H_{10} + 2\ S\ . \tag{2.17}$$
$$\text{(thiacyclopentane)} \qquad \text{(\textit{n}-butane)}$$
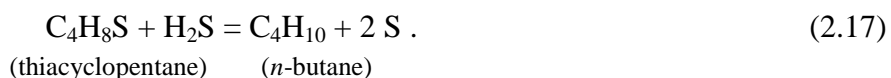
Since the stoichiometry of this reaction is equimolar for the reactants, 0.003 mol or 0.25 g of thiacylopentane must be introduced in the gold capsule. It can be deduced from Table 2.4 that there is generally a good agreement between the amount of H_2S estimated from the ideal gas law (m´ H_2S) and the mass determined by weighing after the welding of the gold capsule (m H_2S). Note however that m´ H_2S < m H_2S for Experiments 2b, 3a, 6e and 9a, while m´ H_2S > m H_2S for Experiments 6c, 6d, and 10b. These differences can tentatively be explained for Experiments 2b, 3a, 6e and 9a either by a loss of some H_2S or of some of the OSC reactant during the welding process, and for Experiments 6c, 6d and 10b by the introduction of liquid nitrogen inside the gold capsule. The latter possibility is confirmed by the detection of organic nitrogen compounds at the end of the reactions (see below). Finally, Experiments 15 and 16 represent sulfurization (reverse) experiments which have been performed to verify that H_2S was actually produced by reacting hydrocarbons and elemental sulfur under similar condtions of temperature and pressure and for similar reaction times.

2.3. Results

In order to facilitate the thermodynamic interpretation of the experimental results summarized below, it is preferable to present these results first in terms of general observations on the consumption of H_2S and the precipitation of elemental sulfur, and subsequently in a more detailed manner by considering the nature of the gaseous, liquid or solid products formed at the end of the experiments.

2.3.1. Consumption of H_2S

The amount of H_2S gas remaining at the end of each experiment was evaluated from the ideal gas law and a measurement of pressure P_2 (see Section 2.1.4 above), assuming that all the gas present at the end of a given experiment was H_2S. This assumption is justified by the fact that only limited generation of carbon dioxide (CO_2) and/or methane (CH_4) occured during the experiments. The details of the ideal gas calculations yielding the remaining amount of H_2S at the end of each experiment are given in Table 2.5. It can be deduced from this table that H_2S has been consumed in Experiments 1, 2a, 2b, 3a, 3b, 6c, 6d, 6e, 6f, 7 and 8b, which involved *n*-butyl methyl sulfide, thiacylopentane, 2-methylthiacyclopentane, 2-methylthiophene, ethylthiophene, and 2,5-dimethylthiophene. In contrast, H_2S was produced during the reactions involving 2-methylbenzo[*b*]thiophene, dibenzo[*b,d*]thiophene, 4-methyl-dibenzo[*b,d*]thiophene and 4,6-dimethyldibenzo[*b,d*]thiophene (i.e. Experiments 10a, 10b, 11, 12, 13 and 14). This H_2S generation most probably resulted from the thermal decomposition of these compounds. Production of H_2S has been reported in a pyrolysis study of dibenzo-[*b,d*]thiophene (Dartiguelongue et al., 2006), although at higher temperatures (480-500ºC) and with no H_2S initially present. No consumption or production was observed in the case of benzenethiol (Experiment 4), which may be due to the lower temperature (120ºC) at which this experiment was carried out. Changes in H_2S concentrations appear to be less clear for Experiments 5, 6a, 6b, 8a and 9b. The decrease in the amount of H_2S observed for Experiment 9a which involved benzo[*b*]thiophene is probably due to a leakage during the transfer from the gold capsule to the gas line and should therefore not be considered as a consumption of H_2S. Finally, in agreement with previous observations (e.g. Schmid, 1986), a limited generation of H_2S was observed in Experiments 15 and 16, which concerned the reaction of *n*-octane and *n*-octadecane, respectively, with elemental sulfur.

Table 2.4. Summary of temperatures, pressures, and durations of, and amounts of reactants used in the sulfurization/desulfurization experiments.

Experiment	Reactants	T (ºC)	P (bar)	Time (days)	m OSC (g)	m H_2O (g)	m H_2S (g) [a]	P_1 H_2S (bar)	P_2 H_2S (bar)	dP (bar)	m´ H_2S (g) [b]
1	*n*-Butyl methyl sulfide + H_2S + H_2O	150	500	14	0.120	0.050	0.101	11.100	0.035	11.065	0.084
2a	Thiacyclopentane + H_2S + H_2O	150	500	14	0.257	0.044	0.102	11.700	0.038	11.662	0.087
2b	Thiacyclopentane + H_2S + H_2O	150	500	14	0.250	0.200	0.028	11.300	0.060	11.240	0.085
3a	2-Methylthiacyclopentane + H_2S + H_2O	150	500	14	0.252	0.087	0.053	11.100	0.035	11.065	0.084
3b	2-Methylthiacyclopentane + H_2S + H_2O	150	500	14	0.222	0.103	0.095	11.000	0.035	10.965	0.083
4	Benzenethiol + H_2S + H_2O	120	500	14	0.105	0.020	0.093	11.100	0.070	11.030	0.083
5	Thiophene + H_2S + H_2O	120	500	14	0.162	0.018	0.086	10.700	0.063	10.637	0.080
6a	2-Methylthiophene + H_2S + H_2O	150	500	14	0.098	0.051	0.076	11.100	0.158	10.942	0.084
6b	2-Methylthiophene + H_2S + H_2O	150	500	14	0.084	0.037	0.079	10.100	0.150	9.950	0.076
6c	2-Methylthiophene + H_2S + H_2O	150	500	21	0.085	0.039	0.196	13.700	3.000	10.700	0.082
6d	2-Methylthiophene + H_2S + H_2O	150	500	21	0.084	0.035	0.150	10.100	1.000	10.000	0.077
6e	2-Methylthiophene + H_2S + H_2O	150	500	30	0.122	0.069	0.041	10.800	0.022	10.778	0.081
6f	2-Methylthiophene + H_2S + H_2O	150	500	30	0.100	0.058	0.097	11.600	0.019	11.581	0.087
7	Ethylthiophene + H_2S + H_2O	150	500	14	0.166	0.060	0.092	11.100	0.100	11.000	0.083
8a	2,5-Dimethylthiophene + H_2S + H_2O	150	500	14	0.153	0.037	0.083	11.400	0.040	11.360	0.086
8b	2,5-Dimethylthiophene + H_2S + H_2O	150	500	14	0.391	0.170	0.088	10.700	0.080	10.620	0.080
9a	Benzo[*b*)thiophene + H_2S + H_2O	120	500	14	0.737	0.028	0.054	10.900	0.065	10.835	0.081
9b	Benzo[*b*)thiophene + H_2S + H_2O	120	500	14	0.696	0.016	0.089	10.900	0.070	10.830	0.081
10a	2-Methylbenzo[*b*]thiophene + H_2S + H_2O	150	500	14	0.211	0.093	0.091	11.000	0.023	10.977	0.082
10b	2-Methylbenzo[*b*]thiophene + H_2S + H_2O	150	500	21	0.064	0.032	1.094	10.200	0.070	10.130	0.078
11	2-Methylthiophene + 2-methylbenzo[*b*]-thiophene + H_2S + H_2O	150	500	14	0.020/ 0.049	0.138	0.088	11.000	0.070	10.930	0.083

Table 2.4. (Continued).

Experiment	Reactants	T (ºC)	P (bar)	Time (days)	m OSC (g)	m H$_2$O (g)	m H$_2$S (g) [a]	P$_1$ H$_2$S (bar)	P$_2$ H$_2$S (bar)	dP (bar)	m´ H$_2$S (g) [b]
12	Dibenzo[b,d]thiophene + H$_2$S + H$_2$O	150	500	14	0.110	0.066	1.094	11.300	0.03	11.270	0.084
13	4-Methyldibenzo[b,d]thiophene + H$_2$S + H$_2$O	150	500	14	0.134	0.064	0.091	11.200	0.025	11.175	0.084
14	4,6-Dimethyldibenzo[b,d]thiophene + H$_2$S + H$_2$O	150	500	14	0.128	0.045	0.094	11.200	0.028	11.172	0.084
15	n-Octane + sulfur + H$_2$O	150	500	14	0.165 [c]	0.045	0.045 [d]	—	—	—	—
16	n-Octadecane + sulfur + H$_2$O	200	500	7	0.435 [c]	—	0.057 [d]	—	—	—	—

[a] Value obtained by weighing [b] Value calculated from the values of P$_1$ and P$_2$ and the ideal gas law [c] Mass of the hydrocarbon reactant [d] Mass of elemental sulfur

Table 2.5. Summary of ideal gas calculations performed at the end of the experiments.

Experiment	Organic sulfur or hydrocarbon reactant	m´ H$_2$S (g) [a]	T (°C) [b]	P$_2$ (bar) [c]	V$_1$ + V$_3$ (cm^3) [b]	m´´ H$_2$S (g) [d]	δn H$_2$S (x 10^3)
1	*n*-Butyl methyl sulfide	0.084	294.15	1.77	32.1186	0.079	-0.147
2a	Thiacyclopentane	0.087	298.15	1.70	32.1186	0.075	-0.352
2b	Thiacyclopentane	0.085	294.15	1.40	32.1186	0.063	-0.646
3a	2-Methylthiacyclopentane	0.084	298.15	1.13	32.1186	0.050	-0.998
3b	2-Methylthiacyclopentane	0.083	298.15	1.28	32.1186	0.057	-0.763
4	Benzenethiol	0.083	298.15	1.88	32.1186	0.083	0.000
5	Thiophene	0.080	298.15	1.79	32.1186	0.079	-0.029
6a	2-Methylthiophene	0.084	288.15	1.82	32.1186	0.083	-0.029
6b	2-Methylthiophene	0.076	288.15	1.66	32.1186	0.076	0.000
6c	2-Methylthiophene	0.082	292.15	15.44	2.7776 [e]	0.060	-0.646
6d	2-Methylthiophene	0.077	292.15	17.07	2.7776 [e]	0.067	-0.293
6e	2-Methylthiophene	0.081	296.15	17.20	2.7776 [e]	0.067	-0.411
6f	2-Methylthiophene	0.087	296.15	17.07	2.7776 [e]	0.067	-0.587
7	Ethylthiophene	0.083	298.15	1.46	32.1186	0.064	-0.558
8a	2,5-Dimethylthiophene	0.086	298.15	1.92	32.1186	0.085	-0.029
8b	2,5-Dimethylthiophene	0.080	294.15	1.58	32.1186	0.071	-0.264
9a	Benzo[*b*]thiophene	0.081	298.15	1.45	32.1186	0.064	-0.499
9b	Benzo[*b*]thiophene	0.081	298.15	1.79	32.1186	0.079	-0.059
10a	2-Methylbenzo[*b*]thiophene	0.082	295.65	1.90	32.1186	0.085	0.088
10b	2-Methylbenzo[*b*]thiophene	0.078	292.15	2.78	32.1186	0.125	1.379
11	2-Methylthiophene + 2-methylbenzo[*b*]thiophene	0.083	294.15	1.91	32.1186	0.085	0.059
12	Dibenzo[*b,d*]thiophene	0.084	295.65	2.07	32.1186	0.092	0.235
13	4-Methyldibenzo[*b,d*]thiophene	0.084	295.65	1.90	32.1186	0.085	0.029
14	4,6-Dimethyldibenzo[*b,d*]thiophene	0.084	295.65	2.04	32.1186	0.091	0.205
15	*n*-Octane	—	296.15	0.05	32.1186	0.002	0.059
16	*n*-Octadecane	—	293.15	0.70	32.1186	0.002	0.059

[a] Mass of H$_2$S calculated prior to the experiment from the values of P$_1$ and P$_2$ and the ideal gas law (see Table 2.4) [b] Actual room temperature during the pressure reading [c] see Section 1.2.4 and Figure 2.7 [d] Amount of H$_2$S calculated at the end of the experiments [e] Due to a leakage problem during the opening of the capsule, the volume here represents V$_2$ + V$_3$ (see Figure 2.7)

2.3.2. Precipitation of elemental sulfur

Both Raman spectroscopic observations and GC-MS analysis of the liquid phase recovered at the end of Experiments 6a-6f, 7, 8a and 8b indicated that elemental sulfur formed as a result of the interactions between H$_2$S and 2-methylthiophene, 2-ethylthiophene and 2,5-dimethylthiophene. In contrast, there was no indication of sulfur formation in the other reactions which also resulted in the consumption of H$_2$S and involved *n*-butyl methyl sulfide, thiacylopentane, and 2-methylthiacyclopentane. A crystal of rhombic sulfur floating in a drop of organic liquid as observed under the optical microscope of the Raman spectrometer after

Experiment 6a is shown in Figure 2.9a. The Raman spectrum of this sulfur crystal is shown in Figure 2.9b. Further detection of elemental sulfur during the GC-MS analysis will be commented in Section 2.3.4.

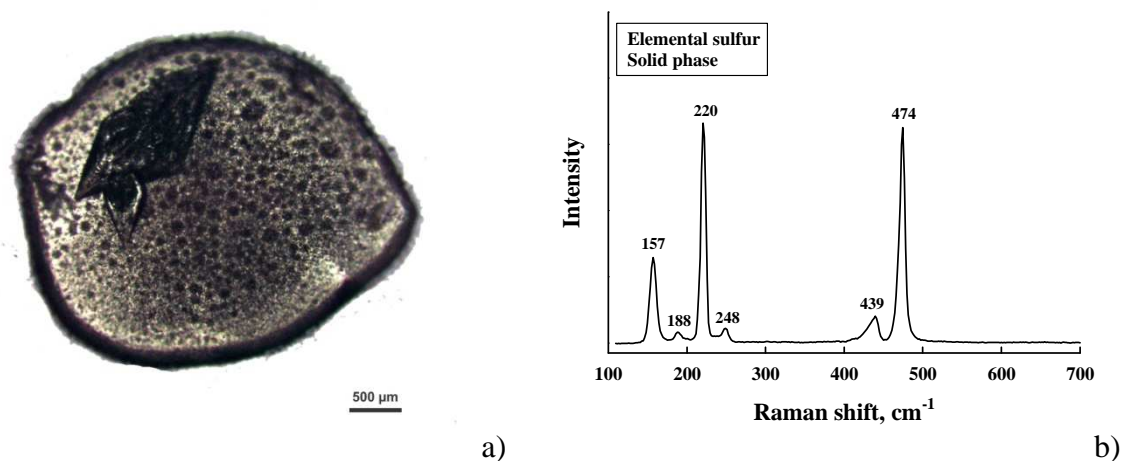a)   b)

Figure 2.9. Raman analysis of the reaction product of Experiment 6a: a) Optical microscope observation; b) Raman spectrum showing the characteristic peaks of sulfur (e.g. see Anderson and Loh, 1969).

2.3.3. Composition of the gas phase

The results of Raman analysis of the gases recovered at the end of the experiments are summarized in Table 2.6. Some representative Raman spectra are shown in Figure 2.10. These results indicate that H_2S was still present at the end of the experiments, and was by far the most abundant species in the gas phase. The formation of small amounts of carbon dioxide (CO_2) was observed in many experiments. Methane (CH_4) was also detected in a number of experiments, although its formation was found to be less common than CO_2. Methane was formed in greater amounts compared to CO_2 in the experiments in which 2-methylthia-cyclopentane was used as a reactant (Experiments 3a and 3b), most probably as a result of the loss of the methyl group. In contrast, methane was not observed in the experiment with 2-methylthiophene (Experiments 6a-6d) while CH_4 and CO_2 were produced in approximately equal proportions in the experiments with thiophene and 2,5-dimethylthiophene. Hydrogen (H_2) was produced in small amounts in only one reaction, which involved 2-methylbenzo[*b*]-thiophene (Experiment 10b). Finally, as mentioned above, a small amount of H_2S was generated as a result of the reaction between the two *n*-alkanes and elemental sulfur (Experiments 15-16 and Figure 2.10, bottom right).

Table 2.6. Summary of gaseous species identified by Raman spectroscopy at the end of the experiments. The concentrations are given in mol % (n.a. = not analyzed, n.d. = not detected).

Experiment	Organic sulfur or hydrocarbon reactant	H_2S	CO_2	CH_4	H_2
1	*n*-Butyl methyl sulfide	98.7	1.2	0.1	n.d.
2a	Thiacyclopentane	100	n.d.	n.d.	n.d.
2b	Thiacyclopentane	98.7	1.3	n.d.	n.d.
3a	2-Methylthiacyclopentane	95.8	2.7	1.6	n.d.
3b	2-Methylthiacyclopentane	97.3	2.3	0.4	n.d.
4	Benzenethiol	100	n.d.	n.d.	n.d.
5	Thiophene	96.3	2.0	1.7	n.d.
6a	2-Methylthiophene	99.1	0.9	n.d.	n.d.
6b	2-Methylthiophene	99.2	0.8	n.d.	n.d.
6c	2-Methylthiophene	99.4	0.6	n.d.	n.d.
6d	2-Methylthiophene	97.4	2.6	n.d.	n.d.
6e	2-Methylthiophene	n.a.	n.a.	n.a.	n.a.
6f	2-Methylthiophene	n.a.	n.a.	n.a.	n.a.
7	Ethylthiophene	100	n.d.	n.d.	n.d.
8a	2,5-Dimethylthiophene	97.7	1.5	0.8	n.d.
8b	2,5-Dimethylthiophene	98.7	1.1	0.2	n.d.
9a	Benzo[*b*]thiophene	99.4	0.6	n.d.	n.d.
9b	Benzo[*b*]thiophene	99.6	0.4	n.d.	n.d.
10a	2-Methylbenzo[*b*]thiophene	n.a.	n.a.	n.a.	n.a.
10b	2-Methylbenzo[*b*]thiophene	98.8	1.1	n.d.	0.1
11	2-Methylthiophene + 2-methylbenzo[*b*]thiophene	99.5	0.5	n.d.	n.d.
12	Dibenzo[*b,d*]thiophene	n.a.	n.a.	n.a.	n.a.
13	4-Methyldibenzo[*b,d*]thiophene	n.a.	n.a.	n.a.	n.a.
14	4,6-Dimethyldibenzo[*b,d*]thiophene	n.a.	n.a.	n.a.	n.a.
15	*n*-Octane	100	n.d.	n.d.	n.d.
16	*n*-Octadecane	100	n.d.	n.d.	n.d.
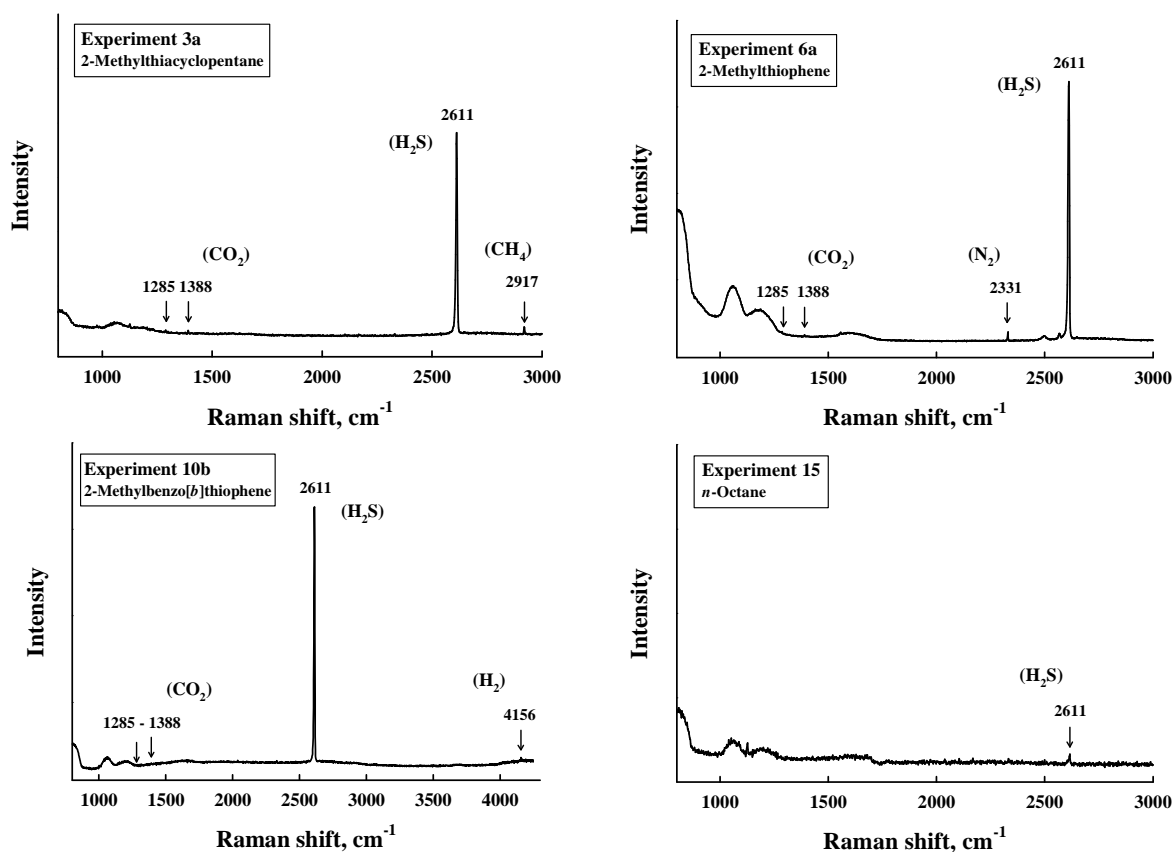
Figure 2.10. Raman spectra showing the different gaseous species generated during some of the experiments detailed in Tables 2.4-2.6. Peak identifications based on Raman shift values tabulated by Schrötter (1995).

2.3.4. Composition of the organic liquid phase

The reaction products identified by GC-MS analysis of the liquid mixtures recovered at the end of the experiments have been listed in Table 2.7 and their molecular structures are shown in Figure 2.11. Representative gas chromatograms and mass spectra are presented in Figures 2.12-2.17. Under the conditions of temperature and H_2S pressure considered for the experiments, no reaction products besides CH_4 and CO_2 (Table 2.6) were identified in the case of Experiment 1, for which the reactant was n-butyl methyl sulfide. At the lower temperature (120ºC) considered for Experiments 4 and 5 which involved benzenethiol and thiophene, no reaction seemed to have occurred if one except a small generation of CH_4 and CO_2 in the case of thiophene (Table 2.6). No reaction products were generated either in the case of the reactions involving benzo[b]thiophenes and dibenzo[b,d]thiophenes (Experiments 9-14). In the latter case, the absence of reaction is consistent with the preliminary thermodynamic calculations presented in the first part of the manuscript. These calculations suggested that very high pressures of H_2S would be required in order to form elemental sulfur

142

benzo[*b*]thiophenes and dibenzo[*b,d*]thiophenes. In Experiment 11, where a mixture of 2-methylbenzo[*b*]thiophene and 2-methylthiophene was reacted with H_2S, several of the compounds generated in Experiments 6a-6f (which used 2-methylthiophene as a unique reactant) were also identified.

Table 2.7. Reaction products identified by GC/MS analysis for the experiments detailed in Table 2.4.

Product	Formula	Experiments	Relative abundance
1,4-Butanedithiol	$C_4H_{10}S_2$	2a, 2b	+++
1,5-Pentanedithiol	$C_5H_{12}S_2$	3a, 3b	+++
1,6-Hexanedithiol	$C_6H_{14}S_2$	7	+
1,3-Benzenedithiol	$C_6H_6S_2$	7	++
Diethyl trisulfide	$C_4H_{10}S_3$	3a, 3b	++
1,2-Bis(ethylthio)propane	$C_7H_{16}S_2$	3a, 3b	+
1,5-Bis(ethylthio)pentane	$C_9H_{20}S_2$	3a, 3b	++++
3-Ethyl-5-methyl-1,2,4-trithiacyclopentane	$C_5H_{10}S_3$	6a-f	+
1,2-Dithiacyclohexane	$C_4H_8S_2$	2a, 2b	++++
2-Methyl-1,3-dithiacyclohexane	$C_5H_{10}S_2$	6a-f	++
1,3,5-Trithiacycloheptane	$C_4H_8S_3$	2a, 2b	+
1,2-Dithiacycloheptane	$C_5H_{10}S_2$	6a-f, 11	++++
1,4-Dithiacyclohept-2-ene	$C_5H_8S_2$	6a-f	+++
4,6-Dimethyl-[1,2,3]-trithiacyclohexane	$C_5H_{10}S_3$	3a, 3b, 6a-f	+++
1,2-Dithiacyclooctane	$C_6H_{12}S_2$	7, (8a, 8b)	+++, (+)
Methyl butanedithioate	$C_5H_{10}S_2$	6a-f	++
Ethyl butanedithioate	$C_6H_{12}S_2$	7	++
2-Isopropylthiophene	$C_7H_{10}S$	7	+++
3-(Methylthio)-thiophene	$C_5H_6S_2$	6a-f	+++
2-Methyl-5-*n*-propylthiophene	$C_8H_{12}S$	8a, 8b	++++
2-Methyl-5-methylthio-thiophene	$C_6H_8S_2$	7	++
2-Methyl-4-methylthio-2,3-dihydrothiophene	$C_6H_{10}S_2$	7	++
2,2´-(1,2-Ethanediyl)-bis-thiophene	$C_{10}H_{10}S_2$	6a-f, 11	+
2-(2,5-Dimethylthien-3-yl)-5-methylthiophene	$C_{12}H_{14}S_2$	8a, 8b	++
Elemental sulfur	S	6a-f, 7, (8a, 8b), 11	++, ++++, (+), ++
4,5-Dihydro-3(2*H*)-thiophenone	C_4H_6OS	2a, 2b	++
2-Methyl-5-thiophenecarboxylic acid	$C_6H_6O_2S$	8a, 8b	+++
Thiacyclohexane dioxide	$C_5H_{10}O_2S$	3a, 3b	++
2-Methyl-2-hydroxymethyl-[1,3]-dithiane	$C_6H_{12}OS_2$	6a-f	+
5-(Ethylthio)-1-pentanol	$C_7H_{16}OS$	3a, 3b	++
1-(4-hydroxy-3-thienyl)-ethanone	$C_6H_6O_2S$	7	++
1,1-Ethanediol diacetate	$C_6H_{10}O_4$	7	++
4-Methoxy-3-penten-2-one	$C_6H_{10}O_2$	8a, 8b	+++
2,6-Di-*tert*-butyl-4-methylphenol	$C_{15}H_{24}O$	2a, 2b	+++
Acetaldehyde dimethylhydrazone	$C_4H_{10}N_2$	3a, 3b	++
[1-(2,2-dimethylhydrazino)ethyl]ethyldiazene	$C_6H_{16}N_4$	2a, 2b	++
Pterin	$C_6H_5N_5O$	3a	+

HS—[CH₂]₄—SH
1,4-Butanedithiol ($C_4H_{10}S_2$)

1,5-Pentanedithiol ($C_5H_{12}S_2$)

1,3-Benzenedithiol
($C_6H_6S_2$)

1,6-Hexanedithiol ($C_6H_{12}S_2$)

Diethyl trisulfide ($C_4H_{10}S_3$)

1,2-Bis(ethylthio)propane ($C_7H_{16}S_2$)

1,5-Bis(ethylthio)pentane ($C_9H_{20}S_2$)

3-Ethyl-5-methyl-1,2,4-trithia-
cyclopentane ($C_5H_{10}S_3$)

1,2-Dithiacyclohexane
($C_4H_8S_2$)

2-Methyl-1,3-dithiacyclo-
hexane ($C_5H_{10}S_2$)

4,6-Dimethyl-1,2,3-trithia-
cyclohexane ($C_5H_{10}S_3$)

1,2-Dithiacycloheptane
($C_5H_{10}S_2$)

1,3,5-Trithiacycloheptane
($C_4H_8S_3$)

1,4-Dithiacyclohept-2-ene
($C_5H_8S_2$)

1,2-Dithiocyclooctane
($C_6H_{12}S_2$)

Methyl butanedithioate
($C_5H_{10}S_2$)

Ethyl butanedithioate
($C_6H_{12}S_2$)

2-Isopropylthiophene
($C_7H_{10}S$)

3-(Methylthio)-thiophene
($C_5H_6S_2$)

2-Methyl-5-n-propylthiophene
($C_8H_{12}S$)

2-Methyl-5-(methylthio)-thiophene
($C_6H_8S_2$)

2-Methyl-4-(methylthio)-2,3-dihydrothiophene
($C_6H_{10}S_2$)

2,2′-(1,2-Ethanediyl)-bis-thiophene
($C_{10}H_{10}S_2$)

2-(2,5-Dimethylthien-3-yl)-5-methylthiophene
($C_{12}H_{14}S_2$)

Figure 2.11. Molecular structures of the reaction products identified by GC/MS analysis
for the experiments detailed in Table 2.4.

144

4,5-Dihydro-3(2*H*)-thiophenone
(C$_4$H$_6$OS)

2-Methyl-5-thiophenecarboxylic acid
(C$_6$H$_6$O$_2$S)

Thiacyclohexane dioxide
(C$_5$H$_{10}$O$_2$S)

2-Methyl-2-hydroxymethyl-1,3-
dithiacyclohexane (C$_6$H$_{12}$OS$_2$)

5-Ethylthio-1-pentanol
(C$_7$H$_{16}$OS)

1-(4-Hydroxyl-3-thienyl)-ethanone
(C$_6$H$_6$O$_2$S)

1,1-Ethanediol diacetate
(C$_6$H$_{10}$O$_4$)

2,6-Di-*tert*-butyl-4-methylphenol
(C$_{15}$H$_{24}$O)

Acetaldehyde dimethylhydrazone
(C$_4$H$_{10}$N$_2$)

4-Methoxy-3-penten-2-one (C$_6$H$_{10}$O$_2$)

[1-(2,2-Dimethylhydrazino)ethyl]ethyldiazene
(C$_6$H$_{16}$N$_4$)

Pterin (C$_6$H$_5$N$_5$O)

Figure 2.11. *(Continued)*.

It can be deduced from Table 2.7 that alkanedithiols, *n*-alkyldisulfides, and cyclic disulfides (dithiacycloalkanes) appear to be the most abundant compounds formed by reaction between H$_2$S gas and liquid thiacyclopentane, 2-methylthiacyclopentane, 2-methylthiophene, 2-ethylthiophene, and 2,5-dimethylthiophene. In the case of 2-methylthiophene and 2-ethylthiophene, sulfur is also added to the thiophenic rings to form (methylthio)-thiophenes. Other thiophenic compounds containing two thiophenic rings, as well as a thiophenecarboxylic acid have also been detected, although in lesser amounts. No *n*-alkanes were detected among the reaction products. Note that the three oxygen-bearing and three nitrogen-bearing compounds listed in Table 2.7 most certainly represent experimental artifacts, which in the case of the nitrogen-bearing compounds were produced as a result of

145
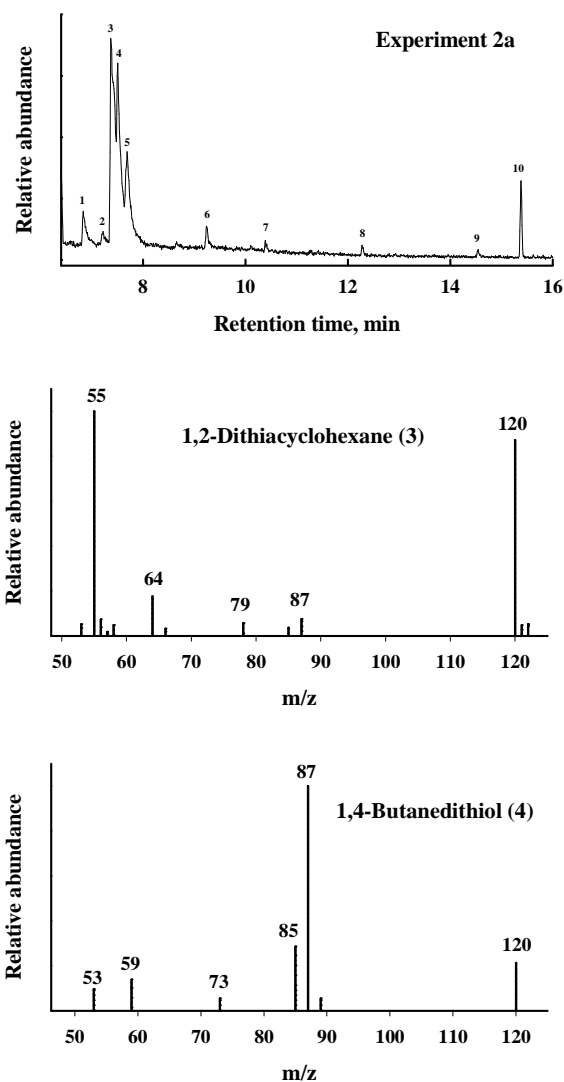
Figure 2.12. Gas chromatogram and mass spectra for major reaction products formed in Experiment 2a. The numbers of the peaks in the gas chromatogram correspond to the following compounds: 1 and 7 = 4,5-dihydro-3(2*H*)-thiophenone (C_4H_6OS); 2,3 and 6 = 1,2-dithiacyclohexane ($C_4H_8S_2$); 4 = 1,4-butanedithiol ($C_4H_{10}S_2$); 5 = [1-(2,2-dimethylhydrazino)ethyl]ethyldiazene ($C_6H_{16}N_4$); 8 = 1,3,5-trithiacycloheptane ($C_4H_8S_3$); 9 = acetaldehyde dimethylhydrazone ($C_4H_{10}N_2$); 10 = 2,6-di-*tert*-butyl-4-methylphenol ($C_{15}H_{24}O$).
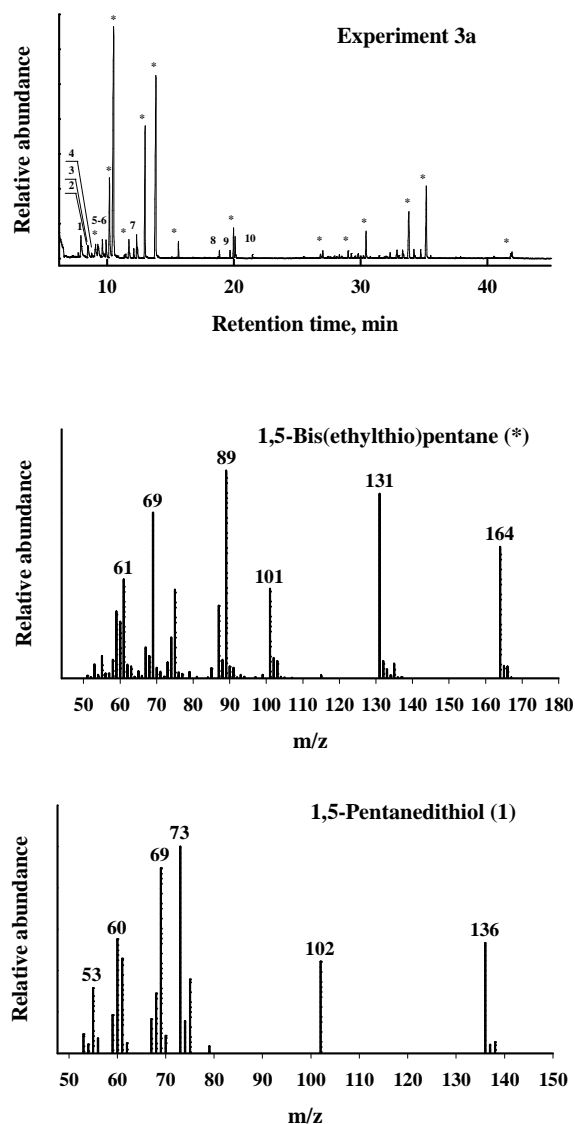
Figure 2.13. Gas chromatogram and mass spectra for major reaction products formed in Experiment 3a. The numbers of the peaks in the gas chromatogram correspond to the following compounds: 1 = 1,5-pentanedithiol ($C_5H_{10}S_2$); 2 = thiacyclohexane dioxide ($C_5H_{10}O_2S_2$); 3 = diethyltrisulfide ($C_4H_{10}S_3$); 4 = 1,2-bis(ethylthio)-propane ($C_7H_{16}S_2$); 5 = 5-bis(ethylthio)-1-pentanol ($C_7H_{16}OS$); 6 and 10 = unidentified compound; 7 = 4,6-dimethyl-1,2,3-trithiacyclohexane ($C_5H_{10}S_3$); 8 and 9 = pterin ($C_6H_5N_5O$); * = 1,5-bis(ethylthio)pentane ($C_9H_{20}S_2$).
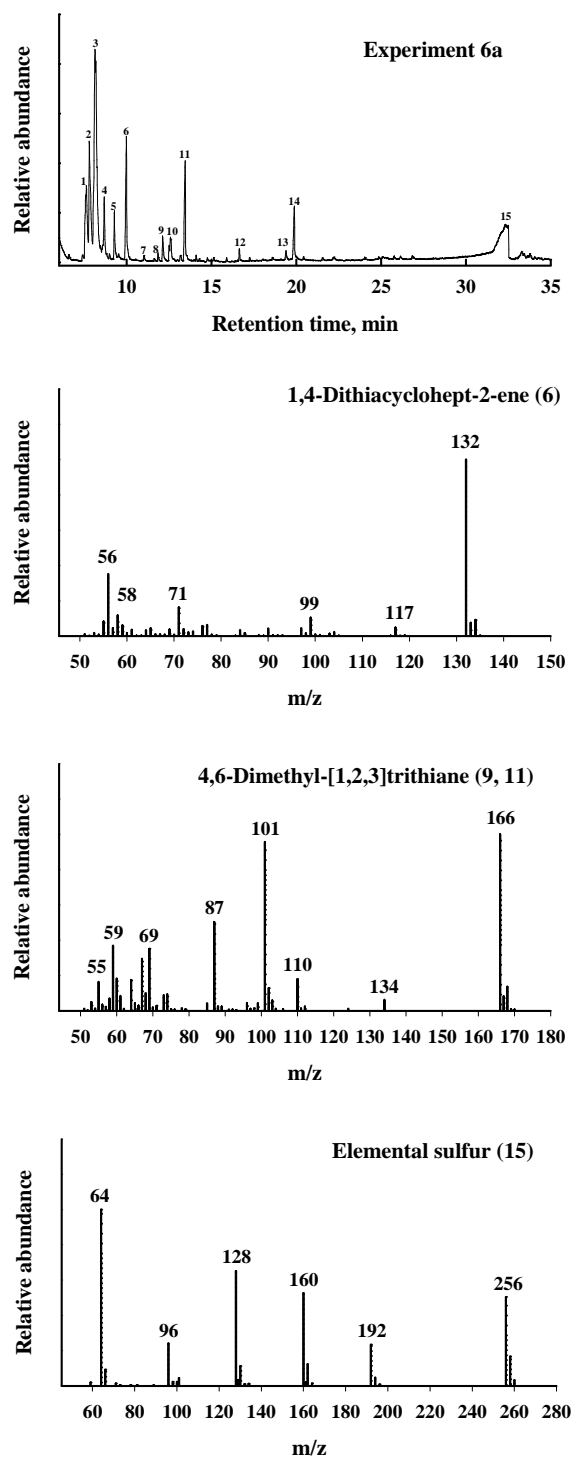
Figure 2.14. Gas chromatogram and mass spectra for major reaction products formed in Experiment 6a. The numbers of the peaks in the gas chromatogram correspond to the following compounds: 1 and 2 = 3-(methyl-thio)-thiophene ($C_5H_6S_2$); 3 and 14 = 1,2-dithiacycloheptane ($C_5H_{10}S_2$); 4 = 2-methyl-1,3-dithiacyclohexane ($C_5H_{10}S_2$); 5 = methyl butanedithioate ($C_5H_{10}S_2$) ; 6 = 1,4-dithiacyclohept-2-ene ($C_5H_8S_2$); 7 = 3-ethyl-5-methyl-1,2,4-trithiocyclopentane ($C_5H_{10}S_3$); 8 = 2-methyl-2-hydroxymethyl-1,3-dithiacyclohexane ($C_6H_{12}OS_2$); 9, 10 and 11 = 4,6-dimethyl-1,2,3-trithiacyclohexane ($C_5H_{10}S_3$); 12 = 2,2´-(1,2-ethanediyl)-bis-thiophene ($C_{10}H_{10}S_2$); 13 = 2-Methylthiophene (C_5H_6S); 15 = elemental sulfur (S).

148
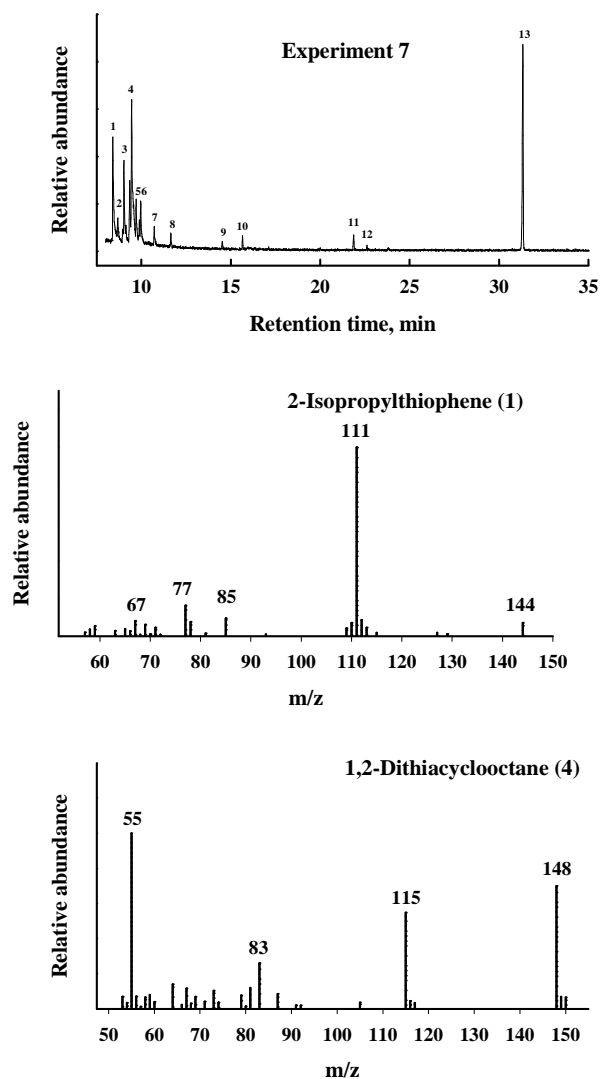
Figure 2.15. Gas chromatogram and mass spectra for major reaction products formed in Experiment 7. The numbers of the peaks in the gas chromatogram correspond to the following compounds: 1 = 2-isopropylthiophene ($C_7H_{10}S$); 2 = 2-methyl-5-(methylthio)-thiophene ($C_6H_8S_2$); 3 and 10 = unidentified compound; 4 = 1,2-dithiacyclooctane ($C_6H_{12}S_2$); 5 = ethyl butanedithioate ($C_6H_{12}S_2$); 6 =1,1-ethanediol diacetate ($C_6H_6O_2S$); 7 = 1-(4-hydroxyl-3-thienyl)-ethanone ($C_6H_6O_2S$); 8 = 2-methyl-4-(methylthio)-2,3-dihydrothiophene; 9 = 4-chloro-5-(hydroxymethyl)-1,3-benzenediol ($C_7H_7ClO_3$); 11 = 1,3-benzenedithiol ($C_6H_6S_2$); 12 = 1,6-hexanedithiol ($C_6H_{14}S_2$); 13 = elemental sulfur (S).
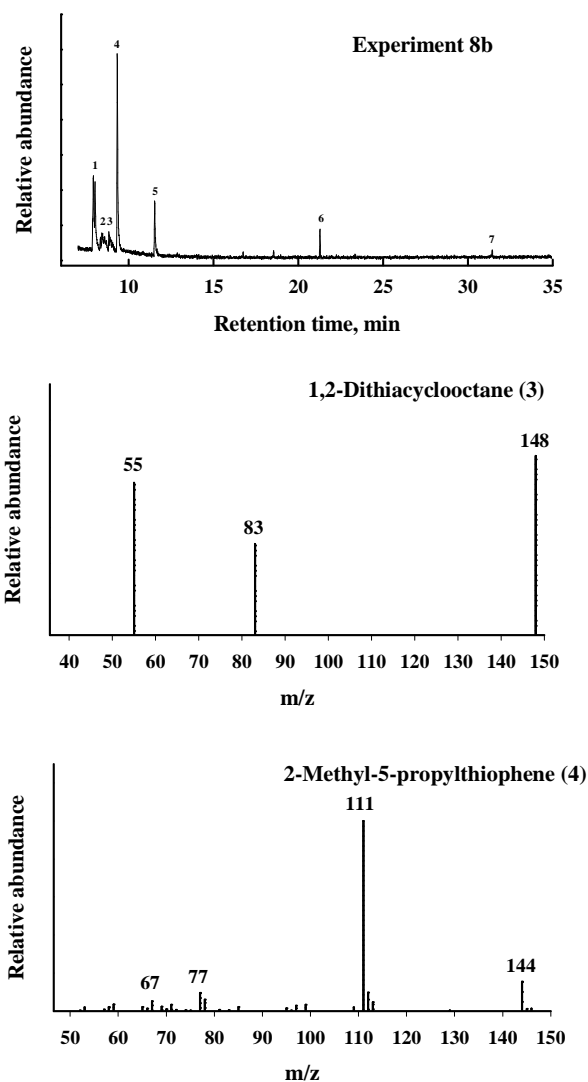
Figure 2.16. Gas chromatogram and mass spectra for major reaction products formed in Experiment 8b. The numbers of the peaks in the gas chromatogram correspond to the following compounds: 1 = 2-isopropylthiophene ($C_7H_{10}S_2$); 2 = unidentified compound; 3 = 1,2-dithiacyclooctane ($C_6H_{12}S_2$); 4 = 2-methyl-5-*n*-propylthiophene ($C_8H_{12}S$); 5 = 2-methyl-5-thiophenecarboxylic acid ($C_6H_6O_2S$); 6 = 2-(2,5-dimethylthien-3-yl)-5-methylthiophene ($C_{12}H_{14}S_2$); 7 = elemental sulfur.
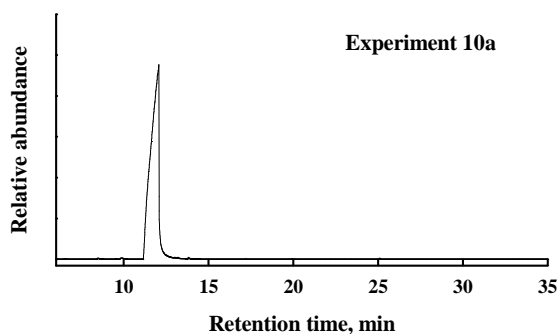
Figure 2.17. Gas chromatogram obtained at the end of Experiment 10a. The only peak detected corresponds to 2-methylbenzo[*b*]thiophene.

liquid nitrogen entering the capsule during welding. No explanation can be easily advanced for the formation of the oxygen-bearing compounds.

2.4. Thermodynamic interpretation

2.4.1. Thermodynamic properties

The results of the experiments described above can be interpreted with the aid of temperature – $\log f_{H_2S_{(g)}}$ diagrams such as those presented in the first part of the manuscript. The thermodynamic properties and heat capacity coefficients used to construct the appropriate diagrams are summarized in Table 2.8. The properties and coefficients of *n*-pentane, *n*-nonane, *n*-tetradecane and *n*-propylbenzene were taken from Helgeson et al. (1998), those of phenanthrene from Richard and Helgeson (1998), and those of *n*-butyl methyl sulfide, thiacyclopentane, 2-methylthiacyclopentane, 2-methylthiophene, 2,5-dimethylthiophene, 2-methylbenzo[*b*]thiopehene and 4,6-dimethylbenzo[*b,d*]thiophene from Richard (2001). The properties and coefficients for 1,4-butanedithiol, 1,5-pentanedithiol, 1,5-bis-(ethylthio)-pentane, 2-ethylthiophene, and 2-methyl-5-*n*-propylthiophene were estimated from group contributions given by Helgeson et al. (1998) and Richard (2001). Finally, the properties and coefficients for 1,2-dithiacyclohexane and 1,2-dithiacycloheptane were estimated in the present study from those of the corresponding cycloalkanes and thiacycloalkanes recommended by Helgeson et al. (1998) and Richard (2001), respectively, and group stoichiometry expressions written as:

$$\Xi_{1,2\text{-dithiacyclohexane}} = 2\Xi_{(6)>S} + 4\Xi_{(6)>CH_2} - \Xi_{\text{correction}} \qquad (2.18)$$

and

$$\Xi_{1,2\text{-dithiacycloheptane}} = 2\Xi_{(7)>S} + 5\Xi_{(7)>CH_2} - \Xi_{\text{correction}} \qquad , \qquad (2.19)$$

151

Table 2.8. Standard molal thermodynamic properties and heat capacity power function coefficients of liquid hydrocarbons and organic sulfur compounds considered in the calculations reported in this section.

Compound	Formula	ΔG_f° [a]	ΔH_f° [a]	S° [b]	V° [c]	C_P° [b]	a [b]	b [d]	c [e]
n-Pentane [f]	C_5H_{12}	-2084	-41207	63.04	111.7	40.13	-0.90	118.9	4.958
n-Nonane [f]	C_9H_{20}	2975	-65805	93.99	175.0	67.95	8.35	169.3	8.106
n-Tetradecane [f]	$C_{14}H_{30}$	9293	-96553	132.69	258.2	104.81	26.36	217.7	12.041
n-Propylbenzene [f]	C_9H_{12}	29909	-9128	68.82	148.8	51.17	11.32	119.3	3.804
n-Octylbenzene [f]	$C_{14}H_{22}$	36230	-39876	107.51	234.0	85.79	21.90	185.4	7.657
1,4-Butanedithiol [g]	$C_4H_{10}S_2$	4968	-25072	76.22	110.3	48.92	31.89	47.1	2.656
1,5-Pentanedithiol [g]	$C_5H_{12}S_2$	6232	-31222	83.96	126.1	55.84	33.96	60.4	3.443
n-Butyl methyl sulfide [h]	$C_5H_{12}S$	4336	-34328	72.24	124.2	47.61	19.1	83.6	3.190
1,5-Bis(ethylthio)pentane [g]	$C_9H_{20}S_2$	17545	-51554	108.24	196.2	84.25	45.44	104.8	6.711
Thiacyclopentane [h]	C_4H_8S	9213	-17147	49.67	88.7	33.55	11.33	68.5	1.600
2-Methylthiacyclopentane [h]	$C_5H_{10}S$	8355	-25054	58.63	107.5	41.07	15.25	81.1	1.456
1,2-Dithiacyclohexane [g]	$C_4H_8S_2$	15432	-20642	55.98	102.3	40.61	27.22	56.6	-3.100
1,2-Dithiacycloheptane [g]	$C_5H_{10}S_2$	9895	-23867	65.11	113.7	41.47	33.64	65.7	-10.451
2-Methylthiophene [h]	C_5H_6S	27443	10747	52.22	96.8	35.79	16.27	59.3	1.636
2-Ethylthiophene [g]	C_6H_8S	28850	4899	60.49	122.1	42.58	17.63	75.4	2.200
2,5-Dimethylthiophene [h]	C_6H_8S	27013	2465	58.49	114.5	42.61	16.74	74.7	3.210
2-Isopropylthiophene [h]	$C_7H_{10}S$	29078	-2830	66.41	131.0	47.40	20.13	85.6	1.558
2-Methyl-5-*n*-propylthiophene [g]	$C_8H_{12}S$	29685	-9533	74.5	156.9	56.18	19.41	106.8	4.394
2-Methylbenzo[*b*]thiophene [h]	C_9H_8S	44104	18898	60.40	133.3	51.09	28.94	76.7	-0.636
4,6-Dimethyldibenzo[*b,d*]thiophene [h]	$C_{14}H_{12}S$	54882	14355	78.34	182.3	72.84	50.45	97.6	-5.964

[a] cal mol^{-1} [b] cal mol^{-1}K^{-1} [c] cm^{3}mol^{-1} [d] cal mol^{-1}K^{-2} [e] cal K mol^{-1} [f] Helgeson et al. (1998) [g] Estimated in the present study – see text [h] Richard (2001)

where Ξ stand for a given thermodynamic property or heat capacity coefficient of the subscripted compound or group, or a correction brought to the group estimate for this property or coefficient to account for the fact that the two sulfur atoms are nearest neighbors in the structures of the dithiacycloalkanes. The group properties and coefficients for the $(6)>CH_2$ and $(7)>CH_2$ groups are first obtained by dividing respectively by six and seven those given by Helgeson et al. (1998) for liquid cyclohexane (C_6H_{12}) and cycloheptane (C_7H_{14}) in accord with

$$\Xi_{(6)>CH_2} = \Xi_{cyclohexane}/6 \qquad (2.20)$$

and

$$\Xi_{(7)>CH_2} = \Xi_{cycloheptane}/7 \; . \qquad (2.21)$$

These group properties and coefficients are subsequently combined with those given by Richard (2001) for liquid thiacyclohexane ($C_5H_{10}S$) and thiacycloheptane ($C_6H_{12}S$) to obtain those for the $(6)>S$ and $(7)>S$ groups in accord with

$$\Xi_{(6)>S} = \Xi_{thiacyclohexane} - 5 \times \Xi_{(6)>CH_2} \qquad (2.22)$$

and

$$\Xi_{(7)>S} = \Xi_{thiacycloheptane} - 6 \times \Xi_{(7)>CH_2} \; . \qquad (2.23)$$

Finally, the correction for the two neighboring sulfur atoms in the dithiacycloalkanes was obtained from the properties and coefficients given by Richard (2001) for sulfide (—S—) and disulfide (—S-S—) groups in saturated liquid compounds in accord with

$$\Xi_{correction} = 2\, \Xi_{-S-} - \Xi_{-S\text{-}S-} \; . \qquad (2.24)$$

This correction renders the 1,2-dithiacycloalkanes more stable compared to their isomeric 1,3- or 1,4- counterparts.

2.4.2. Redox considerations

The precipitation of elemental sulfur as a result of the oxidation of H_2S and/or organic sulfur requires the transfer of two electrons in accord with

$$S^{2-} = S^0 + 2\, e^- \qquad (2.25)$$

The transfer of electrons is accomplished by reduction of the organic sulfur compounds used as reactants in the experiments. Values of the average oxidation state of carbon (z_C) in the reactants and in some important reaction products detected by the GC-MS analysis have been calculated according to the method of Helgeson (1991) and are given in Table 2.9.

It can be deduced from this table that the reactions which involved thiacylopentane or 2-methylthiacyclopentane and H_2S gas produced compounds with exactly (or nearly exactly) the same z_C value, which means that there was no transfer of electrons and therefore no precipitation of sulfur could result from these reactions. In contrast, the reactions involving 2-methylthiophene, 2-ethylthiophene or 2,5-dimethylthiophene and H_2S gas produced compounds with significantly lower values of z_C. Elemental sulfur was formed from H_2S during these reactions because sufficient electrons were made available in the system.

Table 2.9. Average oxidation state of carbon in the reactants and products of the experiments carried out in the present study.

Experiment	Reactant	z_C	Main reaction product	z_C
1	*n*-Butyl methyl sulfide	-2	CH_4	-4
2a, 2b	Thiacyclopentane	-1.5	1,2-Dithiacyclohexane	-1.5
			1,4-Butanedithiol	-1.5
3a, 3b	2-Methylthiacyclopentane	-1.6	1,5-Bis(ethylthio)pentane	-1.78
			1,5-Pentanedithiol	-1.6
4	Benzenethiol	-0.67	None	—
5	Thiophene	-0.5	CH_4	-4
6a-6f	2-Methylthiophene	-0.8	1,2-Dithiacycloheptane	-1.6
			3-(Methylthio)-thiophene	-0.4
7	Ethylthiophene	-1.0	1,2-Dithiacyclooctane	-1.67
			2-Isopropylthiophene	-1.14
8a, 8b	2,5-Dimethylthiophene	-1.0	2-Methyl-5-*n*-propylthiophene	-1.8
			2-Methyl-5-thiophenecarboxylic acid	-0.16
9a, 9b	Benzo[*b*]thiophene	-0.5	None	—
10a, 10b	2-Methylbenzo[*b*]thiophene	-0.67	None	—
11	2-Methylthiophene +	-0.8	1,2-Dithiacycloheptane	-1.6
	2-methylbenzo[*b*]thiophene	-0.67	None	—
12	Dibenzo[*b,d*]thiophene	-0.5	None	—
13	4-Methyldibenzo[*b,d*]thiophene	-0.62	None	—
14	4,6-Dimethyldibenzo[*b,d*]thiophene	-0.71	None	—

2.4.3. Equilibrium activity and fugacity diagrams

We will now try to rationalize the experimental observations summarized above from a thermodynamic point of view by constructing equilibrium activity and fugacity diagrams for the conditions of the experiments. The following discussion is organized by categories of organic sulfur reactants.

154

2.4.3.1. *n*-Butyl methyl sulfide – It can be deduced from Tables 2.5 and 2.6 that some H_2S has been consumed during Experiment 1 (which involved *n*-butyl methyl sulfide), while some CO_2 was generated along with a smaller amount of CH_4. The generation of CO_2 from *n*-butyl methyl sulfide corresponds to an oxidation reaction which may be written for $H_{2(g)}$ as

$$C_5H_{12}S_{(l)} + 10\ H_2O_{(l)} = 5\ CO_{2(g)} + H_2S_{(g)} + 15\ H_{2(g)}\ . \qquad (2.26)$$
<div align="center">(n-butyl methyl
sulfide)</div>
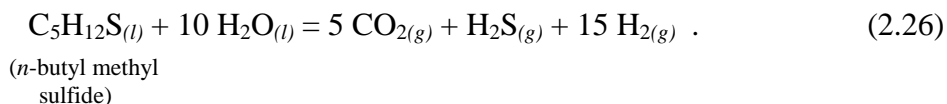
The equilibrium constant at 150ºC and 500 bar of Reaction (2.26) listed in Table 2.10 has been used together with an expression of the law of mass action written as

$$\log K_{(2.26)} = 5 \log f_{CO_{2(g)}} + \log f_{H_2S_{(g)}} + 15 \log f_{H_{2(g)}} - \log a_{C_5H_{12}S_{(l)}} \qquad (2.27)$$

to construct the fugacity diagram shown in Figure 2.18. Since only gases appear to have been produced in the reaction, this diagram has been constructed for a unit activity of *n*-butyl methyl sulfide. The vertical grey line in the diagram corresponds to the fugacity of pure H_2S gas at the temperature and pressure conditions of the experiment ($\log f_{H_2S_{(g)}} = 2.30$). From the mole percentage shown in Table 2.6, it can be estimated that the partial pressure of CO_2 gas may have reached 5-7 bar at the end of the experiment, which would be consistent with $\log f_{CO_{2(g)}} \sim 0.7$-$0.8$ and $f_{H_{2(g)}} \sim 0.025$ bar. The latter value would correspond to an amount of H_2 gas which would most likely be undetectable by Raman spectroscopy. Therefore, it is probable that *n*-butyl methyl sulfide established equilibrium with CO_2, H_2 and H_2S in Experiment 1. However, H_2S is a product in Reaction (2.26), whereas the mass balance calculation in Table 2.5 suggests that H_2S was consumed in the reaction. Compositional considerations indicate that a consumption of H_2S would require *n*-butyl methyl sulfide to be reduced to an *n*-alkane (or methylalkane) with a number of carbon atoms lower than 5, since the reduction to *n*-pentane appears to be a colinear reaction which does not involve H_2S:

Table 2.10. Logarithmic values of the equilibrium constants as a function of temperature at 500 bar for reactions involving the organic sulfur reactants used in the experiments and the products identified by the GC/MS analysis – see Table 2.7 and Figure 2.10.

Reactant	Product		Reactions	100ºC	150ºC	200ºC	250ºC	300ºC
n-Butyl methyl sulfide	CO_2 gas	(2.26)	$C_5H_{12}S_{(l)} + 10\ H_2O_{(l)} = 5\ CO_{2(g)} + H_2S_{(g)} + 15\ H_{2(g)}$	-30.548	-17.933	-8.277	-0.716	5.302
	n-Pentane	(2.28)	$C_5H_{12}S_{(l)} = C_5H_{12(l)} + S_{(c\ or\ l)}$	3.665	3.216	2.880	2.625	2.428
	Methane	(2.29)	$C_5H_{12}S_{(l)} + 4\ H_2S_{(g)} = 5\ CH_{4(g)} + 5\ S_{(c\ or\ l)}$	19.170	16.758	14.900	13.410	12.181
Thiacyclopentane	1,2-Dithiacyclohexane	(2.32)	$C_4H_8S_{(l)} + H_2S_{(g)} = C_4H_8S_2 + H_{2(g)}$	-3.461	-3.306	-3.167	-3.041	-2.926
	1,4-Butanedithiol	(2.33)	$C_4H_8S_{(l)} + H_2S_{(g)} = C_4H_{10}S_{2(l)}$	-3.324	-3.474	-3.583	-3.667	-3.735
2-Methylthiacyclopentane	1,5-Pentanedithiol	(2.34)	$C_5H_{10}S_{(l)} + H_2S_{(g)} = C_5H_{12}S_{2(l)}$	-4.603	-4.639	-4.662	-4.678	-4.693
	1,5-Bis(ethylthio)pentane	(2.35)	$9\ C_5H_{10}S_{(l)} + 5\ H_2S_{(g)} = 5\ C_9H_{20}S_{2(l)} + 4\ S_{(c\ or\ l)}$	-40.090	-40.330	-40.477	-40.607	-40.751
2-Methylthiophene	1,2-Dithiacycloheptane	(2.57)	$C_5H_6S_{(l)} + 2\ H_2S_{(g)} = C_5H_{10}S_{2(l)} + S_{(c\ or\ l)}$	-2.780	-4.447	-5.743	-6.778	-7.620
2-Ethylthiophene	2-Isopropylthiophene	(2.58)	$7\ C_6H_8S_{(l)} + 2\ H_2S_{(g)} = 6\ C_7H_{10}S_{(l)} + 3\ S_{(c\ or\ l)}$	2.386	-0.499	-2.763	-4.597	-6.119
2,5-Dimethylthiophene	2-Methyl-5-n-propylthiophene	(2.59)	$4\ C_6H_8S_{(l)} + 2\ H_2S_{(g)} = 3\ C_8H_{12}S_{(l)} + 3\ S_{(c\ or\ l)}$	-2.459	-4.309	-5.722	-6.838	-7.740
2-Methylbenzo[b]thiophene	1,5-Bis(ethylthio)pentane	(2.81)	$C_9H_8S_{(l)} + 6\ H_2S_{(g)} = C_9H_{20}S_{2(l)} + 5\ S_{(c\ or\ l)}$	-22.734	-25.231	-27.101	-28.555	-29.713
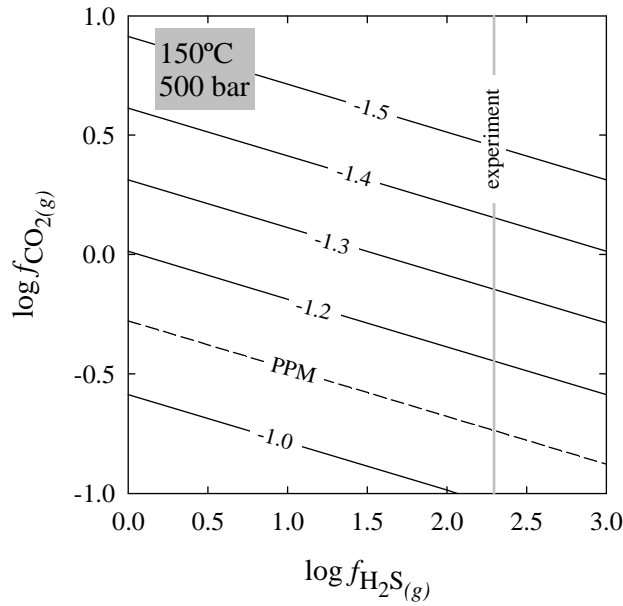
Figure 2.18. Log $f_{H_2S_{(g)}}$ – log $f_{CO_{2(g)}}$ diagram representing the equilibrium relations among n-butyl methyl sulfide, H_2S gas, CO_2 gas and H_2 gas. The diagram has been constructed for a unit activity of n-butyl methyl sulfide. The labels on the solid equilibrium lines correspond to logarithmic values of the fugacity of H_2 gas. The dashed line corresponds to the pyrite-pyrrhotite-magnetite (PPM) buffer. The vertical grey line corresponds to the logarithm of the fugacity of H_2S estimated for the conditions of the experiment.

$$C_5H_{12}S_{(l)} \quad = \quad C_5H_{12(l)} + S_{(c \text{ or } l)} \quad\quad\quad (2.28)$$
$$\text{(}n\text{-butyl methyl} \quad\quad \text{(}n\text{-pentane)}$$
$$\text{sulfide)}$$
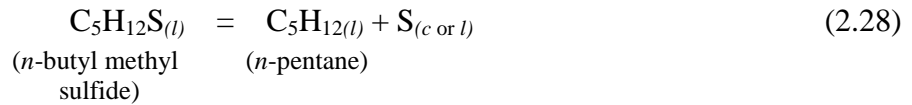
It can be deduced from the log K values listed in Table 2.10 that Reaction (2.28) is favored, i.e. n-pentane should be ~ 1600 times more abundant than n-butyl methyl sulfide. However, from the GC-MS analysis of the liquid phase at the end of the experiment, it appears that this reaction did not proceed. The production of methane from n-butyl methyl sulfide would consume H_2S in accord with

$$C_5H_{12}S_{(l)} \; + 4\,H_2S_{(g)} \quad = \quad 5\,CH_{4(g)} + 5\,S_{(c \text{ or } l)} \quad\quad\quad (2.29)$$
$$\text{(}n\text{-butyl methyl} \quad\quad\quad \text{(methane)}$$
$$\text{sulfide)}$$
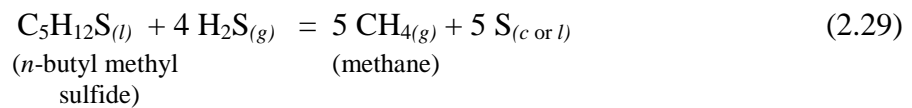
Considering the log K value listed in Table 2.10 for Reaction (2.29) in an expression of the law of mass action written as

$$\log f_{CH_{4(g)}} = \left(\log K_{(2.29)} + 4\log f_{H_2S_{(g)}}\right)/5 \quad\quad\quad (2.30)$$

and the fugacity of H_2S obtained in the experiment (log $f_{H_2S_{(g)}} = 2.30$), we obtain for methane

$$\log f_{CH_{4(g)}} = 5.189\,. \quad\quad\quad (2.31)$$

This result is in agreement with thermodynamic arguments presented by Shock (1988) and Helgeson et al. (1993) which demonstrate that methane cannot reach equilibrium with CO_2

157

gas or the liquid hydrocarbons of crude oils at the temperature and pressure conditions characteristic of sedimentary basins. The fugacities of methane at equilibrium with CO_2 or hydrocarbons are in excess of tens of thousands of bars, which corresponds to pressures that are physically unattainable at sedimentary depths. Accordingly, we will consider that methane was produced at a very slow rate, and that the equilibrium state corresponding to Reaction (2.29) was not established at the end of Experiment 1.

It can be deduced from the stoichiometries of Reactions (2.26) and (2.28) that 0.2 mole of H_2S is produced for each mole of CO_2 produced, while 4 moles of H_2S are consumed for each mole of CH_4 produced. Combining these figures with the number of moles of H_2S estimated in Table 2.5 from pressure measurements before and after Experiment 1 ($2.521 \cdot 10^{-3}$ mol and $2.294 \cdot 10^{-3}$ mol, respectively) and the number of moles of H_2S, CO_2 and CH_4 after this experiment calculated from the mole fractions listed in Table 2.6 ($2.294 \cdot 10^{-3}$ mol, $2.789 \cdot 10^{-5}$ mol and $2.324 \cdot 10^{-6}$ mol, respectively), we obtain a net consumption of $3.721 \cdot 10^{-6}$ mol of H_2S, which is 61 times smaller than the difference between the number of moles of H_2S estimated before and after the experiment. The reason for this disagreement may be due to a leakage problem during the piercing of the capsule.

2.4.3.2. Thiacyclopentanes – No elemental sulfur formed as a result of the reaction between thiacyclopentane (Experiments 2a and 2b) and 2-metylthiacyclopentane (Experiments 3a and 3b) with H_2S. However, a significant amount of H_2S was consumed in these experiments (Table 2.5). The major reaction products identified by the GC-MS analysis are 1,2-dithiacyclohexane and 1,4-butanedithiol for the experiments with thiacyclopentane, and 1,5-bis(ethylthio)pentane and 1,5-pentanedithiol for the experiments with 2-methylthiacyclopentane. With the exception of 1,5-bis(ethylthio)pentane, it can be deduced from Table 2.9 that the average oxidation state of carbone (z_C) in these products is the same as that in the reactants from which they were generated. These observations are consistent with the following reactions:

$$C_4H_{8}S_{(l)} + H_2S_{(g)} \quad = \quad C_4H_8S_{2(l)} + H_{2(g)} \tag{2.32}$$
$$\text{(thiacyclopentane)} \qquad \text{(1,2-dithiacyclohexane)}$$

and

$$C_4H_8S_{(l)} + H_2S_{(g)} \quad = \quad C_4H_{10}S_{2(l)} \tag{2.33}$$
$$\text{(thiacyclopentane)} \qquad \text{(1,4-butanedithiol)}$$

for Experiments 2a and 2b, and

$$C_5H_{10}S_{(l)} + H_2S_{(g)} \quad = \quad C_5H_{12}S_{2(l)} \tag{2.34}$$
$$\text{(2-methylthiacyclopentane)} \qquad \text{(1,5-pentanedithiol)}$$

158

and

$$9 \ C_5H_{10}S_{(l)} + 5 \ H_2S_{(g)} \quad = \quad 5 \ C_9H_{20}S_{2(l)} + 4 \ S_{(c \ or \ l)} \tag{2.35}$$

$$\text{(2-methylthiacycopentane)} \qquad \text{(1,5-bis(ethylthio)pentane)}$$
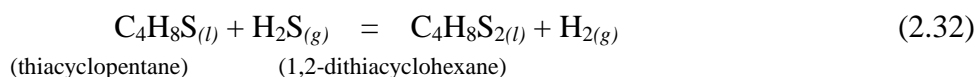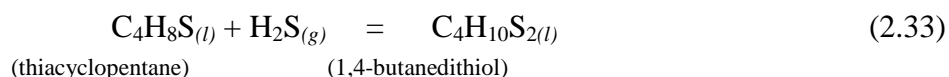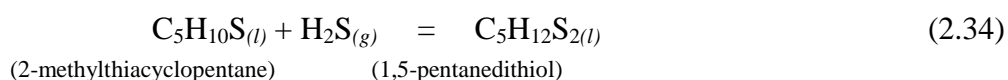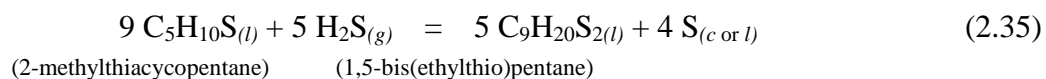
for Experiments 3a and 3b. The stoichiometries of these reactions are consistent with the consumption of H_2S noted in Table 2.5. Logarithmic values of the equilibrium constants for Reactions (2.32)-(2.35) have been computed as a function of temperature at 500 bar and listed in Table 2-10.

Since Reaction (2.32) appears to be redox dependent, we will discuss it separately. The log K value at 150ºC and 500 bar listed in Table 2.10 for this reaction has been used together with an expression of the law of mass action written as

$$\log\left(a_{C_4H_8S_{(l)}}/a_{C_4H_8S_{2(l)}}\right) = \log f_{H_2S_{(g)}} - \log f_{H_{2(g)}} - \log K_{(2.32)} \tag{2.36}$$

to generate the activity-fugacity diagram depicted in Figure 2.19. It can be deduced from this diagram that for redox conditions close to the pyrite-pyrrhotite-magnetite (PPM) buffer and the value of $\log f_{H_2S_{(g)}}$ established in the experiment the molar proportions of thiacyclopentane and 1,2-dithiacyclohexane would be nearly equal. This again suggests that an equilibrium state may have been reached among thiacyclopentane and 1,2-dithiacyclohexane and H_2S gas in Experiment 2a.

The reaction between thiacylopentane and H_2S gas also produced a significant amount of 1,4-butanedithiol in accord with Reaction (2.33), for which the expression of the law of mass action is:

$$\log\left(a_{C_4H_{10}S_{2(l)}}/a_{C_4H_8S_{(l)}}\right) = \log K_{(2.33)} + \log f_{H_2S_{(g)}} \ . \tag{2.37}$$

Taking this expression together with the value listed for log $K_{(2.33)}$ in Table 2.10 and the value of $\log f_{H_2S_{(g)}}$ considered representative for the experiments, the logarithm of the activity ratio between 1,4-butanedithiol and thiacyclopentane in Equation (2.37) at the end of the experiment would have been

$$\log\left(a_{C_4H_{10}S_{2(l)}}/a_{C_4H_8S_{(l)}}\right) = \text{-1.177} \ . \tag{2.38}$$
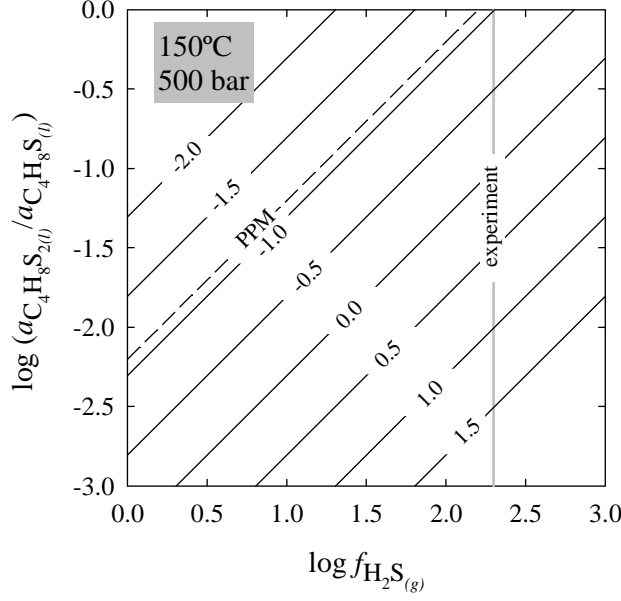
Figure 2.19. Log $f_{H_2S_{(g)}}$ – log diagram at 150°C and 500 bar. The labels on the solid equilibrium lines correspond to logarithmic values of the fugacity of H_2 gas. The dashed line corresponds to the pyrite-pyrrhotite-magnetite (PPM) buffer. The vertical grey line corresponds to the logarithm of the fugacity of H_2S estimated for the conditions of the experiment.

Let us now consider the relative stabilities of thiacyclopentane, 1,2-dithiacyclohexane and 1,4-butanedithiol in terms of the redox conditions in the experiments. Reactions (2.32) and (2.33) represent in fact combined sums of the following redox half-reactions:

$$C_4H_8S_{(l)} + 5.5\ O_{2(g)} = 4\ CO_{2(g)} + H_2S_{(g)} + 3\ H_2O_{(l)}\quad, \tag{2.39}$$

(thiacyclopentane)

$$C_4H_8S_{2(l)} + 5\ O_{2(g)} = 4\ CO_{2(g)} + 2\ H_2S_{(g)} + 2\ H_2O_{(l)} \tag{2.40}$$

(1,2-dithiacyclohexane)

and

$$C_4H_{10}S_{2(l)} + 5.5\ O_{2(g)} = 4\ CO_{2(g)} + 2\ H_2S_{(g)} + 3\ H_2O_{(l)} \tag{2.41}$$

(1,4-butanedithiol)
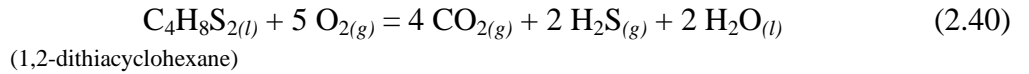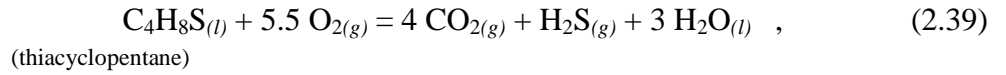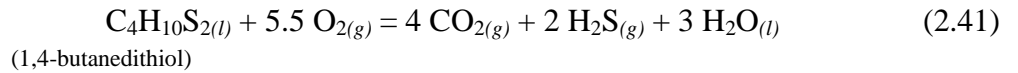
for which the equilibrium constants are

$$\log K_{(2.39)} = 290.931\quad, \tag{2.42}$$

$$\log K_{(2.40)} = 267.509 \tag{2.43}$$

and

$$\log K_{(2.41)} = 294.405 \tag{2.44}$$

These equilibrium constants have been used together with expressions of the law of mass action written as

$$\log K_{(2.39)} = 4 \log f_{CO_{2(g)}} + \log f_{H_2S_{(g)}} - \log a_{C_4H_8S_{(l)}} - 5.5 \log f_{O_{2(g)}}\ , \tag{2.45}$$

$$\log K_{(2.40)} = 4 \log f_{CO_{2(g)}} + 2 \log f_{H_2S_{(g)}} - \log a_{C_4H_8S_{2(l)}} - 5 \log f_{O_{2(g)}} \tag{2.46}$$

and

$$\log K_{(2.40)} = 4 \log f_{CO_{2(g)}} + 2 \log f_{H_2S_{(g)}} - \log a_{C_4H_{10}S_{2(l)}} - 5.5 \log f_{O_{2(g)}} \qquad (2.47)$$

to generate the $\log f_{O_{2(g)}} - \log a_{C_nH_mS_{p(l)}}$ diagram shown in Figure 2.20 *(a)*. This diagram has been constructed for $\log f_{H_2S_{(g)}} = 2.30$ and a fugacity of CO_2 gas fixed at 1 bar (which accounts for the small amount of CO_2 produced in Experiment 2b – see Table 2.5). It can be deduced from this diagram that the redox conditions for which thiacyclopentane ($C_4H_8S_{(l)}$), 1,2-dithiacyclohexane ($C_4H_8S_{2(l)}$) and 1,4-butanedithiol ($C_4H_{10}S_{2(l)}$) would constitute most of the liquid phase after the reaction are within one log unit from the $\log f_{O_{2(g)}}$ value defined by the pyrite-pyrrhotite-magnetite (PPM) buffer. In addition, it appears that the concentration of 1,2-dithiacyclohexane ($C_4H_8S_{2(l)}$) would be similar to that of thiacyclopentane ($C_4H_8S_{(l)}$), but higher than that of 1,4-butanedithiol ($C_4H_{10}S_{2(l)}$). The latter observation is in agreement with the relative concentrations of the two products deduced from the gas chromatogram shown in Figure 2.11. It can also be deduced from Figure 2.20 *(a)* that the relative abundances of thiacyclopentane ($C_4H_8S_{(l)}$) and 1,4-butanedithiol ($C_4H_{10}S_{2(l)}$) are independent of $\log f_{O_{2(g)}}$, which is consistent with the fact that electrons are conserved among these two compounds and H_2S in Reaction (2.33). In contrast, these relative abundances depend on $\log f_{H_2S_{(g)}}$, as can be seen in Figure 2.20 *(b)*. This figure has been constructed for $\log f_{O_{2(g)}} = -52.45$ and $\log f_{CO_{2(g)}} = 0$.
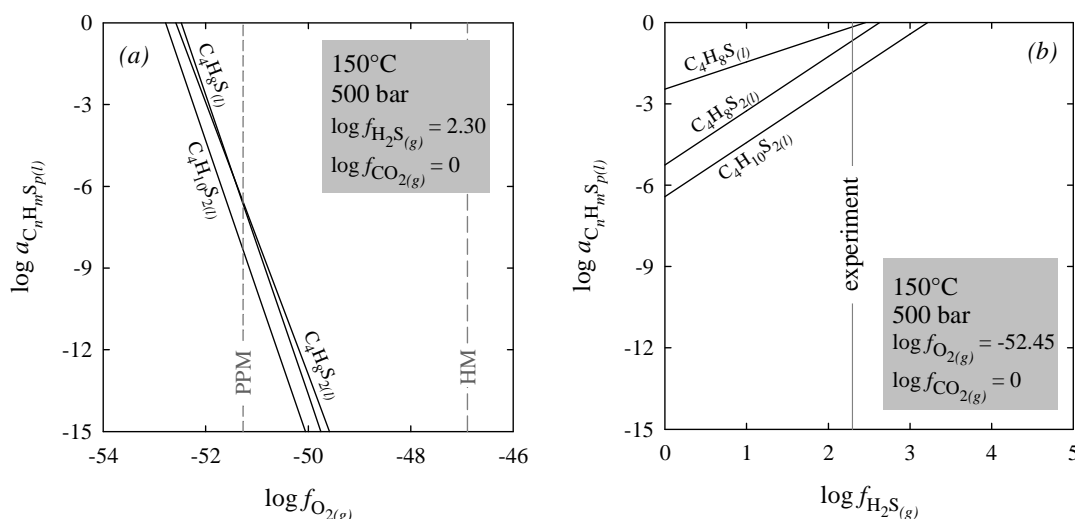
Figure 2.20. Log $f_{O_{2(g)}}$ – log $a_{C_nH_mS_{p(l)}}$ and log $f_{H_2S_{(g)}}$ – log $a_{C_nH_mS_{p(l)}}$ diagrams showing the relative abundances of thiacyclopentane ($C_4H_8S_{(l)}$), 1,2-dithiacyclohexane ($C_4H_8S_{2(l)}$), and 1,4-butanedithiol ($C_4H_{10}S_{2(l)}$) for Experiments 2a and 2b.

The relative abundances of 2-methylthiacyclopentane ($C_5H_{10}S_{(l)}$), 1,5-pentanedithiol ($C_5H_{12}S_{2(l)}$) and 1,5-bis(ethylthio)pentane ($C_9H_{20}S_{2(l)}$) at the end of Experiments 3a and 3b can be evaluated from the reactions

$$C_5H_{10}S_{(l)} + 7\ O_{2(g)} = 5\ CO_{2(g)} + H_2S_{(g)} + 4\ H_2O_{(l)} \quad , \tag{2.48}$$

<div style="text-align:center">(2-methylthia-
cyclopentane)</div>

$$C_5H_{12}S_{2(l)} + 7\ O_{2(g)} = 5\ CO_{2(g)} + 2\ H_2S_{(g)} + 4\ H_2O_{(l)} \tag{2.49}$$

<div style="text-align:center">(1,5-pentanedithiol)</div>

and

$$C_9H_{20}S_{2(l)} + 13\ O_{2(g)} = 9\ CO_{2(g)} + 2\ H_2S_{(g)} + 8\ H_2O_{(l)} \quad , \tag{2.50}$$

<div style="text-align:center">(1,5-bis(ethylthio)pentane)</div>
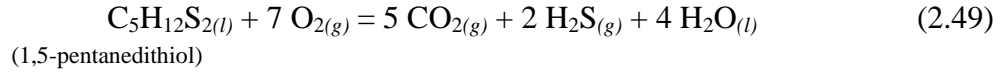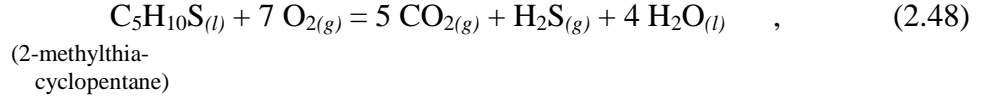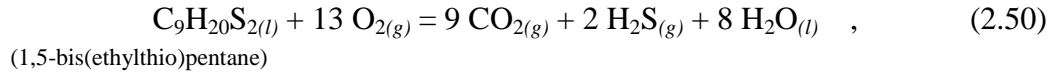
for which the equilibrium constants at 150ºC and 500 bar are

$$\log K_{(2.48)} = 367.597 \tag{2.51}$$

$$\log K_{(2.49)} = 372.237 \tag{2.52}$$

$$\log K_{(2.50)} = 687.264\ . \tag{2.53}$$

These equilibrium constants have been used together with the following expressions of the law of mass action

$$\log K_{(2.48)} = 5 \log f_{CO_{2(g)}} + \log f_{H_2S_{(g)}} - \log a_{C_5H_{10}S_{(l)}} - 7 \log f_{O_{2(g)}} \quad , \tag{2.54}$$

$$\log K_{(2.49)} = 5 \log f_{CO_{2(g)}} + 2 \log f_{H_2S_{(g)}} - \log a_{C_5H_{10}S_{2(l)}} - 7 \log f_{O_{2(g)}} \tag{2.55}$$

and

$$\log K_{(2.50)} = 9 \log f_{CO_{2(g)}} + 2 \log f_{H_2S_{(g)}} - \log a_{C_9H_{20}S_{2(l)}} - 13 \log f_{O_{2(g)}} \tag{2.56}$$

to generate the $\log f_{O_{2(g)}} - \log a_{C_nH_mS_{p(l)}}$ and $\log f_{H_2S_{(g)}} - \log a_{C_nH_mS_{p(l)}}$ diagrams shown in Figure 2.21 *(a)* and *(b)*. It can be deduced from these diagrams that comparable activities of the reactant and the two major products are obtained for redox conditions which again are slightly more reducing than those corresponding to the pyrite-pyrrhotite-magnetite buffer. It should be noted here that although 1,5-bis(ethylthio)pentane ($C_9H_{20}S_{2(l)}$) was formed in higher amounts compared to 1,5-pentanedithiol ($C_5H_{12}S_{2(l)}$) in Experiments 3a and 3b (see Figure 2.12), consideration of Figure 2.21 *(a)* indicates that this only happens for values of $a_{C_nH_mS_{p(l)}}$ > 1. However, lowering the value of $\log f_{CO_{2(g)}}$ would make the equilibrium lines for $C_9H_{20}S_{2(l)}$ and $C_5H_{12}S_{2(l)}$ to intersect at lower values of $\log a_{C_nH_mS_{p(l)}}$.
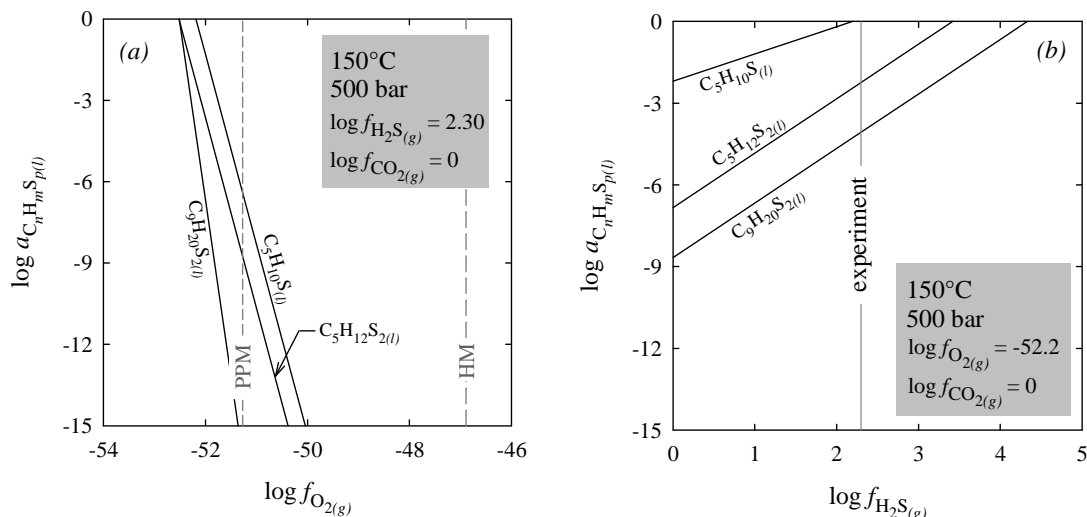
Figure 2.21. Log $f_{O_{2(g)}}$ – log $a_{C_nH_mS_{p(l)}}$ and log $f_{H_2S_{(g)}}$ – log $a_{C_nH_mS_{p(l)}}$ diagrams showing the relative abundances of 2-methylthiacyclopentane ($C_5H_{10}S_{(l)}$), 1,5-pentanedithiol ($C_5H_{12}S_{2(l)}$) and 1,5-bis(ethylthio)pentane ($C_9H_{20}S_{2(l)}$) for Experiments 3a and 3b.

2.4.3.3. Thiophenes

Besides some CO_2 and CH_4, no other products were generated during Experiment 5, which involved thiophene and H_2S. This experiment will not be further discussed.

Elemental sulfur formed as a result of the reactions of 2-methylthiophene (Experiments 6a-6f), 2-ethylthiophene (Experiment 7), and 2,5-dimethylthiophene (Experiments 8a and 8b) with H_2S. A significant amount of H_2S was consumed in Experiments 6a-6f, 7, 8a and 8b (Table 2.5). Other major products detected by the GC-MS analysis include 1,2-dithiacycloheptane (Experiments 6a-6f), 1,2-dithiacyclooctane (Experiments 7, 8a and 8b), 2-isopropylthiophene (Experiment 7), and 2-methyl-5-n-propylthiophene (Experiments 8a and 8b). In the absence of estimates for the thermodynamic properties for 1,2-dithiacyclooctane, the reactions considered for the discussion are the following:

$$C_5H_6S_{(l)} + 2\ H_2S_{(g)} = C_5H_{10}S_{2(l)} + S_{(c\ or\ l)}\ , \tag{2.57}$$
$$\text{(2-methylthiophene)} \qquad \text{(1,2-dithiacycloheptane)}$$

$$7\ C_6H_8S_{(l)} + 2\ H_2S_{(g)} = 6\ C_7H_{10}S_{(l)} + 3\ S_{(c\ or\ l)} \tag{2.58}$$
$$\text{(2-ethylthiophene)} \qquad \text{(2-isopropylthiophene)}$$

and

$$4\ C_6H_8S_{(l)} + 2\ H_2S_{(g)} = 3\ C_8H_{12}S_{(l)} + 3\ S_{(c\ or\ l)}\ . \tag{2.59}$$
$$\text{(2,5-dimethylthiophene)} \qquad \text{(2-methyl-5-}n\text{-propylthiophene)}$$
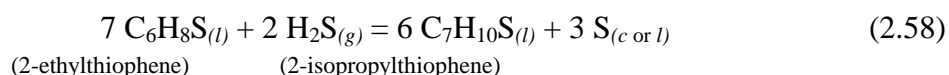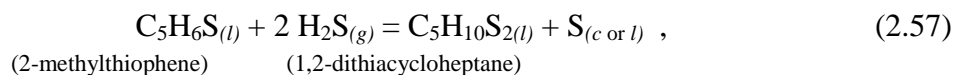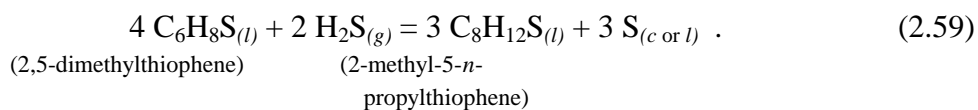
Logarithmic values of the equilibrium constants for Reactions (2.57)-(2.59) have been computed as a function of temperature at 500 bar and listed in Table 2-10. The relative

abundances of the various reactants and products are represented as a function of $\log f_{O_{2(g)}}$ and $\log f_{H_2S_{(g)}}$ in Figure 2.22 *(a)* and *(b)* for Experiments 6a-6f, in Figure 2.23 *(a)* and *(b)* for Experiment 7, and in Figure 2.24 *(a)* and *(b)* for Experiments 8a and 8b. The equilibrium lines in these figures correspond to the following reactions:

$$C_5H_6S_{(l)} + 6\ O_{2(g)} = 5\ CO_{2(g)} + H_2S_{(g)} + 2\ H_2O_{(l)}\ , \qquad (2.60)$$
(2-methylthiophene)

$$C_5H_{10}S_{2(l)} + 6.5\ O_{2(g)} = 5\ CO_{2(g)} + 2\ H_2S_{(g)} + 3\ H_2O_{(l)}\ , \qquad (2.61)$$
(1,2-dithiacyclopentane)

$$C_6H_8S_{(l)} + 7.5\ O_{2(g)} = 6\ CO_{2(g)} + H_2S_{(g)} + 3\ H_2O_{(l)}\ , \qquad (2.62)$$
(2-ethylthiophene)

$$C_7H_{10}S_{(l)} + 9\ O_{2(g)} = 7\ CO_{2(g)} + H_2S_{(g)} + 4\ H_2O_{(l)}\ , \qquad (2.63)$$
(2-isopropylthiophene)

$$C_6H_8S_{(l)} + 7.5\ O_{2(g)} = 6\ CO_{2(g)} + H_2S_{(g)} + 3\ H_2O_{(l)} \qquad (2.64)$$
(2,5-dimethylthiophene)

and

$$C_8H_{12}S_{(l)} + 10.5\ O_{2(g)} = 8\ CO_{2(g)} + H_2S_{(g)} + 5\ H_2O_{(l)} \qquad (2.65)$$
(2-methyl-5-*n*-propylthiophene)
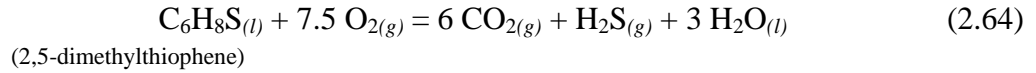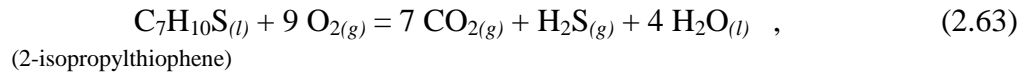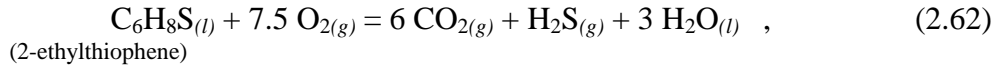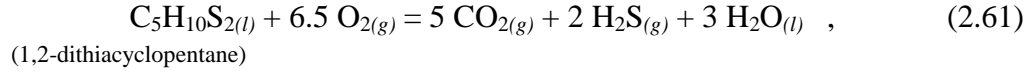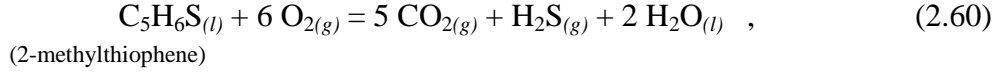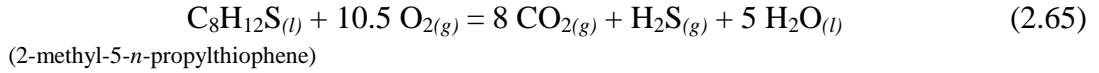
for which the equilibrium constants at 150ºC and 500 bar are

$$\log K_{(2.60)} = 320.221 \qquad (2.66)$$
$$\log K_{(2.61)} = 346.573 \qquad (2.67)$$
$$\log K_{(2.62)} = 398.151 \qquad (2.68)$$
$$\log K_{(2.63)} = 475.545 \qquad (2.69)$$
$$\log K_{(2.64)} = 397.287 \qquad (2.70)$$

and

$$\log K_{(2.65)} = 553.056\ . \qquad (2.71)$$

The equilibrium lines have been drawn from the following expressions of the law of mass action:

$$\log K_{(2.60)} = 5 \log f_{CO_{2(g)}} + \log f_{H_2S_{(g)}} - \log a_{C_5H_6S_{(l)}} - 6 \log f_{O_{2(g)}}\ , \qquad (2.72)$$

$$\log K_{(2.61)} = 5 \log f_{CO_{2(g)}} + 2 \log f_{H_2S_{(g)}} - \log a_{C_5H_{10}S_{2(l)}} - 6.5 \log f_{O_{2(g)}}\ , \qquad (2.73)$$

$$\log K_{(2.62)} = 6 \log f_{CO_{2(g)}} + \log f_{H_2S_{(g)}} - \log a_{C_6H_8S_{(l)}} - 7.5 \log f_{O_{2(g)}}\ , \qquad (2.74)$$

$$\log K_{(2.63)} = 7 \log f_{CO_{2(g)}} + \log f_{H_2S_{(g)}} - \log a_{C_7H_{10}S_{(l)}} - 9 \log f_{O_{2(g)}}\ , \qquad (2.75)$$

$$\log K_{(2.64)} = 6 \log f_{CO_{2(g)}} + \log f_{H_2S_{(g)}} - \log a_{C_6H_8S_{(l)}} - 7.5 \log f_{O_{2(g)}}\ , \qquad (2.76)$$

and

$$\log K_{(2.60)} = 5 \log f_{CO_{2(g)}} + \log f_{H_2S_{(g)}} - \log a_{C_5H_6S_{(l)}} - 6 \log f_{O_{2(g)}} \quad . \quad (2.77)$$

It can be deduced from Figures 2.22-2.24 that comparable concentrations of the reactants and products in Experiments 6a-6f, 7, 8a and 8b are again obtained for $\log f_{O_{2(g)}}$ values which are in the -52.2 to -52.5 range, i.e. slightly more reducing than the pyrite-pyrrhotite-magnetite (PPM) buffer.
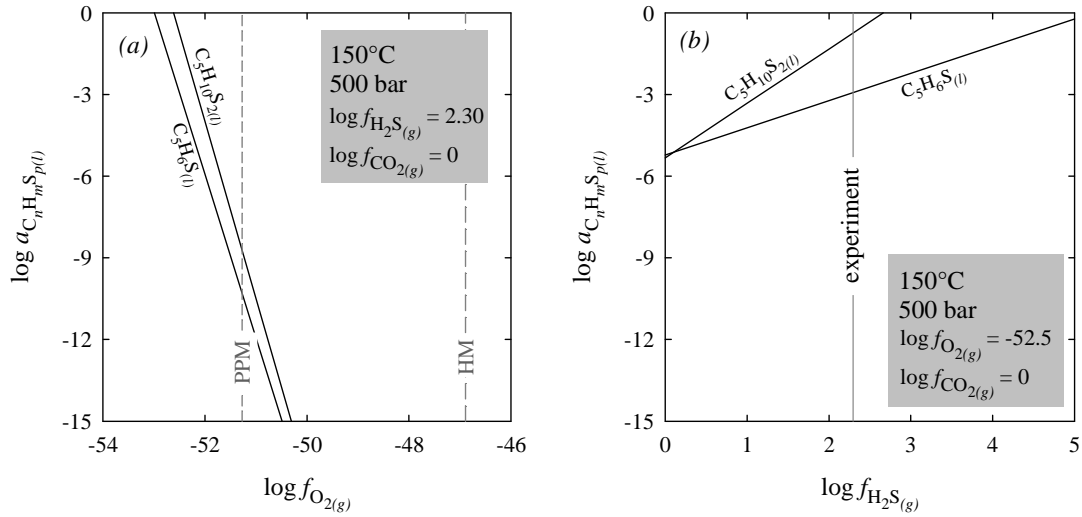
Figure 2.22. Log $f_{O_{2(g)}}$ – log $a_{C_nH_mS_{p(l)}}$ and log $f_{H_2S_{(g)}}$ – log $a_{C_nH_mS_{p(l)}}$ diagrams showing the relative abundances of 2-methylthiophene ($C_5H_6S_{(l)}$) and 1,2-dithiaheptane ($C_5H_{10}S_{2(l)}$) for Experiments 6a-6f.
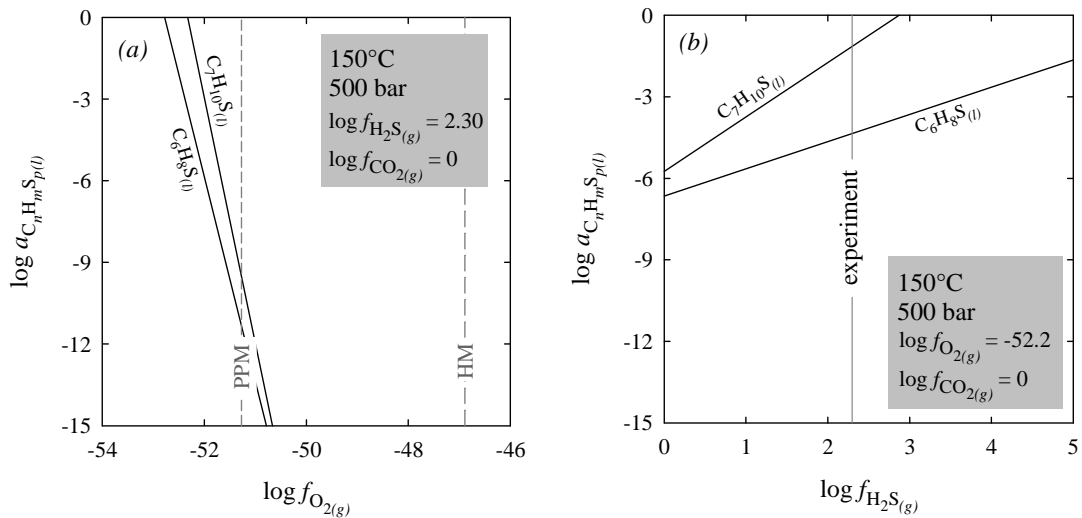
Figure 2.23. Log $f_{O_{2(g)}}$ – log $a_{C_nH_mS_{p(l)}}$ and log $f_{H_2S_{(g)}}$ – log $a_{C_nH_mS_{p(l)}}$ diagrams showing the relative abundances of 2-ethylthiophene ($C_6H_8S_{(l)}$) and 2-isopropylthiophene ($C_5H_{10}S_{2(l)}$) for Experiment 7.
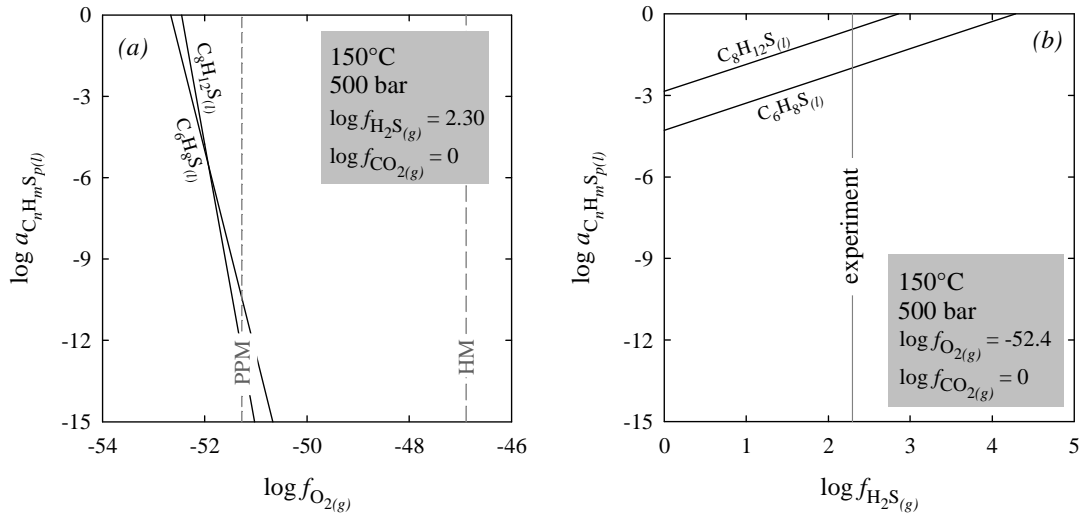
Figure 2.24. Log $f_{O_{2(g)}}$ – log $a_{C_nH_mS_{p(l)}}$ and log $f_{H_2S_{(g)}}$ – log $a_{C_nH_mS_{p(l)}}$ diagrams showing the relative abundances of 2,5-dimethylthiophene ($C_6H_8S_{(l)}$) and 2-methyl-5-*n*-propylthiophene ($C_8H_{12}S_{(l)}$) for Experiments 8a and 8b.

As noted above, significant amounts of elemental sulfur were formed at the end of the experiments in which thiophenes were used as reactants, i.e. Experiments 6a-6f, 7, 8a and 8b. The stability field of sulfur can be delimited in a log $f_{O_{2(g)}}$ – log $f_{H_2S_{(g)}}$ diagram by considering the reaction

$$S_{(c \text{ or } l)} + H_2O_{(l)} = H_2S_{(g)} + 0.5\ O_{2(g)} \tag{2.78}$$
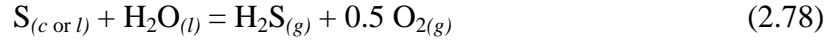
for which the equilibrium constant at 150°C and 500 bar is

$$\log K_{(2.78)} = -21.904\ . \tag{2.79}$$

This value was used together with an expression of the law of mass action written as

$$\log K_{(2.78)} = \log f_{H_2S_{(g)}} + 0.5 \log f_{O_{2(g)}} \tag{2.80}$$

to generate the stability diagram shown in Figure 2.25. It can be deduced from this diagram that for a value of log $f_{H_2S_{(g)}}$ which is consistent with the experimental conditions, equilibrium with elemental sulfur would requires a log $f_{O_{2(g)}}$ value which is far more oxidizing than those estimated from the composition of the liquid phase at the end of the experiments. The reason for this is not obvious at the present stage. However, although we do not have much constraint for this, adopting higher values of $f_{CO_{2(g)}}$ in the construction of the log $f_{O_{2(g)}}$ – log $a_{C_nH_mS_{p(l)}}$ diagrams would result in more oxidizing conditions for the loci of the intersections of the equilibrium activity lines.
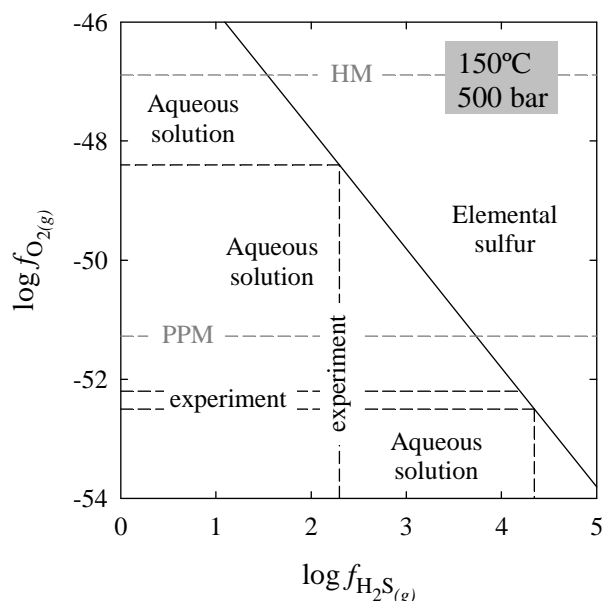
Figure 2.25. Log $f_{O_{2(g)}}$ – log $f_{H_2S_{(g)}}$ diagram showing the stability domain of elemental sulfur.

2.4.3.4. Benzo[*b*]thiophenes and dibenzo[*b,d*]thiophenes

As suggested on the basis of thermodynamic calculations in the first part of the manuscript, benzo[*b*]thiophenes and dibenzo[*b,d*]thiophenes are probably too stable to react with H_2S under the conditions of our experiments or under sedimentary basin conditions in general. This was found consistent with the absence of reaction noted at the end of Experiments 9a, 9b, 10a, 10b and 11-14, besides some generation of CO_2 or CH_4. In the thermodynamic calculations reported above, hydrocarbons were considered as reaction products. Instead, our experiments suggest that under high $f_{H_2S_{(g)}}$ values, sulfur is incorporated into the structure of thiolanes and thiophenes to yields di-*n*-alkylthiols as well as aliphatic and cyclic disulfides. In agreement with this observation, we can write in the case of 2-methylbenzo[*b*]thiophene the following hypothetical reaction:

$$C_9H_8S_{(l)} + 6\ H_2S_{(g)} = C_9H_{20}S_{2(l)} + 5\ S_{(c\ or\ l)} \qquad (2.81)$$

(2-methylbenzo[*b*]-
thiophene)   1,5-bis(ethylthio)-
                 pentane
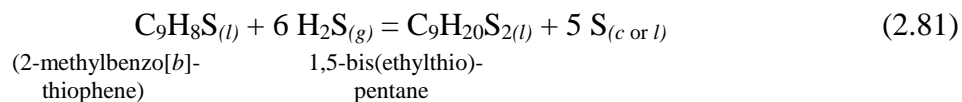
Equilibrium constants calculated from this reaction as a function of temperature at 500 bar have been listed in Table 2.10. The relative abundance of 2-methylbenzo[*b*]-thiophene and 1,5-bis(ethylthio)pentane can be assessed from the following half-reactions

$$C_9H_8S_{(l)} + 10.5\ O_{2(g)} = 9\ CO_{2(g)} + H_2S_{(g)} + 3\ H_2O_{(l)} \qquad (2.82)$$

(2-methylbenzo[*b*]-
thiophene)

and

$$C_9H_{20}S_{2(l)} + 13\ O_{2(g)} = 9\ CO_{2(g)} + 2\ H_2S_{(g)} + 8\ H_2O_{(l)} \qquad (2.83)$$

1,5-bis(ethylthio)-
pentane

167
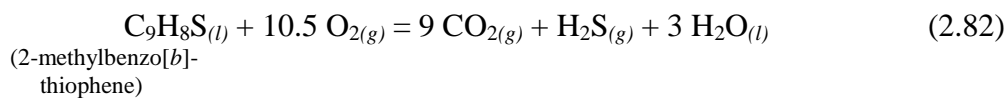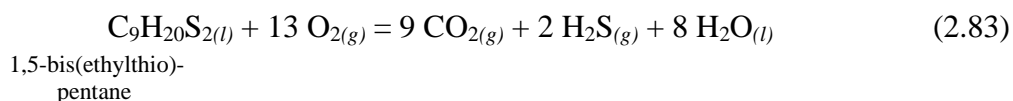
for which the equilibrium constants at 150°C and 1 bar are

$$\log K_{(2.82)} = 552.513 \qquad (2.84)$$

and

$$\log K_{(2.83)} = 687.264 \; . \qquad (2.85)$$

These equilibrium constants have been used together with the following expressions of the law of mass action

$$\log K_{(2.82)} = 9 \log f_{CO_{2(g)}} + \log f_{H_2S_{(g)}} - \log a_{C_9H_8S_{(l)}} - 10.5 \log f_{O_{2(g)}} \; , \qquad (2.86)$$

and

$$\log K_{(2.83)} = 9 \log f_{CO_{2(g)}} + 2 \log f_{H_2S_{(g)}} - \log a_{C_9H_{20}S_{2(l)}} - 13 \log f_{O_{2(g)}} \qquad (2.87)$$

to generate the $\log f_{O_{2(g)}} - \log a_{C_nH_mS_{p(l)}}$ and $\log f_{H_2S_{(g)}} - \log a_{C_nH_mS_{p(l)}}$ diagrams shown in Figure 2.26 *(a)* and *(b)*. It can be deduced from these diagrams that some 1,5-bis(ethylthiopentane) could have in principle formed from the reaction between H_2S and 2-methylbenzo[*b*]thiophene in Experiments 10a and 10b. It is probable that Reaction (2.81) proceeded at a too slow rate for any equilibrium state to be established under the conditions of the experiments.
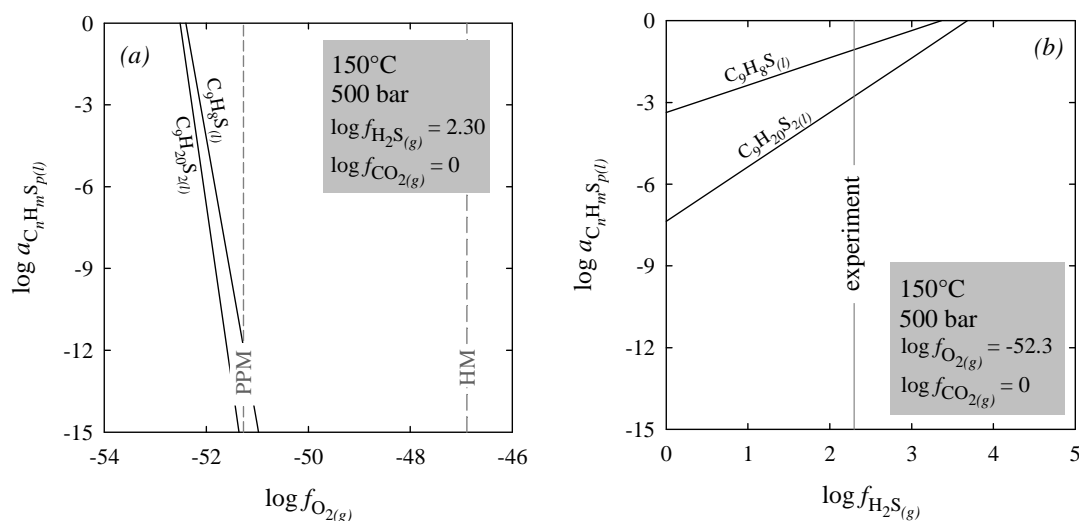
Figure 2.26. Log $f_{O_{2(g)}}$ – log $a_{C_nH_mS_{p(l)}}$ and log $f_{H_2S_{(g)}}$ – log $a_{C_nH_mS_{p(l)}}$ diagrams showing the relative abundances of 2-methylbenzo[*b*]thiophene ($C_9H_8S_{(l)}$) and 1,5-bis(ethylthio)pentane ($C_9H_{20}S_{2(l)}$) for Experiments 10a and 10b.

2.5. Conclusions

We started from the hypothesis that the injection of CO_2-H_2S gas mixtures in sulfur-rich petroleum reservoirs may lead to a desulfurization of the sulfur-rich crude and the precipitation of elemental sulfur in the reservoirs. This hypothesis, which was based on the results of thermodynamic calculations and numerous experimental observations according to which hydrocarbons react with elemental sulfur to produce organic sulfur compounds and H_2S, has been evaluated by carrying out gold-cell experiments in which organic sulfur compounds have been reacted with H_2S in the presence of water at 150ºC and 500 bar. The organic sulfur compounds used in the experiments included one *n*-alkyl sulfide, thiolanes, benzenethiol, thiophenes, benzo[*b*]thiophenes and dibenzo[*b*,*d*]thiophenes. Consumption of H_2S has been observed in the reactions involving the thiolanes and thiophenes. The reaction between H_2S and thiolanes yielded dithianes and dithiols, with no change in the average oxidation state of carbon between the reactants and products. As a result, no elemental sulfur was formed in the reactions involving the thiolanes. In contrast, the reaction between H_2S and alkylthiophenes yielded reaction products in which the average oxidation state of carbon was significantly different that that of the reactants, which allowed the formation of elemental sulfur. Finally, benzo[*b*]thiophenes and dibenzo-[*b*,*d*]thiophenes did not react under the conditions of the experiments, which appears to be consistent with thermodynamic predictions.

3. EXPERIMENTAL SIMULATION OF THERMOCHEMICAL SULFATE REDUCTION (TSR) IN FUSED SILICA CAPILLARIES

A series of experiments on thermochemical sulfate reduction (TSR) have been carried out using the technique of fused silica capillaries presented by Chou et al. (2008a). In these experiments, hydrocarbons (*n*-octane and *n*-octene) were reacted with 0.5 *m* solutions of aqueous sulfate (sodium sulfate Na_2SO_4 or magnesium sulfate $MgSO_4$) as a function of temperature and under pressures of the order of 1 kbar. The two different sulfates were used in order to verify the common acceptance that Mg^{2+} ions are required to initiate the TSR reaction (see Part I).

3.1. Materials and experimental methods

3.1.1. Flexible fused silica capillary tubing

The fused silica capillary tubing used for the experiments was provided by Polymicro Technologies, LLC (model TSP 100375). This tubing has a round cross-section and an internal diameter (ID) of 100 ± 4 µm, while the external diameter (OD) is 363 ± 10 µm (Figure 2.27). The capillary tube is coated with a polyamide layer of 20 µm thickness, which must be removed by burning to permit observation under an optical microscope.
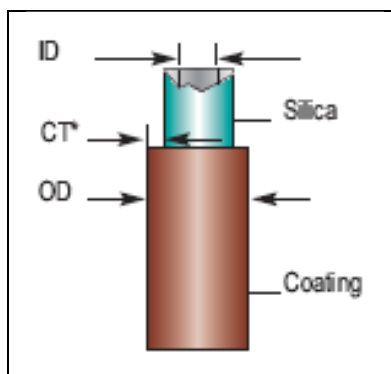
Figure 2.27. Schematic representation of the fused silica capillary tubing: ID = internal diameter, OD = outside diameter, CT = polyamide coating thickness (www.polymicro.com).

3.1.2. Reactants

Sodium sulfate (Na_2SO_4 98%) and magnesium sulfate ($MgSO_4$ anhydrous, 99%) were purchased from Prolabo® and Aldrich-Chemie, respectively. Small amounts of these salts were oven-dried for 24 hours prior to preparing the solutions. Two 0.5 *m* solutions were prepared by dissolving 6.018 mg $MgSO_4$ and 7.102 mg Na_2SO_4 in two times 100 ml ultra pure water (ELGA LabWater PURELAB Option-Q). The *n*-octane (>

99%) and 1-octene (99.5%) were obtained from Sigma-Aldrich and Fluka®, respectively.

3.1.3. Sample loading

Each silica tube was cut into capsules 6-7 cm in length. The polyamide coating layer was removed by burning, and the capsules were welded at one end under a propane/oxygen flame. The sealed end of the capsules were checked under an optical microscope. An aliquot of sulfate solution was first introduced by heating at the closed end of a capsule with a lighter, and subsequently displaced towards that closed end by centrifugating with a SIGMA 1-15 microcentrifuge (12000 rpm, 30 sec). The capsule was inserted in a glass tube to prevent from breaking during centrifugation. An aliquot of hydrocarbon liquid was then introduced by heating the center of the capsule, and again displaced towards that closed end by centrifugation. Typically, 0.010-0.020 g of sulfate solution and 0.006-0.020 of liquid hydrocarbon were introduced in the capsules. Reference capsules containing only an aliquot of either the 0.5 m Na_2SO_4 solution or 0.5 m $MgSO_4$ solution were also prepared, as well as reference capsules for the two hydrocarbons.

Each loaded capsule was subsequently connected to a gas loading apparatus (Figure 2.28) to remove the air present in the capsule prior to welding the remaining open end. The connected capsule was submerged in liquid nitrogen to freeze the aqueous solution and hydrocarbon reactant. The air present in the capsule was purged by opening the valves below volume V_2 and left and right of volume V_5 in Figure 2.28. The existence of leaks or the presence of air are contolled by the pressure sensor (designated by P) of the gas loading apparatus. After the air was purged, the valves were closed, and the open end of the capsule welded under a propane/oxygen flame. The final length of the capsules after welding was usually less than 2.5 cm. The capsules were subsequently observed under an optical microscope equipped with a measurement device. Measurement of the length of the capsule occupied by the aqueous solution and by the hydrocarbon liquid allowed to estimate the volumes of aqueous sulfate solution and hydrocarbon reactant introduced in the capsules (Figure 2.29).

3.1.4. Heating of the capsules and Raman microspectrometry

The capsules were brought to high temperature using two different methods:

- Microthermometry stage: the capsules were heated to 150 – 400ºC at a heating rate of 50ºC/min on a Linkam MDS600 heating stage. The microthermometry

stage was mounted on a Labram Jobin-Yvon Raman microspectrometer equipped with an argon laser emitting at 514.5 nm, which allowed a continuous monitoring of the changes occuring within the capsules over reaction times which were typically less than 10 hours.

- Heat oven: the capsules were heated to 300 – 400ºC in a Hermann Moritz type MF4 oven for 2 to 10 days, depending on the temperature. After cooling, they were centrifugated with a SIGMA 1-15 microcentrifuge (12000 rpm, 30 sec) to displace the aqueous and hydrocarbon phases towards the bottom of the capsule. The liquid and gas phases were analyzed by Raman microspectrometry at room temperature.

(a)   *(b)*
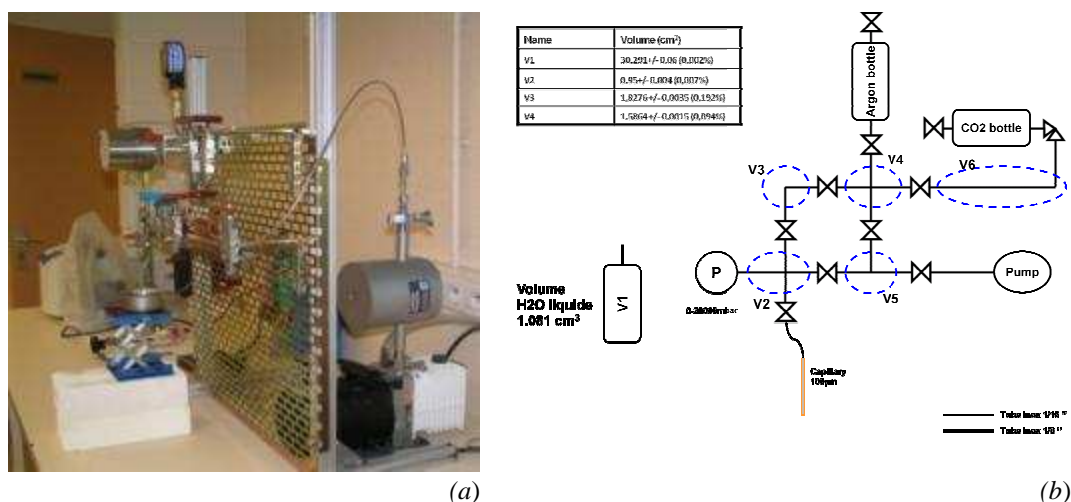
Figure 2.28. *(a)* Photographic and *(b)* schematic representation of the gas loading apparatus (designed by P. Robert, G2R, Nancy).
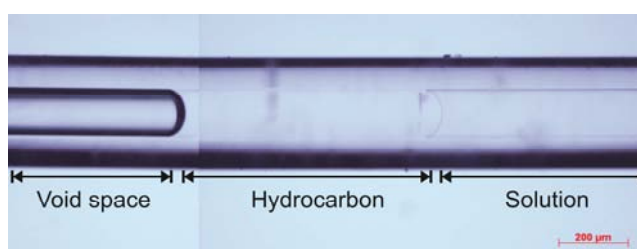
Figure 2.29. Fused silica capsule as observed under the optical microscope.

3.2. Results and discussion

3.2.1. Thermal evolution of the aqueous sulfate solution

The thermal evolution of the 0.5 m Na_2SO_4 aqueous solution observed by heating the capsules on the microthermometry stage is illustrated by the Raman spectra shown in Figure 2.30. Since similar heating experiments with $MgSO_4$ solutions have given identical results, only those for Na_2SO_4 will be discussed here.

172
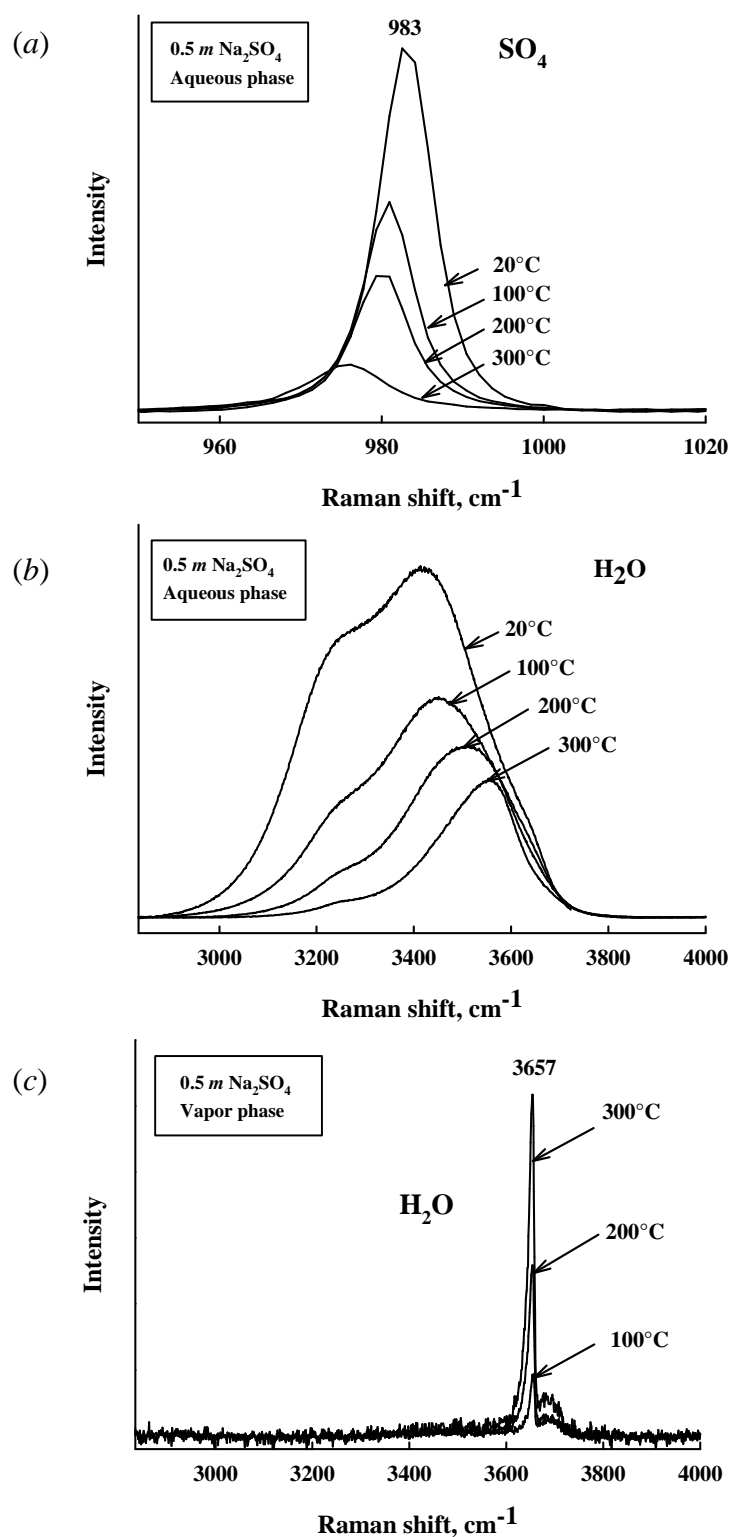
Figure 2.30. Raman spectra showing the thermal evolution of the 0.5 m Na_2SO_4 aqueous solution – (*a*) SO_4; (*b*) H_2O – and (*c*) the vapor phase above that solution (H_2O bands).

It can be deduced from Figure 2.30. *(a)* that the sulfate (SO_4) peak (which occurs at 983 cm^{-1} at ambient temperature decreased in intensity and shifted to lower wavenumbers with increasing of temperature from 20 to 300ºC. The same observation

applies to the Raman bands of water (H_2O – Figure 2.30. *(b)*). In contrast, the Raman bands of H_2O in the vapor phase increase in intensity (but still shift to lower wavenumbers) with increasing temperature (Figure 2.30 *(c)*).

3.2.2. Thermal evolution of the hydrocarbon liquids

Reference capsules containing either *n*-octane or 1-octene were also heated to 400ºC at 50ºC/min. The associated changes observed in the Raman spectra were the same for both *n*-octane and 1-octene, which homogenized and started to fluoresce at ~ 350ºC. This is illustrated in Figure 2.31 for 1-octene heated to 400ºC. Identification of the Raman bands of 1-octene at 25ºC is based on Cleveland (1943). It can be seen in Figure 2.31 that the intensity of the bands decrease with increasing temperature until most of them disappear above 350ºC.
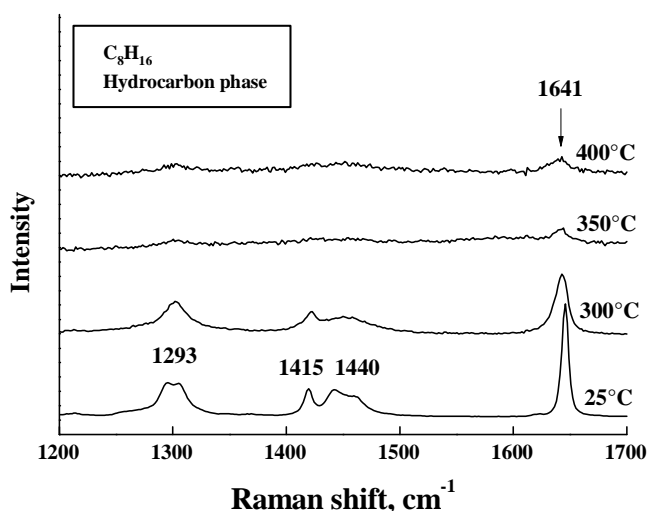
Figure 2.31. Raman spectra showing the thermal evolution of 1-octene.

3.2.3. Thermal evolution of the aqueous sulfate – hydrocarbon mixture

Two capsules containing mixtures of aliquots of the aqueous 0.5 *m* Na_2SO_4 solution and of either *n*-octane or *n*-octene were heated at 50ºC/min on the microthermometry stage up to the homogenization temperature (T_h=370°C) in the case of 1-octene, and up to 400ºC in the case of *n*-octane for which $T_h = 420$ºC.

The liquid (aqueous and hydrocarbon) as well as the gas phase have been analyzed by Raman microspectrometry at the temperatures of the experiments. Representative spectra for the aqueous and hydrocarbon phases are shown in Figure 2.32 for the reaction between the aqueous sulfate solution and 1-octene. The gas phase was also analyzed but the obtained spectra did not reveal any significant bands besides H_2O vapor and traces of 1-octene. Although a comparison of these spectra indicate the presence of 1-octene in the aqueous phase (bands at 1641, 2873, 2924 and 2999 cm^{-1}), a

174

complete fluorescence of the hydrocarbon phase at the homogenization temperature as well as fluorescence of the aqueous phase upon cooling renders the microthermomety stage heating method of limited application for investigating the TSR reaction.
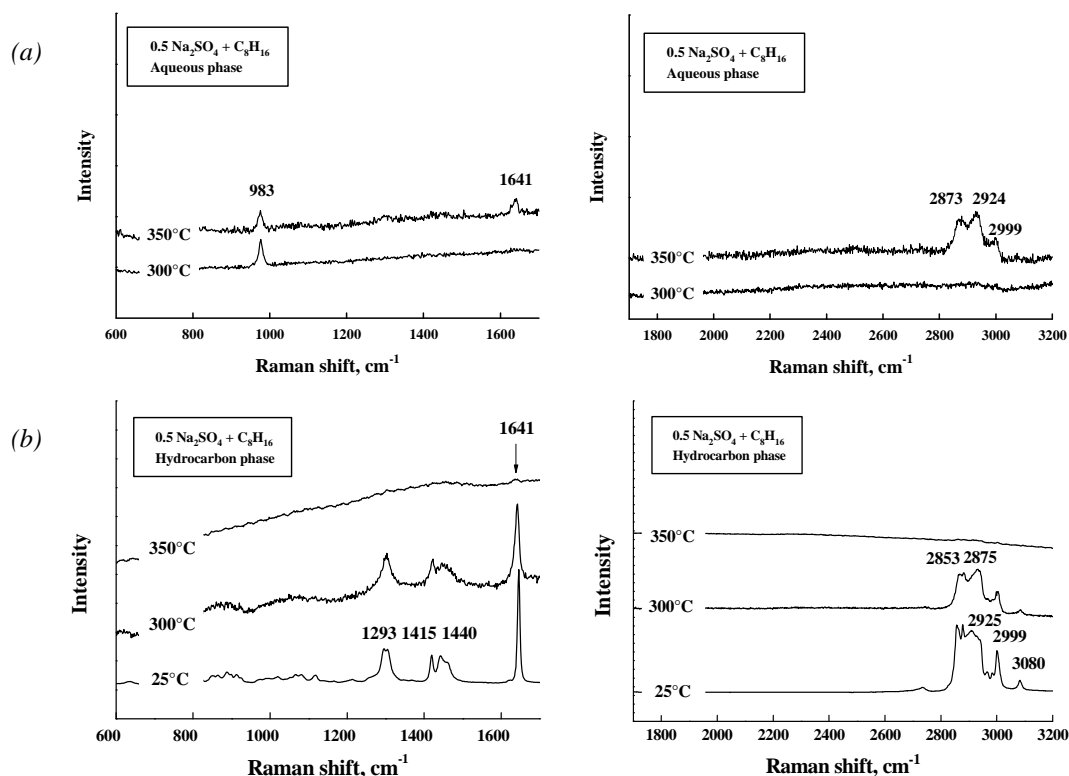
Figure 2.32. Raman spectra illustrating the evolution of the sulfate-hydrocarbon system with increasing temperature: *(a)* aqueous solution; *(b)* liquid hydrocarbon phase.

3.2.4. Oven heating experiments

Capsules containing mixtures of an aliquot of either the 0.5 *m* Na_2SO_4 or $MgSO_4$ solution and an aliquot of either *n*-octane or 1-octene were oven heated at 300ºC for 2, 7 and 10 days, at 350ºC for 4 days, and at 400°C during 46 hours. The Raman measurements were carried out at room temperature. Representative spectra are shown in Figures 2.33 and 2.34 for the gas and aqueous phases, respectively. The corresponding reactions are indicated in the spectra. No spectra are shown for the hydrocarbon phases, which displayed too much fluorescence. The relative proportions of the gases generated are also given in Table 2.11.

It can be deduced from Figure 2.33 and Table 2.11 that only a limited amount of CO_2 was generated at 300ºC after 10 days of reaction between aqueous $MgSO_4$ and both *n*-octane and 1-octene. As was the case for the experiments on the microthermometry stage, dissolved hydrocarbons were found in the aqueous phase for both experiments (not shown). No H_2S was detected neither in the aqueous phase nor in the gas phase.

175
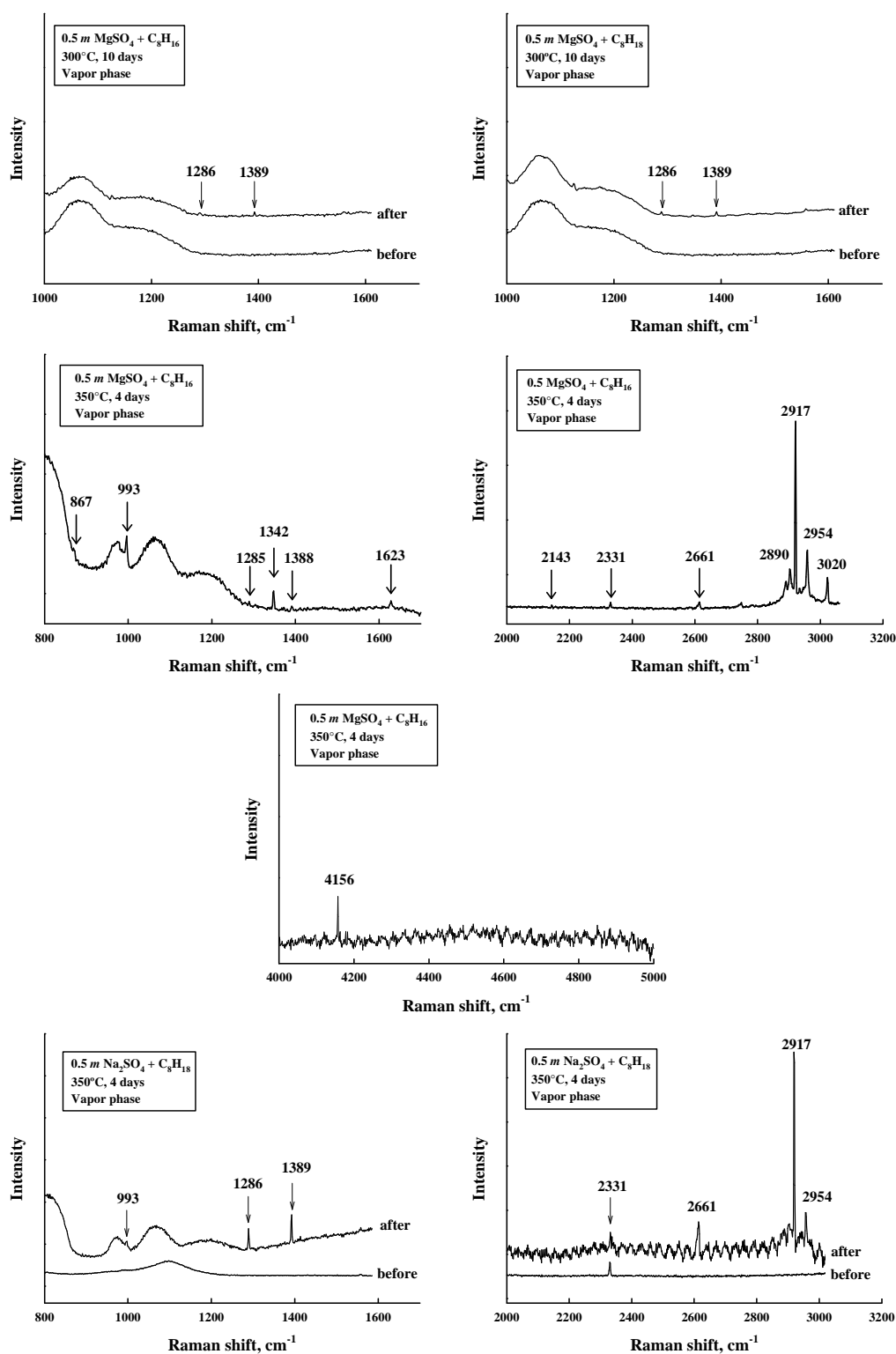
Figure 2.33. Raman spectra of the gas phase after thermochemical sulfate reduction experiments. The conditions for the experiments are indicated in each spectrum. The various Raman peaks identified in the spectra correspond to the following species: H_2S (2661 cm^{-1}), CO_2 (1286 and 1389 cm^{-1}), CO (2143 cm^{-1}), CH_4 (2917 cm^{-1}), C_2H_6 (993 and 2954 cm^{-1}), C_3H_8 (867 and 2890 cm^{-1}), C_2H_4 (1342, 1623 and 3020 cm^{-1}), N_2 (2331 cm^{-1}), and H_2 (4156 cm^{-1}). Peak identifications based on Raman shift values tabulated by Schrötter (1995).

Table 2.11. Gaseous species detected by Raman spectroscopy at the end of the TSR experiments carried out in fused silica capillaries (n.d. = not detected).

Reactants	T (°C)	Time (d)	CO	CO_2	H_2S	H_2	CH_4	C_2H_4	C_2H_6	C_3H_8
$MgSO_4 + C_8H_{18}$	300	10	n.d.	100	n.d.	n.d.	n.d.	n.d.	n.d.	n.d.
	350	4	n.d.	n.d.	15.2	n.d.	70.3	n.d.	14.5	n.d.
$Na_2SO_4 + C_8H_{18}$	350	4	n.d.	52.9	14.3	n.d.	30.3	n.d.	2.4	n.d.
$MgSO_4 + C_8H_{16}$	300	10	n.d.	100	n.d.	n.d.	n.d.	n.d.	n.d.	n.d.
	350	4	7.4	4.7	5.0	18.3	56.3	-	6.9	1.5
$Na_2SO_4 + C_8H_{16}$	350	4	n.d.	n.d.	n.d.	n.d.	100	n.d.	n.d.	n.d.

In contrast, the production of H_2S has been observed at 350ºC along with CO_2, which suggests that thermochemical sulfate reduction (TSR) occured at that temperature. Other gases detected in the experiments include methane (CH_4), ethane (C_2H_6), ethene (C_2H_4), propane (C_3H_8), carbon monoxide (CO), and hydrogen (H_2). The peak at 2331 cm^{-1} corresponds to atmospheric nitrogen (N_2). Although it may appear from Table 2.11 that more H_2S was generated in the reactions involving *n*-octane (C_8H_{18}), more experiments of this kind using different hydrocarbon reactants are required in order to rationalize the observed gas distributions. In particular, no explanation can be given for the fact that CO_2 was not observed in the experiment involving aqueous $MgSO_4$ and *n*-octane, or for the fact that only methane was produced in the experiment with Na_2SO_4 and 1-octene. It is however interesting to note that H_2S is generated by reduction of sulfate from both Na_2SO_4 and $MgSO_4$ solutions, which is somewhat contradictory with the hypothesis of Tang and co-workers (see footnote 2) that Mg^{2+} may act as an initiator of the TSR reaction.

The decrease in sulfate concentration with increasing temperature in the TSR experiments at 350ºC and 400ºC can be followed from the corresponding decrease in intensity of the peaks at 983 cm^{-1} (Figure 2.34). Other species detected in the aqueous solutions after the TSR reactions include dissolved hydrocarbon species (2933 cm^{-1} for *n*-octane and 2938 cm^{-1} for 1-octene), as well as H_2S (2591 cm^{-1}), hydrosulfide anion (HS$^-$, 2573 cm^{-1}) and dissolved CO_2 (1387 cm^{-1}). The peak at 2330 cm^{-1} again corresponds to atmospheric N_2, while that at 1602 cm^{-1} which was only observed in the experiment at 400ºC is tentatively attributed to the vibration of a carbonyl group and most probably represents an artefact due to the reaction between the aqueous solution and the capillary tube.
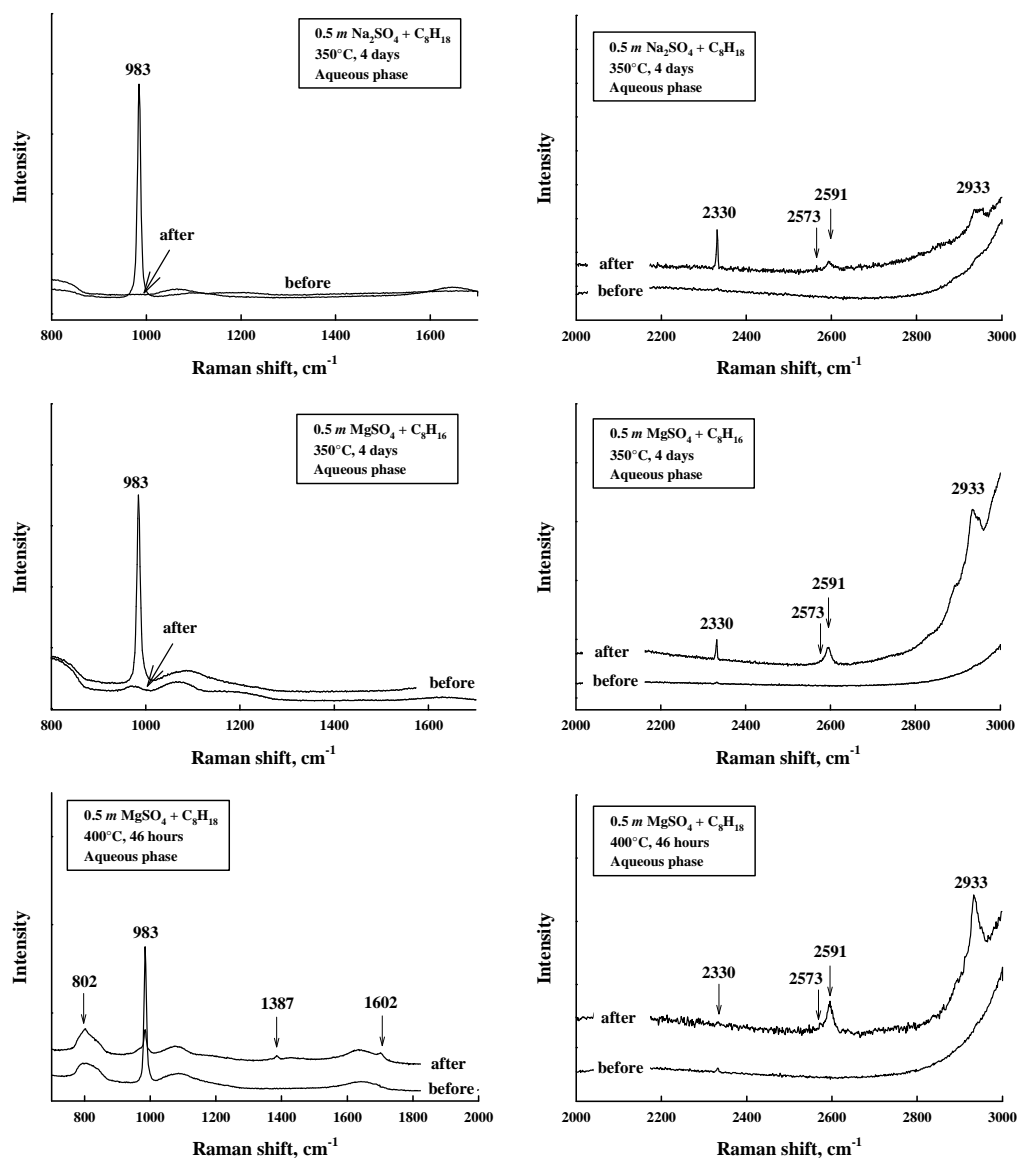
Figure 2.34. Raman spectra of the aqueous phase after thermochemical sulfate reduction experiments. The conditions for the experiments are indicated in each spectrum. The various Raman peaks identified in the spectra correspond to the following species: SO_4^{2-} (983 cm^{-1}), H_2S (2591 cm^{-1}), HS$^-$ (2573 cm^{-1}), CO_2 (1387 cm^{-1}), *n*-octane (2933 cm^{-1}), *n*-octene (2938 cm^{-1}). Peak identifications based on Raman shift values given by Dubessy et al. (1992), Wood et al. (2002), and others.

3.3. Concluding remarks

Preliminary experiments on thermochemical sulfate reduction (TSR) have been carried out using the fused silica capillary technique recently developed by Chou et al. (2008a). A major advantage of the technique is the possibility to use it in conjunction with *in situ* Raman spectroscopy observations of the gas phase. Such observations of the aqueous phase are currently limited due to problems encountered with the fluorescence of liquid hydrocarbons. No such problems were encountered by Chou et al. (2008b) in their experiments on TSR using methane as a reactant. In the meantime, oven heating

experiments can be used. The results of the experiments indicate that TSR can only be initiated at 350ºC using this technique, perhaps due to the inherent short durations of the experiments. However, it appears from our experiments that the TSR reaction proceeds regardless of the metal cation of the sulfate salt being used for the experiments. This calls into question the hypothesis according to which Mg^{2+} may act as an initiator for the TSR reaction under sedimentary basin conditions. With rare exceptions, formation waters usually contain low amount of dissolved Mg^{2+}, which further renders the above hypothesis doubtful. The preliminary results obtained in this study should encourage further experiments, in particular in an effort to rationalize the observations made with respect to the production of low-molecular weight compounds during TSR, but also to establish the relative contributions of different types of hydrocarbons to the generation of H_2S in terms of reaction stoichiometries.

PART III – PETROGRAPHIC AND FLUID INCLUSION STUDY OF THE AKTOTE FIELD

In this last part of the manuscript, we report the results of petrographic observations and fluid inclusion studies on carbonate rock samples from a petroleum reservoir of the Pre-Caspian Basin. The purpose of this study was to reconstruct the diagenetic history of the reservoir within the context of sulfur geochemistry since this reservoir may have been affected by thermochemical sulfate reduction.

1. GEOLOGICAL SETTING AND PETROLEUM DEPOSITS OF THE PRE-CASPIAN BASIN

The Pre-Caspian Basin, which hosts some of the world´s largest hydrocarbon reserves (among which the Tengiz, Kashagan, and Aktote oil fields) is located in the northern part of the Caspian Sea (Figure 3.1). This basin covers an area of approximately 540,000 km^2, and is bordered to the north by the Russian Platform, to the northeast by the Ural Mountains, to the southeast by the Northern Ustyurt Block, to the southwest by the Karpinsky Ridge, and to the northwest by the Pachelma aulacogen (Figure 3.2, Brunet et al., 1999). There are several tectonic hypotheses for the subsidence and subsequent formation of the Pre-Caspian Basin, including intracontinental rifting, oceanisation of the continental crust, a subduction-related formation of eclogites at the base of an oceanic crust, or subduction-collision processes (Brunet et al., 1999; Ulmishek, 2001; Volozh et al., 2003).

The Pre-Caspian Basin is one of the deepest sedimentary basins in the world, with more than 20 kilometers of accumulated sediments in its central part (Figure 3.3), which is known as the *central depression*. This depression is limited to the north and south by the Aralsor-Khobda and Elton-Inder faults. The general stratigraphy of the Pre-Caspian Basin is recalled in Figure 3.4, while two cross-sections through the North Karazhanbas and Kashagan oil fields and through the Karaton, Tengiz and Yuzhnaya gas fields are presented in Figure 3.5. The various sedimentary formations are refered to as pre-salt and post-salt sediments with respect to the salt deposits of the Kungurian (Lower Permian) Formation. According to the seismic interpretations of Volozh et al. (2003), the > 20 km thick sedimentary deposits of the Pre-Caspian Basin consist of

- Pre-salt: 4 km Riphean (Meso- to Neoproterozoic) clastic and carbonate rocks, 2 km of Lower Paleozoic clastics, 2 km of Upper Ordovician to Silurian carbonates, 4 km of Devonian to Lower Permian clastics;
- Salt: 4 km of salt deposits of the Kungurian formation;

Figure 3.1. The Caspian Sea area, with the location of the Kashagan, Kairan, Karaton, Aktote, Tengiz, Yuzhnaya, and North Karazhanbas oil fields I-I' and II-II' refer to the cross sections shown in Figure 3.5. (modified from: http://www.hydrocarbons-technology.com/projects/tengiz/tengiz1.html).

Figure 3.2. Location of the Pre-Caspian Basin and main regional tectonic units (Brunet et al., 1999).
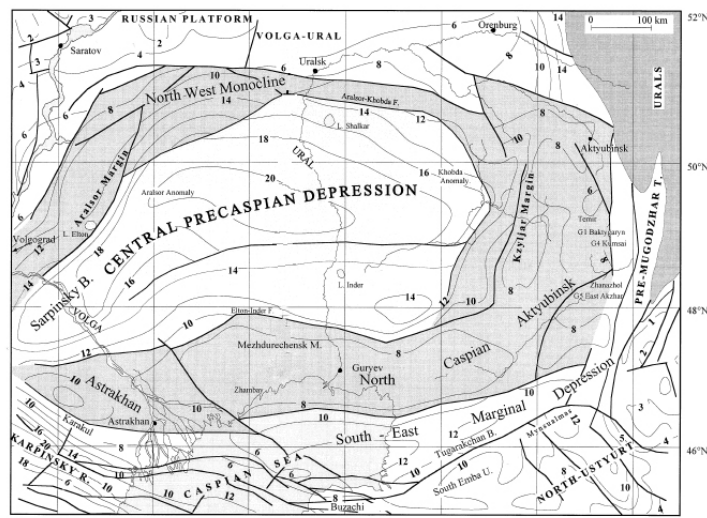
Figure 3.3. Structural map of the Pre-Caspian basin (Brunet et al., 1999).

181

- Post-salt: 2 km of Upper Permian to Triassic red beds, 2.5 km of Jurassic-Cainozoic carbonates and clastics.

The post-salt sediments consist of Lower Triassic to Paleogene sandstones, siltstones, shales, claystones, and carbonates. The underlying impervious rock is represented by the Kungurian evaporites which mostly consist of halite and sylvite, and the topmost layer of which consists of anhydrite. The pre-salt sediments are essentially represented by Devonian to Carboniferous carbonate rocks, with minor clastics.

All of the giant oil and gas fields (Tengiz, Zhanazhol, Astrakhan, Kashagan) of the Pre-Caspian Basin are located within the Astrakhan-Aktyubinsk system of highs, south of the Central Depression (Figure 3.3). The oil and gas fields are hosted in pre-salt reservoirs within a carbonate platform which ranges in age from Upper Devonian to Upper Carboniferous (Ulmishek, 2001; Ronchi et al., 2010). The Aktote oil field, which is the subject of the present study, is located between the Kashagan and Tengiz oil fields (Figure 3.1). The latter two oil fields are well correlated from a stratigraphic point of view (Ulmishek, 2001; Ronchi et al., 2010). Therefore, it is anticipated that the observations made below for the samples of the Aktote field can be compared to those made by other investigators for the Kashagan or Tengiz oil fields.

The hydrocarbons hosted in the pre-salt reservoirs of the Pre-Caspian Basin may have been generated from a number of source rocks, including Middle Devonian clays, Middle Carboniferous carbonates, and Lower Permian shales (Pairazian, 1999). However, geochemical evidence would suggest that a major part of the hydrocarbons was generated from the Middle Carboniferous carbonate source rocks, which have a total organic carbon (TOC) content of 2.0-3.5 %. The kerogen mostly corresponds to type II marine organic matter, with minor amounts of type III terrestrial organic matter (Pairazian, 1999). Rock-eval pyrolysis data have indicated generation potentials of $1\text{-}2\times10^5$ t km^{-2} of crude oil and $200\text{-}400\times10^6$ m^{3}km^{-2} of gas for the Middle Carboniferous source rocks. According to the *Oil and Gas Journal* of January 2009, the proven reserves of Kazakhstan amount to 30 billion barrels of crude oil and 85 trillion cubic feet of natural gas, respectively. Of these proven reserves, 53.9 percent are found in the Pre-Caspian Basin (*The Agency of Statistics of the Republic of Kazakhstan*, www.stat.kz). However, the probable reserves may be much higher than their proven counterparts.

DEPTH, m	AGE		FORMATION	THICKNESS, m	LITHOLOGY		
		P-Q		270			POST-SALT DEPOSITS
	CRET.	Upper		520			
		Lower		1450			
3000 m	JURASSIC		T	2822 / 2835			
	PERMIAN		KUNGURIAN			SALT	
			ART.	3858 / 3630			
4000 m	CARBONIFEROUS	SERP. BASHK.					PRE-SALT DEPOSITS
		VISEAN					
		TOURNAISIAN					
	DEVONIAN	FRASN. - FAMEN.		4735			
5000 m							
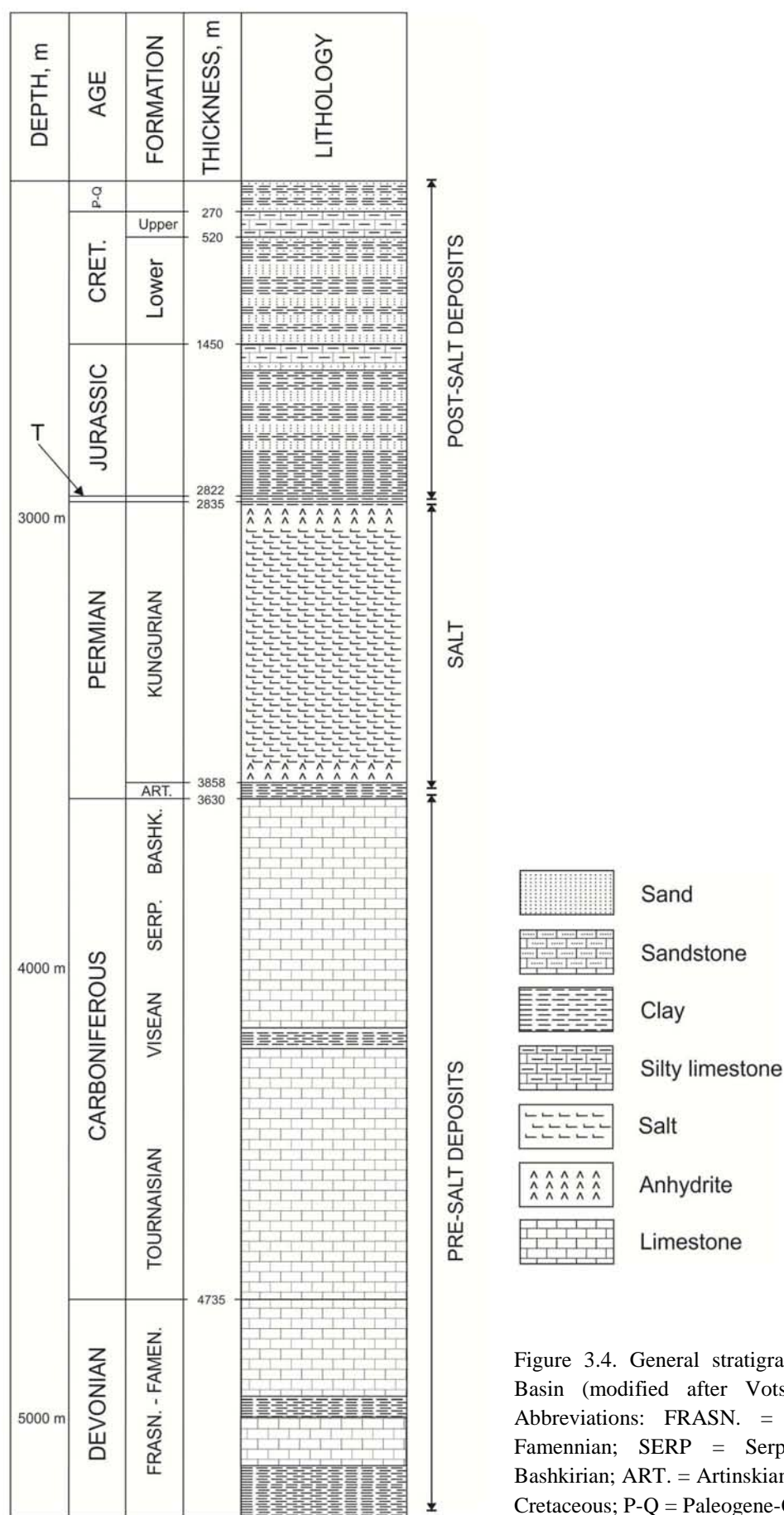
Figure 3.4. General stratigraphy of the Pre-Caspian Basin (modified after Votsalevsky et al., 1998). Abbreviations: FRASN. = Frasnian; FAMEN. = Famennian; SERP = Serpukhovian; BASHK. = Bashkirian; ART. = Artinskian; T. = Triassic; CRET. = Cretaceous; P-Q = Paleogene-Quaternary.

Legend:
- Sand
- Sandstone
- Clay
- Silty limestone
- Salt
- Anhydrite
- Limestone

183

Most of the hydrocarbon deposits of the Pre-Caspian Basin contain high concentrations of sulfur. For example, the reservoir fluid of the Tengiz oil field contains 13 mol % of H_2S (Warner et al., 2007), while the associated gas contains 20% by volume of H_2S (Anissimov and Moskowsky, 1998). Similar concentrations have been found at Kashagan, where the H_2S concentration of the fluid is 16 mol % (Ronchi et al., 2010). The fluid of the Aktote reservoir, which is the subject of the present study, contains 24 mol % of H_2S (Agip KCO, 2006, unpublished report). These high H_2S concentrations may be attributed to thermochemical sulfate reduction (TSR). Evidence suggesting that TSR has occurred at Tengiz has been presented by Collins et al. (2006). Although no such evidence was found at Kashagan, Ronchi et al. (2010) do not discard the possibility that TSR may also have occurred in this reservoir.

a)

b)
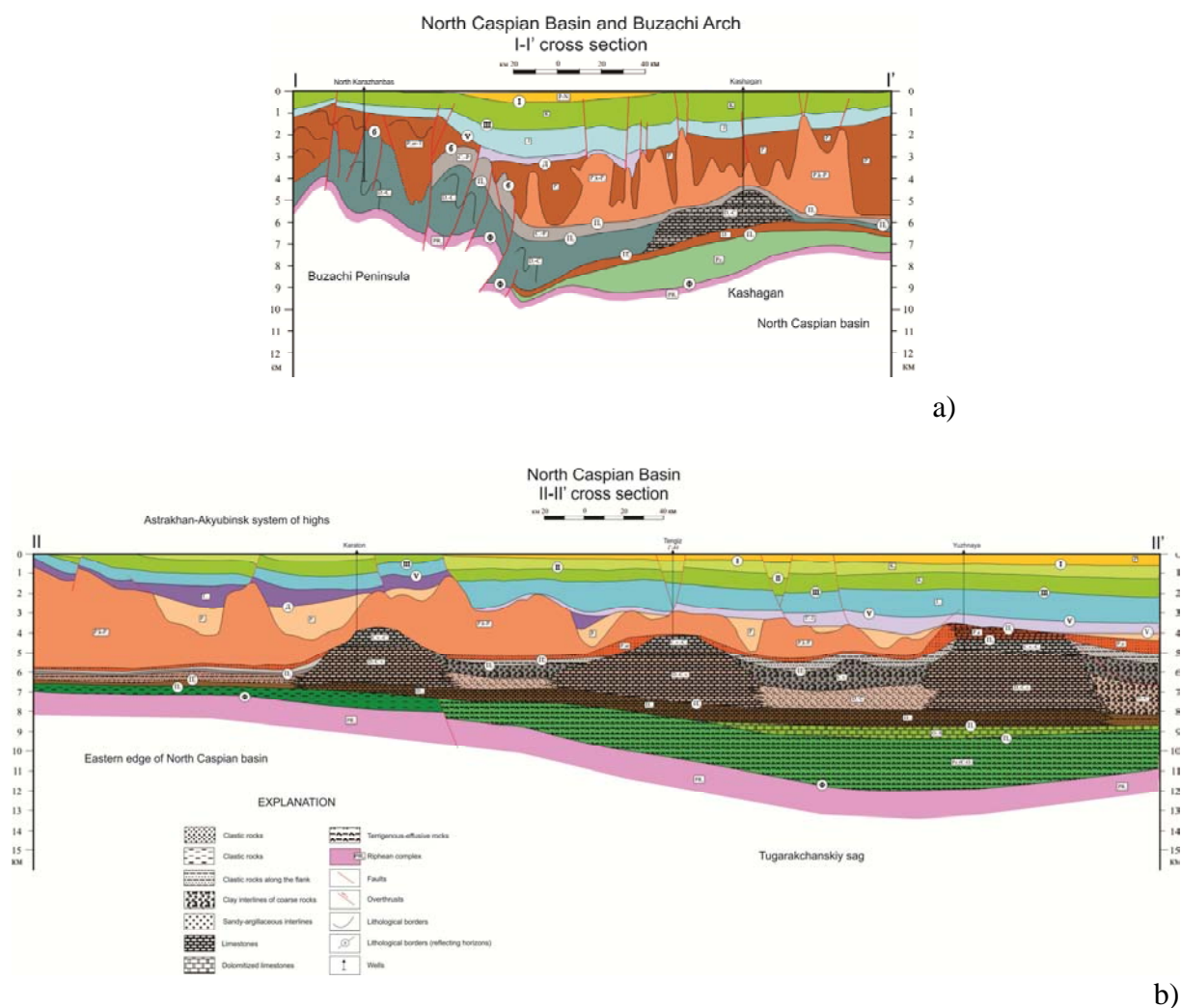
Figure 3.5. Cross sections through (a) North Karazhanbas and Kashagan oil fields (I-I'); b) Karaton, Tengiz and Yuzhnaya gas fields (II-II') – modified after Garagash et al. (2004) and Volozh (unpublished report). See Figure 3-1 for the orientation of the cross sections.

2. MATERIALS AND METHODS

2.1. Sample preparation

The petrographic and fluid inclusion study reported in this part of the manuscript has been performed on ten reservoir rock samples from the Aktote oil field. These samples were obtained from NCOC (North Caspian Operating Company). Eight samples (Ax-1 to Ax-8) are of Bashkirian age, one (Ax-9) is of Serpukhovian age, and one (Ax-10) is of Devonian age. Double-polished thin (30 µm) and thick (100-150 µm) sections were prepared in the *Service Commun de Litholamellage* of Nancy-Université. The petrographic observations and chemical analyses were made on the thin sections, while the thick sections were used for the fluid inclusion studies (see Table 3.0). The thick sections were placed in acetone during one night, then rinsed with ethanol to remove the epoxy resin prior to the microthermometric measurements.

2.2. Petrographic study

In an attempt to reconstruct the diagenetic processes which have affected the petrophysical and geochemical properties of the Aktote reservoir, optical microscopy observations and cathodoluminescence analysis have been used. In addition, mineral surface morphology and trace element contents were determined by scanning electron microscopy (SEM) and electron microprobe analysis, respectively.

2.2.1. Optical microscopy and UV-fluorescence

Optical microscopic observations have been made under transmitted light, polarized light and reflected light with an Olympus BX-50 microscope equipped with x2, x5, x10, x20 and x50 objective lenses. This microscope is also equipped with an excitation filter U-MNU3 (360-370 nm) and an emission filter LP400 (> 400 nm) for UV-fluorescence observations. UV-fluorescence microscopy was used to observe cement zoning, as well as to locate hydrocarbon inclusions.

2.2.2. Cathodoluminescence (CL)

Cathodoluminescence observations of carbonate and fluorite cements have been carried out with a cold-cathode CL equipment from CITL (model CL 8200 MK4) mounted on an Olympus BX-50 microscope. The observations were made under a voltage of 14-15 kV and a 400-500 µA electron gun current.

Table 3.0. Summary of analytical techniques used for petrography observations, chemical analyses and fluid inclusion studies.

		Analytical techniques	Derived information
Thin sections	Mineral diagenesis	Optical microscopy	Carbonate mineralogy
		Cathodoluminescence	Chronology of cementation phases
		Scanning Electron Microscopy (SEM)	Surface morphology
		Electron microprobe	Trace element content
Thick sections	P-T-X constraints on fluid evolution	UV-fluorescence	Identification of aqueous and petroleum inclusions
		Aqueous inclusions	
		Microthermometry	Homogenization temperatures
		Raman microspectrometry	Salinity and concentration of volatiles (H_2S, CO_2, CH_4)
		Aqueous inclusion thermodynamic (AIT) modelling	*P-T* reconstruction from isopleths and isochores in the CH_4–H_2O–NaCl system
		Petroleum inclusions	
		Fourier transform infrared (FT-IR) spectrometry	Composition of petroleum inclusions (CH_4, CO_2, *n*-alkanes)
		Confocal Laser Scanning Microscopy (CLSM)	Gas/oil volume ratio at 20ºC
		Petroleum inclusion thermodynamic (PIT) modelling	*P-T* reconstruction from isopleths and isochores

2.2.3. Scanning electron microscopy (SEM)

Scanning electron microscopy (SEM) observations were made with a Hitachi S4800 electron microscope under a voltage of 10-20 kV at the *Service Commun de Microscopies Electroniques et de Microanalyses X* of Nancy-Université. Secondary electron (SE) images of mineral surface morphologies and back-scattered electron (BSE) images showing the distribution of chemical elements in the samples were obtained on carbon-metallized thin sections. Finally, semi-quantitative elemental analyses of the samples were obtained by energy-dispersive X-ray spectroscopy (EDX).

2.2.4. Electron microprobe analysis

In order to determine the major and trace (Ca, Mg, Sr, Fe, Mn) element contents of carbonate cements, electron microprobe analyses were performed with a CAMECA SX 100 microprobe at the *Service Commun de Microscopies Electroniques et de Microanalyses X* of Nancy-Université. The operating voltage during the analyses varied between 0.5 and 50 kV, depending on the element being analyzed.

2.3. Fluid inclusion study

Fluid inclusion analysis was carried out using microthermometry, Raman and infrared microspectroscopies, and laser scanning confocal microscopy (LSCM). Based on the hypothesis that aqueous and hydrocarbon fluid inclusions contained within a given sample have been trapped simultaneously, aqueous inclusion thermodynamic (AIT) and petroleum inclusion thermodynamic (PIT) modeling was subsequently performed to determine the temperature and pressure conditions of trapping of the petroleum fluids in the reservoir using the thermal, compositional and volumetric data obtained by the microthermometric and Raman analysis.

2.3.1. Microthermometry

Microthermometric measurements of the homogenization and freezing temperatures of aqueous inclusions as well as of the homogenization temperatures of hydrocarbon inclusions were made on a Linkam MDS 600 microthermometry stage mounted on an Olympus BX-50 microscope. Two fluid inclusions in a natural sample from a petroleum reservoir of the North Sea were used as a reference for calibration of the microthermometry stage. The homogenisation temperature (T_h) corresponds to the transformation of a biphasic (liquid and vapor, $l+v$) inclusion to a monophasic (l or v) inclusion. This allows to recalculate the temperature and pressure conditions under which this fluid inclusion was trapped within the host mineral. Although freezing temperature is generally used to estimate the salinity of aqueous fluid inclusions, it requires cooling the sample to temperatures well below -40ºC, which are not appropriate for such fragile minerals as calcite, dolomite or fluorite (Bourdet, 2008). Consequently, salinity was estimated by Raman microspectrometry following the method described by Dubessy et al. (2002) – see below. In case of one phase hydrocarbon inclusion a freezing treatment is applied in order to nucleate a vapor phase.

2.3.2. Raman microspectrometry

Raman microspectrometry measurements have been made with a Labram Jobin-Yvon Raman spectrometer equipped with an argon laser at 514.4 nm and a Linkam MDS 600 microthermometry stage. These measurements allowed an estimation of the chlorinity and volatile content of the aqueous fluid inclusions. The salinity was estimated using the method developed by Dubessy et al. (2002). This method is based on the modification of the Raman band corresponding to the stretching vibrations ν(OH) of water following the addition of a known concentration of a chloride salt of geological interest (e.g. NaCl, $CaCl_2$, …).

Estimation of the content of dissolved methane was made following a calibration method using Raman spectroscopy on synthetic fluid inclusions. This method, originally proposed by Dubessy et al. (2001) for the CH_4-H_2O system, has been subsequenly extended to the CH_4-H_2O-NaCl system by Guillaume et al. (2003), and to the H_2S-H_2O-NaCl system by Jacquemet (2006).

2.3.3. Aqueous inclusion thermodynamic (AIT) modelling

The software program developed by Dubessy et al. (2001) for the thermodynamic modelling of fluid inclusion compositions was used in the present study to estimate the pressure-temperature (*P-T*) conditions at which the aqueous fluid inclusions were trapped in their host minerals. This program, which is based on the model of Duan et al. (1992 – see Part I) for the CH_4-H_2O-NaCl system, requires as input data the molalities of CH_4 and NaCl to calculate the bubble point pressure curve of the solution as a function of temperature between 0ºC and 400ºC at fixed values of CH_4 and NaCl molalities, i.e. isopleths. Such isopleths have been represented for NaCl molalities of 0 *m* and 1 *m* in Figure 3.6. It can be deduced from this figure that increasing both the salinity and methane concentration of the fluid raise the boiling pressure at all temperatures.
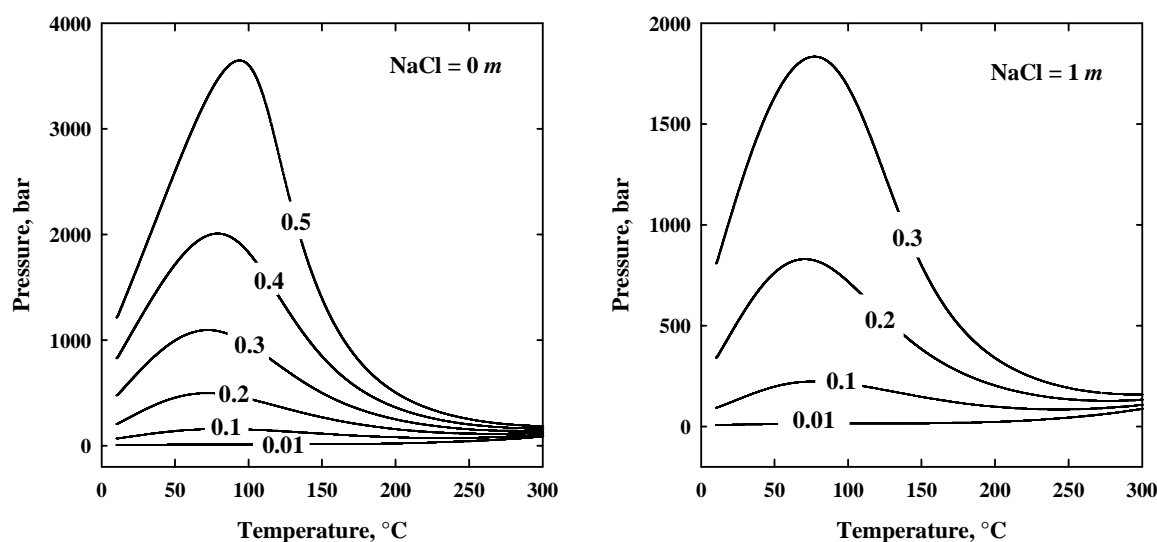
Figure 3.6. Projection of CH_4 isopleths in the *P-T* plane of the system CH_4-H_2O-NaCl for two different NaCl molalities. The number on the curves correspond to CH_4 molalities (after Dubessy et al., 2001).

Since the original equation of state of Duan et al. (1992) does not allow the calculation of isochores, the model of Duan and Mao (2006) was used for that purpose. This model represents an improvement with respect to the capabilities of the Duan et al. (1992) equation of state, which allows an accurate prediction of liquid densities. One implication of this is the

possibility to predict homogenization pressures and densities at homogenization of fluid inclusions, knowing their temperatures of homogenization and their compositions (i.e. molalities of NaCl and CH_4). The calculations have been carried out on the http://www.geochem-model.org/models/h2o_ch4_nacl/ website. An example of isopleth and isochores in the CH_4-H_2O-NaCl system calculated using the model of Duan and Mao (2006) is shown in Figure 3.7 for a fluid composition corresponding to 1 *m* NaCl and 0.2 *m* CH_4. The calculations are compared to the isopleth calculated using the original equation of state of Duan et al. (1992), and to the isochores calculated using the equation of state of Zhang and Frantz (1987). Prior to the appearance of the Duan and Mao (2006) model, the equation of Zhang and Frantz (1987), which is for the H_2O-NaCl system, has been used to calculate approximate isochores for fluid inclusions having the same salinity as the methane-bearing inclusions (e.g. see Pironon, 2004). It can be deduced from Figure 3.7 that the isochores calculated from the model of Duan and Mao (2006) or from the equation of state of Zhang and Frantz (1987) are close to each other. In contrast, the isopleths computed from the equation of state of Duan et al. (1992) and from the improved model of Duan and Mao (2006) tend to depart from each other in the lower temperature range.
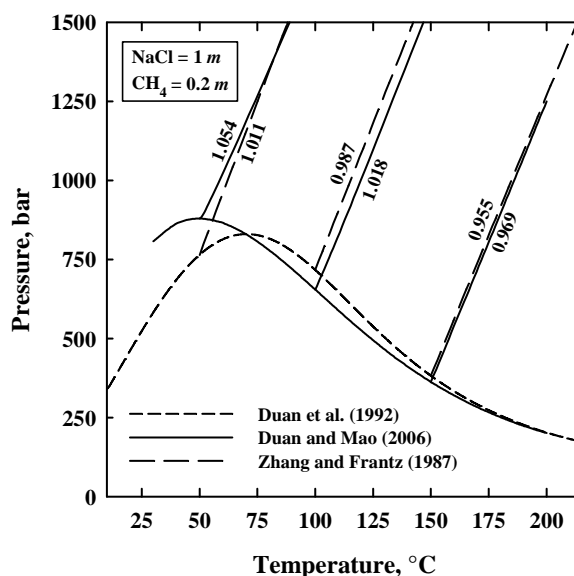
Figure 3.7. Isopleth and isochores in the system CH_4-H_2O-NaCl for a fluid composition corresponding to 1 *m* NaCl and 0.2 m CH_4. The numbers on the isochores correspond to fluid densities in g·cm^{-3}. These isochores were calculated from the equation of state of Zhang and Frantz (1987) and the model of Duan and Mao (2006), while the isopleths were calculated from the Duan et al. (1992) equation of state and the improved model of Duan and Mao (2006).

2.3.4. Confocal scanning laser microscopy (CSLM)

Confocal scanning laser microscopy (CSLM) has been used to measure the gas/oil volume ratios of the hydrocarbon inclusions previously identified by UV-fluorescence. Application of the CLSM technique to the study of hydrocarbon inclusions has been described in details by Pironon et al. (1998). The measurements were carried out on thick sections of hydrocarbon inclusion-bearing samples using a Bio-Rad (Zeiss) Radiance 2100 Rainbow confocal scanning laser microscope equipped with an argon laser emitting at 488 nm and mounted on a Nikon TE2000-U inverted microscope. The samples were fixed on a glass plate using paraffin prior to their observation under the microscope. Image acquisition was checked under a 60x oil immersion objective. The CSLM measurements were first converted to two-dimensional (2D) image stacks, which were subsequently transformed to image files with the public domain Image-J software (http://rsbweb.nih.gov/ij/). These image files were subsequently analyzed with the aid of the IGOR Pro version 3.16 software (WaveMetrics, Inc.) to compute the bulk volume of the hydrocarbon inclusions, from which the gas/oil volume ratio (noted F_V) can be obtained from a measurement of the diameter of the gas bubble measured by conventional transmission optical microscopy assuming a spherical shape of this bubble (Pironon et al., 1998, 2001).

2.3.5. Fourier transform infrared (FT-IR) spectroscopy

Fourier transform infrared (FT-IR) spectroscopy measurements were made to estimate the compositions (CO_2, CH_4, and higher *n*-alkanes) of the hydrocarbon inclusions, following the methodology presented by Pironon et al. (2001). All measurements were made at the *Laboratoire Environnement et Minéralugie* (LEM, Vandoeuvre-lès-Nancy) with a Bruker EQUINOX 55 FT-IR spectrometer equipped with a Bruker microscope. The spectra have been recorded at 25ºC with a spectral resolution of 4 cm^{-1} and an acquisition time of about 3 minutes. They were subsequently treated with the Bruker OPUS sofware (version 4.0). After a treatment for baseline subtraction, as well as for subtraction of water and atmospheric CO_2, integration of the contributions for methane + higher *n*-alkanes (noted A_X) and for CO_2 (A_{CO_2}) is performed between 3200 and 2800 cm^{-1}. The methane contribution (A_{CH_4}) is removed from A_X using the standard petroleum inclusion Q21 from the Québec City Promontory nappe area (Pironon et al., 2001). This correction yields the *n*-alkane contribution (A_{alk}), the average composition of which can be estimated from the CH_2/CH_3 peak area ratio (Pironon and

Barrès, 1990). Finally, the proportion of methane in the inclusion is determined as the difference between A_X and A_{alk}.

2.3.6. Petroleum inclusion thermodynamic (PIT) modelling

Phase equilibria modelling with the PIT (Petroleum inclusion thermodynamic) program (Thiéry et al., 2000, 2002) was carried out to reconstruct the temperature and pressure conditions of trapping of the hydrocarbon inclusions (and by extension the conditions under which the petroleum was emplaced in the reservoir) or those of subsequent events which may have affected the petroleum reservoir system. This modelling also allows to estimate the gross composition of the hydrocarbon mixtures contained in these inclusions. The PIT program uses a two-parameter compositional model proposed by Montel (1993). These two parameters, which are denoted by α and β, are representative of the heavy (C_{11+}) fraction and of the methane content of the oil, respectively. The compositions of natural hydrocarbon mixtures define a general correlation in a diagram in which the α and β parameters are plotted as a function of each other (Figure 3.8 – Thiéry et al., 2000). Heavy oils are characterized by high values of α and low values of β, while light oils and gas condensates correspond to higher values of β and lower values of α. In practice, the PIT program contains a search routine to find the set of α and β parameters which best fits the homogenization temperatures (T_h) of the hydrocarbon inclusions and their "gas filling degree" (F_V), which have been determined by microthermometry and confocal scanning laser microscopy, respectively (see above). There is not a unique set of values of the α and β parameters which reproduces the T_h and F_V values of a given hydrocarbon inclusion. Instead, a series of values of α and β is obtained, which corresponds to the red line shown in Figure 3.8. The correct set of (α,β) values is assumed to be the one corresponding to the intersection between the red line and the compositonal trend defined by the natural crude oils (Pironon, 2004). If the composition corresponding to this set of (α,β) values compares favorably to the composition (methane content) deduced from the FT-IR spectroscopy measurements (see above), then this composition is used together with the Peng-Robinson equation of state (Peng and Robinson, 1976 – see Part I) to generate a temperature-pressure phase diagram for the hydrocarbon inclusion. A typical temperature-pressure diagram for a hydrocarbon inclusion is shown in Figure 3.9.
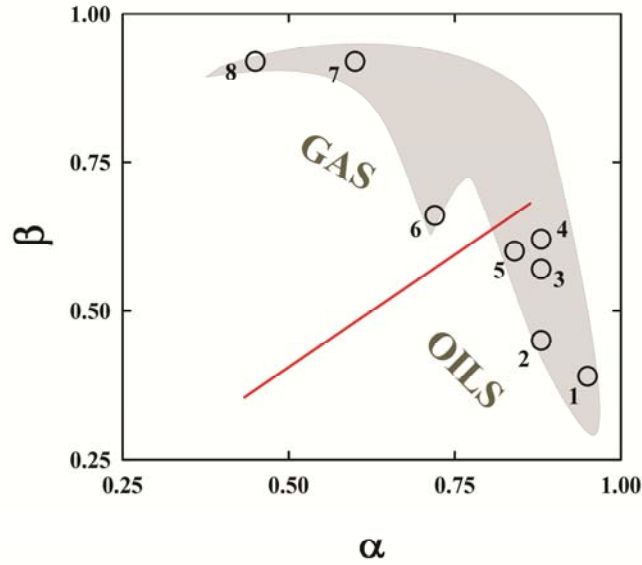
Figure 3.8. Compositional correlation in the α-β diagram (after Thiéry et al., 2000). The symbols correspond to values of α and β determined for a set of natural reference crude oils: (1) heavy oil, (2) CO_2-rich oil, (3) light oil, (4) light oil, (5) "critical oil", (6) gas condensate, (7) wet gas, (8) dry gas. The red line represents the set of values of α and β which are compatible with the measured values of T_h and F_V for a given hydrocarbon inclusion. The intersection between the red line and the green curve representing the compositional trend defined by the natural crude oils corresponds to the "correct" values of α and β from which the temperature-pressure phase diagram is constructed for the hydrocarbon inclusions – see text.

.
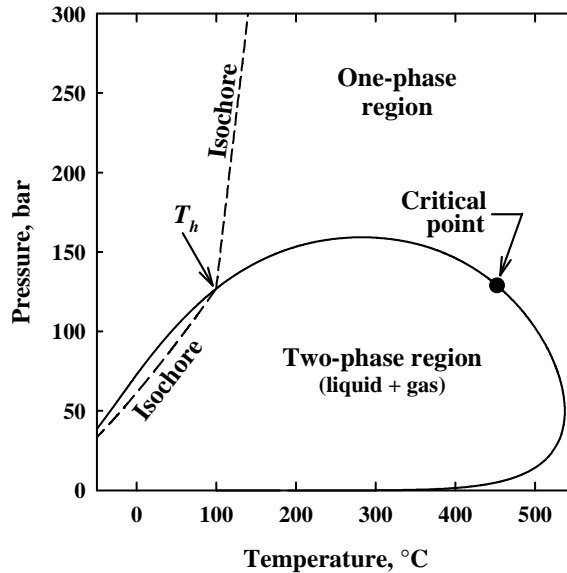
Figure 3.9. Example of temperature-pressure diagram obtained from the Peng-Robinson equation of state using compositional α and β parameters determined for hydrocarbon fluid inclusions (after Pironon, 2004).

2.3.7. P-T reconstruction

If one considers that aqueous and hydrocarbon inclusions coexisting in the same sample (i.e. coeval inclusions) have been trapped under the same conditions of temperature and pressure, an estimate of these conditions may be obtained from the intersection of the isochores of the aqueous and hydrocarbon inclusions (Pironon, 2004). A composite diagram in which the isopleths and isochores of hypothetical coeval aqueous and hydrocarbon inclusions have been represented schematically in Figure 3.10 for the case of gas-undersaturated inclusions.
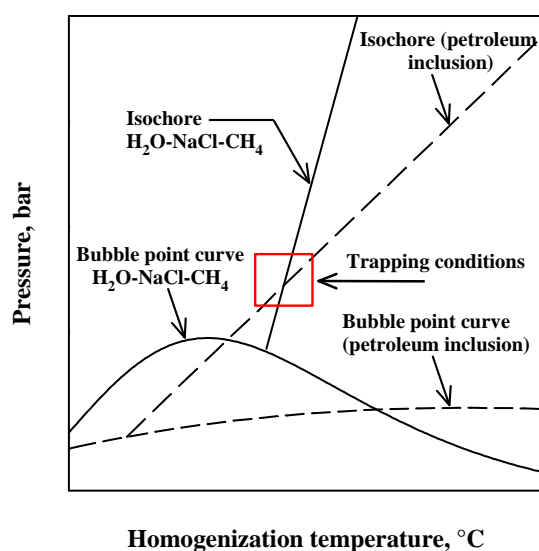
Figure 3.10. Bubble point curves and isochores of coeval aqueous and petroleum inclusions. The intersection of the two isochores corresponds the *P-T* trapping conditions of the inclusions.

193

3. RESULTS

3.1. Petrography and diagenesis

3.1.1. Optical microscopy

Photomicrographs of Bashkirian, Serpukhovian and Devonian samples are shown in Figures 3.11 and 3.12. These samples are represented by bioclastic packstones (Figure 3.11b), oolitic-skeletal grainstones (Figure 3.12a), foraminiferal algal grainstones (Figure 3.12c), and pelletal grainstones (Figure 3.12e) which may contain foraminifers, crinoid fragments, oolites, or scleractinian corals. The samples are partially or fully dolomitized. Dolomitization appears to increase with increasing depth. Both fibrous (Figure 3.11a) and syntaxial cements are observed, the former around ooliths and the latter as crinoid overgrowths (Figure 3.11b). Calcite cements are also observed as fracture fillings (Figure 3.11c), as well as stylolite pore fillings (Figure 3.11d).
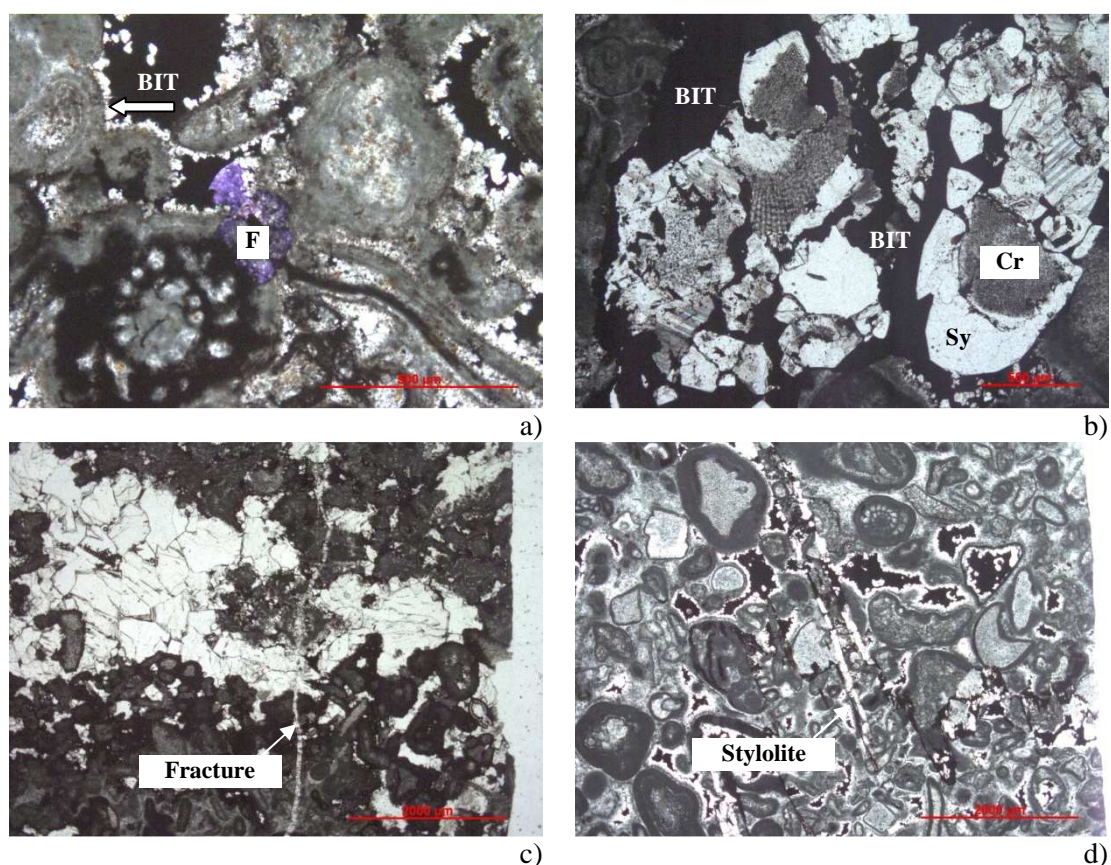
Figure 3.11. a) Ax-4 sample: fibrous calcite cement (white arrow) and fluorite (F); b) Ax-6 sample: crinoid-rich bioclastic packstone with syntaxial (Sy) calcite overgrowth on crinoid (Cr). Bitumen (BIT) precipitation may have interrupted the precipitation of calcite cement; c) Ax-3 sample: foraminiferal algal grainstone composed of foraminifera within bitumen. Fracture filled by calcite spar; d) Ax-5 sample: foraminiferal algal grainstone, crinoid fragments and stylolite pores filled by calcite.

Dolomite is observed as isopachous rims around oolites (Figure 3.12a) and on the walls of open vugs (Figure 3.12b). Bitumen is present in open pores and vugs (Figure 3.12a and 3.12b), in foraminifera (Figure 3.12c), and in stylolite pores (Figure 3.12d).
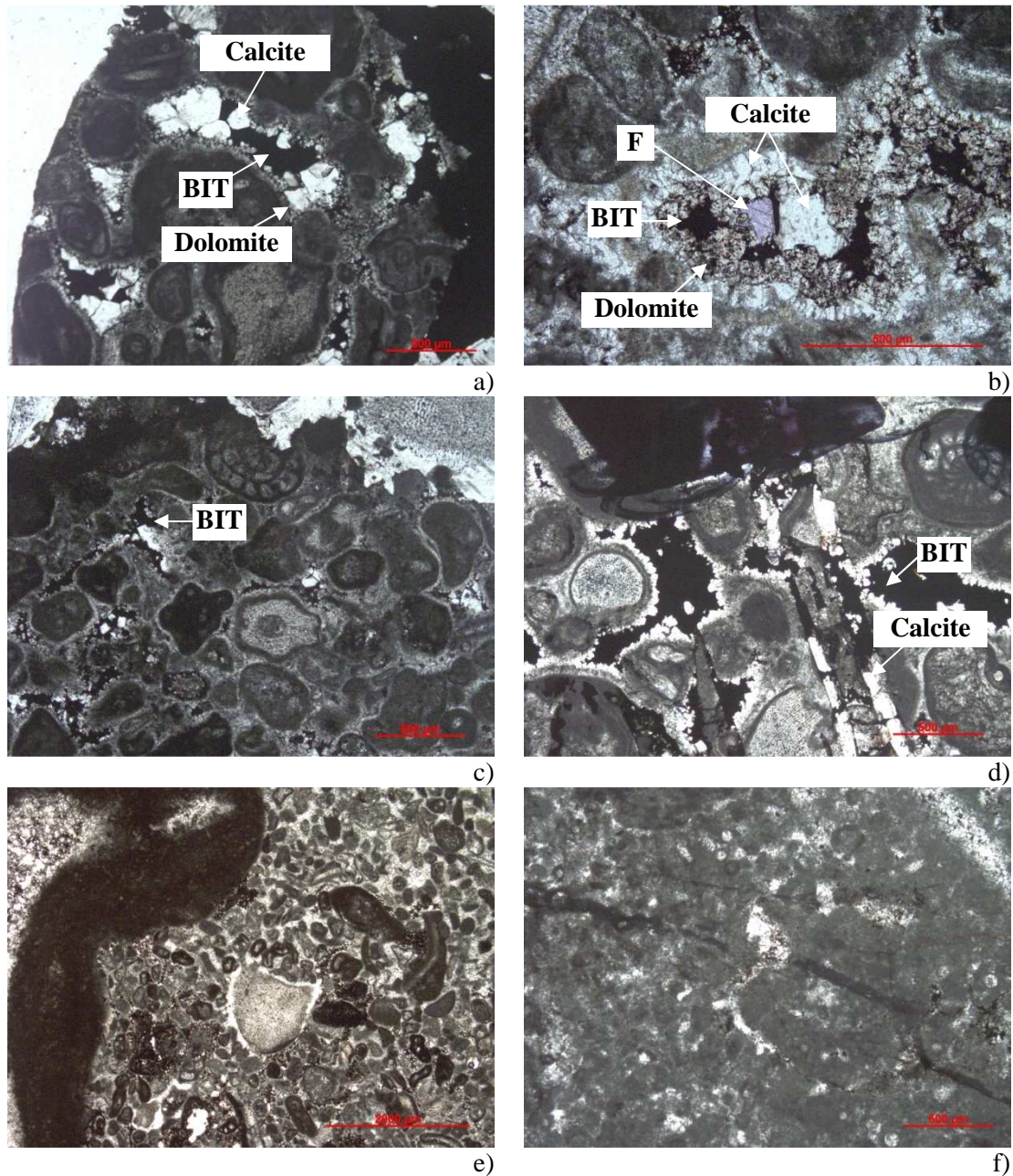
Figure 3.12. a) Ax-6 sample, oolitic-skeletal grainstone: isopachous dolomite, open pores, and vugs filled by calcite and bitumen; b) Ax-5 sample, oolitic-skeletal grainstone: open vugs filled by dolomite, calcite, bitumen, and fluorite; c) Ax-1 sample, foraminiferal algal grainstone, foraminifera filled with bitumen; d) Ax-4 sample, foraminiferal algal grainstone: crinoid fragments, bitumen along stylolite, in stylolite pores and vugs filled by bitumen and calcite; e) Ax-9 sample, pelletal and foraminiferal algal grainstone: pellets, foraminifera, and crinoid fragments; f) Ax-10 sample, dolomitized pelletal grainstone: bitumen and calcite fillings in hairline fissures and fractures.

3.1.2. Cathodoluminescence (CL)

Cathodoluminescence observations has indicated the existence of both carbonate (calcite, dolomite) and non-carbonate (fluorite) cements. Several types of calcite cements can be recognized by their luminescence, which is characterized by black, dark red orange, pure yellow orange, and light red colors. Dolomite cements are characterized by bright pink to pink colors. Fluorite appears black in CL. The different generations of cements identified in the samples have been listed in Table 3.1 along with their occurences. These cements are described in detail below.

Calcite cement A. This cement is a syntaxial, non luminescent early cement occuring around crinoids. It is sometimes composed by a complex sequence of subzones (Figure 3.13), two successive subzones being separated by a phase of dissolution or corrosion.

Calcite cement B. This cement is also a syntaxial calcite cement, occasionally broadly zoned and characterized by a dark red orange color in CL. This cement is subsequent to the early calcite cement A (Figure 3.13).

Calcite cements C1 and C2. Calcite C1 is a syntaxial calcite cement which was precipitated after cement B. This cement is characterized by a pure yellow orange in CL. Cement C1 fills open fractures which crosscut crinoids, cement A and cement B (Figure 3.13). Therefore, fracturation was posterior to cement B. Calcite C1 cement is observed only in Bashkirian samples.

Calcite C2 is an overgrowth calcite which follows cement C1. It is characterized by a dark red orange in CL (Figure 3.13) and is only observed in Bashkirian samples.

<div align="center">a)   b)</div>
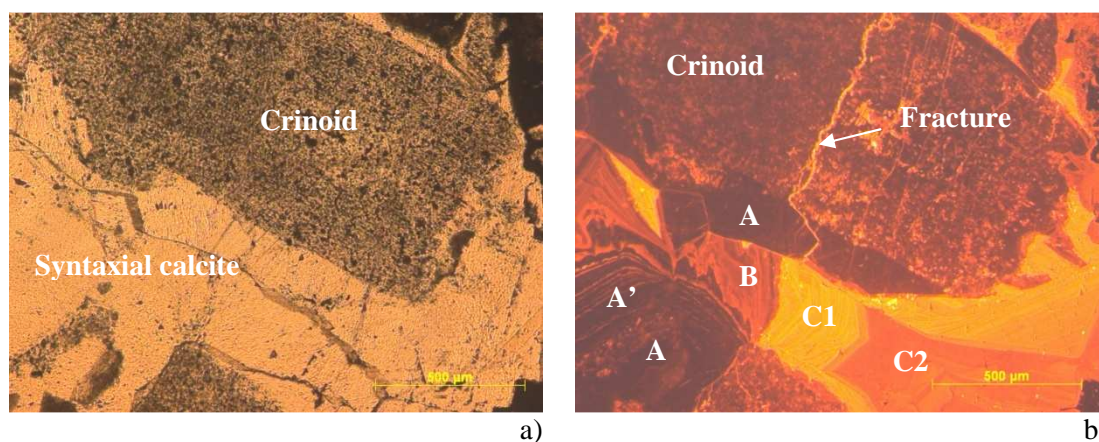
Figure 3.13. Overgrowth calcite cement on crinoids, Ax-1 sample: a) – transmitted light, b) – cathodoluminescence (sequence of A and A' subzones, and B, C1 and C2 calcite cements. Fracture filled by C1 cement).

Dolomite cement D. Precipitation of dolomite cement resulted in the development of isopachous rims around calcite cements B or C (Figure 3.14) or a host grain. It also occurs as fillings in open fractures (Figure 3.16) and on the walls of open vugs (Figure 3.17). The colors in CL vary from bright red to bright pink. This dolomite cement is observed in samples from Bashkirian, Serpukhovian, and Devonian age.
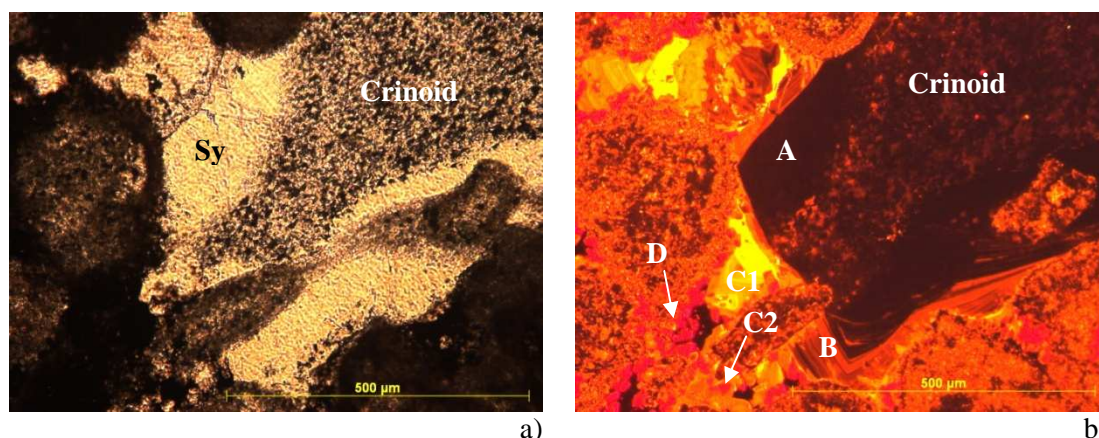
Figure 3.14. Overgrowth calcite cement on crinoid. Ax-2 sample: a) – transmitted light, b) – cathodoluminescence (A, B, C1, and C2 - calcite cements, D - dolomite).

Bitumen. Bitumen emplacement occurred before and after the dolomitization stage. Pre-dolomite bitumen emplacement is observed in samples without dolomite cement. It occurs as fillings in open vugs, along stylolites, and in stylolite pores (Figure 3.15). Stylolitisation occurred just after or during the precipitation of calcite C2 cement. Post-dolomite bitumen is observed in fractures (Figure 3.16) and open vugs (Figure 3.17) in dolomite-bearing samples.
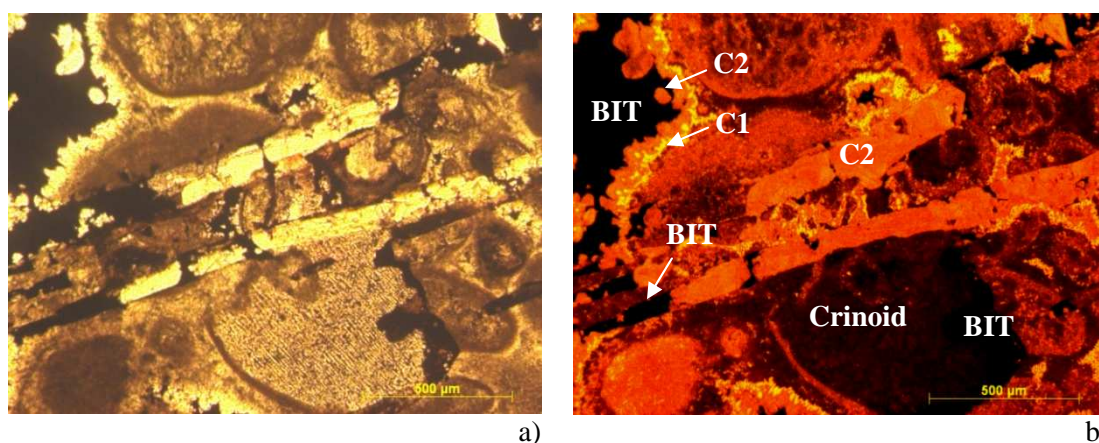
Figure 3.15. Crinoid and calcite cements cut by stylolite. Ax-4 sample: a) – transmitted light, b) – cathodoluminescence (A, C1, C2 - calcite cements, BIT – pre-dolomite bitumen).

Calcite cement E. Cement E corresponds to a late calcite precipitated after dolomite cement D. It is characterized by a dark red orange color in CL and is observed in Bashkirian samples only. This cement, which is associated with bitumen, is observed crosscutting the

previous calcite and dolomite cements (Figure 3.16), as well as in open vugs (Figure 3.17) with fluorite (Figure 3.17) and barite (Figure 3.18).
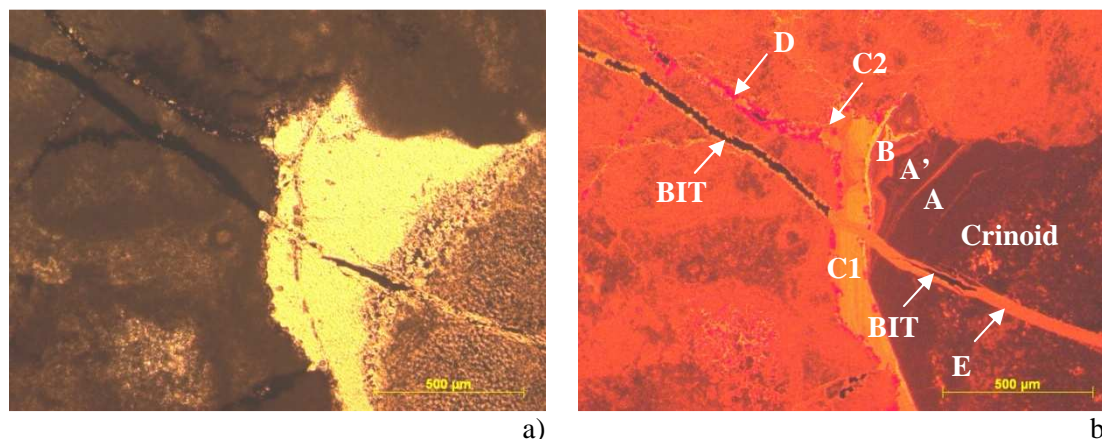
Figure 3.16. Overgrowth calcite cement on crinoid. Ax-7 sample: a) – transmitted light, b) – cathodoluminescence (A/A', B, C1, C2 - calcite cements, D - dolomite, BIT – post-dolomite bitumen, E – calcite cement).

Fluorite F. Fluorite was precipitated after dolomite and is associated in open vugs with cement E, barite and bitumen (Figures 3.17 and 3.18). Fluorite appears black in CL.
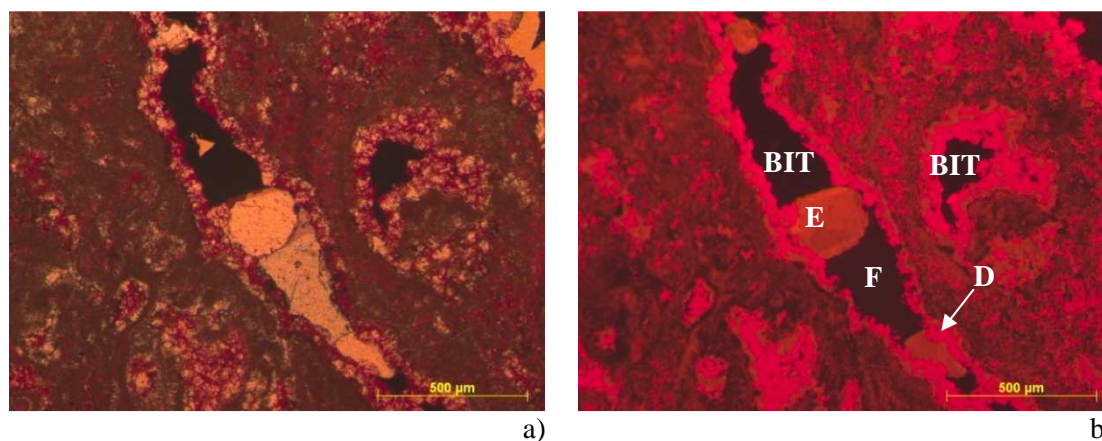
Figure 3.17. Late calcite cement E, fluorite and post-dolomite bitumen in open vugs. Ax-5 sample: (a) – transmitted light, (b) – cathodoluminescence (D - dolomite, BIT – post-dolomite bitumen, E – calcite cement, and F - Fluorite).

Table 3.1. Occurence of the various types of cements in the Ax samples.

Stage	Sample	A	B	C1	C2	D	E	F
Bashkirian	Ax-1	+	+	+	+	-	-	-
Bashkirian	Ax-2	+	+	+	+	+	+	-
Bashkirian	Ax-3	+	+	+	+	-	-	-
Bashkirian	Ax-4	+	+	+	+	-	-	+
Bashkirian	Ax-5	+	+	+	-	+	+	+
Bashkirian	Ax-6	+	+	+	+	+	+	+
Bashkirian	Ax-7	+	+	+	+	+	+	-
Bashkirian	Ax-8	+	+	-	-	+	-	+
Serpukhovian	Ax-9	+	+	-	-	+	-	-
Devonian	Ax-10	+	+	-	-	+	-	+

3.1.3. SEM and electron microprobe analyses

SEM observations and chemical analyses have been carried out to further characterize the mineralogy of the Aktote reservoir. In addition to calcite and dolomite, fluorite, barite, pyrite, halite, phosphates, elemental sulfur, and anhydrite have been identified. Fluorite and barite associated with the late calcite cement E and post-dolomite bitumen (Figure 3.18a). The observation of fluorite in cathodoluminescence is confirmed by SEM analysis (Figure 3.18b). Other minerals observed around crinoids, as well as in pores and open fractures, include sulfur, anhydrite, pyrite, halite, and phosphate minerals (Figure 3.19a and b and Figure 3.20).

a)   b)
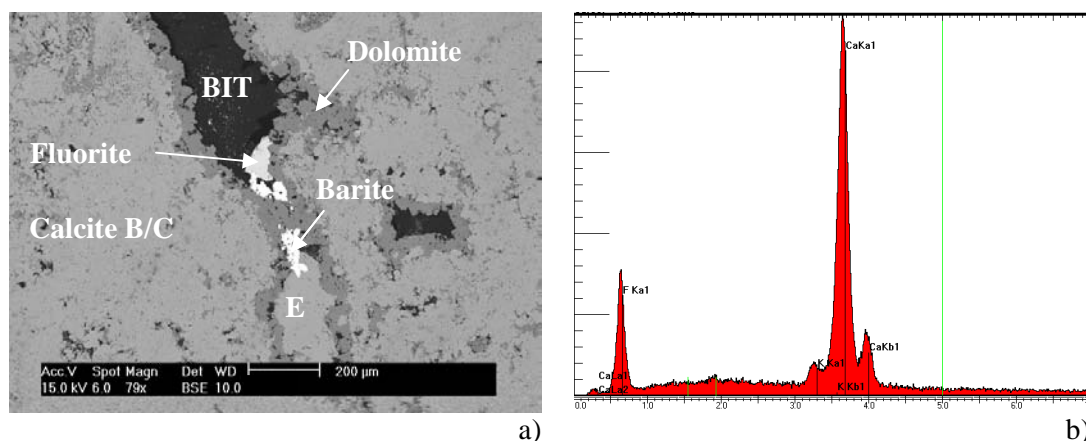
Figure 3.18. SEM identification of minerals in Ax-5 sample: a) Post-dolomite bitumen (BIT), calcite E, fluorite, and barite in isolated vug; b) Fluorite spectra.

Rare anhydrite is found in open pores (Figure 3.20a), sometimes associated with halite or other chloride salts (Figure 3.20b).

a)   b)
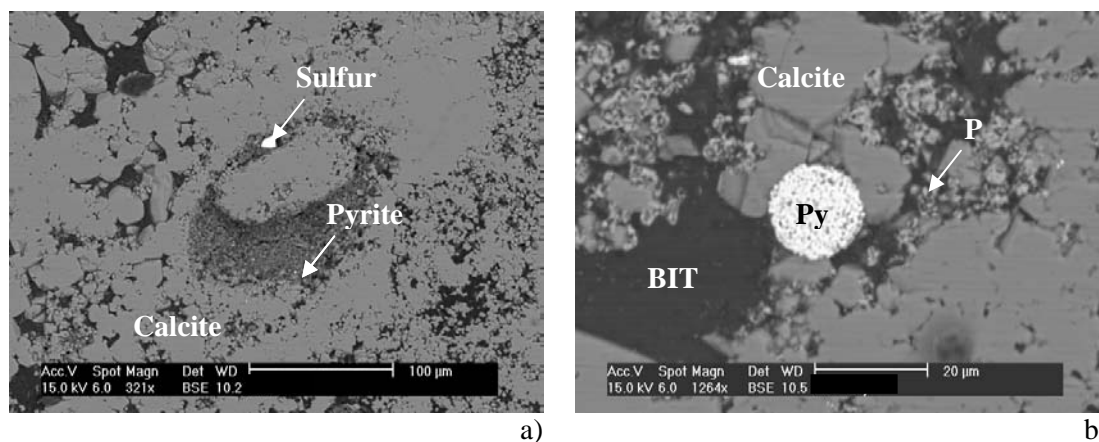
Figure 3.19. SEM identification of minerals in Ax-1 sample: a) Distribution of the sulfur and pyrite (Py) around a calcite grain; b) Pre-dolomite bitumen (BIT), pyrite (Py) and phosphates (P) in open pores.

a)   b)
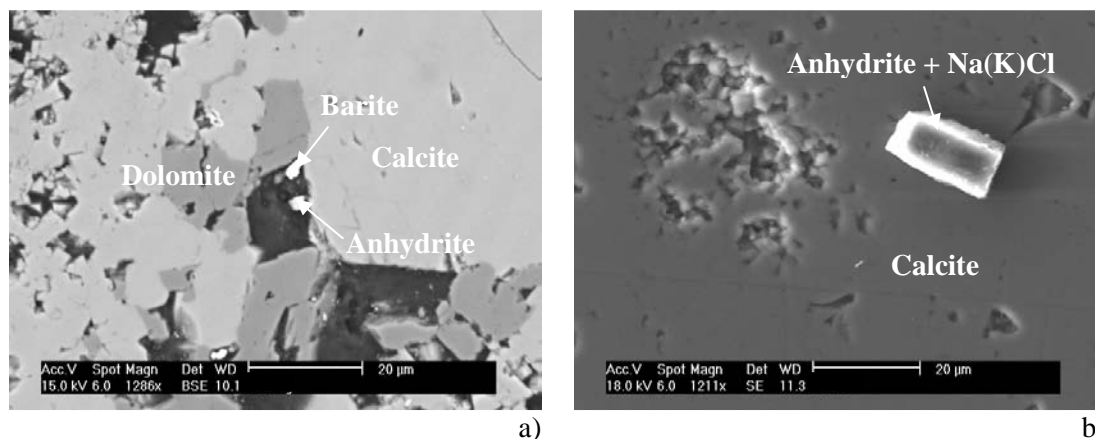
Figure 3.20. SEM identification of minerals in Ax-2 sample: a) Barite and anhydrite in open pore; b) Anhydrite associated with minor chloride salts (Na(K)Cl).

Trace element contents of the carbonate cements determined by electron microprobe analysis are given in Table 3.2. Location of the microprobe measurements are identified for sample Ax-2 on the CL microphotograph shown in Figure 3.21a. A comparative plot of the trace element contents in this sample is shown in Figure 3.21b. It can be seen in this table that the Mn content is highest in the C1 cement as well as in the dolomite cement. The latter cement is also significantly enriched in Sr compared to the other cements. The Fe content does not show significant variations among the various cements, although it can be deduced from Table 3.2 that the Fe content is below the detection limit for cements C1 and D, which have the highest Mn content. These observations are comparable to those made by Ronchi et al. (2010) for carbonate cements from the Kashagan reservoir. The variation of luminescence observed in Figure 3.21a among the different cements can be related to their Mn contents.

a)   b)
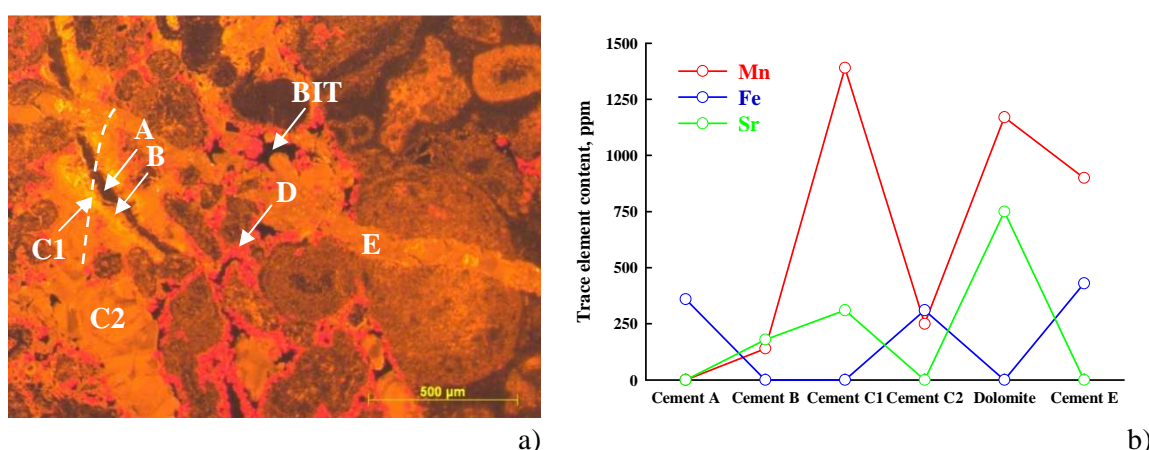
Figure 3.21. Trace element contents in the carbonate cements of sample Ax-2: a) – cathodoluminescence (A, B, C1, C2 - pre-dolomite cements, D – dolomite, BIT - bitumen, E – late calcite cement) ; b) – Variations of the Mn, Fe and Sr contents among the various cements.

Table 3.2. Trace element contents (ppm) of the carbonate cements in the Ax samples.
(n.a. not analyzed, b.d.l. below detection limit).

Sample	Trace element	Cement A	Cement B	Cement C1	Cement C2	Dolomite D	Cement E
Ax-1	Mn	b.d.l.	270	2570	80	n.a.	n.a.
	Sr	b.d.l.	290	b.d.l.	b.d.l.	n.a.	n.a.
	Fe	b.d.l.	b.d.l.	b.d.l.	b.d.l.	n.a.	n.a.
	Mg	610	1670	1870	1140	n.a.	n.a.
Ax-2	Mn	b.d.l.	140	1390	250	1170	720
	Sr	b.d.l.	180	310	b.d.l.	750	b.d.l.
	Fe	360	b.d.l.	b.d.l.	310	b.d.l.	180
	Mg	940	850	670	18420	125820	790
Ax-2	Mn	470	400	3820	n.a.	1980	1860
	Sr	b.d.l.	780	90	n.a.	b.d.l.	b.d.l.
	Fe	b.d.l.	b.d.l.	b.d.l.	n.a.	b.d.l.	310
	Mg	660	1180	2790	n.a.	125500	2040
Ax-3	Mn	b.d.l.	n.a.	4860	330	n.a.	n.a.
	Sr	b.d.l.	n.a.	b.d.l.	b.d.l.	n.a.	n.a.
	Fe	50	n.a.	b.d.l.	b.d.l.	n.a.	n.a.
	Mg	1190	n.a.	2000	2050	n.a.	n.a.
Ax-4	Mn	b.d.l.	n.a.	530	b.d.l.	n.a.	n.a.
	Sr	b.d.l.	n.a.	b.d.l.	b.d.l.	n.a.	n.a.
	Fe	b.d.l.	n.a.	b.d.l.	180	n.a.	n.a.
	Mg	1140	n.a.	900	400	n.a.	n.a.
Ax-5	Mn	b.d.l.	140	n.a.	n.a.	4320	960
	Sr	b.d.l.	240	n.a.	n.a.	110	b.d.l.
	Fe	b.d.l.	150	n.a.	n.a.	b.d.l.	410
	Mg	1580	1750	n.a.	n.a.	123290	1220
Ax-6	Mn	n.a.	n.a.	1030	b.d.l.	n.a.	n.a.
	Sr	n.a.	n.a.	b.d.l.	b.d.l.	n.a.	n.a.
	Fe	n.a.	n.a.	b.d.l.	350	n.a.	n.a.
	Mg	n.a.	n.a.	1400	800	n.a.	n.a.
Ax-7	Mn	b.d.l.	200	1160	470	570	b.d.l.
	Sr	b.d.l.	b.d.l.	b.d.l.	b.d.l.	570	b.d.l.
	Fe	b.d.l.	b.d.l.	b.d.l.	b.d.l.	b.d.l.	b.d.l.
	Mg	440	1270	4230	2070	127730	650
Ax-8	Mn	b.d.l.	1560	n.a.	n.a.	840	n.a.
	Sr	b.d.l.	50	n.a.	n.a.	20	n.a.
	Fe	b.d.l.	b.d.l.	n.a.	n.a.	440	n.a.
	Mg	2590	3160	n.a.	n.a.	124690	n.a.
Ax-9	Mn	b.d.l.	250	n.a.	n.a.	780	n.a.
	Sr	210	b.d.l.	n.a.	n.a.	b.d.l.	n.a.
	Fe	240	510	n.a.	n.a.	b.d.l.	n.a.
	Mg	1920	4800	n.a.	n.a.	126870	n.a.
Ax-10	Mn	b.d.l.	480	n.a.	n.a.	b.d.l.	n.a.
	Sr	b.d.l.	b.d.l.	n.a.	n.a.	80	n.a.
	Fe	b.d.l.	140	n.a.	n.a.	b.d.l.	n.a.
	Mg	2400	1510	n.a.	n.a.	125680	n.a.

3.2. Fluid inclusion study

Aqueous and hydrocarbon inclusions in calcite grains, calcite cements and fluorite from carbonate samples of the Aktote reservoir have been studied using microthermometry as well as Raman and infrared spectroscopies to estimate their compositions and to attempt to reconstruct the temperature-pressure history of the reservoir and the conditions of hydrocarbon emplacement. Aqueous and petroleum inclusions were distinguished by UV fluorescence. Both types of inclusions are generally 2-phase, liquid and vapor inclusions. Their homogenization temperatures were determined by microthermometry heating. The composition of aqueous inclusions was estimated by Raman microspectrometry. Gas/oil ratios (F_V) of the petroleum inclusions were measured using confocal scanning laser microscopy (CSLM). The compositional, volumetric and phase behavior informations obtained from the microthermometric, spectrometric, and confocal microscopy measurements were used together with thermodynamic modelling calculations to reconstruct the temperature-pressure history of, and the conditions of hydrocarbon emplacement in the reservoir.

3.2.1. Fluid inclusion petrography

Petroleum inclusions were distinguished from their aqueous counterparts based on their fluorescence under 360-370 nm UV light. Petroleum inclusions have been observed in crinoid fragments (Figure 3.22a-b), in calcite cement overgrowths on crinoid fragments (Figure 3.22c-d), in fracture-filling calcite cement (Figure 3.22e-f), and in calcite cement in stylolite pores (3.22g-h). No fluorescent inclusions have been observed in fluorite.

Aqueous inclusions were recognized by optical microscopic observation in overgrowth, calcite cements filling stylolite pores and open vugs, as well as in fluorite.

3.2.2. Fluid inclusion description

Microfractures and hairline fissures in crinoid fragments contain numerous biphasic, blue and yellow fluorescent hydrocarbon inclusions which are approximately 5-10 µm in size (e.g. Figure 3.22b). However, the gas/oil ratio of these hydrocarbon inclusions could not be measured with enough precision by CSLM.

Pre-dolomite cements, including overgrowth calcites and stylolite filling calcites, contain both aqueous and blue hydrocarbon inclusions (Figure 3.23a). Some colorless hydrocarbon inclusions have also been observed in some overgrowth calcites of sample Ax-7. The size of the aqueous inclusions is approximately 4-8 µm. The blue hydrocarbon inclusions are in the 3-10 µm range, while the colorless inclusions are 10-15 µm in size.
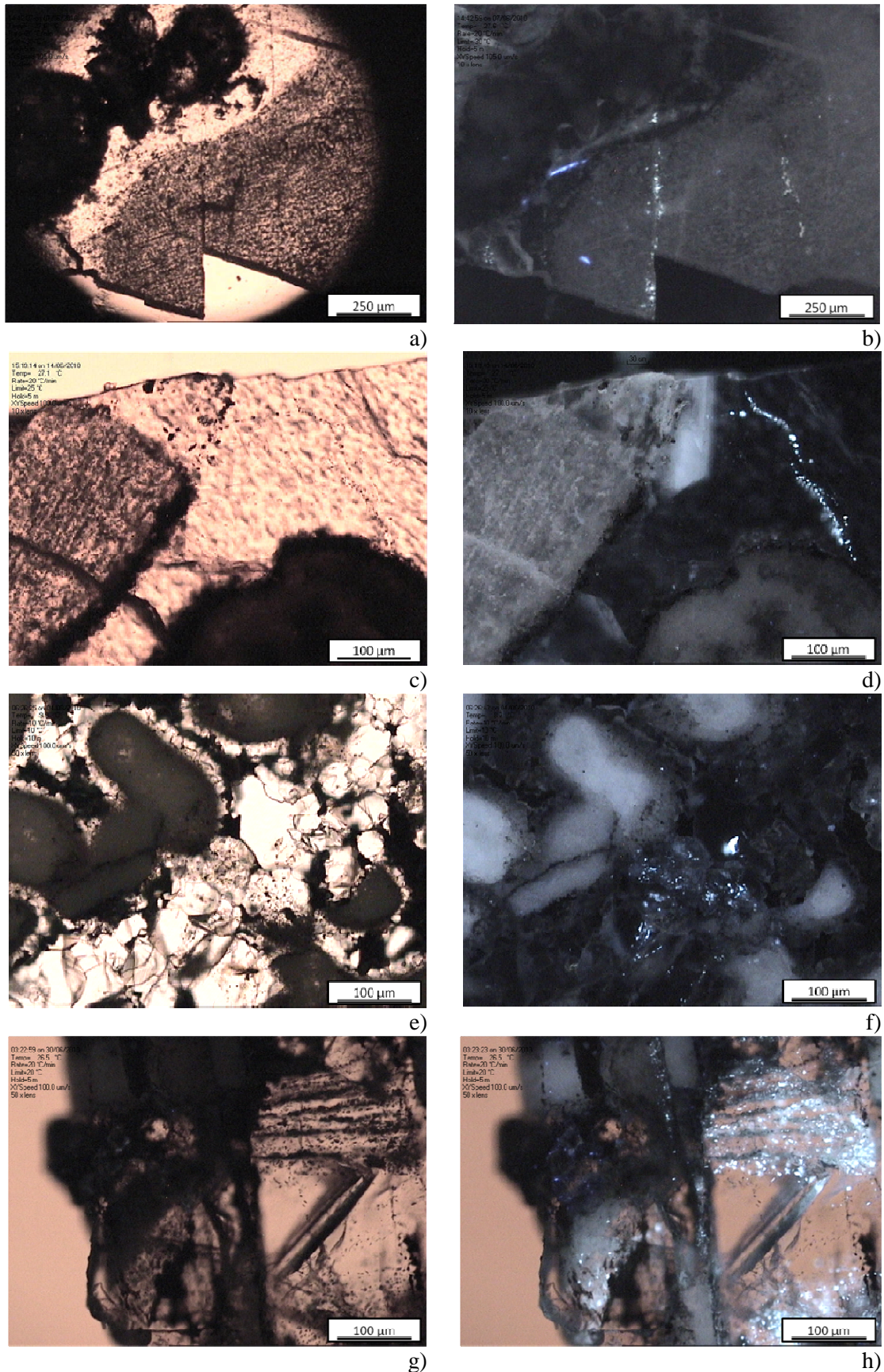
Figure 3.22. Photomicrographs of aqueous and hydrocarbon inclusions observed under transmitted light and UV fluorescence: a-b) Ax-1 sample, hydrocarbon inclusions within crinoid fragment; c-d) Ax-2 sample, hydrocarbon inclusions in overgrowth calcite; e-f) Ax-3 sample, hydrocarbon inclusions in calcite-filled fracture; g-h) Ax-4 sample, hydrocarbon and aqueous inclusions in calcite-filled stylolite pores.
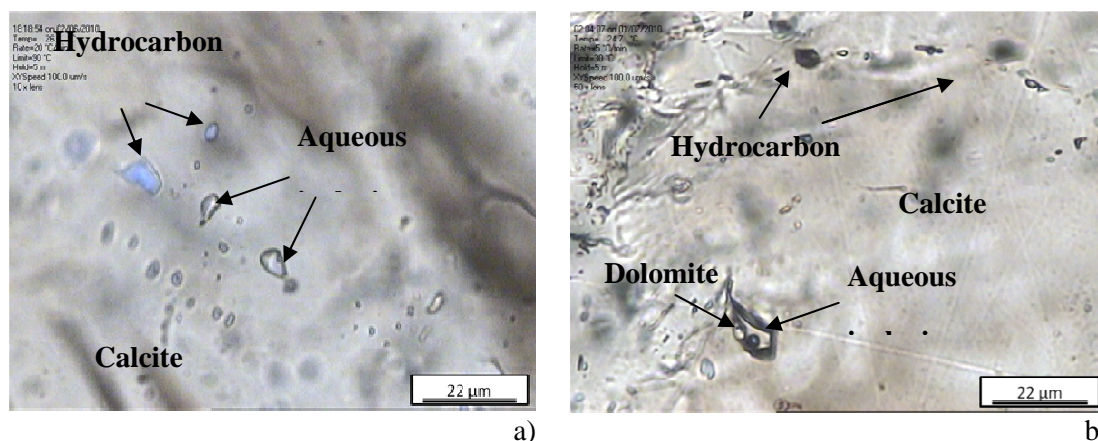
Figure 3.23. Photomicrograph of aqueous and hydrocarbon inclusions observed under transmitted light and UV fluorescence: a) Ax-1 sample, cogenetic aqueous and hydrocarbon inclusions in pre-dolomite calcite cement; b) Ax-5 sample, cogenetic aqueous and hydrocarbon inclusions in post-dolomite calcite cement.

Pre-dolomite, fracture-filling calcite cements contain blue hydrocarbon inclusions, which are approximately 5-10 µm in size (Figure 3.22f), but no aqueous inclusions. In addition, the occurrence of colorless hydrocarbon inclusions has also been noticed in a fracture-filling cement of sample Ax-3. These colorless inclusions are 10-15 µm in size.

Post-dolomite calcite cements are characterized by aqueous fluid inclusions and blue hydrocarbon inclusions (Figure 3.23b), the size of which is also in the 5-10 µm range. Finally, the aqueous inclusions hosted by the Bashkirian and Devonian fluorites have an approximate size of 10 µm. Finally, neither aqueous nor hydrocarbon inclusions have been observed in the dolomite cements.

The estimation of the temperature and pressure conditions under which the hydrocarbon fluid was emplaced in the reservoir requires that the microthermometric measurements be performed on aqueous and hydrocarbon fluid inclusions which are cogenetic, i.e. trapped within the same mineral or cement (Figure 3.23).

3.2.3. Microthermometry

The results of microthermometric measurements performed on calcite- and fluorite-hosted aqueous fluid inclusions and on calcite-hosted hydrocarbon inclusions are presented under the form of histograms in Figures 3.24a and 3.24b, respectively. It can be seen in these figures that the homogenization temperatures of the aqueous inclusions are higher than those of their hydrocarbon counterparts. The homogenization temperatures of the aqueous inclusions in pre-dolomite calcite cements range between 75ºC and 95°C, while those of aqueous inclusions in post-dolomite calcite cements range between 75ºC and 120°C (Figure 3.24a). The aqueous fluid inclusions in fluorite homogenize between 85ºC and 115°C, the

homogenization temperatures being generally higher in fluorites of the Devonian sample (Figure 3.24a).

The homogenization temperatures of the blue and yellow hydrocarbon inclusions range between 25 and 55°C with a mode at ~ 45-50ºC. The colorless hydrocarbon inclusions homogenize at temperatures between 30 and 55°C (Figure 3.24b).

It can be seen in Figure 3.24a that two aqueous fluid inclusions in a post-dolomite calcite have unusually high homogenization temperatures of 115-120°C. This may either be due to volume stretching during heating, which results in an increase of homogenization temperatures (e.g. Prezbindowski and Larese, 1984), or reflect the circulation of hydrothermal fluids within the reservoir – see discussion below.
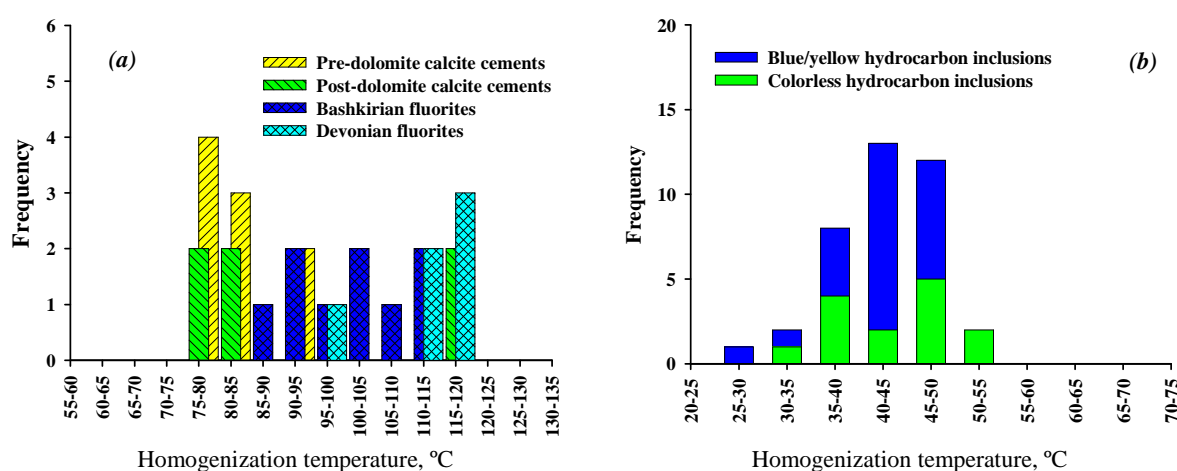
Figure 3.24. Histograms of homogenization temperatures for *(a)* aqueous inclusions; *(b)* hydrocarbon inclusions.

3.2.4. Raman and Fourier Transform Infrared (FT-IR) spectroscopies

3.2.4.1. Raman microspectrometry

The salinity and composition of aqueous inclusions in calcite cements and in fluorite have been determined by Raman microspectrometry. Selected Raman spectra obtained for samples Ax-4 and Ax-10 are shown in Figure 3.25. Aqueous inclusions in the calcite cement from sample Ax-4 (Figures 3.25a et 3.25b) contain the following dissolved species: SO_4^{2-} (984 cm^{-1}), HS$^-$ (2574 cm^{-1}), $H_2S_{(aq)}$ (2590 cm^{-1}) and $CH_{4(aq)}$ (2917 cm^{-1}). The peaks between 3000 and 3700 cm^{-1} in Figure 3.25b correspond to vibrations of liquid H_2O. The peaks at 713, 1088, 1437 and 1750 cm^{-1} in Figure 3.25a correspond to lattice vibrations (ν_1-ν_4) of calcite (e.g. Urmos et al., 1991). Comparison in Figure 3.25c of the spectrum obtained for an inclusion in sample Ax-2 with a reference spectrum for calcite reveals the presence of elemental sulfur in that inclusion (peaks at 221 and 474 cm^{-1}).
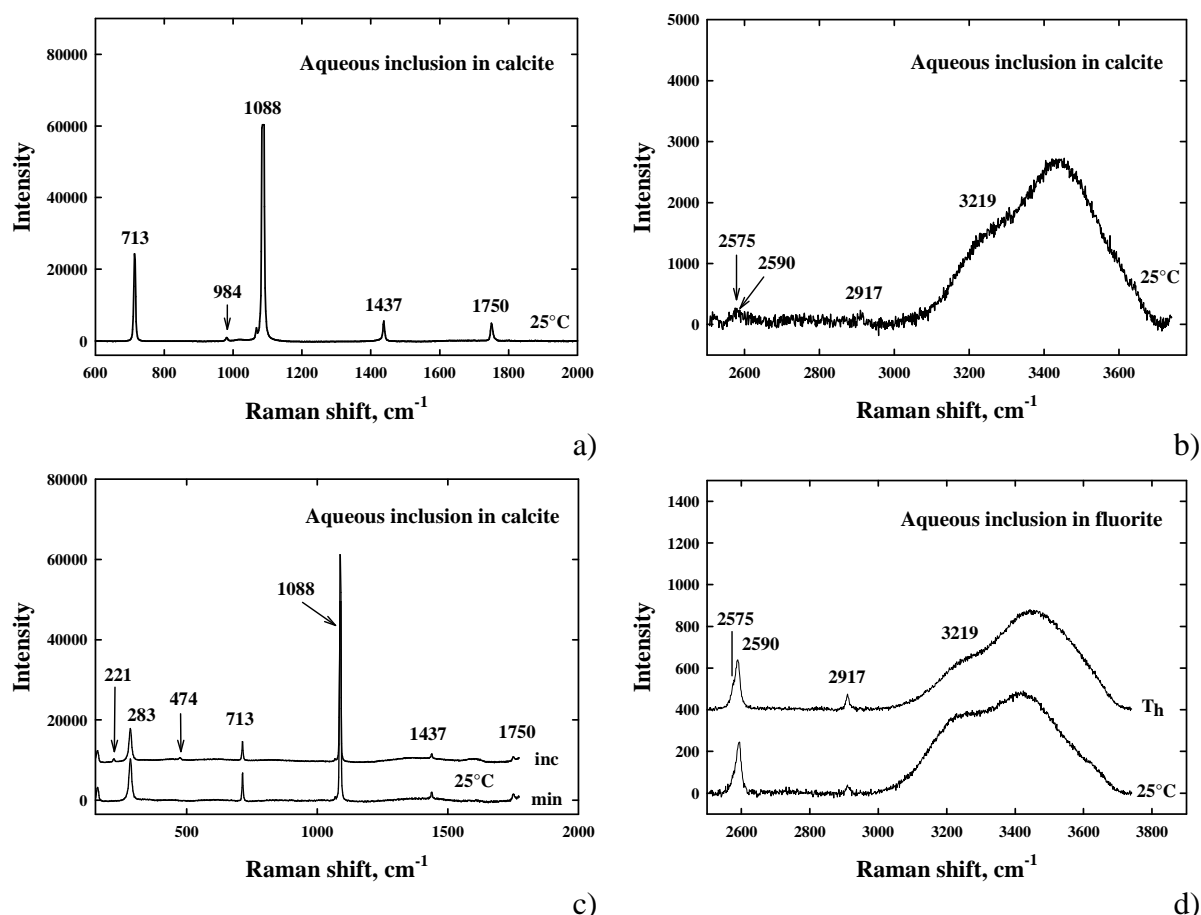
Figure 3.25. Raman spectra of aqueous fluid inclusions: a) sample Ax-4, aqueous SO_4^{2-} and calcite bands (see text); b) sample Ax-4, $H_2S_{(aq)}$, HS^-, and $CH_{4(aq)}$; c) sample Ax-2: elemental sulfur peaks (221 and 474 cm^{-1}) – a reference Raman spectrum of calcite is shown for comparison (min = mineral, inc = inclusion); d) sample Ax-10: $H_2S_{(aq)}$ and $CH_{4(aq)}$ in an aqueous inclusion in fluorite.

Aqueous inclusions in fluorite (Figure 3.25d) also contain dissolved sulfate (not shown), as well as $H_2S_{(aq)}$, HS^-, and $CH_{4(aq)}$. HS^- appears as a shoulder on the H_2S peak. Coexistence of H_2S and HS^- with dominant H_2S indicates pH around of 6 and 7 (Jacquemet, 2006). A spectrum acquired at the homogenization temperature (T_h) is also shown in Figure 3.25d, which allows the estimation of the gas concentrations by integration of the Raman peaks – see below. Finally, we note that neither dissolved CO_2 nor bicarbonate (HCO_3^-) were identified in the aqueous inclusions.

The chloride concentrations in the aqueous fluid inclusions have been estimated using the method proposed by Dubessy et al. (2002), which is based on the modifications by the chloride ion of the Raman band corresponding to the stretching vibrations of water. The concentrations of dissolved methane and hydrogen sulfide were estimated from the measured gas/H_2O band area ratios at the homogenization temperatures of the inclusions (Dubessy et al., 2001; Guillaume et al., 2003; Jacquemet, 2005). Due to fluorescence problems,

measurements could only be made on a limited number of aqueous inclusions. The results are summarized in Table 3.3.

Table 3.3. Summary of microthermometry and Raman analyses on aqueous fluid inclusions.

Stage	Sample	Host mineral	Cement	T_h, °C	m_{NaCl}	m_{CH_4}	m_{H_2S}
Bashkirian	Ax-1	Calcite	C1	92	1.37	0.120	0.800
	Ax-1	Calcite	C1	92	0.74	0.146	1.500
	Ax-4	Calcite	C2	78	1.19	0.094	0.300
	Ax-5	Calcite	E	120.0	0.90	0.210	0.800
	Ax-6	Fluorite	F	92.5	1.60	0.208	0.520
Devonian	Ax-10	Fluorite	F	102	0.08	0.200	2.000
	Ax-10	Fluorite	F	113	0.29	0.190	1.650
	Ax-10	Fluorite	F	119	0.35	0.330	1.740
	Ax-10	Fluorite	F	119	0.10	0.310	1.740
	Ax-10	Fluorite	F	119	0.14	0.250	1.790
	Ax-10	Fluorite	F	110	0.85	0.290	1.480

It can be deduced from Table 3.3 that with the exception of cement E, the homogenization temperatures are lower for the Bashkirian samples than for the Devonian samples. The salinities are higher in the Bashkirian samples, but the methane concentrations are lower compared to the Devonian samples. In contrast, the H_2S concentrations are higher in the latter samples, with values as high as 1.5 – 2.0 molal.

3.2.4.2. Fourier-transform infrared spectroscopy (FT-IR)

In order to obtain some information on the molecular composition of the hydrocarbon inclusions, FT-IR analyses were performed on doubly polished thick sections. A requirement of the FT-IR analysis is that the measurements must be performed on inclusions which are >10 µm in size. As a result, only three inclusions could be measured in the present study. Infrared spectra are recorded for the host mineral and the bulk inclusion. The contributions from the mineral as well as from atmospheric CO_2 and H_2O are subsequently substracted. An example of spectrum obtained after substraction of these contributions is shown in Figure 3.26. The peaks at 2962 and 2875 cm^{-1} correspond to the methyl groups of n-alkanes, while those at 2927 and 2858 cm^{-1} correspond to their methylene groups. The shoulder peak at 3010 cm^{-1} corresponds to methane. Carbon dioxide, which should appear at 2341 cm^{-1} was not observed in the inclusions. A treatment of the FT-IR spectra following the method proposed by Pironon et al. (2001) and described in Section *2.3.5* above, allowed to calculate the compositions of the hydrocarbon inclusions. The results of the calculations are given in Table 3.4. From the CH_2/CH_3 area ratios, an average chain length of 5 to 6 or 6 to 7 carbon atoms

for the the *n*-alkanes is obtained. This corresponds to a molar composition of the hydrocarbon inclusions with approximately one third of methane and two thirds of higher alkanes.
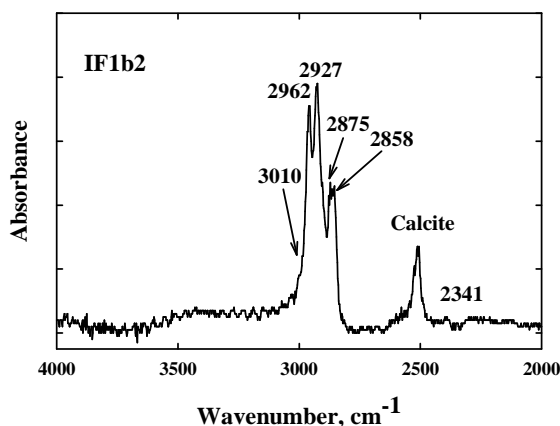
Figure 3.26. FT-IR spectrum of a hydrocarbon inclusion in sample Ax-7.
The different peaks are identified in the text.

Table 3.4. Summary of FT-IR analyses on hydrocarbon inclusions.

Stage	Sample	Mineral	T_h ,°C	CH_4 mol%	CO_2 mol%	Alk. mol%	CH_2/CH_3	Alkanes
Bashkirian	Ax-7	Calcite	38.5	34.5	0.00	65.5	1.70	C_5-C_6
Bashkirian	Ax-7	Calcite	36.4	36.4	0.00	63.6	2.20	C_6-C_7
Bashkirian	Ax-7	Calcite	53.6	35.1	0.00	64.9	1.80	C_5-C_6

3.2.5. Confocal Laser Scanning Microscopy (CLSM)

CLSM analysis has been performed on hydrocarbon inclusions in calcite cements of all the samples available for the study. All hydrocarbon inclusions were homogenized to liquid phase. Their homogenization temperatures, bubble volumes, bulk volumes (i.e. the volumes of the hydrocarbon inclusions), and gas/oil ratios (F_v) expressed in percent and calculated from

$$F_v = \frac{v_{bubble}}{v_{inclusion} + v_{bubble}} \times 100$$

are summarized in Table 3.5. The gas/oil ratios have been plotted against homogenization temperatures and bulk volumes in Figure 3.27a and b, respectively. The dashed curves in Figure 3.27a represent calibration curves established by Bourdet et al. (2008) on the basis of measurements made on reference crude oils. It can be deduced from Table 3.5 and Figure 3.27b that higher Fv (> 5%) correspond to the smallest inclusions. Three hypotheses can be proposed to explain Fv variations: 1) different chemical types of hydrocarbons are trapped into the inclusions; 2) some inclusions can be affected by stretching; 3) artifact during volume

208

estimating. Generally, the stretching concerns the biggest inclusions whereas calculation artifact concerns the smallest volumes. Stretching results in increased expansion of the gas bubble inside the inclusion volume.

Table 3.5. Summary of CLSM analyses of hydrocarbon inclusions from the Aktote reservoir.

Sample	Cement	Inclusion	T_h, °C	Bubble volume, μm^3	Bulk volume, μm^3	Gas/oil ratio (F_v) at 20ºC, %	Relative error, %
Ax-1	C1	1	42.0	0.776	10.1	7.13	17.61
	C1	2	44.0	0.239	1.49	13.8 [a]	9.091
Ax-2	B	3	39.5	5.50	242	2.22	56.54
	B	4	33.3	0.382	37.2	1.02	123.6
Ax-3	B	5	41.0	14.1	1248	1.12	112.4
	B	6	36.0	3.05	200	1.50	83.65
	B	7	47.0	23.4	780	2.91	43.14
Ax-4	C2	8	35.5	14.3	143	9.09 [a]	13.82
	C2	9	27.7	1.46	102	1.41	89.04
	C2	10	37.8	2.65	103	2.51	50.10
Ax-5	E	11	44.0	2.05	48.1	4.09	30.74
	E	12	47.4	2.35	18.7	11.2 [a]	11.25
	E	13	47.4	9.99	283	3.41	36.85
Ax-6	B	14	40.0	1.35	124.1	1.08	116.7
	B	15	35.3	2.14	1045	0.204	614.8
Ax-7	E	16	37.0	0.524	13.8	3.66	34.35
	E	17	40.0	0.195	53.6	0.362	346.6
	E	18	33.0	0.624	155	0.401	313.4
	E	19	50.0	9.20	104	8.13	15.46
Ax-8	B	20	34.0	0.860	180	0.476	264.2
	B	21	37.0	0.796	97.0	0.814	154.3
	B	22	33.0	0.660	45.0	1.45	86.93
	B	23	40.0	1.70	49.5	3.32	37.84
	B	24	40.5	0.523	51.1	1.01	124.0
Ax-9	A/B	25	47.0	0.796	41.0	1.90	65.98
	A/B	26	39.0	0.524	38.6	1.34	93.82
Ax-10	A/B	27	40.0	1.95	37.3	4.97	25.29

[a] Higher gas/oil ratios may be due to stretching of the inclusions.
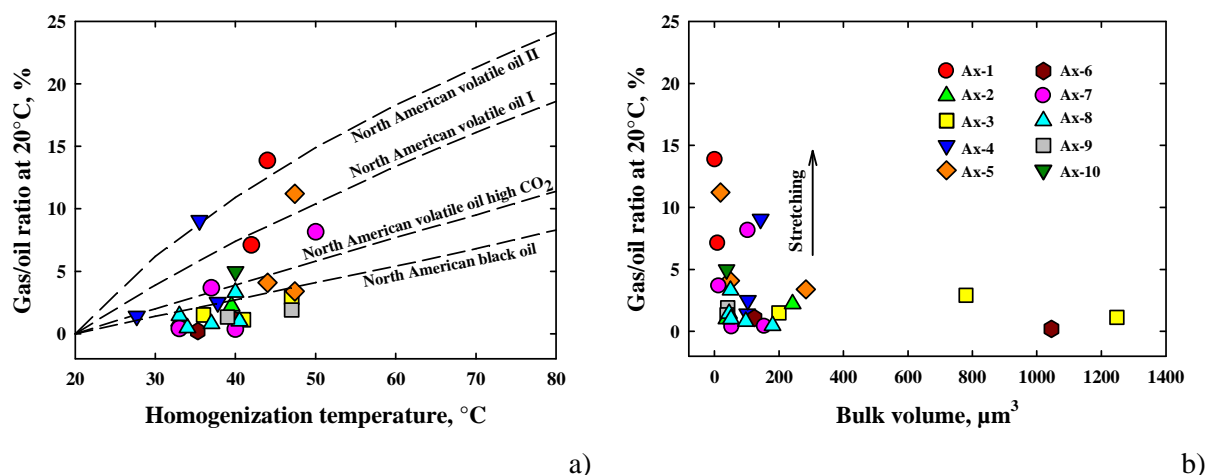
Figure 3.27. Gas/oil ratio of inclusions a) as a function of homogenization temperature (dashed curves correspond to reference natural crude oils – Bourdet et al., 2008); b) as a function of bulk volume.

The factors which may modify the properties of hydrocarbon and aqueous fluid inclusions have been discussed at length in the literature (Leroy, 1979; Bodnar and Bethke, 1984; Goldstein, 1986; Wilkins, 1986; Burruss, 1987; Prezbindwski and Tapp, 1991; Bourdet and Pironon, 2008.). According to these authors, inclusions in fragile minerals can be affected by volume stretching as well as by modifications of their chemical composition and homogenization temperatures under the influence of several natural or artificial factors. Natural factors include for example post-entrapment necking. Artificial factors may stem from microthermometry heating or analytical imprecision, among others. These factors may result in an increase of the homogenization temperatures and a loss of methane in the case of aqueous inclusions (Bourdet and Pironon, 2008). In the case of hydrocarbon inclusions, an increase of homogenization temperatures may also result from stretching, and an apparent increased heaviness of the oil may result from methane leakage out of the inclusion.

Except for the inclusions characterized by high F_v values, it can be deduced from Figure 3.27a that most of the data cluster around or below the reference curve defined by the *North American black oil*, which corresponds to a heavy oil containing 26.57 mol % CH_4 (Bourdet et al., 2008). Some of the hydrocarbon inclusions plotting below this curve in Figure 3.27a have a similar CH_4 content but appear to be enriched in the C_{11}-C_{15} and C_{15+} hydrocarbon fractions compared to the reference *North American black oil*. The present Aktote crude contains approximately 51 mol % CH_4 (unpublished Eni report) and would have a composition similar to that calculated for the colorless inclusions 1, 2, 8, 9, 11 and 12. These inclusions are plotting between the *North American black oil* and the *North American volatile oil high CO₂* reference curves. We propose that the inclusions plotting below the reference curve for the North American black oil represent remnants of a paleohydrocarbon fluid.

3.2.6. Estimation of the composition of the hydrocarbon inclusions with the PIT software

Hydrocarbon inclusion compositions have been calculated with the PIT software (Thiéry et al., 2000) using the homogenization temperatures (T_h) and gas/oil ratios (F_v) listed in Table 3.5. No calculations could be performed for those inclusions for which the F_v values were less than 1% (i.e. inclusions 15, 17, 18, 20 and 21). The modelled compositions are detailed in Table 3.6. The values of α and β listed in the table represent the coordinates of the intersection between the αβ line calculated by the PIT software for a given pair of T_h and F_v values and the αβ trend defined by natural crude oils of different compositions (Thiéry et al., 2000). It can be seen in Table 3.6 that methane concentrations range from 16 to 58 mol % in Bashkirian inclusions, while the Serpukhovian and Devonian inclusions contain ~ 21 mol % and ~ 47 mol % methane, respectively.

Table 3.6. Composition of hydrocarbon inclusions (mol %) calculated from their T_h and F_v values using the PIT software (Thiéry et al., 2000).

Sample	Inclusion	T_h, ºC	F_v, %	α	β	C_1	C_2	C_3	$n\text{-}C_4$	$i\text{-}C_4$	$n\text{-}C_5$	$i\text{-}C_5$	$n\text{-}C_6$	$n\text{-}C_7$	$n\text{-}C_8$	$n\text{-}C_9$	$n\text{-}C_{10}$	$n\text{-}C_{11}\text{-}n\text{-}C_{15}$	$n\text{-}C_{15+}$
Ax-1	1	42.0	7.13	0.877	0.550	50.18	8.950	6.625	1.328	2.975	1.823	2.927	3.087	3.327	2.883	2.513	2.200	9.608	1.656
	2	44.0	13.8	0.875	0.622	58.43	9.143	6.032	1.147	2.570	1.495	2.400	2.377	2.562	2.192	1.889	1.637	7.012	1.102
Ax-2	3	39.5	2.22	0.891	0.390	29.62	6.065	6.304	1.489	3.336	2.330	3.740	4.779	5.151	4.684	4.270	3.897	19.68	4.646
	4	33.0	1.02	0.895	0.360	23.32	4.467	5.268	1.308	2.930	2.129	3.417	4.733	5.101	4.772	4.473	4.197	24.61	9.266
Ax-3	5	41.0	1.12	0.953	0.370	16.83	2.656	3.630	0.931	2.085	1.564	2.511	3.959	4.266	4.122	3.990	3.866	27.61	21.98
	6	36.0	1.50	0.910	0.380	26.08	5.200	5.793	1.409	3.157	2.255	3.620	4.824	5.199	4.800	4.441	4.113	22.43	6.676
	7	47.0	2.91	0.900	0.380	28.14	5.631	6.018	1.435	3.214	2.265	3.637	4.709	5.075	4.657	4.284	3.947	21.07	5.908
Ax-4	8	35.5	9.09	0.851	0.590	58.31	9.560	6.342	1.198	2.684	1.551	2.490	2.581	2.781	2.324	1.955	1.653	5.981	0.583
	9	27.7	1.41	0.878	0.580	53.29	9.047	6.400	1.257	2.817	1.693	2.718	2.787	3.004	2.596	2.258	1.973	8.686	1.458
	10	37.8	2.51	0.895	0.410	33.15	6.670	6.490	1.480	3.320	2.270	3.640	4.450	4.790	4.330	3.920	3.560	17.80	4.130
Ax-5	11	44.0	4.09	0.877	0.430	50.18	8.955	6.625	1.328	2.975	1.823	2.927	3.087	3.327	2.883	2.513	2.200	9.608	1.562
	12	47.4	11.2	0.839	0.590	55.16	9.181	6.333	1.228	2.752	1.633	2.622	2.670	2.877	2.469	2.133	1.851	7.874	1.201
	13	47.4	3.41	0.897	0.400	31.73	6.376	6.365	1.469	3.292	2.268	3.641	4.515	4.867	4.416	4.020	3.666	18.73	4.630
Ax-6	14	40.0	1.08	0.938	0.360	28.14	5.631	6.018	1.435	3.214	2.265	3.637	4.709	5.075	4.657	4.284	3.947	21.07	5.908
	15	35.3	0.204 [a]	-	-	-	-	-	-	-	-	-	-	-	-	-	-	-	-
Ax-7	16	37.0	3.66	0.887	0.500	43.18	8.190	6.720	1.420	3.170	2.030	3.260	3.610	3.890	3.440	3.050	2.720	12.78	2.530
	17	40.0	0.362 [a]	-	-	-	-	-	-	-	-	-	-	-	-	-	-	-	-
	18	33.0	0.401 [a]	-	-	-	-	-	-	-	-	-	-	-	-	-	-	-	-
	19	50.0	8.13	0.887	0.550	48.54	8.640	6.536	1.325	2.970	1.840	2.954	3.114	3.356	2.941	2.593	2.296	10.74	2.135
Ax-8	20	34.0	0.476 [a]	-	-	-	-	-	-	-	-	-	-	-	-	-	-	-	-
	21	37.0	0.814 [a]	-	-	-	-	-	-	-	-	-	-	-	-	-	-	-	-
	22	33.0	1.45	0.906	0.370	29.74	6.100	6.327	1.493	3.345	2.335	3.748	4.784	5.156	4.685	4.268	3.893	19.56	4.552
	23	40.0	3.32	0.880	0.450	38.04	7.783	6.962	1.531	3.430	2.269	3.642	4.305	4.640	4.093	3.623	3.215	14.16	2.281
	24	40.5	1.01	0.958	0.400	16.41	2.323	3.201	0.802	1.796	1.335	2.143	3.423	3.689	3.583	3.489	3.402	25.90	28.49
Ax-9	25	47.0	1.90	0.939	0.370	20.71	3.637	4.537	1.136	2.545	1.872	3.004	4.346	4.684	4.453	4.241	4.044	26.33	14.46
	26	39.0	1.34	0.940	0.380	21.27	3.797	4.677	1.168	2.617	1.919	3.080	4.409	4.752	4.504	4.278	4.068	26.04	13.41
Ax-10	27	40.0	4.97	0.900	0.560	47.09	8.776	6.797	1.392	3.119	1.949	3.128	3.392	3.656	3.179	2.780	2.439	10.61	1.692

[a] Compositions could not be calculated for inclusions with gas/oil ratios Fv < 1%.

3.2.7. P-T reconstruction with the PIT software

In order to reconstruct the *P-T* conditions under which the oil was emplaced in the reservoir, isochores and bubble point curves (isopleths) have been calculated with the PIT software from the values of α and β listed in Table 3.6 for the hydrocarbon inclusions from the Ax-1 (pre-dolomite cement C1), Ax-4 (pre-dolomite cement C2) and Ax-5 (post-dolomite cement E) samples. These inclusions were the only ones for which there were cogenetic aqueous inclusions. The isopleths and isochores calculated for the hydrocarbon inclusions are compared in Figure 3.28 to their aqueous counterparts computed from the equation of state and parameters of Duan et al. (1992) and Duan and Mao (2006). The intersections between the isochores for cogenetic aqueous and hydrocarbon inclusions define the *P-T* conditions under which the petroleum was emplaced in the reservoir. It can be deduced from Figure 3.28 that the temperature and pressure conditions recorded by the inclusions in the pre-dolomite cements C1 and C2 of samples Ax-1 and Ax-4 are very similar, i.e. 90-110ºC and 400-550 bar. The pressure is the approximately the same (500-550 bar) for the fluid inclusions in cement E of the Ax-5 sample, but the trapping temperature is higher at 115-120ºC. The intersection at higher pressure results from the higher concentration of methane in the aqueous inclusion of the Ax-5 sample (see Table 3.3). The isochore intersection occurs on the bubble point curve of CH_4-H_2S-NaCl system indicating that aqueous inclusions are saturated with methane. Similar temperature and pressure conditions are deduced from the aqueous inclusions in fluorite. It can be seen from Figure 3.28 that the aqueous inclusions in fluorite have been trapped at temperature and pressure conditions between 100-105°C and 450-470 bar, and 115-118°C and 520-580 bar.

The petrographic observations and fluid inclusion results summarized above are further discussed in the next section.
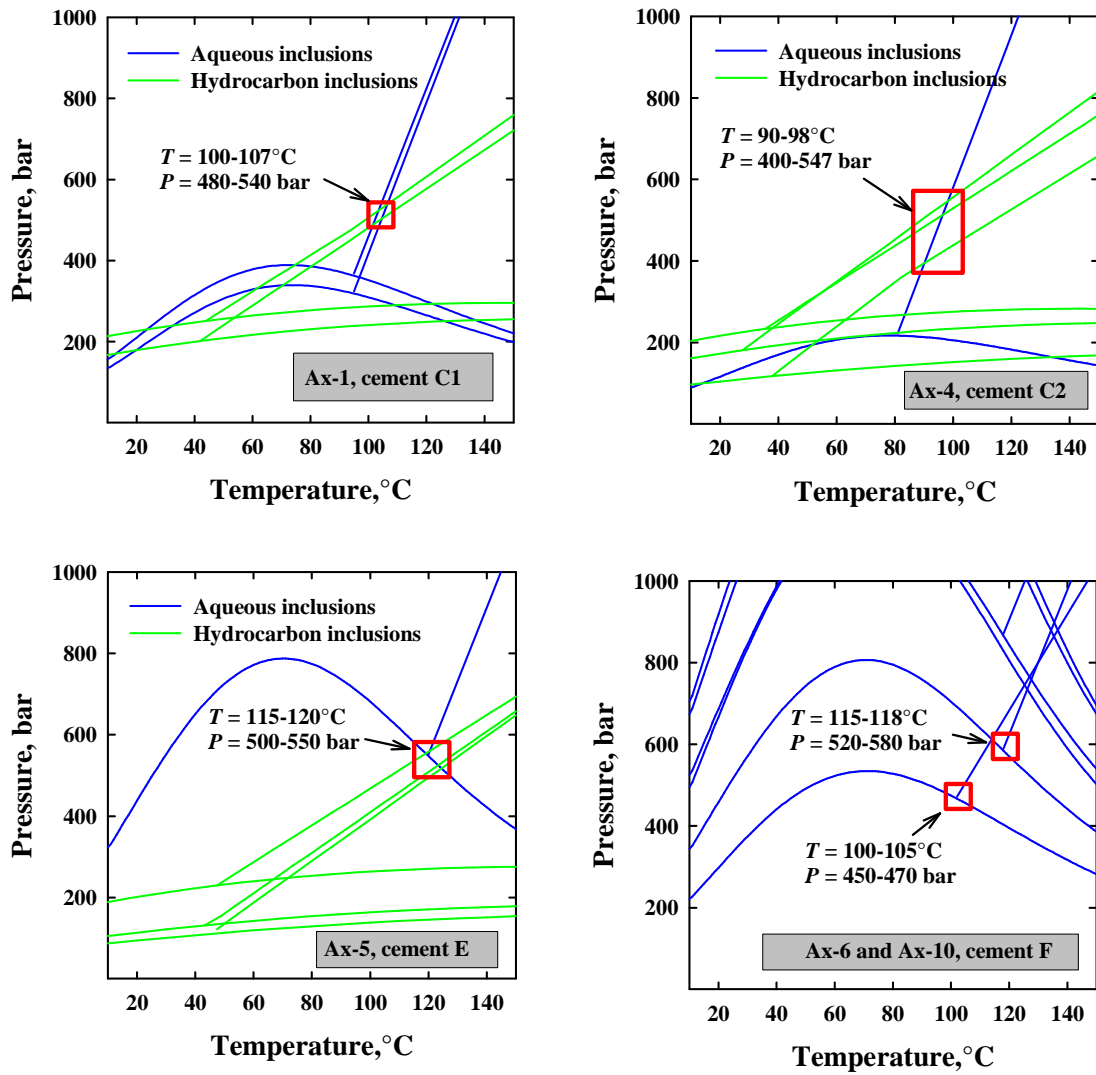
Figure 3.28. *P-T* diagrams for cogenetic aqueous and hydrocarbon inclusions in calcite and fluorite cements.

4. DISCUSSION

In this section, an attempt is made to integrate the petrographic and fluid inclusion results presented above in the context of the diagenetic evolution of the carbonate reservoir of Aktote. The diagenetic events recorded by the different generations of cements, and the fluid inclusions contained in these cements are discussed in chronological order below.

4.1. Eogenesis

Eogenesis is used here to refer to the earliest stage of diagenesis of sediments during which processes such as bacterial reworking of organic matter, early cementation and other low-temperature, shallow burial diagenetic processes take place (e.g. see Moore, 1989). The eogenetic stage at Aktote has been recorded by early fibrous calcites which precede the early, non-luminescent calcite cement A. The precipitation of cement A occurred before the precipitation of luminescent cement B. Both cements A and B occur as syntaxial calcite overgrowths on crinoid fragments. The change in luminescence between cement A and cement B can be attributed to a change in the redox conditions of the depositional environment, reducing conditions favoring the incorporation of Mn^{2+} and Fe^{2+} in calcite (Moore, 1997). Cements A and B have been subjected to fracturation before or during deeper burial of the sediments.

4.2. Post-eogenesis cementation

Upon further burial and the associated increase in temperature and pressure, post-eogenesis calcite cements C1 and C2 were precipitated. Cement C1 occurs as a syntaxial, fracture-filling cement on the eogenetic cements A and B, while cement C2 occurs as a syntaxial cement growing on cement C1. Intersection between the isochores of cogenetic aqueous and hydrocarbon inclusions suggests that the precipitation of cements C1 and C2 occured at 90-110ºC and 400-550 bar (Figure 3.28).

4.3. Stylolitization

Stylolites were observed in Bashkirian sample Ax-4 by optical microscopy and cathodoluminescence. Stylolitization is a process of pressure solution which, in the case of carbonate rocks which have not been affected by tectonics or metamorphism, may be initiated in the first stages of the burial process (Park and Schot, 1968). At Aktote, this stylolitization appears to have taken place after the beginning of the precipitation of calcite cement C2, which appears to be crosscut by stylolites. The stylolite pores are filled by a first generation of solid bitumen, as well as by cement C2 (see Figure 3.15) which continued to precipitate from a Mn-poor fluid after the end of the stylolitization episode and until liquid hydrocarbons migrated into the reservoir.

4.4. Bitumen precipitation

Bitumen has been observed as a stylolite pore filling in sample Ax-4 (Figure 3-15). This suggests that a first event of petroleum emplacement in the Aktote reservoir followed the stylolitization episode. Precipitation of solid bitumen in hydrocarbon reservoirs results from the alteration of liquid petroleum and can be attributed to a number of processes, including biodegradation, devolatilization, water washing, or thermal alteration (Curiale, 1986). In addition, solid bitumen is a common product of thermochemical sulfate reduction (Machel, 2001) showing distinct chemical characteristics (e.g. content of organic sulfur) compared to bitumens produced by thermal alteration (Kelemen et al., 2008). The occurrence of similar solid bitumen has been reported in samples from the Tengiz (Collins et al., 2006; Warner et al, 2007) and Kashagan (Ronchi et al., 2010) reservoirs.

4.5. Dolomitization

Dolomite cement occurs as isopachous rims around ooliths and crinoids (Figures 3.12a and 3.14), as well as around remnants of cements B, C1 and C2 (Figures 14 and 16). Dolomite crystals have also been observed as fillings in open fractures (Figure 3.16) and on the walls of open vugs (Figures 3.12b and 3.17). The occurence of dolomite is relatively limited in the Bashkirian and Serpukhovian samples, but extensive dolomitization has affected the Devonian formation. The precipitation of dolomite after bitumen suggests that the Aktote reservoir has been invaded by an aqueous fluid after the first emplacement of petroleum. A similar conclusion has been reached by Warner et al. (2007), who suggested that the precipitation of post-bitumen calcite must have required the Tengiz reservoir to be filled with an aqueous fluid after the formation of the bitumen.

4.6. Post-dolomite bitumen precipitation

The petrographic observations reported above have indicated that a second (post-dolomite) episode of bitumen precipitation occurred in the Aktote reservoir. This second generation of bitumen has been observed in samples Ax-2, Ax-5, Ax-6, and Ax-7 in open fractures (where it is accompanied by a late calcite cement – Figure 3.16), as well as in open vugs (where it occurs together with the same late calcite cement, but also with fluorite and barite – Figure 3.17). Warner et al. (2007) reported only one generation of solid bitumen in the Tengiz reservoir. The observation of two generations of solid bitumen at Aktote suggests that at least two petroleum emplacement events took place, and may be even three if this second bitumen was not precipitated from the petroleum currently hosted in the reservoir.

4.7. Late calcite precipitation

A post-bitumen late calcite cement (calcite E) has been observed in open fractures (Figure 3.16) and open vugs (Figure 3.17) in samples Ax-2, Ax-5, Ax-6 and Ax-7. From the fluid inclusion data presented above, this late cement was precipitated at temperatures higher than 75-85°C from a fluid with a salinity of 5 weight % NaCl equivalent. Electron microprobe data has indicated that this fluid was Mn-rich. Two aqueous inclusions were found to homogenize at 120°C. These anomalous temperatures can be explained by a volume stretching of the inclusions during natural or laboratory heating, which results in an increase of homogenization temperatures. Alternatively, these higher homogenization temperatures may reflect the circulation of a Mn-rich, CH_4 saturated, low-salinity hydrothermal fluid. The latter hypothesis has been formulated for the Kashagan reservoir by Ronchi et al. (2010), who interpreted fluid inclusions with unusually low salinities and high temperatures of homogenization as *exotic hydrothermal fluids*.

As mentioned before, it is difficult to measure aqueous inclusions in carbonate samples by Raman spectrometry due to carbonate fluorescence and the presence of petroleum inclusions around the aqueous inclusions. As a result, only one ($T_h = 120$°C) of the six inclusions observed in cement E could be measured by Raman spectrometry. Intersection between the isochores of cogenetic aqueous and hydrocarbon inclusions suggests that fluid trapping occurred at 115-120ºC and 500-550 bar (Figure 3.28).

4.8. Late fluid circulation

Petrographic observations showed that both fluorite and barite have precipitated in open vugs along with calcite E cement. Although it is possible that calcite E and fluorite were precipitated concomitantly from the same hydrothermal circulation, the paragenetic relationship between calcite E and fluorite is unclear from the observations in cathodoluminescence. Aqueous fluid inclusions in Bashkirian fluorite have homogenization temperatures of 85-120°C and salinities of 8.0 weight % NaCl equivalent, while those in Devonian fluorite have homogenization temperatures of 100-119°C and salinities of 0.4-2 weight % NaCl equivalent. Although the aqueous inclusions from calcite E and from Bashkirian fluorite homogenize at nearly identical temperatures, it must be pointed out that no hydrocarbon inclusions have been observed in fluorite whereas calcite E contains abundant hydrocarbon inclusions.

4.9. P-T reconstruction

Cogenetic aqueous and petroleum inclusions have been used to estimate the conditions of temperature and pressure under which the petroleum fluid was trapped in the reservoir. These trapping temperatures and pressures have been defined by the intersection of the isochoric lines of aqueous and hydrocarbon inclusions. Minimal trapping conditions of 90°C and 400 bar and maximum trapping conditions of 107°C and 540 bar have been deduced for the reservoir fluid based on inclusions in calcite cements C1 and C2 (see Figure 3.28). In contrast, trapping conditions of 120°C and 550 bar are suggested by inclusions in calcite cement E. Finally, optimal trapping conditions of 118°C and 580 bar have been deduced from the analysis of aqueous inclusions in Devonian fluorite. These estimated *P-T* conditions have been plotted as symbols in Figure 3.29, where they are compared to lithostatic and hydrostatic pressures computed from the time-depth-temperature evolution established for the Kashagan field by Ronchi et al. (2010 – see their Figure 19B). Also shown in Figure 3.29 are the present-day temperature and pressure conditions in the Aktote (Diarov et al., 2006) and Kashagan (www.ncoc.kz) reservoirs.

The paleoconditions deduced from the fluid inclusion analysis and corresponding to the first event of petroleum emplacement at Aktote fall in the vicinity of the hydrostatic curve. Fluid inclusions from late calcite cement and fluorite correspond to the present-day temperature of the reservoir, but to a somewhat lower pressure (500-550 bar).
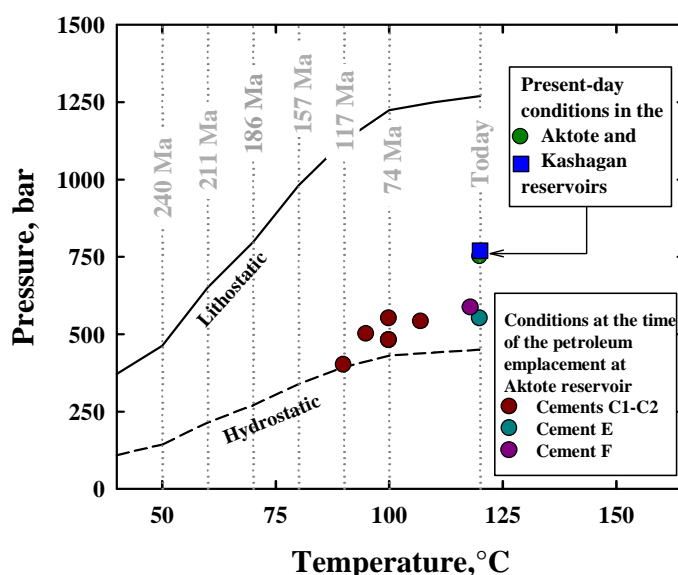
Figure 3.29. Time evolution of the temperature and pressure conditions in the North Caspian Basin. The lithostatic and hydrostatic curves have been calculated from the time-temperature-depth evolution proposed by Ronchi et al. (2010) for the Kashagan reservoir. The present-day conditions in the Kashagan and Aktote reservoirs are represented by the filled blue square and green circle, respectively. Trapping conditions at the time are represented by cement C1-C2 (dark red circle), cement E (dark cyan circle), and cement F (dark pink circle).

4.10. Thermochemical sulfate reduction

Although the subject has been debated for many years, it is generally considered that the initiation of thermochemical sulfate reduction (TSR) requires minimal temperatures of ~ 100-140ºC or higher (Machel, 2001). Such temperatures may have been reached during the possible hydrothermal circulation, which was suggested by the fluid inclusion data obtained for the calcite E cement. Several lines of evidence for the occurrence of TSR in the rim part of the Tengiz reservoir have been presented by Collins et al. (2006), including high burial temperatures (~ 120-140ºC), high concentration of H_2S (13%) in the hydrocarbon phase, and the presence in this part of the reservoir of solid bitumen and dedolomite (both of which are TSR by-products – see e.g. Machel, 2001), as well as anhydrite which is the main source of sulfate in formation waters. High amounts of H_2S in the Kashagan reservoir led Ronchi et al. (2010) to suggest that TSR may also have occurred, but at greater depths than those reached by the drilling operations. The evidence collected in the present and other studies that TSR may also have affected the Aktote reservoir is the following:

- aqueous inclusions in calcite and fluorite contain dissolved H_2S, HS^-, and SO_4^{-2} (pH~6);
- although our optical microscopy observations did not suggest that anhydrite was occuring to any significant extent in the samples, anhydrite dissolution and replacement by calcite in other parts of the Lower Bashkirian formation has been reported by Eni (unpublished report);
- elemental sulfur has been observed by SEM, and detected by Raman spectroscopy. According to Machel (2001), elemental sulfur starts to accumulate as a by-product of TSR when the hydrocarbon reactants have been used up by the reaction;
- the homogenization temperatures of aqueous inclusions in calcite (75-120°C) and fluorite (85-120°C) suggest that the temperature regime may have been sufficient to initiate the TSR reaction.

From these four lines of evidence, and although additional isotopic and organic geochemical evidence would certainly be required to demonstrate it unequivocally, we may hypothesize that TSR has affected the Aktote reservoir as it has affected the Tengiz reservoir, and perhaps the Kashagan reservoir.

5. CONCLUDING REMARKS

A petrographic and fluid inclusion study of samples from a carbonate reservoir from the North Caspian Basin has been performed in order to reconstruct the diagenetic history of and the conditions of the emplacement of the hydrocarbons in the reservoir. Ten samples were made available for the study, including eight samples of Bashkirian age, one sample of Serpukhovian age, and one sample of Devonian age. These samples have been studied using optical microscopy, cathodoluminescence, scanning electron microscopy, electron microprobe, microthermometry, Raman spectrometry, Fourier-transform infrared spectroscopy, and confocal scanning laser microscopy.

Several generations of carbonate cements have been recognized based on optical and cathodoluminescence observations. The cathodoluminescence analysis allowed to reconstruct the diagenetic history of the Aktote reservoir, which is consistent with the following succession: four generations of calcitic (A, B, C1 and C2) cements, followed by a dolomitic (D) cement, and finally a post-dolomite calcite (E) cement. Non-carbonate minerals (fluorite, barite, etc.) were also observed by SEM analysis, for which a hydrothermal origin has been hypothesized. Two phases of bitumen precipitation (just before and after the dolomitization stage) have also been observed by optical microscopy and cathodoluminescence.

Calcite cements A and B correspond to early calcite cements precipitated during the eogenetic stage. Upon shallow burial, these early cements were affected by a first fracturation event. The resulting fractures have been filled by the C1 and C2 generations of cements. Stylolitization occurred concomitantly to the formation of cement C2. The stylolites appear to be filled by a first generation of solid bitumen precipitated as a result of an alteration process of the first petroleum emplaced in the Aktote reservoir. The reservoir was subsequently invaded by aqueous fluids, which precipitated dolomite. The reservoir was subsequently affected by a second fracturation event, which was followed by another event of oil emplacement in the reservoir. Alteration of this oil (which may or may not be the oil present today in the reservoir) resulted in a second generation of solid bitumen in the fractures. Finally, a possible hydrothermal circulation may have precipitated the late calcite cement E, together with fluorite and barite.

A study of aqueous and hydrocarbon fluid inclusions in calcite cements C1 and C2 allowed to estimate the temperature and pressure conditions for the first emplacement of petroleum in the reservoir, with a minimum at 90°C and 400 bar and a maximum at 107°C and 540 bar. The estimated pressure of trapping of the inclusions in cement E is similar at 500-550

bar, but the temperature of trapping is higher at 115-120ºC. Some aqueous inclusions in fluorite homogenized at 100-118°C with trapping pressures at 450-580 bar. The present-day conditions of the reservoir are 120°C and 750 bar. The salinity of the aqueous inclusions appears to be decreasing with increasing depth, which may be interpreted as reflecting the upward migration of a hydrothermal fluid from a deeper source and its progressive mixing with the formation water inside the reservoir. Finally, several lines of evidence suggest that this hydrothermal circulation may have helped initiating thermochemical sulfate reduction (TSR) in the Aktote reservoir.

The chronology of the diagenetic events deduced from the petrographic and fluid inclusion observations is summarized in Figure 3.30.
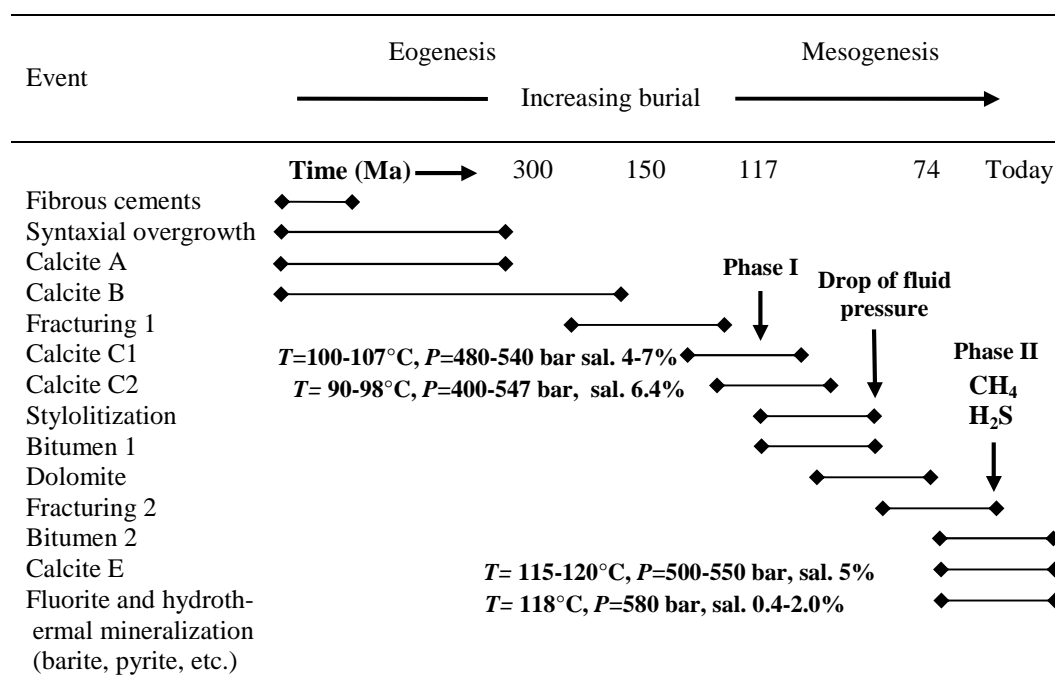
Figure 3.30. Chronology of the cementation paragenesis deduced from the petrographic and fluid inclusion analysis of samples from the Ax well, Aktote field.

GENERAL CONCLUSIONS

A thermodynamic study of the organic/inorganic reactions which control the distribution of sulfur in petroleum systems has been undertaken. These reactions are of importance for a better understanding of thermochemical sulfate reduction (TSR) and the effects of the sequestration of H_2S-CO_2 acid gas mixtures in deep geological formations, and ultimately for the geochemical cycle of sulfur in sedimentary basins.

A review and evaluation has been made of the available thermodynamic properties for minerals, inorganic and organic aqueous species, and organic sulfur compounds in the crystalline, liquid, and ideal gas states, as well as of the existing phase equilibria models which allows to describe the phase relations among sulfur-bearing species in rock-forming minerals, petroleum, formation waters, and gas mixtures in hydrocarbon reservoirs. This review led to the development of predictive calculations of the impact of the injection of H_2S-CO_2 acid gas mixtures in hydrocarbon reservoirs containing sulfur-rich oils. Temperature – $\log f_{H_2S}$ diagrams analogous to the $T - \log X_{CO_2}$ diagrams used in metamorphic petrology have been designed for that purpose. Depending on the nature of the organic sulfur compound being considered, the calculations predict that increasing the H_2S fugacity in a petroleum reservoir (either by acid gas injection or by TSR) should lead to the precipitation of elemental sulfur, and possibly to a desulfurization of the sulfur-bearing crude oil. These predictions are consistent with the fact that elemental sulfur forms under high fugacities of H_2S during the latest stages of TSR. In addition, precipitation of elemental sulfur in sulfur-rich hydrocarbon reservoirs also requires redox conditions which are more oxidizing than the usual redox pyrite-pyrrhotite-magnetite (PPM) buffer, which is characteristic of most petroleum reservoirs (Helgeson et al., 1993). These oxidizing conditions are also consistent with the formation of pyrobitumen at the end of the TSR process.

In an attempt to verify the thermodynamic predictions, gold cell experiments have been carried out in which different organic sulfur compounds were reacted under H_2S pressure at 150ºC and 500 bar during two weeks. Hydrogen sulfide was loaded in the capsules using a gas-loading system designed at the G2R laboratory. The consumption of H_2S in the various reactions was calculated from pressure measurements. The reaction products were analyzed by Raman spectroscopy and gas chromatography – mass spectrometry (GC-MS). Although H_2S has been consumed in most of the experiments, the conversion (oxidation) of this H_2S to elemental sulfur was only observed in the experiments in which the reactant was

an alkylthiophene. The formation of elemental sulfur was not observed with alkylthiolanes as reactants, which we explain in terms of the oxidation state of carbon in alkylthiolanes and the limited electron transfer resulting from that oxidation state. Desulfurization of the organic sulfur compounds was not observed. In contrast, more sulfur was introduced in the structures of these compounds to form disulfides. Benzo[*b*]thiophenes and dibenzo[*b*,*d*]thiophenes did not react with H_2S, in accord with the thermodynamic predictions.

Experiments on thermochemical sulfate reduction (TSR) have also been carried out using the novel technique of fused silica capillaries. Two hydrocarbons (*n*-octane and 1-octene) were reacted at 350-400 with 0.5 *m* aqueous solutions of $MgSO_4$ and Na_2SO_4 for up to 10 days. Experiments have been carried out with a microthermometry heating stage in order to follow the formation of TSR products by Raman spectrometry as a function of reaction progress. However, observation of the aqueous phase is hindered due to fluorescence of the liquid hydrocarbons. A second set of experiments was conducted in which the silica capillaries were oven-heated, and the TSR products analyzed at the end of the experiments. The TSR reaction appears to proceed regardless of the sulfate salt being used, which differs from the hypothesis formulated by other investigators that Mg^{2+} may act as an initiator for the TSR reaction in natural systems. Despite the limitations encountered with the fluorescence problem, this type of experiments nevertheless appears promising and should be pursued in order to gain further insights into the reactions which participate to the overall TSR process.

Finally, a petrographic and fluid inclusion study of samples from a sulfur-rich carbonate reservoir from North Caspian Basin has been carried out in order to reconstruct the diagenetic history of this reservoir. Several observational and analytical techniques have been used, including optical microscopy, cathodoluminescence, scanning electron microscope, electron microprobe, confocal scanning laser microscopy, as well as microthermometry, Raman spectrometry, and Fourier-transform infrared spectroscopy. Several generations of cements have been identified. The chemical compositions deduced from the analysis of the aqueous and hydrocarbon fluid inclusions contained in these cements were used together with thermodynamic models of fluid-phase equilibria to estimate the temperature and pressure conditions of the emplacement of the hydrocarbons in the reservoir. Although hydrogen sulfide, elemental sulfur and bitumen have been observed in the fluid inclusions or on thin sections, further investigations are required to demonstrate that thermochemical sulfate reduction has indeed occurred in this sulfur-rich carbonate reservoir.

REFERENCES

Adam P., Schmidt J. C., Mycke B., Strazielle C.,Connan J., Hut A. Y., Riva A. and Albrecht P. (1993) Structural investigation of nonpolar sulfur cross-linked macromolecules in petroleum. *Geochimica et Cosmochimica Acta* **57**, 3396-3419.

Aizenshtat Z., Krein E.B., Vairavamurthy M.A., and Goldstein T.P. (1995) Role of sulfur in the transformations of sedimentary organic matter: A mechanistic overview. In *Geochemical Transformations of Sedimentary Sulfur* (eds. M.A. Vairavamurthy and M.A.A. Schoonen), *ACS Symposium Series* **612**, pp. 16-37. American Chemical Society.

Amend J.P. and Helgeson H.C. (1997a) Group additivity equations of state for calculating the standard molal themodynamic properties of aqueous organic species at elevated temperatures and pressures. *Geochimica et Cosmochimica Acta* **61**, 11-46.

Amend J.P. and Helgeson H.C. (1997b) Calculation of the standard molal thermodynamic properties of aqueous biomolecules at elevated temperatures and pressures. Part 1. L-α-Amino acids. *Journal of the Chemical Society*, *Faraday Transactions* **93**, 1927-1941.

Amend J.P. and Helgeson H.C. (2000) Calculation of the standard molal thermodynamic properties of aqueous biomolecules at elevated temperatures and pressures. II. Unfolded proteins. *Biophysical Chemistry* **84**, 105-136.

Amrani A., Said-Ahamed W., Lewan M.D., and Aizenshtat Z. (2006) Experiments on $\delta^{34}S$ mixing between organic and inorganic sulfur species during thermal maturation. *Geochimica et Cosmochimica Acta* **70**, 5146-5161.

Anderson A. and Loh Y.T. (1969) Low temperature Raman spectrum of rhombic sulfur. *Canadian Journal of Chemistry* **47**, 879-884.

Anderson G.M. (1991) Organic maturation and ore precipitation in Southeast Missouri. *Economic Geology* **86**, 909-926.

Anderson G.M. (1995) *Thermodynamics of Natural Systems*. Wiley.

Anderson G.M. (2008) The mixing hypothesis and the origin of Mississippi Valley-type ore deposits. *Economic Geology* **103**, 1683-1690.

Anderson G.M. and Crerar D.A. (1993) *Thermodynamics in Geochemistry: The Equilibrium Model.* Oxford.

Anderson G.M. and Thom J. (2008) The role of thermochemical sulfate reduction in the origin of MVT deposits. II. Carbonate-sulfide relationships. *Geofluids* **8**, 27-34.

Anissimov L. and Moscowsky G. (1998) Predicting hydrocarbon accumulations below deep Permian salt in the Pricaspian Basin: the use of shallow geochemical indicator. *Petroleum Geoscience* **4**, 1-6.

Baker R.B. and Reid E.E. (1929) The action of sulfur on normal-heptane and normal-butane. *Journal of the American Chemical Society* **51**, 1566-1567.

Barrett T.J., Anderson G.M., and Lugowski J. (1988) The solubility of hydrogen sulphide in 0–5 m NaCl solutions at 25°–95°C and one atmosphere. *Geochimica et Cosmochimica Acta* **52**, 807-811.

Barton P.B., Jr. (1967) Possible role of organic matter in the precipitation of the Mississippi Valley ores. *Economic Geology Monograph* **3**, 371-378.

Bell R.P. (1931) The electrical energy of dipole molecules in solution, and the solubilities of ammonia, hydrogen chloride, and hydrogen sulphide, in various solvents. *Journal of the Chemical Society*, 1371-1382.

Belenitskaya G.A. (2000) Distribution pattern of hydrogen sulphide-bearing gas in the former Soviet Union. *Petroleum Geoscience*, **6**, 175-187.

Benning L.G. and Seward T.M. (1996) Hydrosulphide complexing of Au(I) in hydrothermal solutions from 150–400ºC and 500–1500 bar. *Geochimica et Cosmochimica Acta* **60**, 1849-1871.

Besserer G.J. and Robinson D.B. (1975) The equilibrium phase properties of the *i*-butane-hydrogen sulfide system. *Journal of Chemical Engineering of Japan* **8**, 11-15.

Bestougeff M. and Combaz A. (1973) Action d'H_2S et de S sur quelques substances organiques actuelles et fossiles. In *Advances in Organic Geochemistry* (eds. B. Tissot and F. Bienner), pp. 747-759. Editions Technip.

Bierlein J.A. and Kay W.B. (1953) Phase-equilibrium properties of system carbon dioxide-hydrogen sulfide. *Industrial and Engineering Chemistry* **45**, 618-624.

Bildstein O., Worden R.H., and Brosse E. (2001) Assessment of anhydrite dissolution as the rate-limiting step during thermochemical sulfate reduction. *Chemical Geology* **176**, 173-189.

Block J. and Waters O.B., Jr. (1968) The $CaSO_4$-Na_2SO_4-NaCl-H_2O system at 25° to 100°C. *Journal of Chemical and Engineering Data* **13**, 336-344.

Blount C.W. and Dickson F.W. (1969) The solubility of anhydrite (CaSO4) in NaCl-H_2O from 100 to 450°C and 1 to 1000 bars. *Geochimica et Cosmochimica Acta* **33**, 227-245.

Bodnar R.J. and Bethke P.M. (1984) Systematics of stretching of fluid inclusions I: Fluorite and sphalerite at 1 atmosphere confining pressure. *Economic Geology* **79**, 141-161.

Bourdet J. and Pironon J. (2008) Strain response and re-equilibration of CH_4-rich synthetic aqueous fluid inclusions in calcite during pressure drops. *Geochimica et Cosmochimica Acta* **72**, 2946-2959.

Bourdet J., Pironon J., Levresse G., and Tritlla J. (2008) Petroleum type determination through homogenization temperature and vapour volume fraction measurements in fluid inclusions. *Geofluids* **8**, 46-59.

Bourdet J., Pironon J., Levresse G., and Tritlla J. (2009) Petroleum accumulation and leakage in a deeply buried carbonate reservoir, Nispero field (Mexico). *Marine and Petroleum Geology* **27**, 1-17.

Brassell S.C., Lewis C.A., de Leeuw J.W., de Lange F., and Sinninghe Damsté J.S. (1986) Isoprenoid thiophenes in recent sediments. *Nature* **320**, 160-162.

Brunet M.F., Volozh Y.A., Antipov M.P., and Lobkovsky L.I. (1999) The geodynamic evolution of the Precaspian Basin (Kazakhstan) along a north-south section. *Tectonophysics* **313**, 85-106.

Burruss R.C. (1987) Diagenetic palaeotemperatures from aqueous fluid inclusions: re-equilibration of inclusions in carbonate cements by burial heating. *Mineralogical Magazine* **51**, 477–481.

Cai C., Hu W., and Worden R.H. (2001) Thermochemical sulphate reduction in Cambro-Ordovician carbonates in Central Tarim. *Marine and Petroleum Geology* **18**, 729-741.

Cai C., Worden R.H., Bottrell S.H., Wang L., and Yang C. (2003) Thermochemical sulphate reduction and the generation of hydrogen sulphide and thiols (mercaptans) in Triassic carbonate reservoirs from the Sichuan Basin, China. *Chemical Geology* **202**, 39-57.

Cai C., Xie Z., Worden R.H., Hu G., Wang L., and He H. (2004) Methane-dominated thermochemical sulphate reduction in the Triassic Feixianguan Formation, East Sichuan Basin, China: towards prediction of fatal H_2S concentrations. *Marine and Petroleum Geology* **21**, 1265-1279.

Capelle G. (1908) Contribution à l'étude de l'action du soufre sur les hydrocarbures. *Bulletin de la Société Chimique de France*, 150-154.

Carroll J.J. and Mather A.E. (1989a) The solubility of hydrogen sulphide in water from 0 to 90°C and pressures up to 1 MPa. *Geochimica et Cosmochimica Acta* **53**, 1163-1170.

Carroll J.J. and Mather A.E. (1989b) Phase equilibrium in the system water-hydrogen sulphide: modelling the phase behavior with an equation of state. *Canadian Journal of Chemical Engineering* **67**, 999-1003.

Chakhmakhchev A., Suzuki M., and Takayama K. (1997) Distribution of alkylated dibenzothiophenes in petroleum as a tool for maturity assessments. *Organic Geochemistry* **26,** 483–490.

Chapoy A., Mohammadi A.H., Tohidi B., Valtz A., and Richon D. (2005) Experimental measurement and pahase behavior modeling of hydrogen sulfide-water binary system. *Industrial & Engineering Chemistry Research* **44**, 7567-7574.

Chou I.M., Song Y., and Burrus R.C. (2008a) A new method for synthesizing fluid inclusions in fused silica capillaries containing organic and inorganic material. *Geochimica et Cosmochimica Acta* **72**, 5217-5231.

Chou I.M., Shang L.B., and Burrus R.C. (2008b) Thermochemical sulfate reduction (TSR) by methane – in situ observation and Raman characterization in fused silica capsules at temperatures up to 450°C. *American Geophysical Union* (abstract P43B-1402).

Clarke E.C.W. and Glew D.N. (1970) Deuterium and hydrogen sulfides: vapor pressures, molar volumes, and thermodynamic properties. *Canadian Journal of Chemistry* **48**, 764-775.

Clarke E.C.W. and Glew D.N. (1971) Aqueous nonelectrolyte solutions. Part VIII. Deuterium and hydrogen sulfides solubilities in deuterium oxide and water. *Canadian Journal of Chemistry* **49**, 691-698.

Cleveland F.F. (1943) Raman Spectra of Hydrocarbons - I. 1-Octene, cis+*trans* 2-Octene, *trans*-3-Octene, *trans*-4-Octene, 4-Octene, and 1-Octyne. *The Journal of Chemical Physics* **11**, 1-6.

Collins J.F., Kenter J.A.M., Harris P.M., Kuanysheva G., Fischer D.J., and Steffen K.L. (2006) Facies and reservoir-quality variations in the Late Visean to Bashkirian outer platform, rim, and flank of the Tengiz buildup, Precaspian Basin, Kazakhstan. In *Giant Hydrocarbon reservoirs of the world: From rocks to reservoir characterization and modelling* (eds. P.M. Harris and L.J. Weber), *AAPG Memoir* **88**, p. 55-95. American Association of Petroleum Geologists.

Connolly C.A., Walter L.M., Baadsgaard H., and Longstaffe F.J. (1990) Origin and evolution of formation waters, Alberta Basin, Wetsern Canada Sedimentary Basin. I. Chemistry. Applied Geochemistry 5, 375-395.

Cox J.D., Wagman D.D., and Medvedev V.A. (1989) Codata Key Values for Thermodynamics. Hemisphere Publishing Corporation.

Cross M.M., Manning D.A.C., Bottrell S.H., and Worden R.H. (2004) Thermochemical sulphate reduction (TSR): experimental determination of reaction kinetics and implications of the observed reaction rates for petroleum reservoirs. *Organic Geochemistry* **35**, 393-404.

Cubitt A.G., Henderson C., Staveley L.A.K., Fonseca I.M.A., Ferreira A.G.M., and Lobo L.Q. (1987) Some thermodynamic properties of liquid hydrogen sulphide and deuterium sulphide. *Journal of Chemical Thermodynamics,* **19**, 703-710.

Curiale J.A. (1986) Origin of solid bitumens, with emphasis on biological marker results. *Organic Geochemistry,* **10**, 559-580.

Dartiguelongue C., Behar F., Budzinski H., Scacchi G., and Marquaire P.M. (2006) Thermal stability of dibenzothiophene in closed system pyrolysis: Experimental study and kinetic modelling. *Organic Geochemistry* **37**, 98-116.

Davis J.B. and D.W. Kirkland (1979) Bioepigenetic sulfur deposits. *Economic Geology* **74**, 462-468.

De Donder Th. (1920) *Leçons de Thermodynamique et de Chimie-Physique*. Gauthier-Villars.

De Donder Th. (1922) L´affinité. Applications aux gaz parfaits. *Bulletin de la Classe des Sciences (Académie Royale de Belgique)* **7**, 197-205.

Dick J.M., LaRowe D.E., and Helgeson H.C. (2006) Temperature, pressure, and electrochemical constraints on protein speciation: Group additivity calculation of the standard molal thermodynamic properties of ionized unfolded proteins. *Biogeosciences* **3**, 311-336.

de Hemptinne J.-C. and Béhar E. (2000) Proprtiétés thermodynamiques de systèmes contenant des gaz acides. *Oil & Gas Science and Technology – Revue de l´IFP* **55**, 617-637.

Dhannoun H.Y. and Fyfe W.S. (1972) Reaction rates of hydrocarbons with anhydrite. *Progress in Experimental Petrology* **2**, 69-71.

Diarov M.D., Kudaykulov A.K., Mardonov B.M., Bolskov A.A., Serikov T.P., Diarova O.M., Ergaliev T.Zh. (2006) *Ecology and Oil and Gas Complex (8 volumes), Ministry of Education and Science of the Republic of Kazakhstan, Atyrau Oil and Gas Institute*, Atyrau, Almaty: Galym.

Ding K., Li S., Yue C., and Zhong N. (2007) Simulation experiments on thermochemical sulfate reduction using natural gas. *Journal of Fuel Chemistry and Technology* **35**, 401-406.

Domalski E.S. and Hearing E.D. (1993) Estimation of the thermodynamic properties of C-H-N-O-S-halogen compounds at 298.15 K. *Journal of Physical and Chemical Reference Data* **22**, 805-1159.

Douglas A.G. and Mair B.J. (1965) Sulfur: role in genesis of petroleum. *Science* **147**, 499-501.

Drever J.D. (1997) *The Geochemistry of Natural Waters* (3rd edition). Prentice-Hall.

Drummond S.E. (1981) Boiling and mixing of hydrothermal fluids: chemical effects on mineral precipitation. Ph.D. thesis, Pennsylvania State University, 400p.

Duan Z. and Mao S. (2006) A thermodynamic model for calculating methane solubility, density and gas phase composition of methane-bearing aqueous fluids from 273 to 523 K and from 1 to 2000 bar. *Geochimica et Cosmochimica Acta* **70**, 3369-3386.

Duan Z., Møller N., and Weare J.H. (1992) An equation of state for the CH_4-CO_2-H_2O system: I. Pure systems from 0 to 1000ºC and 0 to 8000 bar. *Geochimica et Cosmochimica Acta* **56**, 2605-2617.

Duan Z., Møller N., and Weare J.H. (1996) Prediction of the solubility of H_2S in NaCl aqueous solution: an equation of state approach. *Chemical Geology* **130**, 15-20.

Duan Z., Sun R., Liu R., and Zhu C. (2007) Accurate thermodynamic model for the calculation of H_2S solubility in pure water and brines. *Energy & Fuels* **21**, 2056-2065.

Dubessy J., Boiron M-C., Moissette A., Monnin C., and Sretenskaya N. (1992) Determinations of water, hydrates and pH in fluid inclusions by micro-Raman spectrometry. *European Journal of Mineral* **4**, 885-894.

Dubessy J., Buschaert S., Lamb W., Pironon J., and Thiéry R. (2001) Methane-bearing aqueous fluid inclusions: Raman analysis, thermodynamic modeling and application to petroleum basins. *Chemical Geology* **173**, 193-205.

Dubessy J., Lhomme T., Boiron M.C., and Rull F. (2002) Determination of chlorinity in aqueous fluids using Raman spectroscopy of the stretching band of water at room temperature: application to fluid inclusions, *Applied Spectroscopy* **56**, 99-106.

Eakin B.E. and De Vaney W.E. (1974) Vapor-liquid equilibria in hydrogen – hydrogen sulfide – C_9 hydrocarbon systems. *AIChE Symposium Series* **70**, 80-90.

Eastman E.D. and McGavock W.C. (1937) The heat capacity and entropy of rhombic and monoclinic sulfur. *Journal of the American Chemical Society* **59**, 145-151.

Egeberg P.K. and Aagaard P. (1989) Origin and evolution of formation waters from oil fields on the Norwegian shelf. *Applied Chemistry* **4**, 131-142.

Ellis A.J. (1963) The solubility of calcite in sodium chloride solutions at high temperatures. *American Journal of Science* **261**, 259-267.

Feng G.-X. and Mather A.E. (1992) Solubility of hydrogen sulfide in *n*-eicosane at elevated pressure. *Journal of Chemical and Engineering Data* **37**, 412-413.

Feng G.-X. and Mather A.E. (1993a) Solubility of hydrogen sulfide in *n*-hexadecane at elevated pressure. *Canadian Journal of Chemical Engineering* **71**, 327-328.

Feng G.-X. and Mather A.E. (1993b) Solubility of hydrogen sulfide in *n*-dodecane at elevated pressure. *Fluid Phase Equilibria* **87**, 341-346.

Feng G.-X., Mather A.E., and Carroll J.J. (1995) The solubility of hydrogen sulfide in mixtures of *n*-hexadecane and *n*-eicosane. *Canadian Journal of Chemical Engineering* **73**, 154-155.

Fischer K., Chen J., Petri M., and Gmehling J. (2002) Solubility of H_2S and CO_2 in *n*-octyl-2-pyrrolidone and of H_2S in methanol and benzene. *AIChE Journal* **48**, 887-893.

François R. (1987) A study of sulphur enrichment in the humic fraction of marine sediments during early diagenesis. *Geochimica et Cosmochimica Acta* **51**, 17-27.

Freyer D. and Voigt W. (2004) The measurement of sulfate mineral solubilities in the Na-K-Ca-Cl-SO_4-H_2O system at temperatures of 100, 150 and 200°C. *Geochimica et Cosmochimica Acta* **68**, 307-318.

Friedmann W. (1916) Action of sulphur on octane under pressure. *Berichte der Deutschen Chemischen Gesellschaft* **49**, 1344-1352.

Fritz B. (1975) Etude thermodynamique et simulation des réactions entre minéraux et solutions. Application à la géochimie des altérations et des eaux continentales. *Mémoire des Sciences Géologiques* **41**, 152 p.

Fritz B. (1981) Etude thermodynamique et modélisation des réactions hydrothermales et diagénétiques. *Mémoire des Sciences Géologiques* **65**, 197 p.

Gamsjäger H., Lorimer J.W., Salomon M., Shaw D.G., and Tomkins R.P.T. (2010) The IUPAC-NIST solubility data series : A guide to preparatio and use of compilations and evaluations. *Journal of Physical and Chemical Reference Data* **39**, 023101.

Garagash L.A., Lobkovsky L.I., Volozh Yu.A., and Antipov M.P. (2004) Hydrodynamic modeling of evolution of fluid systems of sedimentary basins by the example of Precaspian Basin. In *Sedimentary Basins: Structure, Evolution and Methods of Studies* (eds. Yu.G. Leonov and Yu.A. Volozh), p. 459-469 (in Russian). Nauchnyi Mir.

Gerrard W. (1972) Solubility of hydrogen sulphide, dimethyl ether, methyl chloride and sulphur dioxide in liquids. The prediction of solubility of all gases. *Journal of Applied Chemistry and Biotechnology* **22**, 623-650.

Giauque W.F. and Blue R.W. (1936) Hydrogen sulfide. The heat capacity and vapor pressure of solid and liquid. The heat of vaporization. A comparison of thermodynamic and spectroscopic values of the entropy. *Journal of the American Chemical Society* **58**, 831-837.

Gillespie P.C. and Wilson G.M. (1980) Vapor-liquid equilibrium data on water-substitute gas components: N_2-H_2O, H_2-H_2O, CO-H_2O, H_2-CO-H_2O, and H_2S-H_2O. *Research Report* **41**. Gas Processors Association.

Gillespie S.E., Oscarson J.L., Chen X., Izatt R.M., and Pando C. (1992) Thermodynamic quantities for the interaction of Cl^- with Mg^{2+}, Ca^{2+} and H^+ in aqueous solution from 250 to 325°C. *Journal of Solution Chemistry* **21**, 761-788.

Goldstein R.H. (1986) Reequilibration of fluid inclusions in low temperature calcium-carbonate cement. *Geology* **14**, 792–795.

Goldstein T.P. and Aizenshtat Z. (1994) Thermochemical sulfate reduction. A review. *Journal of Thermal Analysis* **42**, 241-290.

Gransch J. A. and Posthuma J. (1974) On the origin of sulphur in crudes. In *Advances in Organic Geochemistry 1973* (eds. B. Tissot and F. Bienner), pp. 727–739. Editions Technip.

Greenwood H.J. (1967) Mineral equilibria in the system MgO-SiO_2-H_2O-CO_2. In *Researches in Geochemitsry, Volume 2* (ed. P.H. Abelson), pp. 542-567. Wiley.

Guillaume D., Teinturier S., Dubessy J. and Pironon J. (2003) Calibration of methane analysis by Raman spectroscopy in H_2O-NaCl-CH_4 fluid inclusion. *Chemical Geology*, **194**, 41-49.

Haar L., Kell G.S., and Gallagher J.S. (1984) *NBS/NRC Steam Tables: Thermodynamic and Transport Properties and Computer Programs for Vapor and Liquid States of Water in SI Units*. Taylor and Francis.

Hanin S. (2002) Thermoréduction des sulfates dans les réservoirs pétroliers: approche moléculaire. *Thèse de l'Université Louis Pasteur de Strasbourg*, 234 p.

Hanin S., Adam P., Kowalewski I., Huc A.Y., Carpentier B., and Albrecht P. (2002) Bridgehead alkylated 2-thiaadamantanes: novel markers for sulfurisation processes occuring under high thermal stress in deep petroleum reservoirs. *Chemical Communications*, 1750-1751.

Hanor J.S. (2000) Barite-celestine geochemistry and environments of formation. In *Sulfate Minerals: Crystallography, Geochemistry, and Environmental Significance* (eds. C.N. Alpers, J.L. Jambor, and D.K. Nordstrom), *Reviews in Mineralogy* **40**, pp. 193–275. Mineralogical Society of America.

Helgeson H.C. (1968) Evaluation of irreversible reactions in geochemical processes involving minerals and aqueous solutions – I. Thermodynamic relations. *Geochimica et Cosmochimica Acta* **32**, 853-877.

Helgeson H.C. (1969) Thermodynamics of hydrothermal systems at elevated temperatures and pressures. *American Journal of Science* **267**, 729-804.

Helgeson H.C. (1991) Organic/inorganic reactions in metamorphic processes. *Canadian Mineralogist* **29**, 707-739.

Helgeson H.C., Brown T.H., Nigrini A., and Jones T.A. (1970) Calculation of mass transfer in geochemical processes involving aqueous solutions. *Geochimica et Cosmochimica Acta* **34**, 569-582.

Helgeson H.C., Delany J.M., Nesbitt H.W., and Bird D.K. (1978) Summary and critique of the thermodynamic properties of rock-forming minerals. *American Journal of Science* **278-A**, 1-229.

Helgeson, H.C., Knox, A.M.,Owens, C.E., and Shock, E.L. (1993) Petroleum, oil field waters, and authigenic mineral assemblages: Are they in metastable equilibirum in hydrocarbon reservoirs? *Geochimica et Cosmochimica Acta* **57**, 3295-3339.

Helgeson H.C., Owens C.E., Knox A.M., and Richard L. (1998) Calculation of the standard molal thermodynamic properties of crystalline, liquid, and gas organic molecules at high temperatures and pressures. *Geochimica et Cosmochimica Acta* **62**, 985-1081.

Helgeson H.C., Richard L., McKenzie W.F., Norton D.L., and Schmitt A. (2009) A chemical and thermodynamic model of oil generation in hydrocarbon source rocks. *Geochimica et Cosmochimica Acta* **73**, 594-695.

Heydari E. (1997) The role of burial diagenesis in hydrocarbon destruction and H_2S accumulation, Upper Jurassic Smackover Formation, Black Creek field, Mississippi. *The American Association of Petroleum Geologists Bulletin* **81**, 26-45.

Heydari E. and Moore C.H. (1989) Burial diagenesis and thermochemical sulfate reduction, Smackover Formation, southeastern Mississippi salt basin. *Geology* **17**, 1080-1084.

Ho T.Y., Rogers M.A., Drushel H.V., and Koons C.B. (1974) Evolution of sulfur compounds in crude oils. *The American Association of Petroleum Geologists Bulletin* **58**, 2338-2348.

Horton A.W. (1949) The mechanism of the reactions of hydrocarbons with sulfur. *Journal of Organic Chemistry* **14**, 761-770.

Hutcheon I. (1999) Controls on the distribution of non-hydrocarbon gases in the Alberta Basin. *Bulletin of Canadian Petroleum Geology* **47**, 573-593.

Ihmels E.C. and Gmehling J. (2001) Densities of toluene, carbon dioxide, carbonyl sulfide, and hydrogen sulfide over a wide temperature and pressure range in the sub- and supercritical state. *Industrial and Engineering Chemistry Research* **40**, 4470-4477.

Isaksen G.H. and Khalylov M. (2007) Controls on hydrogen sulfide formation in a Jurassic carbonate play, Turkmenistan. In *Oil and Gas of the Greater Caspian area* (eds. P.O. Yilmaz and G.H. Isaksen), *AAPG Studies in Geology* **55**, pp. 133-149.

Ivlev A.A., Pankina R.G., Gal'peri G.D. (1973) Thermodynamics of reactions of sulfurization of oil. *Petroleum Geology* **11**, 70-75.

Jacquemet N. (2006) Durabilité des matériaux de puits pétroliers dans le cadre d'une séquestration géologique de dioxyde de carbone et d'hydrogène sulfuré. *Thèse Université Henri Poincaré, Nancy I,* 302.

Jacquemet N., Pironon J., and Caroli E. (2005) A new experimental procedure for simulation of H_2S+CO_2 geological storage. Application to well cement aging. *Oil & Gas Science and Technology – Revue de l'IFP* **60**, 193-206.

Johnson J.W., Oelkers E.H., and Helgeson H.C. (1992) SUPCRT92: A software package for calculating the standard molal thermodynamic properties of minerals, gases, aqueous species, and reactions from 1 to 5000 bar and 0 to 1000ºC. *Computers and Geosciences* **18**, 899-947.

Kay W.B. and Brice D.B. (1953) Liquid-vapor equilibrium relations in ethane-hydrogen sulfide system. *Industrial and Engineering Chemistry* **45**, 615-618.

Kay W.B. and Rambosek G.M. (1953) Liquid-vapor equilibrium relations in binary systems – Propane-hydrogen sulfide system. *Industrial and Engineering Chemistry* **45**, 221-226.

Kelemen S.R., Walters C.C., Kwiatek P.J., Afeworki M., Sansone M., Freund H., Pottorf R.J., Machel H.G., Zhang T., Ellis G.S., Tang Y., and Peters K.E. (2008) Distinguishing solid bitumens formed by thermochemical sulfate reduction and thermal chemical alteration. *Organic Geochemistry* **39**, 1137-1143.

Kelley K.K. (1960) Data on theoretical metallurgy. XIII. High-temperature, heat-capacity, and entropy data for the elements and inorganic compounds. *Bulletin of the United States Bureau of Mines* **584**, 232 pp.

King M.B. and Al-Najjar H. (1977) The solubilities of carbon dioxide, hydrogen sulfide, and propane in some normal alkane solvents. I. Experimental determinations in the range 15-70°C and comparison with ideal solution values. *Chemical Engineering Science* **32**, 1241-1246.

King M.B., Kassim K., and Al-Najjar H. (1977) The solubilities of carbon dioxide, hydrogen sulfide, and propane in some normal alkane solvents. II. Correlation of data at 25°C in terms of solubility parameters and regular solution theory. *Chemical Engineering Science* **32**, 1247-1252.

Kiyosu Y. (1980) Chemical reduction and sulfur-isotope effects of sulfate by organic matter under hydrothermal conditions. *Chemical Geology* **30**, 47-56.

Kowalewski I., Fiedler C., Parra T., Adam P., and Albrecht P. (2008) Preliminary results on the formation of organosulfur compounds in sulfate-rich petroleum reservoirs submitted to steam injection. *Organic Geochemistry* **39**, 1130-1136.

Kozintseva T.N. (1964) Solubility of hydrogen sulphide in water at elevated temperatures. *Geokhimiya* **8,** 758-764.

LaRowe D.E. and Helgeson H.C. (2006) Biomolecules in hydrothermal systems: Calculation of the standard molal thermodynamic properties of nucleic-acid bases, nucleosides, and nucleotides at elevated temperatures and pressures. *Geochimica et Cosmochimica Acta* **70**, 4680-4724.

Laugier S. And Richon D. (1995) Vapor-liquid equilibria for hydrogen sulfide + hexane, + cyclohexane, + benzene, + pentadecane, and + (hexane + pentadecane). *Journal of Chemical and Engineering Data* **40**, 153-159.

Lee J.I. and Mather A.E. (1977) Solubility of hydrogen sulfide in water. *Berichte der Bunsen-Gesellschaft* **81**, 1020-1023.

Lemmon E.W., McLinden M.O., and Friend D.G., Thermophysical properties of fluid systems. In NIST Chemistry WebBook, NIST Standard Reference Database 69 (eds. P.J. Linstrom and W.G. Mallard), National Institute of Standards and Technology, Gaithersburg MD, 20899, *http://webbook.nist.gov*, (retrieved September 28, 2009).

Lenoir J.-Y., Renault P., and Renon H. (1971) Gas chromatographic determination of Henry´s constants of 12 gases in 19 solvents. *Journal of Chemical and Engineering Data* **16**, 340-342.

Le Tran K. (1971) Etude géochimique de l'hydrogène sulfuré adsorbé dans les sédiments. *Bulletin du Centre de Recherches de Pau – SNPA* **5**, 321-332.

Leroy J. (1979) Contribution à l'étalonnage de la pression interne des inclusions fluides lors de leur décrépitation. *Bulletin de la Société Française de Mineralogie et de Cristallographie* **102**, 584-593.

Levelt Sengers J.M.H., Kamgar-Parsi B., and Sengers, J.V. (1983) Thermodynamic properties of steam in the critical region. *Journal of Physical and Chemical Reference Data* **12**, 1-28.

Lewis G.N. and Randall M. (1911) The heat content of the various forms of sulfur. *Journal of the American Chemical Society* **33**, 476-488.

Lewis L.C. and Fredericks W.J. (1968) Volumetric properties of supercritical hydrogen sulfide. *Journal of Chemical and Engineering Data* **13**, 482-485.

Lisovsky, N.N., Gogonenkov, G.N., and Petzoukha, Yu.A. (1992) The Tengiz oil field in the Pre-Caspian basin of Kazakhstan (former USSR) — Supergiant of the 1980s. In *Giant oil and gas fields of the decade 1978–1988* (ed. M.T. Halbouty), *American Association of Petroleum Geologists Memoir* **54**, 101–122.

Machel H.G. (1986) Early lithification, dolomitization, and anhydritization of Upper Devonian Nisku buildups, subsurface of Alberta, Canada. In *Reef Diagenesis* (eds. J.H. Schroeder and B.H. Purser), pp. 336-356. Springer-Verlag.

Machel H.G. (1987) Saddle dolomite as a by-product of chemical compaction and thermochemical sulfate reduction. *Geology* **15**, 936-940.

Machel H.G. (1987) Some aspects of diagenetic sulphate-hydrocarbon redox reactions. In *Diagenesis of Sedimentary Sequences* (ed. J.D. Marshall), *Geological Society Special Publication No. 36*, pp. 15-28.

Machel H.G. (1998) Comment on "The effects of thermochemical sulfate reduction upon formation water salinity and oxygen isotopes in carbonate reservoirs" by R.H. Worden, P.C. Smalley, and N.H. Oxtoby. *Geochimica et Cosmochimica Acta* **62**, 337-341.

Machel H.G. (1999) Effects of groundwater flow on mineral diagenesis, with emphasis on carbonate aquifers. *Hydrogeology Journal* **7**, 94-107.

Machel H.G. (2001) Bacterial and thermochemical sulfate reduction in diagenetic settings — old and new insights. *Sedimentary Geology* **140**, 143-175.

Machel H.G., Krouse H.R., and Sassen R. (1995) Products and distinguishing criteria of bacterial and thermochemical sulfate reduction. *Applied Geochemistry* **10**, 373-389.

Maier C.G. and Kelley K.K. (1932) An equation for the representation of high temperature heat content data. *Journal of the American Chemical Society* **54**, 3243-3246.

Majer V. and Štulík K. (1982) A study of the stability of alkaline-earth metal complexes with fluoride and chloride ions at various temperatures by potentiometry with ion-selective electrodes. *Talanta* **29**, 145-148.

Majzlan J., Navrotsky A., and Neil J.M. (2002) Energetics of anhydrite, barite, celestine, and anglesite: A high-temperature and differential scanning calorimetry study. *Geochimica et Cosmochimica Acta* **66**, 1839-1850.

Makranczy J., Megyery-Balog K., Rusz L. and Patyi L.(1976) Solubility of gases in normal-alkanes. *Hungarian Journal of Industrial Chemistry* **4**, 269-280.

Mango F.D. (1983) The diagenesis of carbohydrates by hydrogen sulfide. *Geochimica et Cosmochimica Acta* **47**, 1433-1441.

Manzano B.K., Fowler M.G., and Machel H.G. (1997) The influence of thermochemical sulphate reduction on hydrocarbon composition in Nisku reservoirs, Brazeau river area, Alberta, Canada. *Organic Geochemistry* **27**, 507-521.

Marshall W.L., Slusher R., and Jones E.V. (1964) Aqueous systems at high temperature. XIV. Solubility and thermodynamic relationships for $CaSO_4$ in $NaCl-H_2O$ solutions from 40° to 200°C., 0 to 4 molal NaCl. *Journal of Chemical and Engineering Data* **9**, 187-191.

McCollom T.M. et Shock E.L. (1997) Geochemical constraints on chemolithoautotrophic metabolism by microorganisms in seafloor hydrothermal systems. *Geochimica Cosmochimica Acta* **61**, 4375-4391.

Montel F. (1993) Phase Equilibria Needs for Petroleum Exploration and Production Industry. *Fluid Phase Equilibria* **84**, 343-367.

Moore C.H. (1989) *Carbonate diagenesis and porosity. Developments in sedimentology*, *46*. Amsterdam, Oxford: Elsevier, 338 p.

Moore C.H. (1997) *Carbonate diagenesis and porosity. Developments in sedimentology*, *46*. Amsterdam, Oxford: Elsevier, 338 p.

Morse J.W. and Berner R.A. (1995) What determines sedimentary C/S ratios? *Geochimica et Cosmochimica Acta* **59**, 1073-1077.

Mougin P., Lamoureux-Var V., Bariteau A., and Huc A.Y. (2007) Thermodynamic of thermochemical sulphate reduction. *Journal of Petroleum Science and Engineering* **58**, 413-427.

Myers R.J. (1986) The new low value for the second dissociation constant for H_2S. *Journal of Chemical Education* **63**, 687-690.

Newton R.C. and Manning C.E. (2005) Solubility of anhydrite, $CaSO_4$, in $NaCl$-H_2O solutions at high pressures and temperatures: applications to fluid-rock interaction. *Journal of Petrology* **46**, 701-716.

Ng H.-J. and Robinson D.B. (1979) The equilibrium phase properties of selected naphthenic binary systems: carbon dioxide – methylcyclohexane, hydrogen sulfide – methylcyclohexane. *Fluid Phase Equilibria* **2**, 283-292.

Ng H.-J., Kalra H., Robinson D.B., and Kubota H. (1980) Equilibrium phase properties of the toluene – hydrogen sulfide and *n*-heptane – hydrogen sulfide binary systems. *Journal of Chemical Engineering Data* **25**, 51-55.

Nikolayeva O.V., Ryzhenko B.N., and Germanov A.I. (1982) Reduction of sulfate sulfur by hydrocarbons and alcohols in aqueous solution at 200-300°C. *Geochemistry International* **19** (n°3), 88-104.

Nöth S. (1997) High H_2S contents and other effects of thermochemical sulfate reduction in deeply buried carbonate reservoirs: a review. *Geologische Rundschau* **86**, 275-287.

Ohmoto H. (1972) Systematics of sulfur and carbon isotopes in hydrothermal ore deposits. *Economic Geology* **67**, 551-578.

Ohmoto H. and Lasaga A.C. (1982) Kinetics of reactions between aqueous sulfates and sulfides in hydrothermal systems. *Geochimica et Cosmochimica Acta* **46**, 1727-1745.

Ohmoto H. and Goldhaber M.B. (1997) Sulfur and carbon isotopes. In (ed. H.L. Barnes) *Geochemistry of Hydrothermal Ore Deposits*, 3rd edition, pp. 517-611. Wiley.

Orr W.L. (1974) Changes in sulfur content and isotopic ratios of sulfur during petroleum maturation – Study of Big Horn Basin Paleozoic oils. *The American Association of Petroleum Geologists Bulletin* **58**, 2295-2318.

Orr W.L. (1977) Geologic and geochemical controls on the distribution of hydrogen sulfide in natural gas. In *Advances in Organic Geochemistry 1975* (eds. R. Campos and J. Goñi), pp. 571-597. Empresa Nacional Adaro De Investigaciones Mineras, Madrid.

Orr W.L. and Sinninghe Damsté J.S. (1990) Geochemistry of sulfur in petroleum systems. In *Geochemistry of Sulfur in Fossil Fuels* (eds. W.L. Orr and C.M. White), *ACS Symposium Series* **429**, pp. 2-29. American Chemical Society.

Pairazian V.V. (1999) A review of the petroleum geochemistry of the Precaspian Basin. *Petroleum Geoscience* **5**, 361-369.

Park W.C. and Schot E.H. (1968) Stylolites: Their nature and origin. Journal of Sedimentary Petrology **38**, 175-191.

Payzant J. D., Montgomery D. S., and Strausz O. P. (1983) Novel terpenoid sulfoxides and sulfides in petroleum. *Tetrahedron Letters* **24,** 651–654.

Payzant J. D., Montgomery D. S., and Strausz O. P. (1986) Sulfides in petroleum. *Organic Geochemistry* **9,** 357–369.

Peng D.-Y. and Robinson D.B. (1976) A new two-constant equation of state. *Industrial and Engineering Chemistry Fundamentals* **15**, 59-64.

Peters K. E., Walters C. C., and Moldowan J. M. (2005) *The Biomarker Guide. Volume 1: Biomarkers and Isotopes in the Environment and Human History. Volume 2: Biomarkers and Isotopes in Petroleum Exploration and Earth History* (2nd Edition). Cambridge University Press.

Pironon J. (2004) Fluid inclusions in petroleum environments: analytical procedure for PTX reconstruction. *Acta Petrologica Sinica* **20**, 1333-1342.

Pironon J. and Barrès O. (1990) Semi-quantitative FT-IR microanalysis limits: Evidence from synthetic hydrocarbon fluid inclusions in sylvite. *Geochimica et Cosmochimica Acta* **54**, 509-518.

Pironon J., Canals M., Dubessy J., Walgenwitz F., and Laplace-builhe C. (1998) Volumetric reconstruction of individual oil inclusion by confocal scanning laser microscopy, *European Journal of Mineralogy* **10**, 1143-1150.

Pironon J., Thiery R., Ayt Ougougdal M., Beaudoin G., and Walgenwitz F. (2001) FT-IR measurements of petroleum fluid inclusions: methane, n-alkanes and carbon dioxide quantitative analysis, *Geofluids* **1**, 2-10.

Pitzer K.S. (1973) Thermodynamics of electrolytes. I. Theoretical basis and general equations. *Journal of Physical Chemistry* **77**, 268-277.

Pitzer K.S. (1987) Thermodynamic model for aqueous solutions of liquid-like density. In *Thermodynamic Modeling of Geological Materials: Minerals, Fluids and Melts* (eds. I.S.E. Charmichael and H.P. Eugster), *Reviews in Mineralogy, vol. 17*, pp. 97-142. Mineralogical Society of America.

Pitzer K.S., Lippmann D.Z., Curl R.F. Jr., Huggins C.M., and Petersen D.E. (1955) The volumetric and thermodynamic properties of fluids. II. Compressibility factor, vapor pressure and entropy of vaporization. *Journal of the American Chemical Society* **77**, 3433-3440.

Plummer L.N. and Busenberg E. (1982) The solubilities of calcite, aragonite and vaterite in CO_2-H_2O solutions between 0 and 90ºC, and an evaluation of the aqueous model for the system $CaCO_3$-CO_2-H_2O. *Geochimica et Cosmochimica Acta* **46**, 1011-1040.

Pollack N.R., Enick, R.M., Mangone D.J., and Morsi B.I. (1988) Effect of an aqueous phase on CO_2/tetradecane and CO_2/Maljamar-crude-oil systems. *SPE Reservoir Engineering* **3**, 533-541.

Powell R.E. and Eyring H. (1943) The properties of liquid sulfur. *Journal of the American Chemical Society* **65**, 648-654.

Prausnitz J.M., Lichtenthaler R.N. et de Azevedo E.G. (1986) *Molecular Thermodynamics of Fluid-Phase Equilibria* (2nd edition). Pentice-Hall.

Prezbindowski D.R. and Larese R.E. (1987) Experimental stretching of fluid inclusions in calcite – Implications for diagenetic studies. *Geology* **15**, 333-336

Prezbindowski D.R. and Tapp J.B. (1991) Dynamics of fluid inclusions alterations in sedimentary rocks: a review and discussion. *Organic Geochemistry* **17**, 131–142.

Przewocki K., Malinski E., and Szafranek J. (1984) Elemental sulfur reactions with toluene, dibenzyl, *z*-stilbene and their geochemical significance. *Chemical Geology* **47**, 347-360.

Radke M. and Willsch H. (1994) Extractable alkyldibenzothiophenes in Posidonia Shale (Toarcian) source rocks: Relationship of yields to petroleum formation and expulsion. *Geochimica Cosmochimica Acta* **58,** 5223–5244.

Radke M., Welte D.H., and Willsch H. (1991) Distribution of alkylated aromatic hydrocarbons and dibenzothiophenes in rocks of the Upper Rhine Graben. *Chemical Geology* **93**, 325-341.

Rasmussen H.E., Hansford R.C., and Sachanen A.N. (1946) Reactions of aliphatic hydrocarbons with sulfur. *Industrial and Engineering Chemistry* **38**, 376-382.

Rau H. and Mathia W. (1982) Equation of state for gaseous H_2S. *Berichte der Bunsen-Gesellschaft für Physikalische Chemie* **86**, 108-109.

Reamer H.H., Sage B.H., and Lacey W.N. (1950) Volumetric behavior of hydrogen sulfide. *Industrial and Engineering Chemistry* **42**, 140-143.

Reamer H.H., Sage B.H., and Lacey W.N. (1951) Phase equilibria in hydrocarbon systems. Volumetric and phase behavior of the methane – hydrogen sulfide system. *Industrial and Engineering Chemistry* **43**, 976-981.

Reamer H.H., Sage B.H., and Lacey W.N. (1953a) Phase equilibria in hydrocarbon systems. Volumetric and phase behavior of *n*-pentane – hydrogen sulfide system. *Industrial and Engineering Chemistry* **45**, 1805-1809.

Reamer H.H., Sage B.H., and Lacey W.N. (1953b) Phase equilibria in hydrocarbon systems. Volumetric and phase behavior of *n*-decane – hydrogen sulfide system. *Industrial and Engineering Chemistry* **45**, 1810-1812.

Redlich O. and Kwong J.N.S. (1949) On the thermodynamics of solutions. V. An equation of state. Fugacities of gaseous solutions. *Chemical Reviews* **44**, 233-244.

Reid R.C., Prausnitz J.M., and Poling B.E. (1987) *The Properties of Gases and Liquids* (4th ed.). McGraw-Hill.

Renard S. (2010) Rôle des gaz annexes sur l'évolution géochimique d'un site de stockage de carbone. Application à des reservoirs carbonatés. *Thèse de l′Institut National Polytechnique de Lorraine*.

Richard L. (2001) Calculation of the standard molal thermodynamic properties as a function of temperature and pressure of some geochemically important organic sulfur compounds. *Geochimica et Cosmochimica Acta* **65**, 3827-3877.

Richard L. and Helgeson H.C. (1998) Calculation of the thermodynamic properties at elevated temperatures and pressures of saturated and aromatic high molecular weight solid and liquid hydrocarbons in kerogen, bitumen, petroleum, and other organic matter of biogeochemical interest. *Geochimica et Cosmochimica Acta* **62**, 3591-3636.

Richard L. and Helgeson H.C. (2001) Thermodynamic calculation of the distribution of organic sulfur compounds in crude oil as a function of temperature, pressure, and H_2S fugacity. In *Proceedings of the Tenth International Symposium on Water-Rock Interaction* (ed. R. Cidu), pp. 333-335. Swets & Zeitlinger.

Richard L., Neuville N., Sterpenich J., Perfetti E., and Lacharpagne J.C. (2005) Thermodynamic analysis of organic/inorganic reactions involving sulfur: Implications for the sequestration of H_2S in carbonate reservoirs. *Oil & Gas Science and Technology* **60**, 275-285.

Richnow H. H., Jenisch A., and Michaelis W. (1992) Structural investigations of sulphur-rich macromolecular oil fractions and a kerogen by sequential chemical degradation. *Organic Geochemistry* **19,** 351–370.

Robie R.A., Hemingway B.S., and Fisher J.R. (1979) Thermodynamic properties of minerals and related substances at 298.15 K and 1 bar (10^5 Pa) pressure and at higher temperatures. *U.S. Geological Survey Bulletin* **1452**, 456 p.

Robie R.A., Russell-Robinson S., and Hemingway B.S. (1989) Heat capacities and entropies from 8 to 1000 K of langbeinite ($K_2Mg_2(SO_4)_3$), anhydrite ($CaSO_4$) and of gypsum ($CaSO_4.2H_2O$) to 325 K. *Thermochimica Acta* **139**, 67-81.

Robinson D.B., Hughes R.E., and Sandercock J.A.W. (1964) Phase behavior of the *n*-butane – hydrogen sulfide system. *Canadian Journal of Chemical Engineering* **42**, 143-146.

Ronchi P., Ortenzi A., Borromeo O., Claps M., and Zempolich W.G. (2010) Depositional setting and diagenetic processes and their impact on the reservoir quality in the late Visean-Bashkirian Kashagan carbonae platform (Pre-Caspian Basin, Kazakhstan). *AAPG Bulletin* **94**, 1313-1348.

Sakoda N. and Uematsu M. (2004) A thermodynamic property model for fluid phase hydrogen sulfide. *International Journal of Thermophysics*, **25**, 709-737.

Sassen R. (1988) Geochemical and carbon siotopic studies of crude oil destruction, bitumen precipitation, and sulfate reduction in the deep Smackover Formation. *Organic Geochemistry* **12**, 351-361.

Sassen R., McCabe C., Kyle J.R., and Chinn E.W. (1989) Deposition of magnetic pyrrhotite during alteration of crude oil and reduction of sulfate. *Organic Geochemistry* **14**, 381-392.

Schmid J.-C. (1986) Marqueurs biologiques soufrés dans les pétroles. *Thèse de l'Université Louis Pasteur de Strasbourg*, 263 p.

Schmid J.-C., Connan J., and Albrecht P. (1986) Occurence and geochemical significance of long-chain dialkylthiacyclopentanes. *Nature* **329**, 54-56.

Schrötter H.W. (1995) Raman spectra of gases. In *Infrared Raman Spectroscopy: Methods and Applications* (ed. B. Schrader), pp. 277-297. Wiley-VCH.

Schulte M.D. and Rogers K.L. (2004) Thiols in hydrothermal solution: standard partial molal thermodynamic properties and their role in the organic geochemistry of hydrothermal environments. *Geochimica et Cosmochimica Acta* **68**, 1087-1097.

Seewald J.S., Eglinton L.B., and Ong Y.-L. (2000) An experimental study of organic-inorganic interactions during vitrinite maturation. *Geochimica et Cosmochimica Acta* **64**, 1577-1591.

Selleck F.T., Carmichael L.T., and Sage B.H. (1952) Phase behavior in the hydrogen sulfide-water system. *Industrial and Engineering Chemistry* **44**, 2219-2226.

Setchenow J. (1889) Über die Konstitution der Salzlösungen auf Grund ihres Verhaltens zu Kohlensäure. *Zeitschrift für Physikalische Chemie* **4**, 117-125.

Shock E.L. (1995) Organic acids in hydrothermal solutions: Standard molal thermodynamic properties of carboxylic acids and estimates of dissociation constants at high temperatures and pressures. *American Journal of Science* **295**, 496-580.

Shock E.L. and Helgeson H.C. (1988) Calculation of the thermodynamic and transport properties of aqueous species at high temperatures and pressures: Correlation algorithms for ionic species and equation of state predictions to 5 kb and 1000°C. *Geochimica et Cosmochimica Acta* **52**, 2009-2036.

Shock E.L. and Helgeson H.C. (1990) Calculation of the thermodynamic and transport properties of aqueous species at high pressures and temperatures: Standard partial molal properties of organic species. *Geochimica et Cosmochimica Acta* **54**, p. 915-945.

Shock E.L., Helgeson H.C., and Sverjensky D.A. (1989) Calculation of the thermodynamic and transport properties of aqueous species at high temperatures and pressures: Standard partial molal properties of inorganic neutral species. *Geochimica Cosmochimica Acta* **53**, 2157-2183.

Shock E.L. and Koretsky C.M. (1993) Metal-organic complexes in geochemical processes: Calculation of standard partial molal thermodynamic properties of aqueous acetate complexes at high pressures and temperatures. *Geochimica Cosmochimica Acta* **57**, 4899-4922.

Shock E.L. and Koretsky C.M. (1995) Metal-organic complexes in geochemical processes: Estimation of standard partial molal thermodynamic properties of aqueous complexes between metal cations and monovalent organic acid ligands at high pressures and temperatures. *Geochimica Cosmochimica Acta* **59**, 1497-1532.

Shock E.L., Sassani D.C., Willis M., and Sverjensky D.A. (1997) Inorganic species in geologic fluids: Correlations among standard molal thermodynamic properties of aqueous ions and hydroxide complexes. *Geochimica Cosmochimica Acta* **61**, 907-950.

Simonson J.M., Busey R.H., and Mesmer R.E. (1985) Enthalpies of dilution of aqueous calcium chloride to low molalities at high temperatures. *Journal of Physical Chemistry* **89**, 557-560.

Sinninghe Damsté J. S. and de Leeuw J. W. (1990) Analysis, structure and geochemical significance of organically-bound sulphur in the geosphere: State of the art and future research. *Org. Geochem.* **16,** 1077–1101.

Sinninghe Damsté J. S., ten Haven H. L., de Leeuw J. W., and Schenck P. A. (1986) Organic geochemical studies of a Messinian evaporitic basin, northern Apennines (Italy) —II. Isoprenoid and *n*-alkyl thiophenes and thiolanes. *Organic Geochemistry.* **10,** 791–805.

Sinninghe Damsté J. S., de Leeuw J. W., Kock-van Dalen A. C., de Zeeuw M. A., de Lange F., Ripstra W. I. C., and Schenck P. A. (1987) The occurrence and identification of series of organic sulphur compounds in oils and sediments extracts. I. A study of the Rozel Point Oil (U.S.A.). *Geochimica Cosmochimica Acta* **51**, 2369–2391.

Sinninghe Damsté J. S., Ripstra W. I. C., Kock-van Dalen A. C., de Leeuw J. W., and Schenck P. A. (1989a) Quenching of labile functionalised lipids by inorganic sulphur species: Evidence for the formation of sedimentary organic sulphur compounds at the early stages of diagenesis. *Geochimica Cosmochimica Acta* **53,** 1343–1355.

Sinninghe Damsté J. S., Ripstra W. I. C., de Leeuw J. W., and Schenck P. A. (1989b) The occurrence and identification of series of organic sulphur compounds in oils and sediment extracts: II. Their presence in samples from hypersaline and non-hypersaline palaeoenvironments and possible application as source, palaeoenvironmental and maturity indicators. *Geochimica Cosmochimica Acta* **53,** 1323–1341.

Smith J.T. and Ehrenberg S.N. (1989) Correlation of carbon dioxide abundance with temperature in clastic hydrocarbon reservoirs: relationship to inorganic chemical equilibrium. *Marine and Petroleum Geology* **6**, 129-135.

Soave G. (1972) Equilibrium constants from a modified Redlich-Kwong equation of state. *Chemical Engineering Science,* **27,** 1197-1203.

Suleimenov O.M. and Krupp R.E. (1994) Solubility of hydrogen sulfide in pure water and in NaCl solutions, from 20 to 320°C and at saturation pressures. *Geochimica et Cosmochimica Acta* **58**, 2433-2444.

Sverjensky D.A., Shock E.L., and Helgeson H.C. (1997) Prediction of the thermodynamic properties of aqueous complexes to 1000°C and 5 kbar. *Geochimica et Cosmochimica Acta* **61**, 1359-1412.

Tanger J.C. and Helgeson H.C. (1988) Calculation of the thermodynamic and transport properties of aqueous species at high pressures and temperatures; revised equations of state for the standard partial molal properties of ions and electrolytes. *American Journal of Science* **288**, 19-98.

Teinturier S. and Pironon J. (2004) Experimental growth of quartz in petroleum environment. Part I: Procedure and fluid trapping. *Geochimica et Geochimica Acta* 68, 2495-2507.

Teinturier S., Pironon J., and Walgenwitz F. (2002) Fluid inclusions and PVTX modeling examples from the Garn formation in well 6507/2-2, Haltenbanken, Mid-Norway. *Marine and Petroleum Geology* **19**, 755-765.

Thamdrup B., Finster K., Fossing H., Hansen J.W., and Jørgensen B.B. (1994) Thiosulfate and sulfite distributions in porewater of marine sediments related to manganese, iron, and sulfur geochemistry. *Geochimica et Cosmochimica Acta* **58**, 67-73.

Thiéry R., Pironon J., Walgenwitz F., and Montel F. (2000) PIT (Petroleum Inclusion Thermodynamic): a new modeling tool for the characterization of hydrocarbon fluid inclusions from volumetric and microthermometric measurements. *Journal of Geochemical Exploration* **69-70**, 701-704.

Thiéry R., Pironon J., Walgenwitz F., and Montel F. (2002) Individual characterization of petroleum inclusions (composition and P-T trapping conditions) by microthermometry and confocal scanning laser microscopy: inferences from applied thermodynamics of oils. *Marine and Petroleum Geology* **19**, 847-859.

Toland W.G. (1960) Oxidation of organic compounds with aqueous sulfate. *Journal of the American Chemical Society* **82**, 1911-1916.

Tremper K.K. and Prausnitz J.M. (1976) Solubility of inorganic gases in high-boiling hydrocarbon solvents. *Journal of Chemical and Engineering Data* **21**, 295-299.

Trudinger P.A., Chambers L.A., and Smith J.W. (1985) Low-temperature sulphate reduction: biological versus abiological. *Canadian Journal of Earth Sciences* **22**, 1910-1918.

Tseng H.Y. and Pottorf R.J. (2003) The application of fluid inclusion PVT analysis to studies of petroleum migration and reservoirs. *Journal of Geochemical Exploration* **78-79**, 433-436

Tunell G. (1931) The definition and evaluation of the fugacity of an element or compound in the gaseous state. *Journal of Physical Chemistry* **35**, 2885-2913.

Ulmishek G.F. (2001) Petroleum geology and resources of the North Caspian Basin, Kazakhstan and Russia. *U.S. Geological Survey Bulletin* **2201-B**, 25 p.

Urmos J., Sharma S.K., and Mackenzie F.T. (1991) Characterization of some biogenic carbonates with Raman spectroscopy. *American Mineralogist* **76**, 641-646

Vairavamurthy A. and Mopper K. (1987) Geochemical formation of organosulphur compounds (thiols) by addition of H$_2$S to sedimentary organic matter. *Nature* **329**, 623-625.

Valisolalao J., Perakis N., Chappe B., and Albrecht P. (1984) A novel sulfur containing C35 hopanoid in sediments. *Tetrahedron Letters* **25,** 1183–1186.

Valitov N.B. and Valitov R.B. (1975) The role of temperature in formation of sulfur-bearing petroleums and catagenic hydrogen sulfide in carbonate reservoirs (experimental investigations). *Geochemistry International* **12** (n°5), 73-81.

van Kaam-Peters H. M. E., Köster J., de Leeuw J. W., Sinninghe Damsté J. S. (1995) Occurrence of two novel benzothiophene hopanoid families in sediments. *Organic Geochemistry* **23,** 607–616.

Volozh Yu.A., Antipov M.P., Brunet M.-F., Garagash I.A., Lobkovskii L.I., and Cadet J.P. (2003) Pre.Mesozoic geodynamics of the Precaspian Basin (Kazakhstan). *Sedimentary Geology* **156**, 35-58.

Votsalevsky E.S., Bulekbaev Z.E., Iskuzhiev B.A., Kamalov S.M., Korostyshevsky M.N., Kuandykov B.M., Kuantaev N.E., Marchenko O.N., Matloshinsky N.G., Nazhmetdinov A.Sh., Filipjev G.P., Shabatin I.V., Shakhabaev R.S., and Shudabaev K.S. (1998) *Oil and Gas Fields of Kazakhstan Reference Book.*

Warner J.L., Baskin D.K., Hwang R.J., Carlson R.M.K., and Clark M.E. (2007) Geochemical evidence for two stages of hydrocarbon emplacement and the origin of solid bitumen in the giant Tengiz field, Kazakhstan. In *Oil and Gas of the Greater Caspian area* (eds. P.O. Yilmaz and G.H. Isaksen), *AAPG Studies in Geology* **55**, pp.165-169. American Association of Petroleum Geologists.

Weber L.J., Francis B.P., Harris P.M., and Clark M. (2003) Stratigraphy, lithofacies, and reservoir distribution, Tengiz field, Kazakhstan. In *Permo-Carboniferous Carbonate Platforms and Reefs* (eds. W.M. Ahr, P.M. Harris, W.A. Morgan, and I.D. Somerville), *SEPM Special Pubication* **78**, 351-394.

West E.D. (1959) The heat capacity of sulfur from 25 to 450°, the heats and temperatures of transition and fusion. *Journal of the American Chemical Society* **81**, 29-37

Wilkins R.W.T. (1986) The mechanisms of stretching and leaking of fluid inclusions in fluorite. *Economic Geology* **81**, 1003–1008.

Williams-Jones A.E. and Seward T.M. (1989) The stability of calcium chloride ion pairs in aqueous solutions at temperatures between 100 and 360°C. *Geochimica et Cosmochimica Acta* **53**, 313-318.

Winkler L.W. (1906) Gesetzmässigkeit bei der Absorption der Gase in Flüssigkeiten. *Zeitschrift für physikalische Chemie* **55**, 344-354.

Wolery T.J. and Daveler S.A. (1992) EQ6, A computer code for reaction-path modeling of aqueous geochemical systems: Theoretical manual, user´s guide, and related documentation (version 7.0). UCRL-MA-110662-PT-IV, Lawrence Livermore National Laboratory, Livermore, California.

Wood S.A., Tait C.D., and Janecky D.R. (2002) A Raman spectroscopic study of arsenite and thioarsenite species in aqueous solution at 25°C. *Geochemical Transactions* **3(4)**, 31-39.

Worden R.H. and Smalley P.C. (1996) H$_2$S-producing reactions in deep carbonate gas reservoirs: Khuff Formation, Abu Dhabi. *Chemical Geology* **133**, 157-171.

Worden R.H. and Smalley P.C. (1997) The thermal impact of sulphate reduction in the Khuff Formation. In *Geofluids ´97 Extended Abstracts* (eds. J.P. Hendry, P.S. Carey, J. Parnell, A.H. Ruffell, and R.H. Worden), pp. 423-426.

Worden R.H. and Smalley P.C. (2001) H$_2$S in North Sea oil fields: importance of thermochemical sulphate reduction in clastic reservoirs. In *Proceedings of the Tenth International Symposium on Water-Rock Interaction* (ed. R. Cidu), pp. 659-662. Swets & Zeitlinger.

Worden R.H., Smalley P.C., and Oxtoby N.H. (1995) Gas souring by thermochemical sulfate reduction at 140°C. *The American Association of Petroleum Geologists Bulletin* **79**, 854-863.

Worden R.H., Smalley P.C., and Oxtoby N.H. (1996) The effects of thermochemical sulfate reduction upon formation water salinity and oxygen isotopes in carbonate gas reservoirs. *Geochimica et Cosmochimica Acta* **60**, 3925-3931.

Worden R.H., Smalley P.C., and Cross M.M. (2000) The influence of rock fabric and mineralogy on thermochemical sulfate reduction: Khuff Formation, Abu Dhabi. *Journal of Sedimentary Research* **70**, 1210-1221.

Xia J., Pérez-Salado Kamps Á., Rumpf B., and Maurer G. (2000) Solubility of hydrogen sulfide in aqueous solutions of the single salts sodium sulfate, ammonium sulfate, sodium chloride, and ammonium chloride at temperatures from 313 to 393 K and total pressures up to 10 MPa. *Industrial Engineering Chemistry Research* **39**, 1064-1073.

Yang C., Hutcheon I., and Krouse H.R. (2001) Fluid inclusion and stable isotopic studies of thermochemical sulphate reduction from Burnt Timber and Crossfield East gas fields in Alberta, Canada. *Bulletin of Canadian Petroleum Geology* **49**, 149-164.

Yokoyama C., Usui A., and Takahashi S. (1993) Solubility of hydrogen sulfide in isooctane, *n*-decane, *n*-tridecane, *n*-hexadecane and squalane at temperatures from 323 to 523 K and pressures up to 1.6 MPa. *Fluid Phase Equilibria* **85**, 257-269.

Zhang T., Ellis G.S., Wang K., Walters C.C., Kelemen S.R., Gillaizeau B., and Tang Y. (2007) Effect of hydrocarbon type on thermochemical sulfate reduction. *Organic Geochemistry* **38**, 897-910.

Zhang T., Amrani A., Ellis G.S., Ma Q., and Tang Y. (2008) Experimental investigation on thermochemical sulfate reduction by H_2S initiation. *Geochimica et Cosmochimica Acta* **72**, 3518-3530.

Zhang Y. and Frantz J.D. (1987) Determination of the homogenization temperatures and densities of supercritical fluids in the system $NaCl-KCl-CaCl_2-H_2O$ using synthetic fluid inclusions. *Chemical Geology* **64**, 335-350.

LIST OF FIGURES

236

LIST OF TABLES

liquid hydrocarbons and organic sulfur compounds considered in the calculations reported in this section.

APPENDIX

Table A1. Standard molal thermodynamic properties at 25°C and 1 bar and heat capacity power function coefficients of the minerals, inorganic gases, and liquid hydrocarbons and organic sulfur compounds considered in the present study.

	Formula	ΔG_f° [a,b]	ΔH_f° [a]	S° [c]	V° [d]	C_P° [c,e]	a [c]	b [f] $\times 10^3$	c [g] $\times 10^{-5}$
Minerals									
Anhydrite	$CaSO_4$	-315853	-342686 [h]	25.67 [i]	46.02 [j]	24.20	21.74 [k]	19.76 [k]	-3.05 [k]
Calcite	$CaCO_3$	-270100 [l]	-288772 [l]	22.15 [l]	36.934 [l]	19.57	24.98 [l]	5.24 [l]	-6.20 [l]
Sulfur	S	0	0	7.661 [m]	15.511 [n]	5.43	3.70 [o,p]	5.79 [o,p]	0 [o,p]
							3.32 [o,q]	7.03 [o,q]	0 [o,q]
							-56.91 [r,s]	112.2 [r,s]	31.57 [r,s]
							2.05 [r,t]	4.84 [r,t]	11.63 [r,t]
Gases									
Hydrogen sulfide	H_2S	-8021 [u]	-4931 [u]	49.185 [u]	0 [u]	8.17	7.81 [u]	2.96 [u]	-0.46 [u]
Carbon dioxide	CO_2	-94254 [u]	-94051 [u]	51.085 [u]	0 [u]	8.25	10.57 [u]	2.10 [u]	-2.06 [u]
Hydrocarbon liquids									
Methane	CH_4	-8976	-18895 [v]	30.57 [v]	58.2 [v]	14.68	-1.55 [v]	47.6 [v]	1.810 [v]
n-Butane	C_4H_{10}	-3349	-35057 [v]	55.30 [v]	97.0 [v]	33.49	-1.79 [v]	102.6 [v]	4.171 [v]
n-Pentane	C_5H_{12}	-2084	-41207 [v]	63.04 [v]	111.7	40.13	-0.90 [v]	118.9 [v]	4.958 [v]
n-Hexane	C_6H_{14}	-819	-47357 [v]	70.77 [v]	126.8 [v]	46.91	0.58 [v]	133.7 [v]	5.745 [v]
n-Nonane	C_9H_{20}	2975	-65805 [v]	93.99 [v]	175.0 [v]	67.95	8.35 [v]	169.3 [v]	8.106 [v]
n-Dodecane	$C_{12}H_{26}$	6765	-84254 [v]	117.21 [v]	224.6 [v]	89.82	19.16 [v]	197.5 [v]	10.467 [v]
n-Tridecane	$C_{13}H_{28}$	8030	-90404 [v]	124.95 [v]	241.3 [v]	97.28	22.84 [v]	207.2 [v]	11.254 [v]
Cyclohexane	C_6H_{12}	6444	-37321 [v]	48.84 [v]	110.4 [v]	37.17	-1.05 [v]	115.0 [v]	3.500 [v]
Ethylbenzene	C_8H_{10}	28644	-2978 [v]	61.08 [v]	131.7 [v]	44.39	10.01 [v]	103.3 [v]	3.184 [v]
n-Propylbenzene	C_9H_{12}	29909	-9128 [v]	68.82 [v]	148.8 [v]	51.17	11.32 [v]	119.3 [v]	3.804 [v]
2,7-Dimethylnaphthalene	$C_{12}H_{12}$	44198	3632 [w]	67.80 [w]	159.0 [w]	59.74	24.92 [w]	116.8 [w]	0.000 [w]

	Formula	ΔG_f° [a,b]	ΔH_f° [a]	S° [c]	V° [d]	C_P° [c,e]	a [c]	b [f] x10^3	c [g] x10^{-5}
Organic sulfur compounds (liquids)									
n-Decanethiol	$C_{10}H_{22}S$	8397	-66960 [v]	112.19 [v]	193.3 [v]	83.72	27.56 [v]	160.1 [v]	7.489 [v]
Cyclohexanethiol	$C_6H_{12}S$	8711	-33475 [x]	61.80 [x]	123.1 [x]	46.04	14.05 [x]	94.7 [x]	3.342 [x]
Benzenethiol	C_6H_6S	32099	15301 [x]	53.25 [x]	102.7 [x]	41.41	21.68 [x]	57.8 [x]	2.224 [x]
n-Butyl methyl sulfide	$C_5H_{12}S$	4336	-34328 [x]	72.24 [x]	124.2 [x]	47.61	19.1 [x]	83.6 [x]	3.190 [x]
Thiacyclopentane	C_4H_8S	9213	-17147 [x]	49.67 [x]	88.7 [x]	33.55	11.33 [x]	68.5 [x]	1.600 [x]
2-Methylthiacyclopentane	$C_5H_{10}S$	8355	-25054 [x]	58.63 [x]	107.5 [x]	41.07	15.25 [x]	81.1 [x]	1.456 [x]
Thiophene	C_4H_4S	28664	19029 [x]	43.30 [x]	79.5 [x]	29.61	12.78 [x]	51.4 [x]	1.338 [x]
2-Methylthiophene	C_5H_6S	27443	10747 [x]	52.22 [x]	96.8 [x]	35.79	16.27 [x]	59.3 [x]	1.636 [x]
Benzo[*b*]thiophene	C_8H_6S	45324	27180 [x]	51.48 [x]	116.0 [x]	44.91	25.45 [x]	68.8 [x]	-0.934 [x]
2-Methylbenzo[*b*]thiophene	C_9H_8S	44104	18898 [x]	60.40 [x]	133.3 [x]	51.09	28.94 [x]	76.7 [x]	-0.636 [x]
Dibenzo[*b*]thiophene	$C_{12}H_8S$	59558	33155 [x]	60.50 [x]	152.5 [x]	59.07	40.85 [x]	83.6 [x]	-5.964 [x]
4-Methyldibenzo[*b*]thiophene	$C_{13}H_{10}S$	57220	23755 [x]	69.42 [x]	167.4 [x]	65.95	45.65 [x]	90.6 [x]	-5.964 [x]

[a] Cal·mol^{-1} [b] Except otherwise indicated, computed from the values of ΔH_f° and S° and those for the entropies of the elements taken from Cox et al. (1989) [c] Cal mol^{-1}K^{-1} [d] cm^{3}mol^{-1} [e] Computed from Equation (10) [f] Cal mol^{-1}K^{-2} [g] Cal K mol^{-1} [h] Majzlan et al. (2002) [i] Robie et al. (1989) [j] Calculated from cell parameters given by Majzlan et al. (2002) [k] Generated by regression with Equation (10) of experimental heat capacities reported by Robie et al. (1989) [l] Helgeson et al. (1978) [m] Cox et al. (1989) [n] Robie et al. (1979) [o] Generated by linear regression of experimental heat capacities reported by Eastman and McGavock (1937) and West (1959) [p] Rhombic sulfur [q] Monoclinic sulfur [r] Generated by regression with Equation (10) of experimental heat capacities reported by West (1959) [s] Liquid sulfur below 433 K [t] Liquid sulfur above 433 K [u] Value adopted in the slop98.dat database [v] Helgeson et al. (1998) [w] Richard and Helgeson (1998) [x] Richard (2001)

Table A2. Standard molal thermodynamic properties at 25°C and 1 bar and HKF parameters for the aqueous species considered in the present study.

Species	ΔG_f° [a]	ΔH_f° [a]	S° [b]	a_1 [c] x10	a_2 [a] x10^{-2}	a_3 [d]	a_4 [e] x10^{-4}	c_1 [b]	c_2 [e] x10^{-4}	ω [a] x10^{-5}	Reference
CO_3^{2-}	-126191	-161385	-11.95	2.8584	-3.9844	6.4142	-2.6143	-3.3206	-17.1917	3.3914	f
HCO_3^-	-140282	-164898	23.53	7.5621	1.1505	1.2346	-2.8266	12.9395	-4.7579	1.2733	f
$CO_{2(aq)}$ [g]	-92250	-98900	28.1	6.2466	7.4711	2.8136	-3.0879	40.0325	8.8004	-0.02	h
$CH_3COOH_{(aq)}$	-94760	-116100	42.7	8.8031	12.4572	3.5477	-3.2939	40.8037	-0.9218	-0.2337	i
CH_3COO^-	-88270	-116180	20.6	7.7525	8.6996	7.5825	-3.1385	26.3	-3.86	1.3182	i
$CH_3SH_{(aq)}$	-1840	-11650	38.60	8.5523	23.5100	-25.8188	-3.7509	62.0673	-5.5753	-0.8704	j
Ca^{2+}	-132120	-129800	-13.5	-0.1947	-7.2520	5.2966	-2.4792	9.00	-2.522	1.2366	f
$CaCO_{3(aq)}$	-262850	-287390	2.5	-0.3907	-8.7325	9.1753	-2.4179	-11.5309	-9.0641	-0.038	k
$CaHCO_3^+$	-273830	-294350	16.0	3.7060	1.2670	5.2520	-2.8310	41.7220	8.3360	0.3080	l,r
$Ca(CH_3COO)^+$	-221660	-245620	12.5	5.9002	6.6232	3.1505	-3.0527	58.1976	13.8857	0.3636	m
$Ca(CH_3COO)_{2(aq)}$	-311570	-362650	32.3	12.9911	23.9379	-3.6556	-3.7685	115.9068	35.2043	-0.0300	m
$CaCl^+$	-162550	-169250	-1.5	2.6670	-1.2694	6.2489	-2.7265	23.6652	1.2044	0.5756	n
$CaCl_{2(aq)}$	-194000	-211060	6	6.2187	7.4058	2.8322	-3.0851	23.961	3.272	-0.038	k
$CaOH^+$	-171300	-179600	6.7	2.7243	-1.1303	6.1958	-2.7322	11.1286	-2.7493	0.4496	o
$CaSO_{4(aq)}$	-312930	-345900	5	2.4079	-1.8992	6.4895	-2.7004	-8.4942	-8.1271	-0.001	k
Cl^-	-31379	-39933	13.56	4.0320	4.8010	5.5630	-2.847	-4.40	-5.714	1.4560	f
$HCl_{(aq)}$	-30410	-42054	3.2	1.2547	-4.7177	7.6043	-2.5840	16.7134	2.8727	-0.7	q,r
H^+	0	0	0	0	0	0	0	0	0	0	f
$H_2O_{(l)}$	-56688	-68317	16.712	—	—	—	—	—	—	—	p
OH^-	-37595	-54977	-2.56	1.2527	0.0738	1.8423	-2.7821	4.15	-10.346	1.7246	f
Na^+	-62591	-57433	13.96	1.8390	-2.2850	3.2560	-2.726	18.18	-2.981	0.3306	f
$Na(CH_3COO)_{(aq)}$	-150720	-173540	34.2	8.3514	12.6125	0.7884	-3.3003	49.8989	12.2617	-0.0300	m

Species	ΔG_f° [a]	ΔH_f° [a]	S° [b]	a_1 [c] x10	a_2 [a] x10^{-2}	a_3 [d]	a_4 [e] x10^{-4}	c_1 [b]	c_2 [e] x10^{-4}	ω [a] x10^{-5}	Reference
$Na(CH_3COO)_2^-$	-238470	-292400	44.0	16.2062	31.7884	-6.7416	-4.0930	114.6437	31.5846	0.9633	m
$NaCl_{(aq)}$	-92910	-96160	28	5.0364	4.5189	3.9669	-2.9658	10.798	-1.3031	-0.038	k
$NaSO_4^-$	-241476	-273733	25.46	6.4638	8.0045	2.5970	-3.1098	14.4928	-4.1182	1.2422	q,r
SO_4^{2-}	-177930	-217400	4.50	8.3014	-1.9846	-6.2122	-2.6970	1.64	-17.998	3.1463	f
HSO_4^-	-180630	-212500	30.0	6.9788	9.2590	2.1158	-3.1618	20.0961	-1.9550	1.1748	f
$H_2S_{(aq)}$	-6673	-9001	30.0	6.5097	6.7724	5.9646	-3.0590	32.3	4.73	-0.10	h

[a] cal·mol^{-1} [b] cal·mol^{-1}·K^{-1} [c] cal·mol^{-1}·bar^{-1} [d] cal·K·mol^{-1}·bar^{-1} [e] cal·K·mol^{-1} [f] Shock and Helgeson (1988) [g] The properties for this species can be combined with those for liquid H_2O to obtain those of aqueous carbonic acid in accord with $CO_{2(aq)} + H_2O_{(l)} = H_2CO_{3(aq)}$ by making the usual assumption that all dissolved CO_2 is present as H_2CO_3 (Drever, 1997, p. 41) [h] Shock et al. (1989) [i] Shock and Helgeson (1990) [j] Schulte and Rogers (2004) [k] Sverjensky et al. (1997) [l] Values used (but not tabulated) by Shock and Koretsky (1995) [m] Shock and Koretsky (1993) [n] Values taken from the original SPRONS92.DAT database of the SUPCRT92 computer program (Johnson et al., 1992) – see footnote 4 [o] Shock et al. (1997) [p] Johnson et al. (1992) – the apparent standard molal Gibbs energy of formation of liquid water is calculated in the SUPCRT92 computer program using equations of state developed by Levelt Sengers et al. (1983) and Haar et al. (1984) [q] Values used (but not tabulated) by McCollom and Shock (1997) [r] Values adopted in the slop98.dat database